Amyloids:

from molecular structure to mechanical properties

This thesis was reviewed by:

Prof.dr. R. Mezzenga	ETH Zürich
Prof.dr. A. Philipse	Utrecht University
Dr. W. Roos	VU University
Prof.dr. S. Woutersen	University of Amsterdam

The research described in this thesis was performed at the FOM Institute AMOLF, Science Park 104, 1098 XG Amsterdam, the Netherlands. This work is part of the research program of the Foundation for Fundamental Research on Matter (FOM), which is financially supported by the Netherlands Organisation for Scientific Research (NWO).

ISBN/EAN: 978-90-77209-84-4

A digital version of this thesis is available at www.ubvu.vu.nl/dissertations and www.amolf.nl/publications/theses. Printed copies can be obtained by request to the library at FOM Institute AMOLF, library@amolf.nl.

VRIJE UNIVERSITEIT

Amyloids:
from molecular structure to mechanical properties

ACADEMISCH PROEFSCHRIFT

ter verkrijging van de graad Doctor aan
de Vrije Universiteit Amsterdam,
op gezag van de rector magnificus
prof.dr. F.A. van der Duyn Schouten,
in het openbaar te verdedigen
ten overstaan van de promotiecommissie
van de Faculteit der Exacte Wetenschappen
op donderdag 2 oktober 2014 om 9.45 uur
in de aula van de universiteit,
De Boelelaan 1105

door
Corianne Christa Gelderloos

geboren te Apeldoorn

promotor: prof.dr. G.H. Koenderink

Contents

Chapter 1

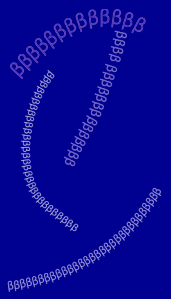

Introduction

Based on:

Corianne C. van den Akker, Michael Schleeger, Mischa Bonn, Gijsje H. Koenderink: *Structural basis for the polymorphism of β-lactoglobulin amyloid-like fibrils*. In: Uversky V, Lyubchenko Y: Bio-nanoimaging: Protein Misfolding & Aggregation. Waltham, MA: Elsevier (2014).

Michael Schleeger, Corianne C. van den Akker, Tanja Deckert-Gaudig, Volker Deckert, Krassimir P. Velikov, Gijsje H. Koenderink, Mischa Bonn: *Amyloids: from molecular structure to mechanical properties*. Polymer 54, 2473–2488 (2013).

1.1 Amyloids

Many peptides and proteins of diverse sequence, native structure, and function self-assemble into morphologically similar fibrillar aggregates known as amyloids.[1] It is increasingly apparent that the amyloid state is an intrinsic characteristic of polypeptide molecules under denaturing conditions.[1] Amyloid fibrils are characterized by a universal core structure of β-strands that runs perpendicular to the long axis of the fibril[2], providing a straight, unbranched structure. Amyloid fibrils show remarkable mechanical properties: they are both strong and rigid, with a Young's modulus comparable to that of silk.[3] The aim of this thesis is to elucidate the biophysical properties of amyloid fibrils over a range of length scales: from their molecular structure to single fibril mechanics and to macroscopic rheology of fibril suspensions.

In this chapter I will provide a background on the current knowledge of the molecular structure and mechanical properties of amyloid fibrils. A variety of bulk spectroscopic techniques have been used to elucidate the molecular structure of amyloids. I will shortly describe these bulk techniques, and introduce two novel spectroscopic techniques that only recently were used for the first time to study amyloids and which I used in this thesis. Furthermore, the different model proteins and peptides that I investigated are described, and I provide a short introduction on polyphenols: natural molecules which are a potential candidate for treatment of amyloid-related diseases. Finally, the scope of this thesis is described.

1.1.1 Pathological amyloids

A broad range of human diseases, generally referred to as (protein) conformational diseases, are related to the formation of amyloids, which typically form extracellular deposits or intracellular inclusions (Figure 1.1a).[2] There are more than 30 different diseases, which can be classified into three different groups. *Systemic amyloidosis* are characterized by the accumulation of mature fibrils on a large scale, where up to kilograms of protein can accumulate in the body and ultimately lead to organ failure and death by physical blockage.[4,5] A second group includes pathological states in which amyloid formation results in a reduction of the *protein quantity* that is available for normal functions, for example in cystic fibrosis.[2] However, the largest group of conformational diseases is associated with the conversion of proteins or peptides into *amyloid fibrils* that form plaques (extracellular) or inclusions (intracellular).[2] The most frequently-occurring examples are Alzheimer's and Parkinson's disease and type II diabetes mellitus. Originally, it was believed that the fibrils were the major toxic species. It is now believed that in many cases the oligomeric species are even more toxic than the fibrils.[6] However, there are many open questions and no definitive conclusions can

be drawn about the mechanisms of cytotoxicity or the generality of these mechanisms for different diseases.[2]

1.1.2 Functional amyloids

While much remains to be discovered regarding disease-related amyloid formation, it is becoming increasingly clear that certain amyloids serve a useful purpose in Nature. There is a growing list of diverse functional amyloids in organisms ranging from bacteria and fungi to invertebrates and man.[2,7] E. coli and salmonella bacteria produce amyloids called curli or tafi, which are thought to have a role in cell adhesion, cell aggregation and biofilm formation (Figure 1.1b).[8-11] A study of biofilm samples harvested from a variety of habitats including lakes and drinking water reservoirs, showed that amyloids are expressed by 5-40% of all bacteria that were found.[12] Amyloids are also found in egg shells of fish and insects, where they are thought to provide protection and stability.[10] In humans, the protein Mα forms amyloids in a highly regulated way after several cleavage steps.[13,16] Mα is the main component of melanosomes, the organelles that synthesize melanin.[7,10] The Mα amyloids are thought to provide a template for the chemical synthesis of melanin.[10] Thus, amyloids do not always represent a 'misfolded' toxic protein structure. It is an interesting question how functional amyloids avoid pitfalls regarding oligomer cytotoxicity.[7] Possible mechanisms are the use of ancillary proteins or the spatial separation provided by different cellular compartments.[7]

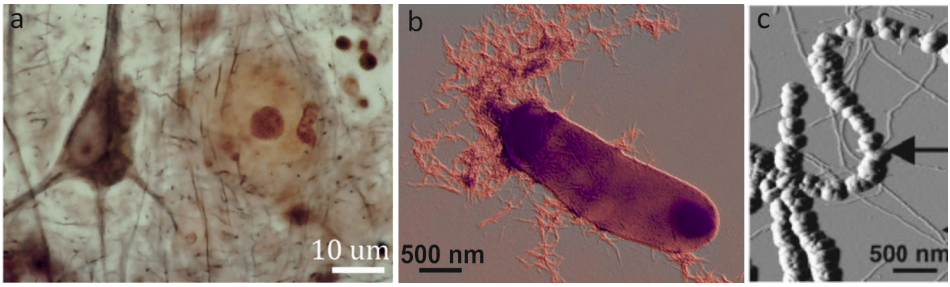

Figure 1.1: a) Examples of disease-related, functional and *de novo* amyloid fibrils. a) Staining of amyloid plaques in the brains of an Alzheimer's patient. Adapted from Graeber et al.[13] b) Transmission electron microscopy image of curli, functional amyloid fibrils formed by bacteria. Adapted from Hammer et al.[14] c) Amyloid fibrils coated with gold, as a possible application of amyloids. Adapted from Scheibel et al.[15]

1.1.3 Applications

From a materials science perspective, the amyloid pathway to form protein fibrils has many advantages. The fibrils readily self-assemble from natural proteins including edible proteins (such as β-lactoglobulin[16]), pharmaceutically relevant proteins (such as insulin[17,18]), or from simpler *de novo* designed peptides.[19,20] Fibrils can also be formed from proteins or peptides fused with functional proteins such as green fluorescent protein or enzymes, or with peptides such as cell adhesion motifs.[21,22] The mechanical properties are remarkably insensitive to the protein sequence,[23] and robust under extreme conditions, such as high temperature, high concentrations of detergents and denaturants, and strong physical forces.[24] All of these properties make amyloid fibrils attractive for applications. Indeed, there has recently been a surge of activity directed at designing materials from amyloids.[25-29] Amyloid fibrils have been coated with metal[24] and conducting polymers[30] to form conducting nanowires (Figure 1.1c). Also their use as drug delivery vehicles[31] or scaffolds in tissue engineering[32,33] are highly promising.

1.2 Structure, formation and polymorphism

1.2.1 Structure

Amyloid fibrils formed from structurally unrelated peptides and proteins share a surprisingly similar structure. The change in secondary structure of the native protein to a β-sheet-rich structure represents one of the main determinants of amyloid formation. Amyloid fibrils show a characteristic X-ray diffraction pattern, caused by a so-called cross-β core structure. This core structure is composed of a stack of β-strands perpendicular to the fibril axis with an axial spacing of 4.8 Å and an intersheet spacing in the order of 9-11 Å.[34,35] The elongated stack is stabilized by a dense network of hydrogen bonds. The sequence-specific side-chains tend to affect the propensity to form fibrils.[36] As an example, a model of a protofibril from human amyloid polypeptide (hIAPP, related to type II diabetes mellitus) is shown in Figure 1.2. A single hIAPP molecule forms two β-sheets, separated by a loop region. Axial views along the fibril backbone reveal the dense stacking of four β-strands from two individual hIAPP molecules per layer. This in-register packing of parallel β-sheets is one of the prominent characteristics of amyloids. A side view (Figure 1.2d) illustrates the 4.8 Å axial spacing between β-strands and the parallel orientation of the β-sheets to the fibril axis. The high degree of structural order within amyloid protofibrils leads to very strong interactions between the protofibrils within a mature amyloid fibril (for instance 310 $k_BT/\mu m$ for insulin[17]).

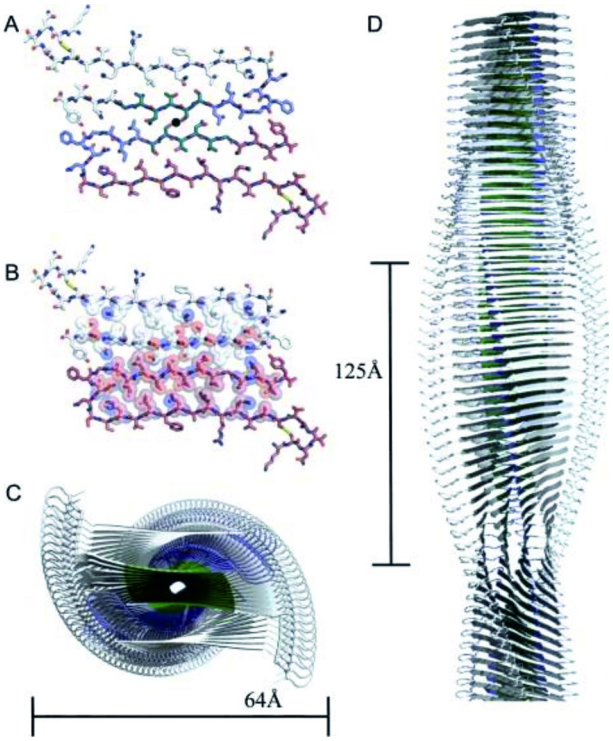

Figure 1.2: Structural model of an amyloid protofibril from human islet amyloid polypeptide (hIAPP) based on the crystal structure from fragments of the peptide. (a) to (c) View along the fibril axis. (a) Two hIAPP molecules, each consisting of a hairpin and a steric zipper interface, mate in a dry steric zipper around the fibril axis. The space filling model (b) emphasizes the tight steric zipper interface of the two IAPP molecules. (c) Stacking of β-sheet segments which are coiled up around the fibril's axis. (d) Side view, revealing the typical 4.8 Å spacing between layers of stacked β-strands. Adapted from Wiltzius et al.[35]

1.2.2 Amyloid formation mechanisms

The generally accepted model for amyloid fibril formation comprises a nucleation and growth pathway. During the nucleation stage, monomers assemble into oligomers, which then form protofilaments. The protofilaments can further associate into fibrils (Figure 1.3). Intrinsically disordered peptides such as hIAPP can form amyloids under physiological conditions. Globular native proteins can be triggered to form amyloids by denaturing conditions. Under normal environmental conditions, natively folded proteins are in equilibrium with their partially unfolded state. This equilibrium can be displaced towards partially or completely unfolded states, if conditions such as temperature and pH are changed outside of the physiological range. Partially unfolded proteins can refold into cross-β-sheet secondary structure,[37] which can induce a linear growth of

oligomers.[38] An alternative mechanism of oligomer formation is via initial hydrolysis of proteins into short aggregation-prone peptide fragments. This mechanism has for instance been demonstrated in case of the milk protein β-lactoglobulin (β-lg), by mass spectrometry measurements. Upon heating at acidic pH, β-lg forms fibrils composed of peptide fragments rather than intact β-lg monomers.[39] The same mechanism has since also been demonstrated for other proteins.[40] Which one of the two routes – partial unfolding or fragmentation – is followed, appears to depend on the conditions employed to promote fibrillation.[2] After the rate-limiting step of oligomer formation, elongation into protofilaments is a rapid process. Based on the observation of spontaneous alignment of protofilaments in atomic force microscopy (AFM) images, it has been suggested that their subsequent association into mature fibrils is driven by short-range attractions.[41] These attractions are presumably hydrophobic in origin.

1.2.3 Polymorphism

Although amyloids fibrils have a universal core structure, the overall structure depends on the peptide composition and on specific assembly conditions, including pH and temperature. Even under identical conditions, amyloid fibrils are polymorphic. Such polymorphic behavior is for instance well-documented for the amyloid β (Aβ) peptide, which forms amyloids with distinct morphologies under quiescent or agitated conditions.[42] Intriguingly, the two fibril types differed in their cytotoxicity in cell culture models.[42] It has been shown that a great variety of polymorphic structures can exist within amyloid fibrils formed from the same protein or peptide.[2,43-46] Variations in the protofilament number and arrangement as well as different polypeptide conformations have been reported.[45] Morphological variations are increasingly emerging as a generic property of amyloid formation. For example, in amyloid samples formed from bovine serum albumin (BSA), six distinct classes of amyloid fibrils were identified by atomic force microscopy (AFM) imaging, including different types of left-handed twisted ribbons, right-handed helical ribbons and nanotubes. The distinct fibril types showed different rigidities and over time, transformations from one type into another were observed.[47] It has been suggested that variations in morphology are linked to heterogeneity in molecular structure.[2,48] Preformed seeds can propagate their morphology and structure, resulting in fibrils that inherit the characteristics of the template.[43] The implications of amyloid polymorphism are wide-spread: on the one hand it complicates understanding the molecular basis of amyloid-related diseases and designing treatments, but on the other hand it provides opportunities for applications of amyloids in for instance materials science and food industry.

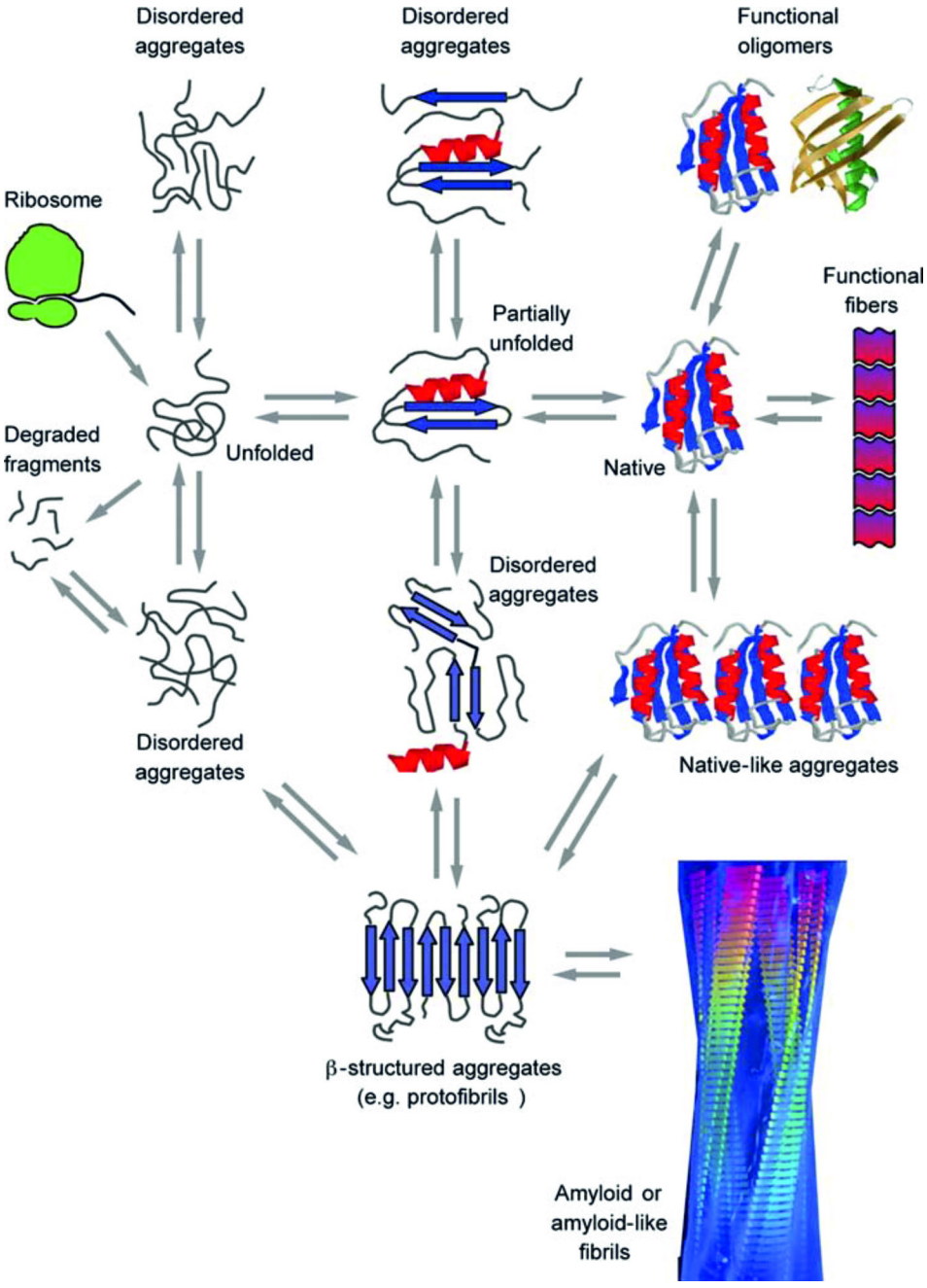

Figure 1.3: A schematic representation of the manifold pathways by which proteins and peptides can convert from folded or unfolded states into amyloid fibrils with a universal cross-β core structure. Figure was adapted from Chiti et al.[2]

1.3 Mechanics

The β-sheet core makes amyloid fibrils rigid, with a Young's modulus similar to that of silk, and strong, with an ultimate tensile strength comparable to that of steel.[3] The origin of these remarkable mechanical properties is still not fully understood. There are several theoretical models which assign the large rigidity and strength of amyloid fibrils to the strong hydrogen-bonding of the β-sheet core.[49,50] However, these models assume a perfectly packed molecular structure, whereas amyloid fibrils may in reality have imperfect β-sheet cores with interruptions along the long axis. Moreover, it is unclear how the side groups on the protofilament surface will affect the mechanical response. Below we will review recent biophysical studies of the mechanical properties of single fibrils, and indicate some experimental techniques that are being used to characterize the mechanics of amyloid fibrils.

1.3.1 Fibril mechanics

1.3.1.1 Bending rigidity and fibril mechanics

A key parameter characterizing the conformation of a biopolymer is its bending rigidity. The bending rigidity is often expressed by the length scale beyond which the fibril shows significant curvature due to thermal forces, quantified by the persistence length, L_p.[51,52] The bending rigidity can be measured by a variety of methods, which are either based on active deformation of the fibrils, or on analysis of their spontaneous, thermal bending fluctuations.

Active deformation of fibrils can be achieved by AFM, as demonstrated in a recent study on insulin amyloid fibrils composed of two protofibrils.[3,50] Essentially, the experiment was a microscopic equivalent of a traditional three-point bending test: fibrils were deposited on a silicon substrate with nanoscale grooves. With an AFM probe, a controlled load was applied on fibrils suspended over a groove, while monitoring the deflection of the cantilever that acts as the force sensor. The Young's modulus was determined from the linear (small-force) part of the deflection curve, giving an average Young's modulus of E = 3.3 ± 0.4 GPa and shear modulus of G = 0.28 ± 0.2 GPa. This Young's modulus corresponds to a persistence length of 42 ± 30 μm, which is much larger than the typical fibril contour length of 3-6 μm. An advantage of this technique is that the measurements are performed on fibrils in their natural, hydrated state. However, the experiments are technically challenging because of the small (~10 nm) diameter of amyloid fibrils.[53]

Technically, it is easier to measure the bending rigidity based on the spontaneous, thermal fluctuations of fibrils. The basic idea is to measure the shape of fluctuating fibrils, either taking snapshots of a large ensemble of fibrils at a given moment in time, or taking time-lapse movies of a single fibril. Until now, most studies of amyloid fibrils used the first method, analyzing the shape of a large ensemble of fibrils immobilized on a surface. Usually, amyloid fibrils are imaged by AFM,[54-57] which requires fibril deposition on a mica or glass surface and drying. Alternatively, cryo-transmission electron microscopy (cryo-TEM) or scanning transmission electron microscopy (STEM) can be used, which has the benefit that fibrils are preserved (snap-frozen) in a hydrated state.[58] The persistence length L_p can be calculated by measuring for each fibril the contour length, C, and the end-to-end distance, E (Figure 1.3). According to the worm-like chain model, the mean-squared end-to-end distance of semiflexible filament on a two-dimensional surface as a function of C depends on L_p as follows:

$$\langle E^2 \rangle_{2D} = 4\, L_p\, C\, (1 - 2\, L_p / C\, (1 - e^{-C/2Lp})).$$

This equation assumes that the fibrils interact weakly with the surface and can relax to a two-dimensional equilibrium conformation.[51,54,57] However, if the interaction between the fibril and the surface is much stronger than the thermal energy, the fibrils will be trapped by the surface, leading to more condensed fibril conformations. In this case, the mean-squared end-to-end distance of the fibril amounts to[54]:

$$\langle E^2 \rangle_{3D} = 4/3\, L_p\, C\, (1 - L_p / C\, (1 - e^{-C/Lp})).$$

An alternative method of determining L_p is by analyzing the correlation of bond angles along the contour:

$$L_p = \langle l \rangle / (1 - \langle \cos \varphi \rangle),$$

where $\langle l \rangle$ is the average segment length and φ is the angle between segments (Figure 1.4).[59]

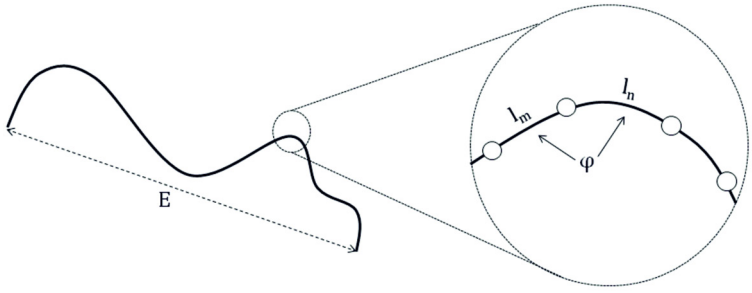

Figure 1.4: Schematic depiction of the end-to-end length E, the segment length l, and the angle between segments φ, for a semiflexible filament.

One of the best-studied types of amyloid fibrils with this analysis method are those formed from the model protein β-lactoglobulin (β-lg). Depending on the self-assembly conditions, these fibrils have widely varying persistence lengths and mostly fall into one of two classes: straight fibrils or worm-like fibrils. Straight fibrils generally have a persistence length that is comparable to the contour length, ranging from about 600 nm to several μm.[55-57,59-63] Worm-like fibrils are much more flexible, with a persistence length of only 10-90 nm.[54,55,57,59-61,63] A third type of morphology, rod-like fibrils with a persistence length of 135 nm, was formed from β-2-microglobulin.[57] It has to be noted that amyloid fibrils are polymorphic; even under a given set of conditions, fibrils have different persistence lengths.

In contrast to nanomechanical manipulation assays, the fluctuation analysis approach gives a global measure of the persistence length of a fibril, because fluctuations are evaluated on a larger length scale. However, fibril imaging by AFM or EM requires deposition on a surface and drying, which can potentially lead to artifacts. One way to overcome this problem is to measure the shape of freely fluctuating fibrils in space by fluorescence microscopy.[64,65] Because of the low resolution of optical microscopes in the z-direction, fibrils are typically confined in a quasi-2D geometry by sandwiching them between two glass cover slips. Rather than extracting the persistence length from the static shape of an ensemble of fibrils, the persistence length is now calculated by tracking the fibril shape fluctuations over time. These experiments have been performed for yeast prion fibrils labeled with a fluorescent dye.[65] The persistence length was found to be a few micrometers, depending on the assembly conditions. In addition to the bending rigidity, also the bending dynamics can be determined from time-lapse movies, as demonstrated for actin filaments and microtubules.[52]

A second way to overcome problems associated with drying or surface immobilization is to perform light scattering of dilute fibril suspensions, again using the worm-like chain model to interpret the data. The persistence length of β-lg amyloid fibrils formed at varying ionic strengths was determined by a combination of light scattering (LS) and small-angle neutron scattering (SANS).[61] The persistence length decreased with increasing ionic strength from 600 to 38 nm. These values are in reasonable agreement with the persistence lengths obtained with imaging techniques.

The persistence length of β-lg fibrils also has been estimated using an adjusted random contact model, based on measurements of the storage (or elastic) modulus *G'* of fibril gels by rheology.[60] The critical percolation concentration was determined by measuring *G'* as a function of protein concentration. It was assumed that for a fibrillar system the percolation mass fraction follows from the number of contacts per fibril and the excluded volume of each fibril. Assuming simple excluded volume interactions, the

excluded volume of the fibril can be determined by the diameter, contour length and persistence length. In case of charged fibrils, an effective diameter has to be used that accounts for the presence of a finite-sized double layer. The estimated persistence length was 1.6 ± 0.4 µm for β-lg fibrils formed at pH=2 and 80 °C, consistent with imaging data.

1.3.1.2 Ultimate tensile strength and fracture behavior

The ultimate strength of single fibrils has been measured by nanomechanical manipulation with AFM. For insulin fibrils, the ultimate strength was measured by actively bending fibrils suspended over a groove with an AFM tip. The mean ultimate strength for fibrils composed of two protofibrils was 0.6 ± 0.4 GPa. Strikingly, this is in the same order of magnitude as the strength of steel (0.6-1.8 GPa) and silk (1.0-1.5 GPa).[3,50] The corresponding breakage force was estimated to be in the range of 300 to 500 pN.[3]

Microscopic insight into the molecular mechanisms that determine the strength of amyloid fibrils can be obtained by force spectroscopy, where peptide strands are pulled out of fibrils immobilized on a surface with a small AFM tip. Such experiments were reported for fibrils formed from Aβ(1-40) or Aβ(25-35) peptides.[66] Strands of more than 100 nm in length could be pulled out of the fibrils and stretched. The measured force-extension behavior was fitted with a worm-like chain model, from which a persistence length of about 0.4 nm was calculated. Based on these results, the authors concluded that the strands were β-sheets that were unzipped from the fibrils. The unzipping process was fully reversible. Fibrils formed from Aβ(1-42) peptide showed a lower unzipping force (~23 pN) than fibrils formed from Aβ(1-40) peptide (~33 pN).[66,67] Unzipping experiments were also attempted on amyloids formed from Als cell adhesion proteins of a fungal pathogen, but in this case unzipping of mature fibrils was not possible. However, zipper interactions were detected between monolayers of Als proteins and an Als amyloid sequence attached to an AFM tip. The characteristic force signatures corresponded to the mechanical unzipping of β-sheet interactions formed between parallel Als proteins, with an unzipping force of about 30 pN.[68]

The weak point of the above mentioned zipping experiments is that the measurements were based on nonspecific binding between tip and fibril. Therefore, the variability between individual measurements likely results from random and multiple attachment sites of the protein to the tip. The nanomechanical properties of human prion protein amyloid (huPrP90-231) were investigated using specific binding between the AFM tip and the fibril.[69] The protein was functionalized by replacing one amino acid for a cysteine, which is known to bind covalently with a gold-coated AFM tip. Again, force-

extension curves showed elastic stretching for small retractions, characteristic of entropic stretching of a disordered peptide chain between the β-sheet core and the covalent attachment to the tip. At larger retractions of the tip, rupture occurred, which likely reflects the mechanical extraction of the prion protein from the core of the amyloid fibril. The force at which rupture took place was dependent on the loading rate, with typical values of order 100 pN.

Surprisingly, although amyloid fibrils are generally regarded as mechanically strong, they do break under the influence of thermal forces. In fact, spontaneous fracture is thought to be a key feature of the kinetics of fibril growth, since fragmentation increases the number of free ends, thus enhancing the rate of fibril growth.[3,70] It has also been shown that amyloid fibrils break easily by elongational flow.[71] Whey protein isolate (WPI) amyloid fibrils already fracture at an elongational flow rate of only 8 s^{-1}, which is much lower than the flow rate where DNA strands break, which is close to 10,000 s^{-1}. The fracture force estimated from these observations was 0.1 pN from the extensional flow experiment and 4 pN from the stability of fibrils against thermal force.[71] It is still unclear how these low fracture forces may be reconciled with the much higher fracture forces of 300-500 pN estimated from active nanomanipulation experiments of insulin fibrils.[3] It will be interesting to connect these mechanical measurements to the underlying molecular structure, which likely varies with the peptide used as well as on the assembly conditions. Information on the molecular structure can be obtained with vibrational spectroscopy, as summarized in section 1.4.4.

1.3.1.3 Extensibility

It was shown that the fundamental structural unit of several kinds of amyloid fibrils including Aβ is the β-helix structure.[72-74] The β-helix is a protein motif formed by the association of parallel β-strands in a helical pattern with either two or three faces (Figure 1.5).[75] The mechanical properties of this structure under tension and compression were studied with molecular dynamics (MD) simulations. The calculated maximum tensile force was 522 pN, while the maximum compressive force was much higher, namely 3,150 pN. The simulations revealed that the β-helix structure is extremely extensible and can sustain tensile strains up to 800% without rupture of the covalently bonded protein backbone.[75] The model that was used only accounts for the core structure of certain amyloids, not including effects of side chains. It will be interesting to test by experiments the prediction that amyloid fibrils should be highly extensible.

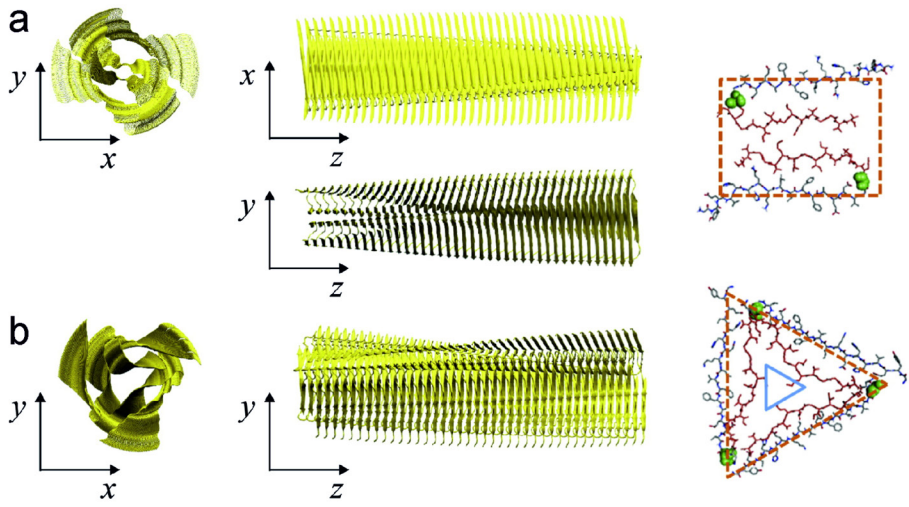

Figure 1.5: Structures of a) twofold and b) threefold symmetric assemblies of Aβ amyloid fibrils. Adapted from Xu et al.[76]

1.3.2 Network mechanics

1.3.2.1 Microscopic properties of amyloid networks

For applications of amyloid fibrils in food products, tissue engineering, and materials sciences, the macroscopic mechanical properties of suspensions and networks of fibrils are relevant. Network mechanics is determined by a combination of fibril mechanics and the spatial organization of fibrils and their interactions. The spatial organization of amyloid fibril networks depends on fibril rigidity: when the fibrils are long, thin, and rigid, they can form liquid crystalline phases or gels already at low concentrations.[77] The interactions between amyloid fibrils are not well-studied, but are thought to be highly dependent on the side chains on the surface of the fibrils, which can for instance confer a pH-dependent electrostatic charge to the fibrils.[53] Bulk rheology has been used to probe the mechanical properties of networks of amyloid fibrils.[59,78,79] The networks generally form weak viscoelastic gels. However, quantitative comparisons between rheology measurements and theory are still lacking, since the fibril morphology was not well-defined.

1.3.2.2 Rheological properties

Rheological properties relate to the flow properties of materials in response to an applied deformation. The most commonly used type of deformation is a shear

deformation, where a material is deformed between two parallel plates by moving one of the plates while the other is kept stationary. Typically, one applies either a steady shear (constant shear rate) or an oscillatory shear of controlled strain amplitude and frequency, and measures the stress response. When the material is a Newtonian fluid with a constant viscosity such as water, the stress in a steady shear measurement is proportional to the applied shear rate with a constant of proportionality that is given by the steady-shear viscosity. In contrast, polymeric materials are usually viscoelastic and non-Newtonian, with a viscosity that does depend on shear rate. Typically, the viscosity is constant at low strain rates, but decreases when the strain rate is raised above a critical value, a response that is known as shear thinning. When the polymer material is elastic, a more suitable measurement is an oscillatory shear measurement. Oscillatory measurements measure the complex shear modulus G^*, which is the constant of proportionality between the stress and the strain. G^* is a complex quantity with a storage modulus G' that reflects the elastic stress response that is in-phase with the applied strain, and a loss modulus G'' that reflects the viscous stress response that is out-of-phase with the applied strain.[77]

Until now, oscillatory measurements of amyloid networks have primarily focused on resolving the gelation time and critical percolation concentration of fibrils formed from food-related proteins including β-lg, bovine serum albumin (BSA) and ovalbumin at pH=2.[60,79-81] Steady shear measurements were used to measure the shear-rate dependence of the viscosity of suspensions of whey protein fibrils with lengths of several μm.[78] In all cases the suspensions were shear-thinning.[78,80] Oscillatory measurements have also been used to measure the influence of pH and ionic strength on gel strength. At pH=3.35, the whey protein β-lg forms worm-like fibrils with a persistence length of 35 nm and a diameter of 5 nm.[59] The viscosity of these fibrillar networks was observed to increase with protein concentration. Amyloid fibrils formed from whey protein concentrate (WPI) in the presence of salt showed a worm-like morphology, while fibrils formed without salt were long and straight. The presence of salts increased the viscosity compared to control fibrils formed without salt.[80] The viscosity depends on different parameters, including the volume fraction of fibrils, the fibril morphology and the interactions between fibrils. Because the effect of mono- and multivalent salts on these parameters was not determined, the mechanism behind the increase in viscosity is still not understood. There are few rheological studies of amyloids other than whey proteins-related fibrils. Weak, solid-like behavior was also reported for hydrogels formed from amyloids of the Alzheimer related Aβ peptide, Aβ(16-20) formed at high concentrations (3% w/v).[79]

An alternative method to measure the rheology of soft polymeric materials is by microrheology (MR), which is a collection of techniques used to determine the local properties of a material from the motion of embedded, small tracer particles. The most popular MR technique is video particle tracking, where the thermally induced motions of the tracer particles are observed by optical microscopy.[82] Particle tracking is a convenient method to obtain a spatial map of variations in the viscoelastic properties of heterogeneous samples.[83] An advantage of MR over bulk rheology is the possibility to use small sample volumes (down to 5 µL) and to determine the rheology over a broad frequency range. Particle tracking MR has been used to study the sol-gel transition in amyloid networks. Gels of β-lg fibrils were prepared at pH=7 and room temperature by adding alcohol.[82] Under these conditions, wormlike fibrils are formed.[84] Latex particles with a diameter of 0.5 µm were used to observe the time evolution of network formation for β-lg concentrations at and above the critical gelation concentration of 4% w/v. Over time, a shift from purely viscous to viscoelastic behavior was observed, indicative of fibril formation. Eventually, a solid gel was formed. Based on the mean squared displacement (MSD) of the probe particles, the elastic and loss moduli over a large frequency range could be calculated. Similar experiments were also performed for β-lg amyloid fibrils formed by decreasing the pH to 2 and heating to 80°C. Under these conditions, the fibrils that are formed are long and straight, and the critical concentration for gel formation was less than 3% w/v. The gels that were formed after about 100 min showed behavior typical of weak gels, with a plateau in *G'* that became more pronounced at longer incubation times up to 200 min.[85]

Particle tracking microrheology has a frequency range that is limited by the camera acquisition rate and also by the inherent localization error of ca. 20-50 nm in the particle position. These limitations can be overcome by using laser tweezers combined with quadrant photodiodes for sub-nanometer localization of probe particles embedded in a network. By using weak laser beams, the thermal fluctuations of the particles can be detected by laser-interferometry. As shown for actin networks and worm-like micelles, this method affords a wide frequency window of 0.1-100 kHz, giving at the same time access to network properties (below ~1 kHz) and single fibril properties (above ~10 kHz)[86,87]. Optical tweezers can also be used for active MR, where a probe particle is actively moved by a laser trap at controlled frequency and amplitude. This method in principle allows measurement of non-linear viscoelastic properties. To our knowledge, this method has not been applied to amyloid fibril networks yet.

1.4 Experimental model systems and techniques

In this thesis I describe the investigation of amyloid fibrils formed from two different model proteins and a model peptide. The model proteins (β-lactoglobulin, β-lg, and hen egg white lysozyme, HEWL) are both food-related; the model peptide (human islet amyloid polypeptide, hIAPP) is related to amyloid formation in patients suffering from type II diabetes mellitus. Since the β-lg amyloid fibrils are the main model system in my thesis, I will focus on these in this section. However, many of the issues described here are playing similar roles in the other two model systems. I summarize the conditions of formation of β-lg amyloid fibrils and the study of molecular packing structure in relation to polymorphism. A variety of spectroscopic techniques used to study the molecular structure of amyloids is briefly introduced. At the end of this section, I describe two spectroscopic techniques that are used in the research described in this thesis.

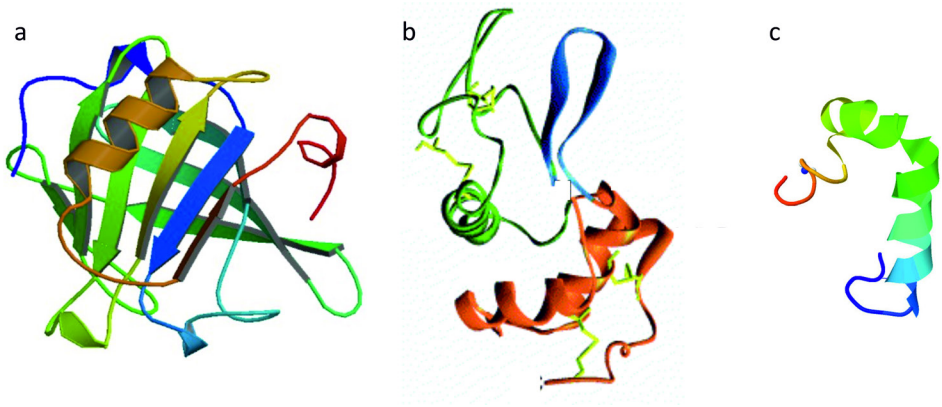

Figure 1.6: Structure of a) β-lactoglobulin (β-lg)[88]; b) hen egg white lysozyme (HEWL)[89]; c) human islet amyloid polypeptide (hIAPP)[90].

1.4.1 β-lactoglobulin

β-lactoglobulin (β-lg) is a protein in milk, which in its native state has a predominantly β-sheet structure (Figure 1.6a).[91] Upon heating it is capable of self-assembling into a variety of supramolecular structures. The fibers in the fine-stranded gels that are formed upon incubation below the isoelectric point (pH=5.1)[92] have been identified as amyloid fibrils.[16] β-lg is of great importance to the dairy industry, similar to other whey proteins, and is particularly useful for controlling the texture of a variety of foods.[93-95] At the same time, its tunable structuring capacity makes β-lg an interesting target for material science.[26] Additionally, β-lg has become a major model protein to investigate the self-assembly mechanism of amyloid fibrils.[91,92,96] Although the formation kinetics

and morphology of β-lg amyloid fibrils have been extensively studied, the secondary structure of the fibrils has still not yet been fully elucidated. Here we review the knowledge that has been accumulated so far on the relation between the fibril morphology and the underlying molecular structure of β-lg amyloids by a variety of experimental techniques. Multi-stranded amyloid ribbons composed of 2 to 16 β-lg protofilaments have been observed, all showing a left-handed twist.[97]

1.4.1.1 Formation of β-lactoglobulin amyloid fibrils

Solution pH

The most widely used protocol to form β-lg amyloid fibrils is incubation in acidified water (pH=2) for several hours at high temperature (80-90°C). It was shown that there is a small effect on the morphology of fibrils when the pH is varied between pH=1.6 and 2.4.[98] In all samples, the majority of the fibrils appeared semiflexible, up to 5 μm long and 5-10 nm in diameter. However, at pH=1.6, a small number of worm-like fibrils were present, while at pH=2.4 some wavy fibrils with a period of ~64 nm were observed. The persistence length of the fibrils varied between 2.1 and 3.1 μm. At higher pH values, between pH=3 to pH=7, short, worm-like fibrils have been observed.[99] At pH=3.35, the contour length of these short wormlike amyloids was about 130 nm and the persistence length ~35 nm.[100]

Solvent

The long, straight fibrils that form at low pH and high temperature are composed of small peptides, due to acid hydrolysis of the β-lg protein.[39] Another route to obtain fibrils is by enzymatic hydrolysis of β-lg at pH=8 and 37°C using the enzyme AspN endoproteinase, which cleaves the peptide bonds N-terminal to aspartic acid residues. When after cleavage the pH is lowered to pH=2 and the temperature to room temperature, long fibrils form.[101] Alternatively, fibrils can be formed at room temperature by incubation in alcohol-water mixtures. Fibrils were shown to form in 50:50 water-alcohol solutions based on methanol, ethanol, propanol and 2,2,2-trifluoroethanol (TFE) at pH=2 and also at pH=7.[92] TFE-induced fibrils appeared more worm-like than heat-induced fibrils, and showed a beaded structure under certain conditions. They were typically 150-500 nm in length and about 7 nm in diameter. The morphology of fibrils formed in methanol, ethanol and propanol depends on the pH: at pH=2 fibrils appeared similar to those formed in water-TFE, while at pH=7 thinner filaments (5 nm) and bundles thereof were observed.

Ionic strength

The morphology of fibrils is highly dependent on the ionic strength of the solution. While at low monovalent salt concentrations long and straight fibrils are formed, at

higher concentrations the fibrils become shorter and worm-like.[102] Yet, fibrils obtained at low and high ionic strength do exhibit a similar diameter and periodic morphology with a periodicity between 22 and 28 nm. This suggests that the general molecular mechanism of fibril formation is independent of the ionic strength. However, the rate of aggregation increases with ionic strength, and the critical concentration decreases.[103-105] Possibly, because at higher ionic strength electrostatic repulsions are weaker, the critical size of a stable nucleus is smaller. Then the nucleation process is no longer necessarily the limiting growth step and the rate of aggregation is faster.

Protein concentration

The critical aggregation concentration (CAC) of β-lg in water at pH=2 and 80°C was determined using Thioflavin T (ThT) fluorescence intensity measurements as 1.6 mg/mL (~87 μM).[106] The rate of aggregation increases with increasing β-lg concentration. Heating 5 mg/mL β-lg solutions at pH=2.5 and 80°C for 4 hrs did not show a loss of native-like β-lg, whereas at concentrations of 80 mg/mL, aggregation was very fast.[103] It was shown that between concentrations of 5 to 40 mg/mL, the concentration only affects the kinetics of fibril formation, while the structure of the fibrils was not influenced.[104]

Shear forces

Agitation of the solution during fibril formation affects the kinetics of fibril formation as well as the final fibril morphology.[107] Shear flow significantly enhances the rate of fibril formation[108] but only when it is applied during the nucleation process. No differences in kinetics for continuous shear (at a shear rate of 200 s^{-1} in a Couette geometry) or short shear pulses of 30 s (at the same shear rate) were observed.[109] However, the length distribution for fibrils formed after continuous shear showed a smaller variance than for fibrils formed upon pulsed shear.[109] The total fibril length concentration increased for increasing shear rate up to a shear rate of 337 s^{-1}. When the shear rate was increased even more, the total fibril length decreased again.[78] This could be related to breakage of fibrils by exposure to high shear rates.[108,110] It has been suggested that breaking of filaments can induce secondary nucleation events, which play an important role in the kinetics of the proliferation of amyloid fibrils (see also section 1.3.1).[111]

1.4.1.2 Structure of β-lactoglobulin amyloid fibrils

Circular dichroism spectroscopy

Circular dichroism (CD) spectroscopy is an excellent technique to determine the secondary structure of proteins and aggregates.[112,113] CD is defined as the unequal absorption of left- (L) and right- (R) handed circularly polarized light. Chiral molecules may absorb these two components to different extents, and may also have different

indices of refraction for the two waves. Absorption in the region between 180 and 240 nm is due to peptide bonds and provides information on the secondary structure. The spectra are usually analyzed using algorithms based on databases compiled for peptides for which the X-ray crystal structure is known.[96] A specific drawback of CD spectroscopy in case of amyloids is the relatively weak contribution of β-sheets. Nevertheless, the secondary structure content of native β-lg, oligomers and aggregates has been successfully determined using CD.[114] The aggregates, a mixture of amyloid fibrils and spherulites, were found to contain higher β-strand and lower α-helical structure contents than the oligomers, which were mainly dimers. Compared to the native protein, oligomers partially lost the helical and β-strand structure (Table 1.1). This is in agreement with the observation that dimers are linked by a disulfide bond, which requires at least unfolding of the protein's main helix.[115]

Table 1.1: Secondary structure content of different stages of β-lg amyloid formation. Adapted from Carrotta et al.[114]

	Native (X-ray)[a]	Native (CD)[b]	Oligomers (CD)[b]	Aggregates (CD)[b]
α-Helix	12%	11%	7%	3%
β-Strand	25%	24%	19%	27%
Turns	7%	14%	15%	10%
Other	56%	51%	59%	60%

[a] Calculated from the structure at pH=8.2 (Qin et al. 1999).

[b] Deconvolution of CD spectra.

CD has also been used to study the effect of shear on the secondary structure of β-lg fibrils (Figure 1.7).[107] After heating, samples were sheared in variable (stirring) or controlled (Couette cell) shear flows. In variable shear, helical fibrils with proportions of 51% β-sheet structure and 32% random coil were formed. However, under controlled shear the fibrils showed a segmented or beaded morphology, a lower β-sheet (44%) and increased α-helix (37%) content. Also a lower mechanical strength was measured for these fibrils in AFM nanomechanical manipulation experiments, where the fibrils were stretched with an AFM tip. The unzipping force, an indication of the energy required to stretch or unravel the fibrils, was ~20 pN for fibrils formed under controlled shear, while variable shear-induced fibrils showed unzipping forces of ~100 pN. Samples that were heated without shearing showed an even higher alpha-helix proportion (49%) compared to the samples heated with controlled shear, and no fibrils were observed in AFM images. This can be explained by the fact that shear increases the rate of fibril formation, and that without shear only oligomers and no fibrils were formed. It has to be noted that the sheared samples showed a large variability in fibrillar and non-fibrillar

structures, and it is unclear how this mixture contributes to spectroscopic measurements, which are intrinsically ensemble measurements.

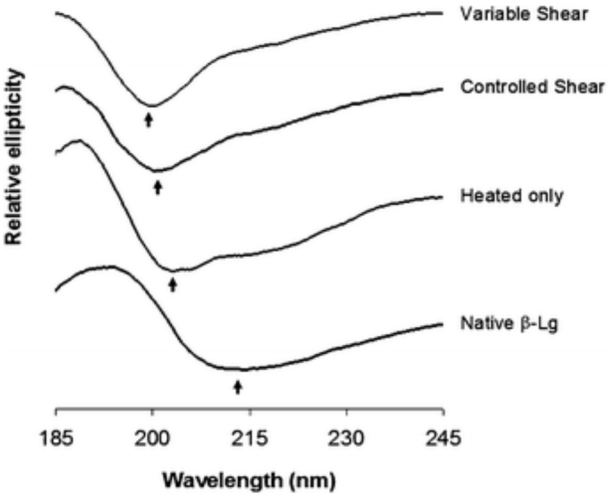

Figure 1.7: CD spectra for native, heated, and heated and sheared β-lg. Samples were heated at 80°C for 12 hrs prior to controlled shear measurements. Variable sheared samples were stirred; controlled shear was performed using a Couette shear cell. The arrows indicate the wavelength of maximum negative ellipticity. Adapted from Dunstan et al.[107]

Fourier transform infrared spectroscopy

Fourier transform infrared (FT-IR) spectroscopy provides insight into the overall secondary structure of proteins. The first FT-IR experiments on proteins were demonstrated in the 1950s.[116] An advantage of infrared absorption spectroscopy is that proteins can be studied in a wide variety of environments: gasses, liquids, solids, crystals, membrane proteins and insoluble aggregates.[117] It is a technique that can be used to rapidly acquire spectra from small amounts (down to ~100 μg) of protein.[118] The most widely used vibrational mode in studies of protein secondary structure is the amide I band, between 1600 and 1700 cm^{-1}. This vibrational mode originates mainly from the C=O stretching vibration of the amide group in the protein backbone, which is sensitive to the hydrogen bonding network of the local secondary structure. The amide I band has spectral overlap with the O-H bending mode of water. To avoid strong water absorption, often high protein concentrations, dried samples or the attenuated total reflection (ATR) mode are employed. An established approach for quantitative analysis of FT-IR data is curve-fitting of the amide I band of a protein with its component bands. Each of the Lorentzian components correlates to a certain secondary structure element through its spectral position. The area of a component band is usually directly related to the amount of the respective secondary structure element.[119] A drawback of FT-IR

spectroscopy for analysis of secondary structure is the difficulty to distinguish between the contributions of unordered and α-helical structures in an aqueous environment.

FT-IR experiments have revealed that worm-like amyloids formed from β-lg in alcohol-water mixtures contain an increased β-sheet content compared to native β-lg.[84] Dependent on the type of alcohol, both the β-sheet and α-helix intensity increase during fibril formation. For heat-induced fibrils formed at pH=2, which are longer and smoother in appearance than the worm-like fibrils, only the β-sheet intensity increased, while the helical intensity remained the same as for native β-lg (Figure 1.8). Because no quantitative analysis of the amide I band was performed, it was not possible to compare the different amyloid types with each other.[84] An alternative route to obtain worm-like fibrils is by disassembly and reassembly of multistranded fibrils formed at low pH and high temperature upon incubation in ethanol-water mixtures.[120] The α-helical content of the worm-like fibrils is lower than that of the multistranded fibrils, while their persistence length is shorter. They are enriched in random coil and turn content and have a different peptide composition compared to the original multistranded fibrils.

Real-time ATR-FTIR experiments have shown that in the first stages of fibril formation from native β-lg, the β-sheet content increases, whereas it decreases again in the fibril elongation stage. The α-helical content first decreases and then increases slightly during elongation.[121] Also, breaking up fibrillar proteins by high pressure microfluidization could be followed using ATR-FTIR.[122] The inter-molecular β-sheet component decreased, which was attributed to breakage of the fibrils into short fibrillar structures. At the same time, the intensity of β-turns and α-helix increased.

Raman spectroscopy

Raman spectroscopy provides information on the vibrational motions of molecules and has been widely used to study protein aggregation.[123] It can be used to elucidate the structure of proteins in aqueous solutions, fibers, films, gels and crystals. The approach to determine a protein secondary structure composition is very similar to that in FT-IR. A key advantage of Raman over FT-IR is that it does not suffer from overlapping water absorption; water vibrations are not Raman active. On the other hand, the process of Raman scattering has a low probability, leading to small signals.

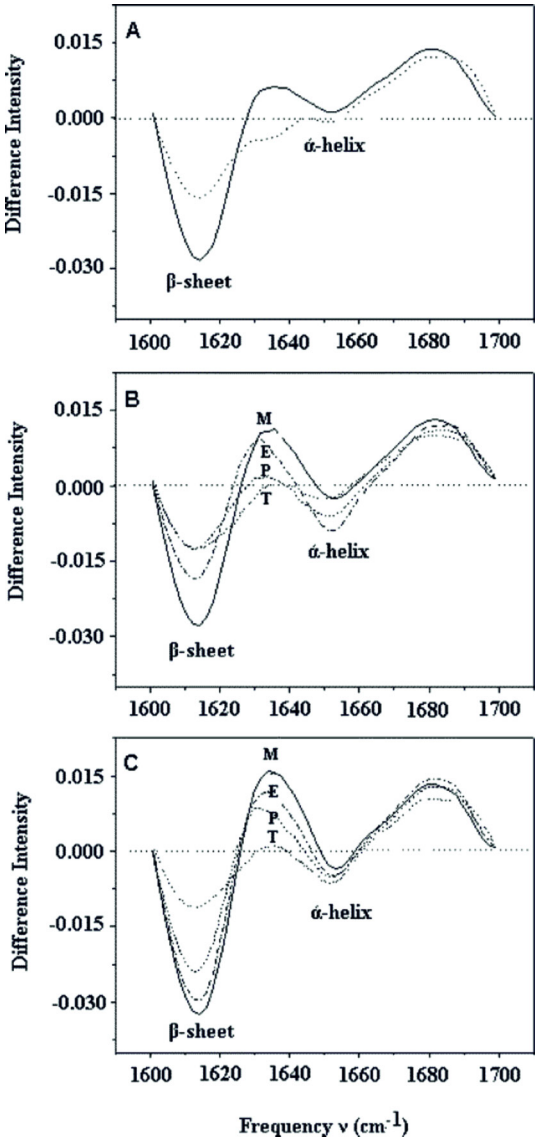

Frequency ν (cm^{-1})

Figure 1.8: Difference FT-IR spectra for β-lg fibrils formed (a) at pH=2, 80°C for 24 hrs at a concentration of 40 mg/mL (broken line) and 100 mg/mL (solid line), (b) at pH=2 in 50% w/w water-alcohol mixtures at β-lg concentration of 3.5% w/w in 40 days, and (c) at pH=2 in 50% w/w water-alcohol mixtures at β-lg concentration of 7.0% w/w in 85 days. M: methanol, E: ethanol, P: propanol, T: TFE. Each spectrum is intensity normalized and the spectrum for native β-lg is subtracted from it. Adapted from Gosal et al.[84]

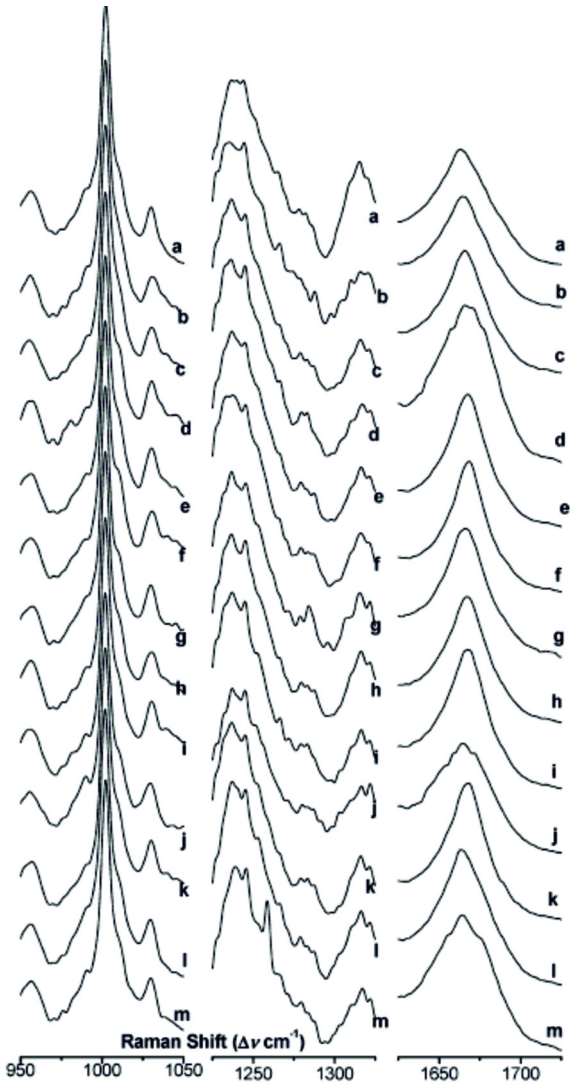

Figure 1.9: Raman spectra of (a) native β-lg; β-lg incubated at 80°C for 14 hrs at a concentration of (b) 40 mg/mL and (c) 80 mg/mL; powdered aggregates from solutions of (d) 20 mg/mL (e) 35 mg/mL (f) 70 mg/mL in 50% v/v methanol; (g) 20 mg/mL (h) 35 mg/mL (i) 70 mg/mL in 50% v/v ethanol; (j) 35 mg/mL (k) 70 mg/mL in 50% v /v propan-2-ol; (l) 35 mg/mL (m) 70 mg/mL in 50% v/v TFE. The 20 and 35 mg/mL alcohol-induced samples were incubated for 40 days, and 70 mg/mL alcohol-induced samples were incubated for 85 days. Showed are the region sensitive for α-helical structure (left), the amide III (middle) and the amide I (right) spectral regions. Adapted from Gosal et al.[84]

The use of high laser intensities to increase the Raman signal can damage protein samples. Sophisticated techniques like surface enhanced Raman scattering (SERS), where metal surfaces are used to enhance the Raman signal for proteins containing chromophores, can lead to a substantial increase of the signal-to-noise ratio.[124]

The β-sheet development during the formation of amyloids can be followed in the amide I spectral region by Raman spectroscopy, as has been shown for α-synuclein.[125,126] Raman spectroscopy on spherulites formed from insulin showed that regardless of whether aggregation was induced at the isoelectric point or away from it, and regardless of the ionic strength, protein aggregation favored the formation of beta-sheet structures.[127] Raman spectroscopy has also been used to compare secondary structure of β-lg fibrils prepared at pH=2 in the presence of various alcohols.[84] Significant differences in the band in the amide I region for the native protein compared to the spectra of the fibrils were observed (Figure 1.9). The shift seems to correlate with the degree of aggregation which has occurred, and is interpreted as a significant change in the existing native β-sheet structure, a net increase in β-sheet, or perhaps both.[84] Upon heating of β-lg monomer at pH=2, the Raman peak positions shifted from 1238 to 1242 cm^{-1}, indicating that β-sheets are strongly hydrogen bonded.[128]

1.4.2 Hen egg white lysozyme

Hen egg white lysozyme (HEWL) is a globular peptide and consists of 129 amino acid residues (Figure 1.6b). In the native state it contains a β-sheet region and several helices. The protein is 40% homologous to human lysozyme, which is involved in systemic amyloidosis.[4] HEWL forms amyloid fibrils upon incubation in acidic solution (pH=2-4) at elevated temperature (37-65°C) for several days.[129] The fibrils show a typical amyloid morphology with a diameter of several nanometer and lengths up to several micrometers. Amyloid fibrils formed at pH=2 and T=65°C are mainly composed of fragments instead of the intact monomer, caused by a hydrolysis step before refolding into the amyloid structure.[40] Fragments involving residues 49-101 were most abundant in the amyloids. Also several fragments derived from the β-sheet region of HEWL form amyloid fibrils upon incubation at acidic pH and elevated temperature.[40,129]

1.4.3 Human Islet Amyloid Polypeptide (hIAPP)

hIAPP (also called amylin) is a short peptide of 37 amino acid residues (Figure 1.6c). hIAPP forms extracellular deposits in the pancreas of type 2 diabetes mellitus patients [130]. *In vivo*, hIAPP is co-secreted with insulin by the β-islet cells of the pancreas. Amyloid fibrils and/or oligomeric forms of hIAPP are thought to induce cell death of islet cells, eventually destroying insulin production.[130-133] Like many amyloidogenic peptides, non-aggregated hIAPP is mainly unstructured.[134] The details of the aggregation of hIAPP *in*

vitro have been described extensively. hIAPP forms amyloid fibrils *in vitro* both in bulk solution and at lipid interfaces.[134-137]

1.4.4 Spectroscopic techniques used in this thesis

In section 1.4.1 I described several conventional spectroscopic techniques that have been used to study the molecular structure of amyloid fibrils, more specifically amyloid fibrils formed from β-lg. An important drawback of these techniques is that they can only be used to measure amyloid fibrils in bulk, which makes it hard to study polymorphic samples. Here I will briefly introduce two main spectroscopic techniques that I used in this thesis to probe the molecular structure of amyloids: vibrational sum-frequency generation spectroscopy (VSFG) and tip-enhanced Raman spectroscopy (TERS). Both are sophisticated techniques that were only recently used for the first time to study the structure of amyloid fibrils or amyloid formation. VSFG is a surface-sensitive technique, enabling the investigation of amyloid formation at model membranes, and TERS combines spectroscopy with high resolution imaging, providing possibilities to study amyloid polymorphism.

1.4.4.1 Vibrational sum-frequency generation spectroscopy

Vibrational sum-frequency generation (VSFG) spectroscopy is a surface-specific vibrational spectroscopic technique that was pioneered in the 1980s.[138] Only recently the first VSFG measurements on the secondary structure of amyloids at interfaces were reported.[139,140] In the nonlinear optical process of VSFG, two pulsed lasers, one at visible and one at infrared (IR) frequency, interact with the molecules at an interface or on a surface. As a result, light at the sum frequency of the visible and IR beams can be generated. The process is resonantly enhanced when the IR frequency matches a surface vibrational mode frequency.[141-143] An advantage of VSFG is its surface-specificity, which makes it possible to look at formation of amyloid on membranes or interfaces. This may be interesting for applications like stabilization of foams by fibrils and in disease-related research. Besides, the same amyloid samples, for instance on mica, can be used for VSFG and for AFM, providing the opportunity to relate the molecular structure of amyloid fibrils to their morphology.

1.4.4.2 Tip-enhanced Raman spectroscopy

An important drawback of traditional spectroscopic techniques like FT-IR, Raman and VSFG spectroscopy is that they can only be used to measure properties of a large ensemble of fibrils. Given that amyloid fibrils are notoriously polymorphic, there is a growing interest in the development of nanoscale techniques like tip-enhanced Raman

spectroscopy (TERS), which can provide 1-10 nm spatial resolution in combination with structurally sensitive spectroscopic information. First TERS spectra, of a C_{60} thin film, were published in 2000.[144] The technique offers depth and lateral spatial resolution in the nanometer range due to a strong field enhancement by a metalized tip of an AFM coupled to a Raman spectrometer.[145] Therefore it provides the opportunity to spatially map the secondary structure and amino acid residue composition along the surface of individual amyloid fibrils.[146,147] Recently it has been shown that amyloid fibrils formed from insulin show a heterogeneous surface structure mainly composed of unordered or α-helical structures, in contrast to the β-sheet-rich core of amyloid fibrils.

1.5 Polyphenols

Plant polyphenols have recently drawn widespread attention as a possible candidate to control amyloid formation and stability. They are recognized as promising drugs for prevention or treatment of Alzheimer's disease.[23,148,149] Polyphenols are ubiquitous compounds in plant-derived food and beverages (e.g. green tea) and have recently been shown to be potential inhibitors of amyloid fibrillization.[148-150] One of the most promising polyphenols for treatment of amyloid-related diseases is epi-gallocatechin-3-gallate (EGCG) (Figure 1.10). It is the most abundant polyphenol in tea leaves.[151] EGCG both inhibits amyloid formation[152-155] and disaggregates or remodels existing amyloid fibrils[152,153,156]. The molecular mechanism by which polyphenols interact with amyloid fibrils and oligomers is not yet elucidated. Both charge-charge interactions and interaction via aromatic residues have been reported.[155,157-160] Polyphenols are thought to have many more beneficial properties based on their antimicrobial properties and their anti-oxidant capacities, including therapeutic potential for cancer[161] and cardiovascular diseases[162]. The strong interactions between polyphenols and amyloid proteins may potentially be used to combat amyloidosis, but proteins could also serve as delivery vehicles of polyphenols with applications in polyphenol-rich food or as drug delivery agents.

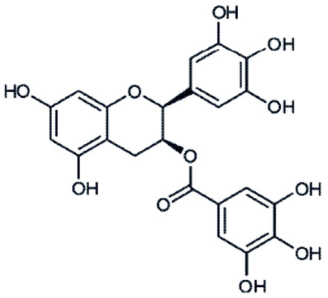

Figure 1.10: The polyphenol EGCG. Adapted from Bieschke et al.[163]

1.6 Scope of this thesis

The central goal in this thesis is to investigate the biophysical properties of amyloid fibrils over a range of length scales: from molecular structure to single fibril rigidity and the mechanics of networks of fibrils (Figure 1.11). To understand and control the assembly process of amyloid fibrils, insights into the relation between the mechanical properties and molecular structure are essential. Furthermore, for the application of amyloids in materials science, tissue engineering and food industry, control over the morphology and structure of amyloid fibrils is needed. My approach is to link the molecular structure of model amyloid fibrils measured by vibrational spectroscopy to the fibril morphology and rigidity measured by AFM, and to understand how these properties in turn control the network mechanics of suspensions of fibrils measured by macroscopic rheometry. An important question in amyloid research is the origin of the polymorphism of amyloid fibrils. Therefore I investigate distinct types of amyloid fibrils on all length scales. Furthermore, I investigate the control of amyloid formation and disaggregation by the polyphenol EGCG.

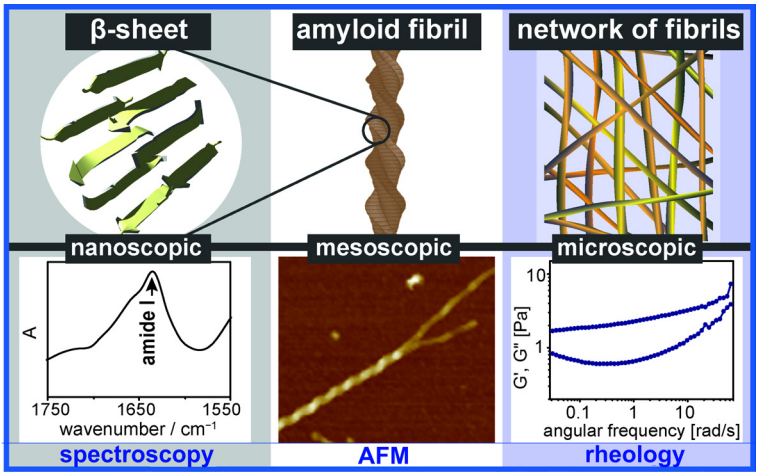

Figure 1.11: Overview of the research on amyloid fibrils over a range of length scales covered in this thesis and the techniques that are used.

The first part of this thesis focuses on the molecular structure of amyloid fibrils and its relation to the structural polymorphism observed for amyloids. In **Chapter 2** we investigate the relation between the molecular structure, morphology and rigidity of two distinct types of amyloid fibrils formed from the milk protein β-lactoglobulin. We show using a combination of vibrational sum-frequency generation spectroscopy (VSFG) and atomic force microscopy (AFM) that the β-sheet structure of long, straight amyloid

fibrils with a persistence length of several micrometer is higher than that of short, worm-like fibrils with a 40 times lower persistence length. In Chapter 3 we investigate the differences in molecular structure and composition of the two fibril types in more detail. We show using mass spectroscopy that the composition of the fibril types is similar. The bulk molecular structure of the fibrils shows a large contribution of the β-sheet core, but surprisingly no differences in structure between the straight and worm-like fibrils. However, differences in structure were observed when the surface of the fibrils was specifically probed using tip-enhanced Raman spectroscopy (TERS). The straight fibrils showed a higher β-sheet content that the worm-like fibrils, although for both fibril types the surface was mainly composed of unordered or α-helical structure. The nanoscale resolution provided by TERS made it possible to show the heterogeneity of the amyloid surface. To elucidate the origin of the difference in morphology and molecular structure, we studied the kinetics of fibril formation, revealing that fast decrease of intact monomers and fast refolding results in worm-like fibrils, while for the highly ordered straight fibrils folding and fibril assembly appears to be slower. Amyloid fibrils formed from the diabetes-related peptide hIAPP were investigated in detail in Chapter 4. With TERS we probed the surface molecular structure and amino acid residue composition with nanometer resolution. Similar to β-lactoglobulin fibrils, the surface of the hIAPP fibrils contains mainly unordered or α-helical structures, in contrast to the β-sheet core that was probed with infrared spectroscopy. Moreover, the surface structure is highly heterogeneous, varying on the nanometer scale. We also show that TERS can probe amyloids formed at a lipid interface, which is more representative of amyloids *in vivo*.

In the second part of this thesis, I investigate the effect of the green tea polyphenol EGCG on the formation of amyloids and on the morphology and rigidity of the amyloid fibrils. In Chapter 5 the inhibitory effect of the polyphenol EGCG on amyloid formation and fibril disaggregation of hIAPP was studied. We show that EGCG is a much less efficient amyloid inhibitor at a phospholipid interface than in bulk solution using a combination of VSFG and AFM. EGCG is not able to disaggregate existing amyloid fibrils at a phospholipid interface, whereas it efficiently disaggregates fibrils in bulk. In Chapter 6 we study the pH-dependent effect of EGCG on amyloid fibrils formed from hen egg white lysozyme (HEWL) using AFM. We find that at acidic pH, EGCG does not affect the morphology or rigidity of amyloids. However, at neutral pH thick fibrils were formed upon incubation with EGCG suggesting that EGCG bundles the fibrils. Electron microscopy imaging revealed that the thick fibrils formed large fibril aggregates, consistent with attractive interactions conferred by EGCG.

In the last part of this thesis I focus on the mechanical properties of amyloid fibrils and networks thereof. In Chapter 7 we determine the persistence length of HEWL amyloid fibrils using two approaches: one based on AFM images of a large ensemble of fibrils, and the other based on time-lapse imaging by fluorescence microscopy of the thermal bending undulations of freely fluctuating fibrils suspended in water. Both approaches reveal a persistence length of several micrometers. However, with time-lapse imaging a large variability for fibrils within the same sample was observed, which is a signature of the marked polymorphism of amyloid fibrils. In Chapter 8, the rheological behaviour of β-lactoglobulin amyloid fibril suspensions is described. We compare the same two distinct fibril types that differ in aspect ratio and persistence length as described in Chapter 2 and 3. Both types of amyloid fibrils behave in suspension as soft solids with an apparent yield stress and a strong shear-thinning response. The shear-thinning behavior over a large range of shear rates was more closely investigated using a combination of rheology and small-angle neutron scattering (rheo-SANS). These results indicate that both fibril suspensions behave rheologically as suspensions of weakly attractive, semi-flexible rods.

References

(1) Dobson, C. M. *Nature* **2003**, *426*, 884.
(2) Chiti, F.; Dobson, C. M. *Annual Review of Biochemistry* **2006**, *75*, 333.
(3) Smith, J. F.; Knowles, T. P.; Dobson, C. M.; Macphee, C. E.; Welland, M. E. *Proceedings of the National Academy of Sciences of the United States of America* **2006**, *103*, 15806.
(4) Pepys, M. B.; Hawkins, P. N.; Booth, D. R.; Vigushin, D. M.; Tennent, G. A.; Soutar, A. K.; Totty, N.; Nguyen, O.; Blake, C. C. F.; Terry, C. J.; Feest, T. G.; Zalin, A. M.; Hsuan, J. J. *Nature* **1993**, *362*, 553.
(5) Tan, S. Y.; Pepys, M. B. *Histopathology* **1994**, *25*, 403.
(6) Lansbury, P. T.; Lashuel, H. A. *Nature* **2006**, *443*, 774.
(7) Otzen, D.; Nielsen, P. H. *Cellular and Molecular Life Sciences* **2008**, *65*, 910.
(8) Olsen, A.; Jonsson, A.; Normark, S. *Nature* **1989**, *338*, 652.
(9) Romling, U.; Bian, Z.; Hammar, M.; Sierralta, W. D.; Normark, S. *Journal of Bacteriology* **1998**, *180*, 722.
(10) Fowler, D. M.; Koulov, A. V.; Balch, W. E.; Kelly, J. W. *Trends in biochemical sciences* **2007**, *32*, 217.
(11) Gebbink, M.; Claessen, D.; Bouma, B.; Dijkhuizen, L.; Wosten, H. A. B. *Nature Reviews Microbiology* **2005**, *3*, 333.
(12) Larsen, P.; Nielsen, J. L.; Dueholm, M. S.; Wetzel, R.; Otzen, D.; Nielsen, P. H. *Environmental Microbiology* **2007**, *9*, 3077.
(13) Gosal, W. S.; Clark, A. H.; Pudney, P. D. A.; Ross-Murphy, S. B. *Langmuir* **2002**, *18*, 7174.
(14) Knowles, T. P.; Smith, J. F.; Craig, A.; Dobson, C. M.; Welland, M. E. *Physical Review Letters* **2006**, *96*, 238301.
(15) Guo, S.; Akhremitchev, B. B. *Biomacromolecules* **2006**, *7*, 1630.
(16) Pastor, M. T.; Esteras-Chopo, A.; Lopez de la Paz, M. *Current Opinion in Structural Biology* **2005**, *15*, 57.
(17) Hamley, I. W. *Angewandte Chemie International Edition* **2007**, *46*, 8128.
(18) Baldwin, A. J.; Bader, R.; Christodoulou, J.; MacPhee, C. E.; Dobson, C. M.; Barker, P. D. *Journal of the American Chemical Society* **2006**, *128*, 2162.
(19) Gelain, F.; Bottai, D.; Vescovi, A.; Zhang, S. *PloS One* **2006**, *1*, e119.
(20) Nyrkova, I. A.; Semenov, A. N.; Aggeli, A.; Bell, M.; Boden, N.; McLeish, T. C. B. *European Physical Journal B* **2000**, *17*, 499.
(21) Scheibel, T.; Parthasarathy, R.; Sawicki, G.; Lin, X. M.; Jaeger, H.; Lindquist, S. L. *Proceedings of the National Academy of Sciences of the United States of America* **2003**, *100*, 4527.
(22) Cherny, I.; Gazit, E. *Angewandte Chemie International Edition* **2008**, *47*, 4062.
(23) Jones, O. G.; Mezzenga, R. *Soft Matter* **2012**, *8*, 876.
(24) Li, C. X.; Mezzenga, R. *Nanoscale* **2013**, *5*, 6207.
(25) Hamada, D.; Yanagihara, I.; Tsumoto, K. *Trends in biotechnology* **2004**, *22*, 93.
(26) Knowles, T. P. J.; Buehler, M. J. *Nature Nano* **2011**, *6*, 469.
(27) Hamedi, M.; Herland, A.; Karlsson, R. H.; Inganas, O. *Nano letters* **2008**, *8*, 1736.
(28) Maji, S. K.; Schubert, D.; Rivier, C.; Lee, S.; Rivier, J. E.; Riek, R. *PLoS biology* **2008**, *6*, 240.
(29) Ryan, D. M.; Nilsson, B. L. *Polymer Chemistry* **2012**, *3*, 18.

(30) Reynolds, N. P.; Styan, K. E.; Easton, C. D.; Li, Y. L.; Waddington, L.; Lara, C.; Forsythe, J. S.; Mezzenga, R.; Hartley, P. G.; Muir, B. W. *Biomacromolecules* **2013**, *14*, 2305.
(31) Graeber, M. B.; Kosel, S.; Egensperger, R.; Banati, R. B.; Muller, U.; Bise, K.; Hoff, P.; Moller, H. J.; Fujisawa, K.; Mehraein, P. *Neurogenetics* **1997**, *1*, 73.
(32) Hammer, N. D.; Schmidt, J. C.; Chapman, M. R. *Proceedings of the National Academy of Sciences* **2007**, *104*, 12494.
(33) Scheibel, T.; Parthasarathy, R.; Sawicki, G.; Lin, X. M.; Jaeger, H.; Lindquist, S. L. *Proceedings of the National Academy of Sciences of the United States of America* **2003**, *100*, 4527.
(34) Jahn, T. R.; Makin, O. S.; Morris, K. L.; Marshall, K. E.; Tian, P.; Sikorski, P.; Serpell, L. C. *Journal of Molecular Biology* **2010**, *395*, 717.
(35) Wiltzius, J. J.; Sievers, S. A.; Sawaya, M. R.; Cascio, D.; Popov, D.; Riekel, C.; Eisenberg, D. *Protein Science* **2008**, *17*, 1467.
(36) Wetzel, R.; Shivaprasad, S.; Williams, A. D. *Biochemistry* **2007**, *46*, 1.
(37) Uversky, V. N.; Fink, A. L. *Biochimica et Biophysica Acta (BBA) – Proteins & Proteomics* **2004**, *1698*, 131.
(38) Adamcik, J.; Mezzenga, R. *Macromolecules* **2011**, *45*, 1137.
(39) Akkermans, C.; Venema, P.; van der Goot, A. J.; Gruppen, H.; Bakx, E. J.; Boom, R. M.; van der Linden, E. *Biomacromolecules* **2008**, *9*, 1474.
(40) Frare, E.; Polverino de Laureto, P.; Zurdo, J.; Dobson, C. M.; Fontana, A. *Journal of Molecular Biology* **2004**, *340*, 1153.
(41) Bolisetty, S.; Adamcik, J.; Mezzenga, R. *Soft Matter* **2011**, *7*, 493.
(42) Petkova, A. T.; Leapman, R. D.; Guo, Z.; Yau, W.-M.; Mattson, M. P.; Tycko, R. *Science* **2005**, *307*, 262.
(43) Volpatti, L. R.; Vendruscolo, M.; Dobson, C. M.; Knowles, T. P. J. *ACS Nano* **2013**, *7*, 10443.
(44) Goldsbury, C.; Frey, P.; Olivieri, V.; Aebi, U.; Müller, S. A. *Journal of Molecular Biology* **2005**, *352*, 282.
(45) Fandrich, M.; Meinhardt, J.; Grigorieff, N. *Prion* **2009**, *3*, 89.
(46) Marshall, K. E.; Serpell, L. C. *Soft Matter* **2010**, *6*, 2110.
(47) Usov, I.; Adamcik, J.; Mezzenga, R. *ACS Nano* **2013**, *7*, 10465.
(48) Kodali, R.; Wetzel, R. *Current Opinion in Structural Biology* **2007**, *17*, 48.
(49) Xu, Z.; Paparcone, R.; Buehler, M. J. *Biophysical journal* **2010**, *98*, 2053.
(50) Knowles, T. P.; Fitzpatrick, A. W.; Meehan, S.; Mott, H. R.; Vendruscolo, M.; Dobson, C. M.; Welland, M. E. *Science* **2007**, *318*, 1900.
(51) Mucke, N.; Klenin, K.; Kirmse, R.; Bussiek, M.; Herrmann, H.; Hafner, M.; Langowski, J. *PloS one* **2009**, *4*, e7756.
(52) Brangwynne, C. P.; Koenderink, G. H.; Barry, E.; Dogic, Z.; MacKintosh, F. C.; Weitz, D. A. *Biophysical journal* **2007**, *93*, 346.
(53) Knowles, T. P.; Buehler, M. J. *Nature Nanotechnology* **2011**, *6*, 469.
(54) Relini, A.; Torrassa, S.; Ferrando, R.; Rolandi, R.; Campioni, S.; Chiti, F.; Gliozzi, A. *Biophysical journal* **2010**, *98*, 1277.
(55) vandenAkker, C. C.; Engel, M. F. M.; Velikov, K. P.; Bonn, M.; Koenderink, G. H. *Journal of the American Chemical. Society* **2011**, *133*, 18030.
(56) Adamcik, J.; Jung, J. M.; Flakowski, J.; De Los Rios, P.; Dietler, G.; Mezzenga, R. *Nature Nanotechnology* **2010**, *5*, 423.
(57) Gosal, W. S.; Morten, I. J.; Hewitt, E. W.; Smith, D. A.; Thomson, N. H.; Radford, S. E. *Journal of Molecular Biology* **2005**, *351*, 850.

(58) Sachse, C.; Grigorieff, N.; Fandrich, M. *Angewandte Chemie-International Edition* **2010**, *49*, 1321.
(59) Mudgal, P.; Daubert, C. R.; Foegeding, E. A. *Food Hydrocolloid* **2009**, *23*, 1762.
(60) Sagis, L. M.; Veerman, C.; van der Linden, E. *Langmuir* **2004**, *20*, 924.
(61) Aymard, P.; Nicolai, T.; Durand, D.; Clark, A. *Macromolecules* **1999**, *32*, 2542.
(62) Veerman, C.; Ruis, H.; Sagis, L. M.; van der Linden, E. *Biomacromolecules* **2002**, *3*, 869.
(63) Jordens, S.; Adamcik, J.; Amar-Yuli, I.; Mezzenga, R. *Biomacromolecules* **2011**, *12*, 187.
(64) Ban, T.; Hamada, D.; Hasegawa, K.; Naiki, H.; Goto, Y. *The Journal of biological chemistry* **2003**, *278*, 16462.
(65) Castro, C. E.; Dong, J.; Boyce, M. C.; Lindquist, S.; Lang, M. J. *Biophysical journal* **2011**, *101*, 439.
(66) Kellermayer, M. S.; Grama, L.; Karsai, A.; Nagy, A.; Kahn, A.; Datki, Z. L.; Penke, B. *The Journal of biological chemistry* **2005**, *280*, 8464.
(67) Karsai, A.; Martonfalvi, Z.; Nagy, A.; Grama, L.; Penke, B.; Kellermayer, M. S. *Journal of structural biology* **2006**, *155*, 316.
(68) Alsteens, D.; Ramsook, C. B.; Lipke, P. N.; Dufrene, Y. F. *ACS nano* **2012**, *6*, 7703.
(69) Ganchev, D. N.; Cobb, N. J.; Surewicz, K.; Surewicz, W. K. *Biophysical journal* **2008**, *95*, 2909.
(70) Tanaka, M.; Collins, S. R.; Toyama, B. H.; Weissman, J. S. *Nature* **2006**, *442*, 585.
(71) Kroes-Nijboer, A.; Venema, P.; Baptist, H.; van der Linden, E. *Langmuir* **2010**, *26*, 13097.
(72) Govaerts, C.; Wille, H.; Prusiner, S. B.; Cohen, F. E. *Proceedings of the National Academy of Sciences of the United States of America* **2004**, *101*, 8342.
(73) Kishimoto, A.; Hasegawa, K.; Suzuki, H.; Taguchi, H.; Namba, K.; Yoshida, M. *Biochemical and Biophysical Research Communications* **2004**, *315*, 739.
(74) Perutz, M. F.; Finch, J. T.; Berriman, J.; Lesk, A. *Proceedings of the National Academy of Sciences of the United States of America* **2002**, *99*, 5591.
(75) Keten, S.; Buehler, M. Journal of *Computer Methods in Applied Mechanics* **2008**, *197*, 3203.
(76) Xu, Z.; Paparcone, R.; Buehler, M. J. *Biophysical journal* **2010**, *98*, 2053.
(77) Loveday, S. M.; Rao, M. A.; Creamer, L. K.; Singh, H. *Journal of food science* **2009**, *74*, R47.
(78) Akkermans, C.; van der Goot, A. J.; Venema, P.; van der Linden, E.; Boom, R. M. *Food Hydrocolloids* **2008**, *22*, 1315.
(79) Krysmann, M. J.; Castelletto, V.; Kelarakis, A.; Hamley, I. W.; Hule, R. A.; Pochan, D. J. *Biochemistry* **2008**, *47*, 4597.
(80) Loveday, S. M.; Su, J. H.; Rao, M. A.; Anema, S. G.; Singh, H. *International Dairy Journal* **2012**, *26*, 133.
(81) Veerman, C.; de Schiffart, G.; Sagis, L. M.; van der Linden, E. *International journal of biological macromolecules* **2003**, *33*, 121.
(82) Corrigan, A. M.; Donald, A. M. *Langmuir* **2009**, *25*, 8599.
(83) Valentine, M. T.; Kaplan, P. D.; Thota, D.; Crocker, J. C.; Gisler, T.; Prud'homme, R. K.; Beck, M.; Weitz, D. A. *Physical review. E* **2001**, *64*, 061506.
(84) Gosal, W. S.; Clark, A. H.; Ross-Murphy, S. B. *Biomacromolecules* **2004**, *5*, 2408.
(85) Corrigan, A. M.; Donald, A. M. *The European physical journal. E, Soft matter* **2009**, *28*, 457.

(86) Koenderink, G. H.; Atakhorrami, M.; MacKintosh, F. C.; Schmidt, C. F. *Physical review letters* **2006**, *96*, 138307.
(87) Atakhorrami, M.; Mizuno, D.; Koenderink, G. H.; Liverpool, T. B.; MacKintosh, F. C.; Schmidt, C. F. *Physical review. E, Statistical, nonlinear, and soft matter physics* **2008**, *77*, 061508.
(88) Hamada, D.; Tanaka, T.; Tartaglia, G. G.; Pawar, A.; Vendruscolo, M.; Kawamura, M.; Tamura, A.; Tanaka, N.; Dobson, C. M. *Journal of Molecular Biology* **2009**, *386*, 878.
(89) Bromley, E. H. C.; Krebs, M. R. H.; Donald, A. M. *Faraday Discussions* **2005**, *128*, 13.
(90) Donald, A. M. *Soft Matter* **2008**, *4*, 1147.
(91) van der Linden, E.; Venema, P. *Current Opinion in Colloid & Interface Science* **2007**, *12*, 158.
(92) Foegeding, E. A. *Food Biophysics* **2006**, *1*, 41.
(93) Hamley, I. W. *Angewandte Chemie-International Edition* **2007**, *46*, 8128.
(94) Lara, C. c.; Adamcik, J.; Jordens, S.; Mezzenga, R. *Biomacromolecules* **2011**, *12*, 1868.
(95) Kuwata, K.; Hoshino, M.; Forge, V.; Era, S.; Batt, C. A.; Goto, Y. *Protein Science* **1999**, *8*, 2541.
(96) Frare, E.; Mossuto, M. F.; Polverino de Laureto, P.; Dumoulin, M.; Dobson, C. M.; Fontana, A. *Journal of Molecular Biology* **2006**, *361*, 551.
(97) Nanga, R. P. R.; Brender, J. R.; Vivekanandan, S.; Ramamoorthy, A. *Biochimica et Biophysica Acta (BBA) - Biomembranes* **2011**, *1808*, 2337.
(98) Loveday, S. M.; Wang, X. L.; Rao, M. A.; Anema, S. G.; Creamer, L. K.; Singh, H. *International Dairy Journal* **2010**, *20*, 571.
(99) Kavanagh, G. M.; Clark, A. H.; Ross-Murphy, S. B. *Langmuir* **2000**, *16*, 9584.
(100) Mudgal, P.; Daubert, C. R.; Foegeding, E. A. *Food Hydrocolloids* **2009**, *23*, 1762.
(101) Akkermans, C.; Venema, P.; van der Goot, A. J.; Boom, R. M.; van der Linden, E. *Food Biophysics* **2008**, *3*, 390.
(102) Kavanagh, G. M.; Clark, A. H.; Ross-Murphy, S. B. *International Journal of Biological Macromolecules* **2000**, *28*, 41.
(103) Schokker, E. P.; Singh, H.; Pinder, D. N.; Creamer, L. K. *International Dairy Journal* **2000**, *10*, 233.
(104) Aymard, P.; Nicolai, T.; Durand, D.; Clark, A. *Macromolecules* **1999**, *32*, 2542.
(105) Arnaudov, L. N.; de Vries, R. *Biomacromolecules* **2006**, *7*, 3490.
(106) Kroes-Nijboer, A.; Venema, P.; Bouman, J.; van der Linden, E. *Food Biophysics* **2009**, *4*, 59.
(107) Dunstan, D. E.; Hamilton-Brown, P.; Asimakis, P.; Ducker, W.; Bertolini, J. *Soft Matter* **2009**, *5*, 5020.
(108) Hill, E. K.; Krebs, B.; Goodall, D. G.; Howlett, G. J.; Dunstan, D. E. *Biomacromolecules* **2005**, *7*, 10.
(109) Akkermans, C.; Venema, P.; Rogers, S.; van der Goot, A.; Boom, R.; van der Linden, E. *Food Biophysics* **2006**, *1*, 144.
(110) Castelletto, V.; Hamley, I. W. *Biomacromolecules* **2006**, *8*, 77.
(111) Knowles, T. P. J.; Waudby, C. A.; Devlin, G. L.; Cohen, S. I. A.; Aguzzi, A.; Vendruscolo, M.; Terentjev, E. M.; Welland, M. E.; Dobson, C. M. *Science* **2009**, *326*, 1533.
(112) Greenfield, N. J. *Nature protocols* **2006**, *1*, 2876.
(113) Kelly, S. M.; Jess, T. J.; Price, N. C. *Biochimica et Biophysica Acta* **2005**, *1751*, 119.
(114) Carrotta, R.; Bauer, R.; Waninge, R.; Rischel, C. *Protein Science* **2001**, *10*, 1312.

(115) Qi, X. L.; Holt, C.; McNulty, D.; Clarke, D. T.; Brownlow, S.; Jones, G. R. *Biochemical Journal* 1997, *324*, 341.
(116) Elliott, A.; Ambrose, E. J. *Nature* 1950, *165*, 921.
(117) Hiramatsu, H.; Kitagawa, T. *Biochimica Et Biophysica Acta-Proteins and Proteomics* 2005, *1753*, 100.
(118) Surewicz, W. K.; Mantsch, H. H.; Chapman, D. *Biochemistry* 1993, *32*, 389.
(119) Arrondo, J. L. R.; Muga, A.; Castresana, J.; Goni, F. M. *Progress in Biophysics & Molecular Biology* 1993, *59*, 23.
(120) Jordens, S.; Adamcik, J.; Amar-Yuli, I.; Mezzenga, R. *Biomacromolecules* 2010, *12*, 187.
(121) Oboroceanu, D.; Wang, L. Z.; Brodkorb, A.; Magner, E.; Auty, M. A. E. *Journal of Agricultural and Food Chemistry* 2010, *58*, 3667.
(122) Oboroceanu, D.; Wang, L.; Kroes-Nijboer, A.; Brodkorb, A.; Venema, P.; Magner, E.; Auty, M. A. E. *International Dairy Journal* 2011, *21*, 823.
(123) Tuma, R. *Journal of Raman Spectroscopy* 2005, *36*, 307.
(124) Campion, A.; Kambhampati, P. *Chemical Society reviews* 1998, *27*, 241.
(125) Hiramatsu, H.; Lu, M.; Matsuo, K.; Gekko, K.; Goto, Y. J.; Kitagawa, T. *Biochemistry* 2010, *49*, 742.
(126) Apetri, M. M.; Maiti, N. C.; Zagorski, M. G.; Carey, P. R.; Anderson, V. E. *Journal of Molecular Biology* 2006, *355*, 63.
(127) Krebs, M. R. H.; Domike, K. R.; Cannon, D.; Donald, A. M. *Faraday Discussions* 2008, *139*, 265.
(128) Ikeda, S. *Spectroscopy* 2003, *17*, 195.
(129) Krebs, M. R. H.; Wilkins, D. K.; Chung, E. W.; Pitkeathly, M. C.; Chamberlain, A. K.; Zurdo, J.; Robinson, C. V.; Dobson, C. M. *Journal of Molecular Biology* 2000, *300*, 541.
(130) Höppener, J. W. M.; Ahrén, B.; Lips, C. J. M. *The New England Journal of Medicin* 2000, *343*, 411.
(131) Kayed, R.; Head, E.; Thompson, J. L.; McIntire, T. M.; Milton, S. C.; Cotman, C. W.; Glabe, C. G. *Science* 2003, *300*, 486.
(132) Engel, M. F. M.; Khemtémourian, L.; Kleijer, C. C.; Meeldijk, H. J. D.; Jacobs, J.; Verkleij, A. J.; de Kruijff, B.; Killian, J. A.; Höppener, J. W. M. *Proceedings of the National Academy of Sciences U.S.A.* 2008, *105*, 6033.
(133) Butterfield, S. M.; Lashuel, H. A. *Angewandte Chemie International Edition* 2010, *49*, 5628.
(134) Kapurniotu, A. *Biopolymers* 2001, *60*, 438.
(135) Padrick, S. B.; Miranker, A. D. *Biochemistry* 2002, *41*, 4694.
(136) Sparr, E.; Engel, M. F. M.; Sakharov, D. V.; Sprong, M.; Jacobs, J.; de Kruijff, B.; Hoppener, J. W. M.; Killian, J. A. *FEBS Letters* 2004, *577*, 117.
(137) Jayasinghe, S. A.; Langen, R. *Biochemistry* 2005, *44*, 12113.
(138) Shen, Y. R. *Nature* 1989, *337*, 519.
(139) Engel, M. F. M.; vandenAkker, C. C.; Schleeger, M.; Velikov, K. P.; Koenderink, G. H.; Bonn, M. *Journal of the American Chemical Society* 2012.
(140) Fu, L.; Ma, G.; Yan, E. C. Y. *Journal of the American Chemical Society* 2010, *132*, 5405.
(141) Chen, X. Y.; Clarke, M. L.; Wang, J.; Chen, Z. *International Journal of Modern Physics B* 2005, *19*, 691.
(142) Castner, D. G.; Ratner, B. D. *Surface Science* 2002, *500*, 28.
(143) Miranda, P. B.; Shen, Y. R. *The Journal of Physical Chemistry B* 1999, *103*, 3292.

(144) Stockle, R. M.; Suh, Y. D.; Deckert, V.; Zenobi, R. *Chemical Physics Letters* **2000**, *318*, 131.
(145) Domke, K. F.; Pettinger, B. *Chemphyschem* **2010**, *11*, 1365.
(146) Deckert-Gaudig, T.; Kammer, E.; Deckert, V. *Journal of biophotonics* **2012**, *5*, 215.
(147) Deckert-Gaudig, T.; Deckert, V. *Physical Chemistry Chemical Physics* **2010**, *12*, 12040.
(148) Ono, K.; Yoshiike, Y.; Takashima, A.; Hasegawa, K.; Naiki, H.; Yamada, M. *J Neurochemistry* **2003**, *87*, 172.
(149) Ehrnhoefer, D. E.; Bieschke, J.; Boeddrich, A.; Herbst, M.; Masino, L.; Lurz, R.; Engemann, S.; Pastore, A.; Wanker, E. E. *Nature Structural and Molecular Biology* **2008**, *15*, 558.
(150) Bieschke, J.; Russ, J.; Friedrich, R. P.; Ehrnhoefer, D. E.; Wobst, H.; Neugebauer, K.; Wanker, E. E. *Proceedings of the National Academy of Sciences U.S.A.* **2010**, *107*, 7710.
(151) Jayasena, T.; Poljak, A.; Smythe, G.; Braidy, N.; Münch, G.; Sachdev, P. *Ageing Research Reviews* **2013**, *12*, 867.
(152) Bieschke, J.; Russ, J.; Friedrich, R. P.; Ehrnhoefer, D. E.; Wobst, H.; Neugebauer, K.; Wanker, E. E. *Proceedings of the National Academy of Sciences of the United States of America* **2010**, *107*, 7710.
(153) Meng, F.; Abedini, A.; Plesner, A.; Verchere, C. B.; Raleigh, D. P. *Biochemistry* **2010**, *49*, 8127.
(154) Ferreira, N.; Saraiva, M. J.; Almeida, M. R. *Febs Letters* **2011**, *585*, 2424.
(155) Lopez del Amo, J. M.; Fink, U.; Dasari, M.; Grelle, G.; Wanker, E. E.; Bieschke, J.; Reif, B. *Journal of Molecular Biology* **2012**, *421*, 517.
(156) Palhano, F. L.; Lee, J.; Grimster, N. P.; Kelly, J. W. *Journal of the American Chemical Society* **2013**, *135*, 7503.
(157) Ozdal, T.; Capanoglu, E.; Altay, F. *Food Research International* **2013**, *51*, 954.
(158) Shoval, H.; Lichtenberg, D.; Gazit, E. *Amyloid* **2007**, *14*, 73.
(159) Azriel, R.; Gazit, E. *Journal of Biological Chemistry* **2001**, *276*, 34156.
(160) Necula, M.; Kayed, R.; Milton, S.; Glabe, C. G. *Journal of Biological Chemistry* **2007**, *282*, 10311.
(161) Fresco, P.; Borges, F.; Diniz, C.; Marques, M. P. *Medicinal research reviews* **2006**, *26*, 747.
(162) Manach, C.; Scalbert, A.; Morand, C.; Remesy, C.; Jimenez, L. *The American journal of clinical nutrition* **2004**, *79*, 727.
(163) Bieschke, J. *Neurotherapeutics* **2013**, *10*, 429.

Chapter 2

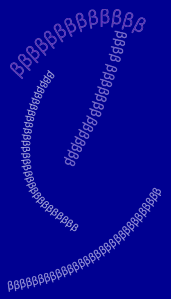

Morphology and persistence length of amyloid fibrils are correlated to peptide molecular structure

Based on: Corianne C. van den Akker, Maarten F.M. Engel, Krassimir P. Velikov, Mischa Bonn, Gijsje H. Koenderink: J. Am. Chem. Soc., 2011, 133 (45), pp 18030–18033

Abstract

The formation of amyloid fibrils is a self-assembly process of peptides or proteins. The superior mechanical properties of these fibrils make them interesting for materials science, but constitute a problem in amyloid-related diseases. Amyloid structures tend to be polymorphic and their structure depends on growth conditions. To understand and control the assembly process, insights into the relation between the mechanical properties and molecular structure are essential. We prepared long, straight as well as short, worm-like β-lactoglobulin amyloid fibrils and determined their morphology and persistence length by atomic force microscopy (AFM) and the molecular conformation using vibrational sum-frequency generation (VSFG) spectroscopy. We show that long fibrils with near-100% β-sheet content have a 40-times higher persistence length than short, worm-like fibrils with β-sheet contents below 80%.

Introduction

Many proteins and peptides of diverse sequence, structure and function spontaneously self-assemble into amyloid-like nanofibrils under a variety of conditions. Such fibrils are found in protein deposits of patients suffering from amyloid-related diseases, including Alzheimer's disease and type II diabetes mellitus.[1] However, the unique chemical and mechanical properties of these fibrils could also be exploited in novel biomaterials.[2] To understand and control amyloid fibril assembly, it is crucial to understand the relation between mechanical properties and molecular structure. Here we show that a distinct correlation exists between amyloid molecular structure and the structural and mechanical properties: long, straight amyloid fibrils with high persistence lengths are characterized by a high β-sheet content. In contrast, short, worm-like fibrils have a 40 times lower persistence length and drastically reduced β-sheet content.

Amyloid-like fibrils are characterized by a universal cross-β structure, in which the peptide backbone is orthogonal to the fibril axis.[3,4] Hydrogen bonds stabilize this structure and cause a high mechanical rigidity.[5] The fibrils are generally a few nanometers in diameter, reaching up to several micrometers in length, and tend to be polymorphic. For example, thin fibrils, twisted ribbons as well as crystalline-like materials have been observed.[6] Aggregates of misfolded proteins were originally discovered through their involvement in Alzheimer's disease. Currently, over 20 protein conformational diseases have been identified, including Creutzfeldt-Jakob disease and type II diabetes mellitus.[1] However, amyloids also perform functional biological roles, for instance to reinforce and structure bacterial biofilms and eggshells of fish and insects.[7-9] Amyloid fibrils are potentially interesting biomaterials, because of their high mechanical, thermal, and chemical stability. The fibrils can be easily functionalized since synthetic peptides with different primary sequences can be used. First applications that have been explored include fibrils as templates for nanowires[10] and as scaffolds for cell culture[11] or controlled drug release[12].

Despite the apparent importance of this class of materials, it has been challenging to relate the molecular structure to fibril morphology. While the molecular pathways of fibril formation have recently been elucidated[13,14], knowledge of the relation between the mechanical properties and molecular structure has been lagging. This is relevant for both applications in novel functional materials and disease-related amyloids. Fiber rigidity (directly related to persistence length) affects the degree to which fibers tangle to form insoluble plaques, which are a major pathological factor in systemic amyloidosis.[15] Further, a higher stiffness has been suggested to promote the disruption of cellular membranes by amyloid fibrils[16] and the mechanical rigidity influences fragmentation, which plays a major role in the kinetics of fibril growth.[5]

Results and discussion

The model protein β-lactoglobulin (β-lg) forms amyloid fibrils upon incubation at low pH and high temperature.[17-22] We prepared β-lg amyloid fibrils of various morphologies by varying the protein concentration between 3.0 and 7.5% and the incubation time between 16 and 96 hrs (SI Methods). The conversion of monomers to fibrils levels off after 24 hrs of incubation (SI Figure 2.1). We studied the morphology and mechanics of amyloid fibrils by atomic force microscopy (AFM) and their molecular conformation by vibrational sum-frequency generation (VSFG) spectroscopy. The strength of combining these techniques is that identical samples can be studied: the same substrate and sample preparation can be used both for AFM and VSFG. AFM gives morphological information about the fiber length, diameter and shape, from which the persistence length can be quantified.[22,23] VSFG provides information on the secondary structure and orientation of materials at surfaces or interfaces.[24] It utilizes two pulsed laser beams: one at visible and one at infrared (IR) frequency. As a result of interaction with the molecules at the surface, light at the sum-frequency of the visible and IR beams is generated. When the IR frequency matches a surface vibrational mode frequency, this process may be resonantly enhanced. Conformations of proteins are investigated by probing the amide I region (1600-1700 cm^{-1}), where β-sheets characteristic of amyloids can be distinguished from structures such as random coils and α-helices.[25] VSFG spectroscopy is a sensitive, label-free method that so far has been rarely used to determine the secondary structure of amyloids.[26,27]

To assess the morphology of the amyloid fibrils, we used tapping mode AFM (SI Methods). The contour length distributions reveal that long, straight fibrils show a broad length distribution, spanning a range of 0.2 μm up to 5 μm, whereas the worm-like fibrils have much shorter lengths (between 0.1 and 0.5 μm) (Figure 2.1a and b, SI Table 2.1). The short fibril length may be a consequence of the formation of more nuclei and therefore more fibrils at high concentrations of β-lg. At lower β-lg concentrations, the elongation rate probably dominates over the nucleation rate, and very long fibrils are formed. The short, worm-like fibrils are reminiscent of previously observed fibrils formed at high ionic strength or in water-solvent mixtures.[18,28]

We measured the height profiles of β-lg fibrils using AFM. The height profiles showed a periodicity of ~10 nm for thin fibrils (presumably protofibrils) and a periodicity of ~36 nm for fibrils composed of two protofibrils (Figure 2.1c and d). These observations are in agreement with previously reported periodicities of β-lg fibrils.[19] We quantified the diameter of the fibrils from their maximum height. As shown in Figure 2.1e and SI Table 2.1, long, straight fibrils have an average diameter of about 2.6 nm after 16 hrs incubation. The diameter distribution is rather broad, with a main population in the

range of 1-3.5 nm, and a tail with thicker fibrils having diameters of 4-6 nm. This observation is consistent with prior AFM studies of β-lg fibrils formed in 24 hrs, which also displayed different populations of fibrils with distinct diameters.[19] After 96 hrs incubation, the diameter distribution is narrower and shifted to larger diameter values. The average diameter is now almost two-fold higher than after 16 hrs incubation, amounting to ~4 nm. Our interpretation is that single protofibrils are predominantly formed for incubation times up to 16 hrs. Thicker fibrils composed of two or more protofibrils are formed after longer incubation times. As shown in SI Table 2.1, the same influence of incubation time on the fibril diameter is seen at other β-lg concentrations. The β-lg concentration itself does not strongly influence the fibril diameter.

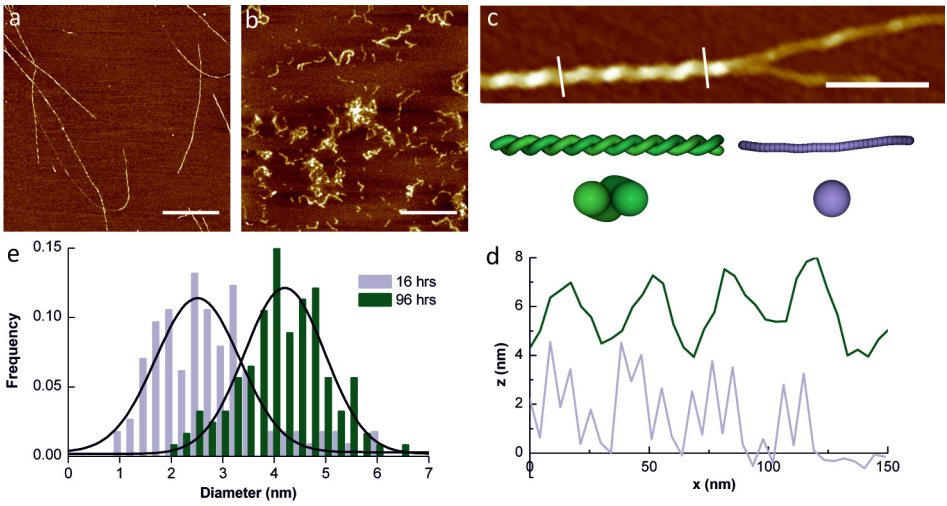

Figure 2.1: a and b) AFM height images of amyloid fibrils prepared in 16 h at (a) 3.0% and (b) 7.5% β-lg. Scale bar is 500 nm. c) A split fibril imaged using AFM in liquid and reconstructions of left-handed helical fibril formation from the twisting of a two-stranded ribbon (left) and a protofibril (right). The white lines indicate fibril sections used for periodicity measurements. Scale bar is 100 nm. d) Cross sections of the fibril shown in (c), showing periodicities of 36 nm for the helical fibril (top) and 10 nm for the protofibril (bottom). e) Diameter distribution of fibrils formed at 3.0% β-lg during incubation times of 16 and 96 h. Black lines are Gaussian fits.

We measured the persistence length from the shape of the fibrils, more specifically from the relation between their contour length, *C*, and end-to-end distance, *E* (SI Methods).[29,30] To calculate the persistence length, E^2 was plotted as a function of *C*. Figure 2.2 shows experimental data with theoretical fits for long, straight and short, worm-like fibrils formed in 16 hrs. There was a clear distinction between the straight fibrils formed at a protein concentration of 3.0% and the worm-like fibrils formed at 7.5% (SI Table 2.1). The straight fibrils have persistence lengths around 3818 ± 164 nm,

while the worm-like fibrils have a persistence length of only 92 ± 7 nm, consistent with previous findings.[31-33] The persistence length decreases for increasing β-lg concentration.

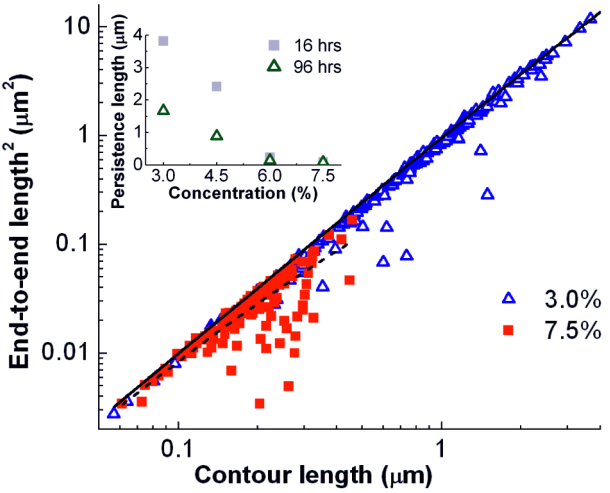

Figure 2.2: Plot of the squared end-to-end distance versus contour length for fibrils formed at 3.0 and 7.5% β-lg in 16 h (symbols) and corresponding fits (solid line: 3.0%; dashed line: 7.5%). Inset: Persistence lengths of fibrils formed at concentrations of 3.0 to 7.5% β-lg in 16 and 96 h.

The observation of two distinct fibril morphologies by AFM raises the question whether the secondary structure of these fibril types is different. To measure the secondary structure content, we acquired VSFG spectra in the amide I region. Figure 2.3a presents the amide I spectra for amyloid fibrils formed at concentrations between 3.0 and 7.5% β-lg in 16 hrs. For the long, straight fibrils formed at 3.0% β-lg, the amide I bands are centered at ~1625 cm^{-1}, which is assigned to β-sheet structure.[34,35] In contrast, the peak position shifts to higher wavenumbers for worm-like fibrils formed at 7.5% β-lg. To analyze the secondary structures of β-lg fibrils, the spectra were fitted using a two-component Lorentzian model. The components center in two regimes: 1620-1643 cm^{-1}, which is assigned to β-sheets, and 1643-1666 cm^{-1}, which is assigned to disordered structures and/or α-helices.[25,34-36] We calculated the fraction of the integrated intensity of peaks fitted to the VSFG data for these two bands (Figure 2.3b). In our analysis we have assumed that the transition dipole and the Raman dipole are the same for the different types of secondary structure, similar to prior studies.[26,27] Although this is not strictly true[36,37], a detailed analysis taking into account the IR and Raman transition dipoles would be extremely difficult due to the complexity (i.e. size distribution, unknown concentration) of the amyloid fibril samples that we use in our study. In

addition, the AFM data show that the fibrils are randomly oriented on the surface, thereby cancelling any orientation dependency in the SFG intensity.

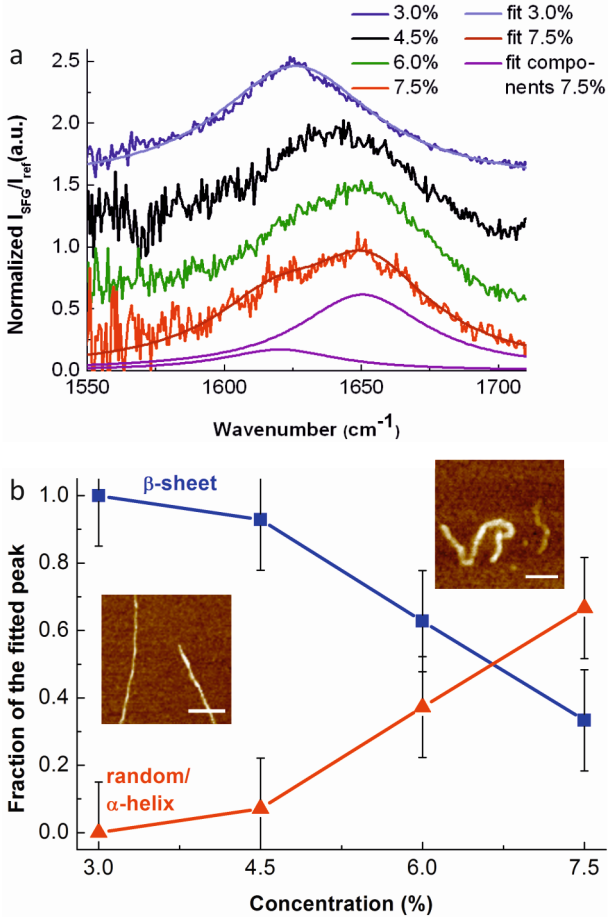

Figure 2.3: a) Normalized VSFG spectra and b) fraction of β-sheet and random/α-helical intensity of fibrils formed at concentrations of 3.0 to 7.5% β-lg in 16 h. Spectra and fractions are averages from three measurements. Spectra have been normalized and are plotted with an offset of 0.5 au along the y-axis. Scale bar in AFM images is 100 nm.

The β-sheet intensity is close to 100% for 3.0% β-lg but drops to approximately 40% when increasing the β-lg concentration to 7.5% for samples incubated for 16 hrs (Figure 2.3). For samples incubated for 96 hrs, the β-sheet intensity also drops, from close to 100% to 55% (SI Figure 2.5). The fits and the fit parameters for each spectrum are shown in SI Figure 2.3 and SI Figure 2.4, and in SI Table 2.2.

The straight and worm-like fibrils therefore do not only possess a different morphology, but also a fundamentally different secondary structure. Worm-like fibrils formed at high β-lg concentrations mainly consist of unordered and/or α-helical structures, whereas straight fibrils are composed of β-sheets. The β-sheet-rich long, straight fibrils have a 40 times higher persistence length compared to the short, worm-like fibrils. The high persistence length likely originates from a strong hydrogen-bonding network in the aligned backbones of the β-sheet-rich fibrils. In contrast, the much lower persistence length of the worm-like fibrils suggests that weaker intermolecular forces are present, as is expected for the less-organized fibrils with reduced β-sheet content that we observe here. Moreover, there may be structural defects in the fibril backbone leading to intrinsic curvature. These notions agree with the recent suggestion of a positive correlation between β-sheet structure and persistence length.[5]

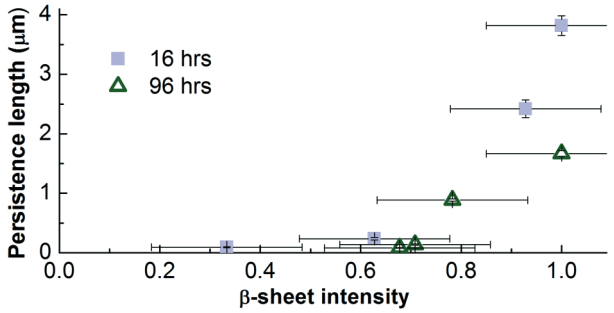

Figure 2.4: Plot of the persistence length versus the intensity of β-sheet content of fibrils formed at concentrations of 3.0 to 7.5% β-lg in 16 and 96 h.

Conclusions

The combined use of AFM and VSFG spectroscopy provides morphological, mechanical and structural information of amyloid fibrils deposited on a solid surface. We show that short, worm-like fibrils formed at high concentrations of β-lg contain less β-sheet content than long, straight fibrils. This can be related to the lower persistence length that is observed. The negative correlation between monomer concentration on the one hand, and β-sheet content, fibril length and persistence length on the other, is presumably related to the formation of more nuclei, and more (proto-)fibrils at high concentration, which then assemble into more disordered structures. Correlating β-sheet content and persistence length suggests that a substantial increase in persistence length can only be achieved at β-sheet contents near 100% (Figure 2.4). These results may aid to the future, rational design of nano-biomaterials with specific mechanical properties.

Materials and methods

Bovine β-lactoglobulin (genetic variants A and B, Sigma, L0130) was dissolved in HCl solution (pH=2). To remove traces of electrolytes, the solution was extensively dialyzed (Slide-a-Lyzer, MWCO 10kDa, Thermo) against an HCl solution (pH=2). Insoluble protein was removed by filtration (0.1 µm filter, Millipore). The final protein concentration was determined using UV spectrophotometry (Perkin Elmer, Lambda 35 UV/VIS Spectrometer) at a wavelength of 278 nm based on an extinction coefficient[38] of 16.8 $mM^{-1}cm^{-1}$. To obtain fibrils of the desired morphology, a range of conditions was tested. The β-lactoglobulin stock solution was diluted with HCl solution (pH=2) to a concentration between 3.0 and 7.5% (w/w). Samples in an eppendorf tube were heated in an oven at 80°C during a period varying between 2 and 96 hours, followed by quenching in ice water. Fibrils were separated from non-aggregated material by centrifuging the solution over centrifugal filters (MWCO 100kDa, Millipore) at 1000 *g* for 30 min.[39] The retentate containing the fibrils was diluted with HCl (pH=2) and centrifuged two additional times over the centrifugal filters to remove residual non-aggregated material. To quantify the extent of protein conversion into fibrils, the total amount of protein in the filtrate was quantified by determining the protein concentration with UV spectrophotometry at 278 nm and weighing the filtrate fraction (SI Figure 2.1). Atomic force microscopy (AFM) on the filtrate confirmed that fibrils were absent in this fraction. Conversion data are averages over at least three independent experiments with standard deviations. The filtered fibril suspension was centrifuged for 5 min at 2000 *g* to remove fibril aggregates. To determine the final protein concentration, fibril solutions were mixed with an equal volume of formic acid to solubilize the aggregated protein. The protein contents of these solutions were measured with the Bio-Rad protein assay (Bradford, Bio-Rad) using monomeric β-lg in 50% formic acid as the standard.[40]

The morphology, dimensions and persistence length of the fibrils were examined using tapping mode AFM with a Dimension 3100 Scanning Probe Microscope (Veeco). For AFM in air, fibril suspensions were diluted in HCl solution (pH=2) to concentrations of ~0.01%. A 20 µl aliquot was put on freshly cleaved mica, incubated for 5 min, washed with HCl solution (pH=2), and dried in air. For imaging in air, silicon cantilevers (force constant 5 N/m) were used. Images were flattened using Nanoscope 6.14 software and the diameter of fibrils was measured from their maximum height. For every condition, we averaged over at least n=110 fibrils. To investigate the effect of drying the fibrils, we also performed AFM experiments on fibrils in solution. For liquid AFM, fibril suspensions were diluted to ~0.1%, a drop was put on freshly cleaved mica, and measurements were performed directly at room temperature using silicon nitride cantilevers (force constant

0.24-0.35 N/m). The mean diameter of long, straight fibrils in liquid after 16 hrs incubation was 2.3 nm (n = 118), while for dried fibrils this was 2.6 nm (n=114). This indicates that the effect of drying on fibril diameter is small.

The contour length (C) of the fibrils and the end-to-end distance (E) between the fibril ends were measured with the Simple Neurite Tracer in Fiji[41] (n ≥ 155). The persistence length, L_p, is given by $\langle E \rangle_{2D} = 4\ L_p C\ (1\text{-}2\ L_p / C\ (1\text{-}e^{-C/2Lp}))$, assuming that the fibrils interact weakly with the mica surface and can relax to a two-dimensional equilibrium conformation.[22,29,30] This assumption is valid when the fibrils have no cross-overs,[23,29] as is clearly the case for all our samples. We verified that there was only one fibril population per sample by calculating the distribution of η, which is defined[30] as the difference between C and E, normalized by C: $\eta = (C - E) / C$. As a consistency check, we also calculated the persistence length based on the average cosine of the angle Θ between tangent vectors of the fibrils[29]: $\langle \cos(\Theta_C)_{2D} \rangle = e^{C/(2Lp)}$. The persistence lengths determined from $\langle E \rangle$ and $\langle \cos(\Theta c) \rangle$ were in good agreement; therefore only values determined from the $\langle E \rangle$ data are shown (SI Table 2.1).

For vibrational sum-frequency generation (VSFG) spectroscopy, a drop of undiluted fibril suspension was put on freshly cleaved mica, incubated for 5 min, washed with HCl (pH=2) and dried in air. The VSFG setup has been described in detail elsewhere.[42] Briefly, a visible beam (VIS) (800 nm, 20-30 μJ/pulse, spectral bandwidth of 25 cm^{-1}) is overlapped at the sample position with an infrared (IR) beam (2-3 μJ/pulse, 150 fs broadband) which is centered at 1640 cm^{-1} and has a spectral bandwidth of 150 cm^{-1}. Both beams are focused down to a ~100 μm beam waist. The incident angles of the VIS and IR beams are 35° and 40°, respectively, both defined relative to the surface normal. The SFG light generated by the sample is detected with a monochromator connected to a charge-coupled device camera. All spectra were collected under unpolarized SFG, *s*-polarized VIS, and *p*-polarized IR conditions and integrated over 6 min. We have repeatedly observed the absence of a psp signal for both β-lg fibrils and human Islet Amyloid Polypeptide (hIAPP) fibrils; therefore we have not used a polarizer in the detection path (SI Figure 2.2). The spectra were normalized to a reference signal from a z-cut quartz plate. Spectral analysis included background subtraction and division by the spectrum of the quartz reference. The SFG spectra for the three locations of one sample were averaged, and subsequently fitted using an equation that is commonly used for fitting of SFG spectra.[24] Fitting was performed using a one- or two-component Lorentzian model and included maximum entropy method (MEM) analysis to verify the fit.[24] The fit yields values for the amplitude and phase of the non-resonant susceptibility, and for the amplitude, wavenumber and line width of each component, as shown in SI Table 2.2. Next, the amplitude divided by the full width at half height (FWHH) is

calculated. This value is proportional to the amount of secondary structure, when assuming that the IR and Raman dipole do not depend on the secondary structure and that orientation effects are cancelled out by the random orientation of the fibrils on the mica. The value of Amp/FWHH has been normalized and plotted against concentration. The errors on these values are estimated to be ±0.15, based on the variation in fit results when different fit assumptions are made.

By comparing SFG spectra from fibrils on mica that were dried or hydrated by D_2O, we confirmed that the structure of wet and dry β-lg fibrils prepared under our conditions is very similar in line with recent studies[43,44].

Acknowledgment

The authors thank Norbert Mücke for help with persistence length calculations. This work is part of the Industrial Partnership Programme (IPP) Bio(-Related) Materials (BRM) of the Stichting voor Fundamenteel Onderzoek der Materie (FOM), which is financially supported by the Nederlandse Organisatie voor Wetenschappelijk Onderzoek (NWO). The IPP BRM is co-financed by the Top Institute Food and Nutrition and the Dutch Polymer Institute.

References

(1) Stefani, M.; Dobson, C. M. *Journal of Molecular Medicin* **2003,** *81*, 678-699.
(2) Cherny, I.; Gazit, E. A*ngewandte Chemie International Edition* **2008,** *47,* 4062-4069.
(3) Krebs, M. R. H.; Domike, K. R.; Cannon, D.; Donald, A. M. *Faraday Discussions* **2008,** *139,* 265-274.
(4) Tycko, R. *Current Opinion in Structural Biology* **2004,** *14,* 96-103.
(5) Knowles, T. P.; Fitzpatrick, A. W.; Meehan, S.; Mott, H. R.; Vendruscolo, M.; Dobson, C. M.; Welland, M. E. *Science* **2007,** *318,* 1900-1903.
(6) Marshall, K. E.; Serpell, L. C. *Soft Matter* **2010,** *6,* 2110-2114.
(7) Fowler, D. M.; Koulov, A. V.; Balch, W. E.; Kelly, J. W. *Trends in Biochemical Sciences* **2007,** *32,* 217-224.
(8) Chiti, F.; Dobson, C. M. *Annual Review of Biochemistry* **2006,** *75,* 333-366.
(9) Otzen, D.; Nielsen, P. H. *Cellular and Molecular Life Sciences* **2008,** *65,* 910-927.
(10) Scheibel, T.; Parthasarathy, R.; Sawicki, G.; Lin, X. M.; Jaeger, H.; Lindquist, S. L. *Proceedings of the National Academy of Sciences U.S.A.* **2003,** *100,* 4527-4532.
(11) Gelain, F.; Bottai, D.; Vescovi, A.; Zhang, S. G. *PLoS One* **2006,** *1,* e119.
(12) Maji, S. K.; Schubert, D.; Rivier, C.; Lee, S.; Rivier, J. E.; Riek, R. *PLoS Biology* **2008,** *6,* 240-252.
(13) Shim, S. H.; Gupta, R.; Ling, Y. L.; Strasfeld, D. B.; Raleigh, D. P.; Zanni, M. T. *Proceedings of the National Academy of Sciences U.S.A.* **2009,** *106,* 6614-6619.
(14) Knowles, T. P. J.; Shu, W.; Devlin, G. L.; Meehan, S.; Auer, S.; Dobson, C. M.; Welland, M. E. *Proceedings of the National Academy of Sciences U.S.A.* **2007,** *104,* 10016-10021.
(15) Tan, S.Y.; Pepys, M.B. *Histopathology* **1994,** *25,* 403-414.

(16) Engel, M.F.M.; Khemtemourian, L.; Kleijer, C.C.; Meeldijk, H.J.D.; Jacobs, J.; Verkleij, A.J.; de Kruijff, B.; Killian, J.A.; Höppener, J.W.M. *Proceedings of the National Academy of Sciences U.S.A.* **2008,** *105,* 6033-6038.
(17) van der Linden, E.; Venema, P. *Current Opinion in Colloid and Interface Science* **2007,** *12,* 158-165.
(18) Gosal, W. S.; Clark, A. H.; Ross-Murphy, S. B. *Biomacromolecules* **2004,** *5,* 2408-2419.
(19) Adamcik, J.; Jung, J. M.; Flakowski, J.; De Los Rios, P.; Dietler, G.; Mezzenga, R. *Nature Nanotechnology* **2010,** *5,* 423-428.
(20) Arnaudov, L. N.; de Vries, R.; Ippel, H.; van Mierlo, C. P. M. *Biomacromolecules* **2003,** *4,* 1614-1622.
(21) Akkermans, C.; Venema, P.; van der Goot, A. J.; Gruppen, H.; Bakx, E. J.; Boom, R. M.; van der Linden, E. *Biomacromolecules* **2008,** *9,* 1474-1479.
(22) Gosal, W. S.; Morten, I. J.; Hewitt, E. W.; Smith, D. A.; Thomson, N. H.; Radford, S. E. *Journal of Molecular Biology* **2005,** *351,* 850-864.
(23) Rivetti, C.; Guthold, M.; Bustamante, C. *Journal of Molecular Biology* **1996,** *264,* 919-932.
(24) Sovago, M.; Vartiainen, E.; Bonn, M. *Journal of Physical Chemistry C* **2009,** *113,* 6100-6106.
(25) Chen, X. Y.; Clarke, M. L.; Wang, J.; Chen, Z. *International Journal of Modern Physics B* **2005,** *19,* 691-713.
(26) Fu, L.; Ma, G.; Yan, E. C. Y. *Journal of the American Chemical Society* **2010,** *132,* 5405-5412.
(27) Fu, L.; Liu, J.; Yan, E.C.Y. *Journal of the American Chemical Society* **2011,** *133,* 8094-8097.
(28) Arnaudov, L. N.; de Vries, R. *Biomacromolecules* **2006,** *7,* 3490-3498.
(29) Mucke, N.; Klenin, K.; Kirmse, R.; Bussiek, M.; Herrmann, H.; Hafner, M.; Langowski, J. *PLoS One* **2009,** *4,* e7756.
(30) Relini, A.; Torrassa, S.; Ferrando, R.; Rolandi, R.; Campioni, S.; Chiti, F.; Gliozzi, A. *Biophysical Journal* **2010,** *98,* 1277-1284.
(31) Jordens, S.; Adamcik, J.; Amar-Yuli, I.; Mezzenga, R. *Biomacromolecules* **2011,** *12,* 187-193.
(32) Aymard, P.; Nicolai, T.; Durand, D.; Clack, A. *Macromolecules* **1999,** *32,* 2542-2552.
(33) Sagis, L. M. C.; Veerman, C.; van der Linden, E. *Langmuir* **2004,** *20,* 924-927.
(34) Tamm, L. K.; Tatulian, S. A. *Quarterly Reviews of Biophysics* **1997,** *30,* 365-429.
(35) Oboroceanu, D.; Wang, L. Z.; Brodkorb, A.; Magner, E.; Auty, M. A. E. *Journal of Agricultural and Food Chemistry* **2010,** *58,* 3667-3673.
(36) Nguyen, K. T.; King, J. T.; Chen, Z. *Journal of Physical Chemistry B* **2010,** *114*, 8291-8300.
(37) Nguyen, K.T.; Le Chair, S.V.; Ye, S.; Chen, Z. *Journal of Physical Chemistry B* **2009,** *113,* 12169-12180.
(38) Veerman, C.; Baptist, H.; Sagis, L. M. C.; van der Linden, E. *Journal of Agricultural and Food Chemistry* **2003,** *51,* 3880-3885.
(39) Bolder, S. G.; Vasbinder, A. J.; Sagis, L. M. C.; van der Linden, E. *International Dairy Journal* **2007,** *17,* 846-853.
(40) Klunk, W. E.; Jacob, R. F.; Mason, R. P. *Analytical Biochemistry.* **1999,** *266,* 66-76.
(41) Longair, M. H.; Baker, D. A.; Armstrong, J. D. *Bioinformatics* **2011,** *27,* 2453-2454.
(42) Smits, M.; Sovago, M.; Wurpel, G. W. H.; Kim, D.; Muller, M.; Bonn, M. *Journal of Physical Chemistry C* **2007,** *111,* 8878-8883.
(43) Shewmaker, F.; Kryndushkin, D.; Chen, B.; Tycko, R.; Wickner, R.B. *Biochemistry* **2009,** *48,* 5074-5082.

(44) Squires, A.M.; Devlin, G.L.; Gras, S.L.; Tickler, A.K.; MacPhee, C.E.; Dobson, C.M. *Journal of the American Chemical Society* **2006,** *128,* 11738-11739.

Supplementary Figures and Tables

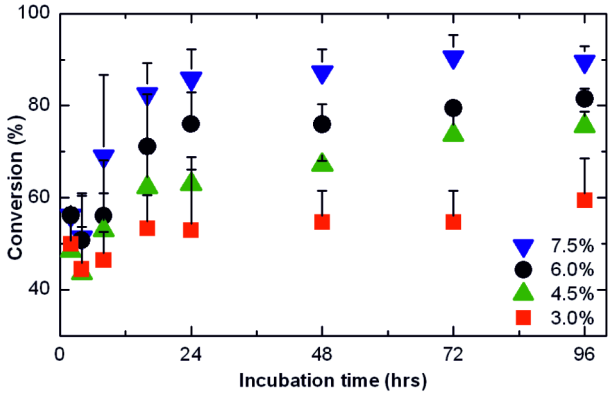

SI Figure 2.1: Conversion of monomer into aggregates for concentrations of 3.0 to 7.5% β-lg over an incubation time varying from 2 to 96 hrs.

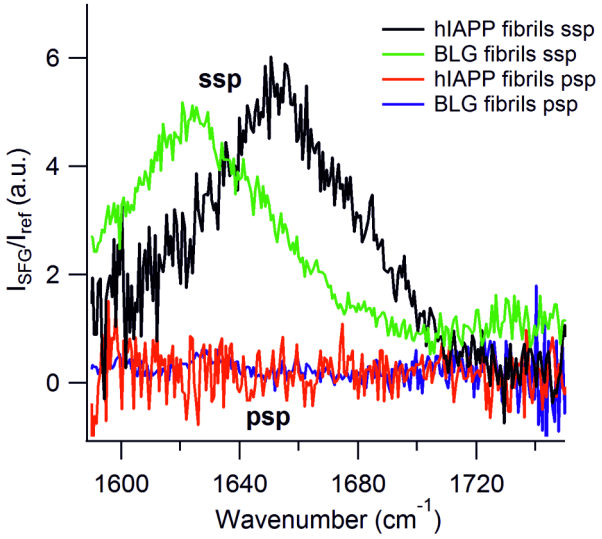

SI Figure 2.2: SFG spectra of β-lg fibrils and hIAPP fibrils show that the SFG signal is absent for the psp polarization, whereas the ssp polarization combination results in a significant SFG signal.

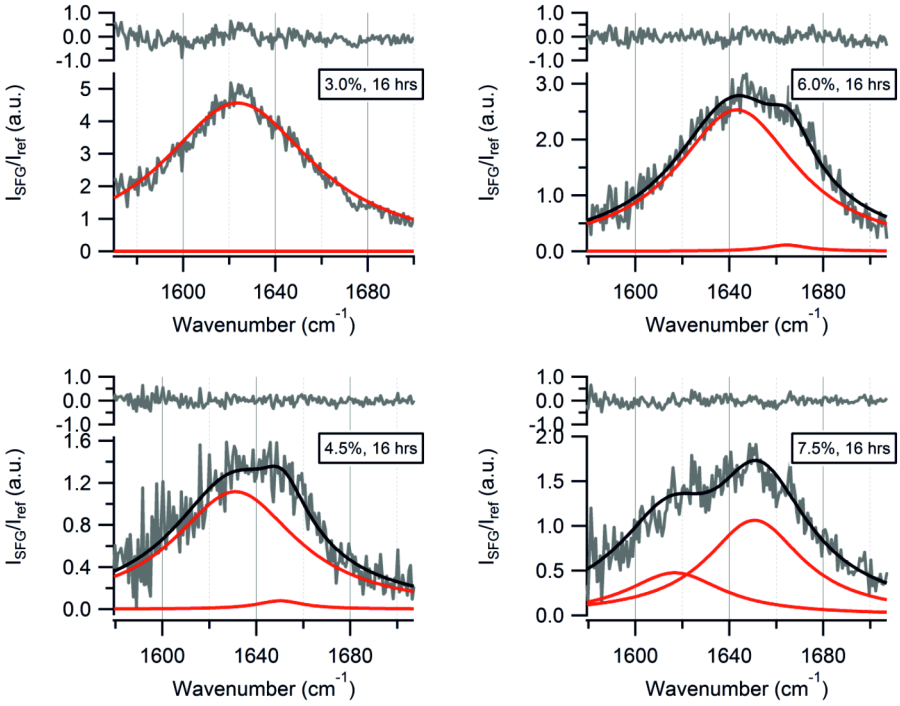

SI Figure 2.3: Fitting of the VSFG spectra of β-lg fibrils prepared from solutions containing 3.0 to 7.5% monomers over a time span of 16 hrs. The spectra are the average of the three spectra measured at three locations of the same sample. The lower panels show data (grey line), the fit (black line), and the components of the fits (red lines). The residuals are shown in the top panels.

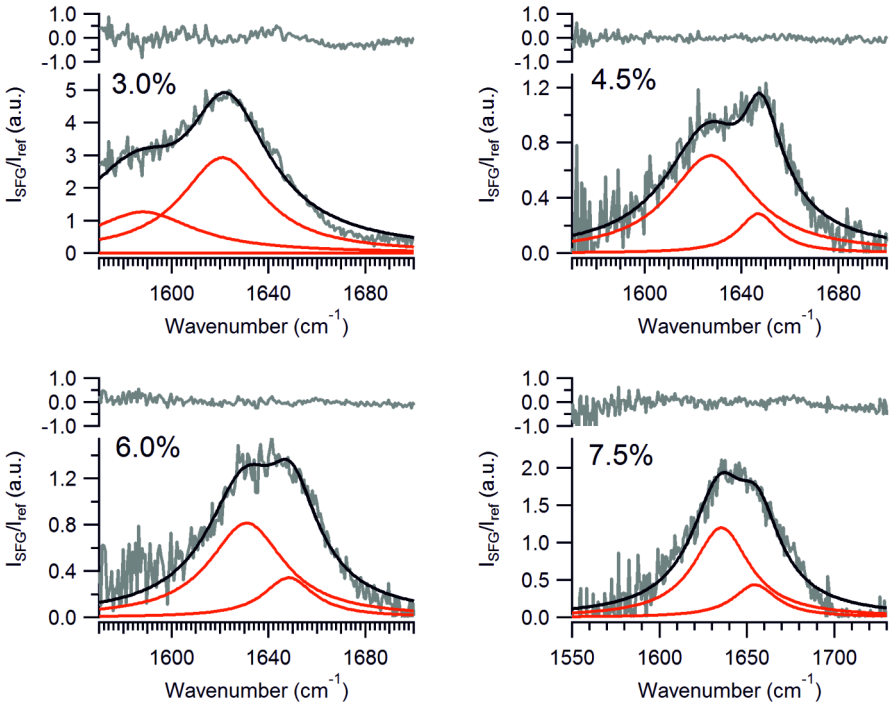

SI Figure 2.4: Fitting of the VSFG spectra of β-lg fibrils prepared from solutions containing 3.0 to 7.5% monomers over a time span of 96 hrs. The spectra are the average of the three spectra measured at three locations of the same sample. The lower panels show data (grey line), the fit (black line), and the components of the fits (red lines). The residuals are shown in the top panels.

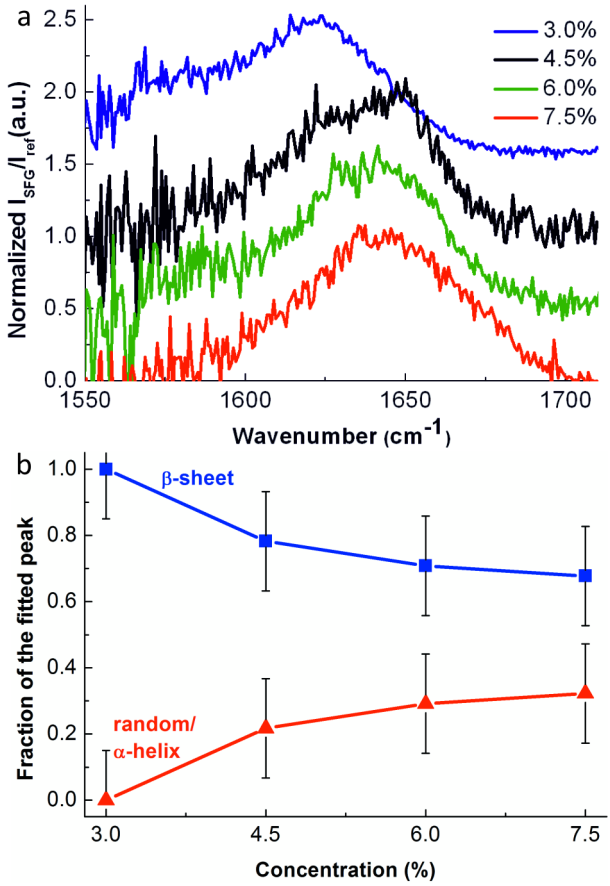

SI Figure 2.5: (a) Normalized VSFG spectra and (b) fraction of β-sheet and random/ α-helix content of fibrils formed at concentrations of 3.0 to 7.5% in 96 hrs. Spectra and fractions are averages from three measurements. Spectra have been normalized and are plotted with a offset of 0.5 a.u. offset along the y-axis.

SI Table 2.1: Average contour length, diameter and persistence length of fibrils formed under different conditions.

Conc. (%)	Time (hrs)	Contour length (μm)	Diameter (nm)	Persistence length (nm)
3.0	16	1.0 ± 0.79	2.6 ± 1.0	3818 ± 164
	96	0.92 ± 0.65	4.1 ± 0.9	1668 ± 46
4.5	16	0.86 ± 0.77	2.8 ± 1.1	2418 ± 149
	96	0.19 ± 0.13	5.2 ± 2.1	886 ± 18
6.0	16	0.41 ± 0.39	5.1 ± 1.0	237 ± 21
	96	0.14 ± 0.05	3.3 ± 1.0	139 ± 10
7.5	16	0.20 ± 0.07	2.9 ± 0.6	91.9 ± 7
	96	0.13 ± 0.04	6.1 ± 1.3	80.6 ± 5

SI Table 2.2: Fit parameters and standard deviations for fits of VSFG spectra.

Conc. (%)*,**	Incubation time (hrs)	Peak area 1 (a.u.)	St.dev. (a.u.)	Freq. 1 (cm^{-1})	St.dev. (cm^{-1})	FWHH 1 (cm^{-1})	St.dev. (cm^{-1})
3.0	16	80	1	1626	1	71	1
3.0	96	36	6	1621	1	42	3
4.5	16	39	5	1635	2	64	4
4.5	96	18	3	1627	2	42	4
6.0	16	32	7	1631	3	57	5
6.0	96	17	4	1631	2	38	4
7.5	16	15	6	1620	2	52	9
7.5	96	21	6	1635	2	39	5

Conc. (%)*,**	Incubation time (hrs)	Peak area 2 (a.u.)	St.dev. (a.u.)	Freq. 2 (cm^{-1})	St.dev. (cm^{-1})	FWHH 2 (cm^{-1})	St.dev. (cm^{-1})
3.0	16	-	-	-	-	-	-
3.0	96	-	-	-	-	-	-
4.5	16	3	3	1656	2	28	12
4.5	96	5	2	1647	1	20	3
6.0	16	19	6	1654	1	39	4
6.0	96	7	3	1648	1	26	4
7.5	16	30	5	1650	2	57	4
7.5	96	10	6	1655	2	31	7

For all fits, the non-resonant amplitude and phase were 0 and -1.6, respectively. The values for the standard deviation result from the fits in Igor. *For the concentration of 3% (16 hrs) a single component fitted the data based on visual inspection of the residuals. **For the concentration of 3% (96 hrs) an additional component at 1588 cm-1 was required, which is tentatively assigned to the contribution of side chains.

Chapter 3

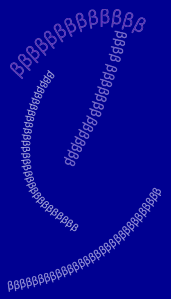

Multimodal spectroscopic study of amyloid polymorphism

Based on: Corianne C. van den Akker, Michael Schleeger, Anne L. Bruinen, Tanja Deckert-Gaudig, Krassimir P. Velikov, Ron M.A. Heeren, Volker Deckert, Mischa Bonn, Gijsje H. Koenderink (submission in preparation).

Abstract

Amyloid fibrils are self-assembled protein aggregates that are formed from unstructured peptides and unfolded proteins. The fibrils are characterized by a universal β-sheet core stabilized with hydrogen bonds, but the overall structure of amyloid fibrils is variable. The milk protein β-lactoglobulin forms amyloid fibrils upon incubation at low pH and high temperature. It is possible to tune the morphology and rigidity of the fibrils by the protein concentration during formation. We investigated the differences in the molecular structure and composition between long, straight and short, worm-like fibrils. We show using mass spectrometry that the peptide composition of the two fibrils types is similar. The bulk molecular structure of the fibrils probed with various spectroscopic techniques shows a large contribution of the β-sheet core, but no difference in structure between straight and worm-like fibrils. We probed specifically the surface of the two amyloid types with high spatial resolution using tip-enhanced Raman spectroscopy (TERS). The surface of the fibrils is heterogeneous in molecular structure and mainly exhibits unordered or α-helical structures. The TERS study reveals that the surface of long, straight fibrils contains more β-sheet structure than the surface of short, worm-like fibrils. To elucidate the origin of the difference in morphology and molecular structure, we studied the assembly kinetics using a combination of atomic force microscopy and mass spectrometry. We show that at high β-lg concentrations peptide refolding into amyloid fibrils takes place faster than at low concentrations. In summary, our data show that the two fibril types are structurally different and that it is only possible to detect differences in molecular structure using surface-specific spectroscopic techniques. The origin of the difference in molecular structure is likely related to the faster formation kinetics at high protein concentrations.

Introduction

Many proteins and peptides are capable of self-assembling into fibrillar aggregates known as amyloids. Amyloid fibrils are found in plaques in organs of patients suffering from diseases like type II diabetes mellitus and Alzheimer's disease.[1] However, Nature also makes functional use of the superior mechanical properties of amyloid fibrils, which are for instance found on the surfaces of fungi and bacteria.[2,3] Their superior mechanical properties also make amyloid fibrils interesting for novel biomaterials.[4] Amyloid fibrils are characterized by a universal cross-β structure, in which the peptide backbones are orthogonal to the fibril axis.[5,6] Hydrogen bonds stabilize the β-sheets and are thought to be primarily responsible for the high mechanical rigidity.[7] Although the structural motif of the amyloid fibril core is known, the overall structure is thought to be more complex and variable. Dependent on the constituent peptide or protein, side chains may protrude from the β-sheet core.[8,9] Moreover, amyloid samples are usually polymorphic and fibrils are often composed of two or more protofilaments, resulting in flat ribbon morphologies or twisted fibrils.[10]

β-Lactoglobulin (β-lg) is the main protein in whey and readily forms amyloid fibrils upon incubation below its isoelectric point (pH 5.1) at elevated temperatures.[11,12] Similar to other whey proteins, β-lg is of great importance to the dairy industry and is particularly useful for controlling the texture of a variety of foods.[13-15] β-lg has been investigated extensively as a model for the self-assembly of proteins into amyloid fibrils.[16-18] We have previously shown that the morphology of β-lg amyloid fibrils can be tuned by changing the protein concentration during incubation (Chapter 2).[19] Two different fibrils types were distinguished: long, straight fibrils and short, worm-like fibrils, with a factor 40 difference in persistence length. Nanoindentation experiments by Bennink et al. showed that indeed the two fibril types have a different Young's modulus.[20] Therefore the fibril types must be different in peptide composition and/or secondary structure content. It has been shown in experiments and modeling that β-sheet structure is associated with a high Young's modulus because of strong hydrogen bonding.[7] A lower Young's modulus is indicative of α-helical/disordered structure.[21]

Here, we perform a detailed spectroscopic investigation of the differences in molecular structure of the core and the surface of the straight and worm-like fibrils formed at different β-lg concentrations, combining bulk, surface-specific and high-resolution vibrational spectroscopies. We focus on the amide I mode, which reports on protein secondary structure. The molecular structure of the surface was measured with tip-enhanced Raman spectroscopy (TERS) and compared to the bulk secondary structure analyzed using Fourier transform infrared (FT-IR), Raman and circular dichroism (CD) spectroscopy. Moreover, we investigate whether the differences in molecular structure

of the two fibril types can be traced to differences in the assembly kinetics. The assembly pathway of β-lg amyloid fibrils is a multi-step process starting with hydrolysis of the protein into peptides, followed by refolding and fibril elongation. The relative timing of these steps may depend on the protein concentration. Therefore, we combined mass spectrometry to detect hydrolysis with AFM to detect fibril formation. Our TERS study reveals that the surface of straight amyloid fibrils formed at low β-lg concentration has a higher β-sheet content than the surface of worm-like fibrils formed at high β-lg concentration. However, with bulk spectroscopic techniques (Raman, FT-IR and CD spectroscopy), it is not possible to detect these highly local differences in molecular structure. The final peptide composition of both fibril types is observed to be very similar, so apparently hydrolysis has proceeded to the same extent in both cases. However, the fibril assembly kinetics are faster at higher concentrations, resulting in fibrils with a worm-like morphology.

Results and discussion

Amyloid fibril morphology. Amyloid fibrils were formed by incubation of an aqueous solution of β-lactoglobulin (β-lg) monomer at pH=2.0 and 80°C for 16 hrs at different protein concentrations, ranging between 3.0% and 7.5%. To characterize the morphology of the fibrils, they were deposited on a mica surface, dried, and imaged by AFM. At the lowest concentration (3.0% β-lg), the fibrils are straight (Figure 3.1a) and their lengths range from a few hundred nanometers up to 5 µm (Figure 3.1e). The average diameter is 2.6 nm ± 1.0 nm, quantified from their maximum height in AFM images. However, the diameter distribution is rather broad, with a main population in the range of 1-3.5 nm, and a tail with thicker fibrils having diameters of 4-6 nm (Chapter 2).[19] These thicker fibrils are composed of 2 or more protofilaments and show a twisted morphology. When the protein concentration is raised to 4.5% β-lg, the fibrils have a similar morphology (Figure 3.1b) but the length distribution shifts to smaller lengths (Figure 3.1f). At still higher concentration (6.0%), the fibrils are predominantly short and do not exhibit the straight morphology observed at low concentrations (Figure 3.1c). A few long fibrils are still observed, but the length distribution is dominated by short fibrils (Figure 3.1g). At the highest protein concentration (7.5% β-lg), the fibrils are all short and worm-like (Figure 3.1d) and they have a beads-on-a-string type morphology (inset Figure 3.1d). The fibril lengths are all below 500 nm (Figure 3.1h) and the average diameter is 2.9 nm ± 0.6 nm.

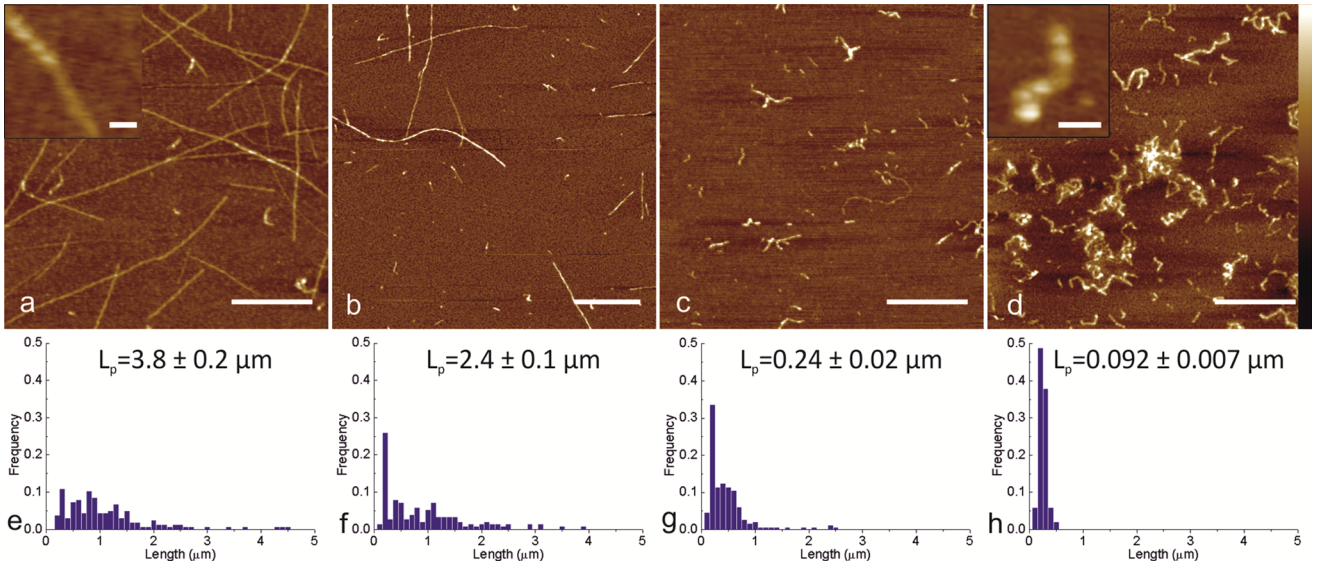

Figure 3.1: AFM images of β-lg amyloid fibrils on mica formed at protein concentrations of a) 3.0%; b) 4.5%; c) 6.0%; d) 7.5%. Scale bars are 500 nm, scale bars in insets are 50 nm. At 3.0% β-lg, long and straight fibrils are observed. Some fibrils are composed of two protofilaments twisted together (see inset in a). At 4.5% and 6.0% β-lg, a small fraction of long fibrils is formed, while a larger fraction contains short fibrils. At 7.5% β-lg, worm-like fibrils with a beaded structure (see inset in d) are formed. e-h) Length distribution of amyloid fibrils formed at β-lg concentrations of 3.0 to 7.5% and average persistence length L_p calculated based on the end-to-end length and the contour length measured in the AFM images.

To quantify the decreased rigidity of fibrils formed at elevated protein concentrations, we calculated the persistence length (L_p) from the end-to-end lengths (E) and contour lengths (C) of the fibrils (SI Figure 3.1). The average value of L_p decreases dramatically with monomer concentration: from 3.8 μm at 3.0% β-lg to 90 nm at 7.5% β-lg. At intermediate protein concentration, we clearly observe two different fibril populations of different rigidities when we plot E^2 vs C (Inset SI Figure 3.1b). Our results are consistent with recent AFM-based nanoindentation experiments by the group of Bennink, which showed that the rigid fibrils formed at low protein concentration have a Young's modulus in the GPa range, whereas the wormlike fibrils formed at high protein concentration have a much lower Young's modulus in the MPa range[20]. The co-existence of straight and wormlike fibrils at intermediate protein concentrations suggests that there is a shift in population with increasing protein concentration.

Amyloid fibril composition. The large difference in morphology and material properties of the different fibril types indicates that either the composition or the secondary structure of the peptides forming the fibrils must be different. To test whether there is a difference in the peptide composition of the two fibril types, we performed mass spectrometry on both fibril types. After incubation of β-lg monomer for 16 hrs, the non-aggregated material was removed by filtration with 100 kDa cut-off filters. The fibrils were dissociated in guanidine chloride buffer and peptide fragments were analyzed with MALDI-TOF spectrometry according to previously published methods[22]. It is expected that upon incubation at pH=2 and 80°C the peptide bonds between aspartic acid residues and adjacent amino acid residue are cleaved.[22-24] The sequence of β-lg with the positions of aspartic acid (D) highlighted are depicted in Figure 3.2a and predicted peptide fragments are listed in SI Table 3.1. The peaks observed in the mass spectra (SI Figure 3.2) were compared to this list of candidate peptides. We observed a high overlap of peptide fragments in straight and worm-like fibrils (Figure 3.2b and c). A few small differences between the fibril types are observed; however, for both fibrils, the entire sequence of β-lg is present in the spectra. This is in disagreement with previous results for fibrils formed at low β-lg concentrations, where only a small number of peptide fragments was observed in the fibrils.[22] The difference may be due to slightly different protocols for fibril formation, or because we were able to measure more sensitively and detect also smaller peptide fractions. To cross-check these data, we also analyzed the full amino acid composition of the filtered fibrils. This analysis revealed that the amino acid composition of both fibril types is almost identical to that of the monomer (Figure 3.2d). This supports the conclusions of mass spectrometry that, although the monomer is hydrolyzed to short peptides, all peptides end up in the fibrils. Taken together, these results show that the final peptide composition is identical for straight and worm-like fibrils.

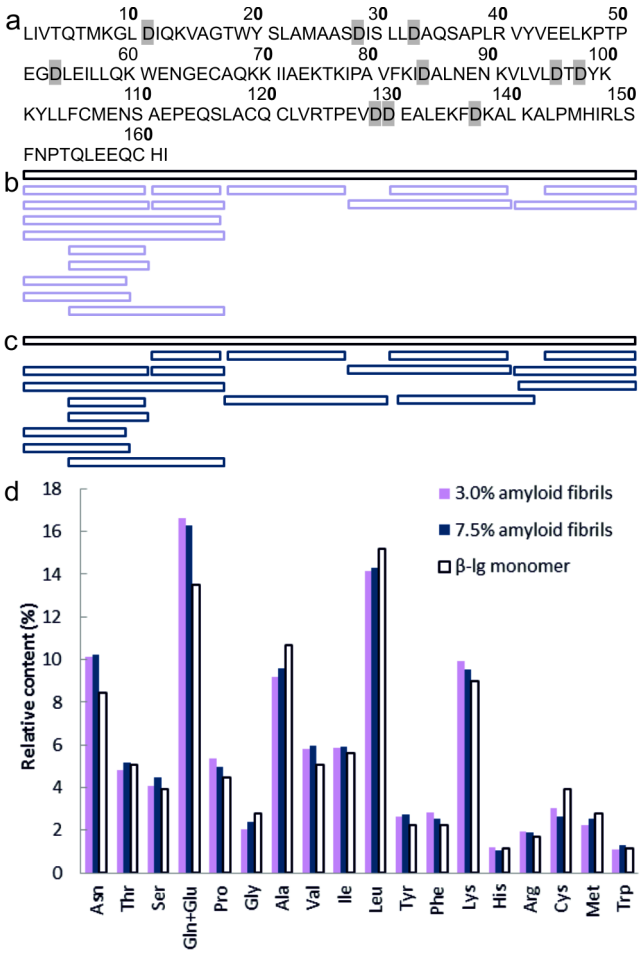

Figure 3.2: a) Amino acid sequence of β-lg monomer. Cleavage positions are at the aspartic acid residues (D) that are highlighted. b and c) Schematic overview of peptides derived from β-lg detected in amyloid fibrils formed at protein concentrations of b) 3.0% or c) 7.5%. In black the intact β-lg monomer (162 residues) is depicted. d) Relative amino acid content of amyloid fibrils formed at 3.0% (purple) or 7.5% (blue) determined by HPLC. White bars are the expected values based on the amino acid sequence of full-length β-lg variant B.

Amyloid fibril molecular structure. Given that the molecular composition of the straight and worm-like fibrils is identical, we assume that the difference in fibril morphology and Young's modulus must arise from a difference in secondary structure. To test this hypothesis, we determined the molecular structure with conventional spectroscopy methods: attenuated total reflection Fourier-transform infrared (ATR/FT-IR), Raman and circular dichroism (CD) spectroscopy. Since all three techniques are ensemble

measurements over a large number of amyloid fibrils, we performed the measurements on the fibrils formed at 3.0% and 7.5% β-lg, where the populations of respectively straight fibrils and wormlike fibrils are most homogeneous. Strikingly, the ATR/FT-IR spectra of the two fibril types are near-identical (Figure 3.3a). The spectral positions of the peak maxima around 1630 cm^{-1} indicate a high β-sheet content as expected for amyloidal samples; the main contribution of the amide I band is assigned to the low frequency band of anti-parallel β-sheet structure. A quantitative secondary structure analysis[25] yielded 75% β-sheets and turns as well as 15-20% unordered or α-helical secondary structures for both fibril types (see also SI Figure 3.3).

Raman spectroscopy reports on the amide I band as well, but with an altered sensitivity to the underlying vibrational normal modes. As a consequence, the high frequency band of the anti-parallel β-sheet structure is more pronounced in the Raman spectra of both samples (Figure 3.3b and SI Figure 3.4). Consistent with the FT-IR spectra, the Raman spectra show a high similarity between the amide I bands and indicate similar secondary structures for both fibril samples.

In addition, we determined the secondary structure of the two fibril types with CD and found 45% β-strands and –turns, 45% unordered structure and less than 10% α-helices for both samples (Figure 3.3c and SI Table 3.2). The quantitative discrepancy between CD and the vibrational spectroscopy techniques can be explained by the weaker sensitivity of CD to β-sheets and/or the weaker sensitivity of vibrational spectroscopy to unordered structures.

None of the spectroscopic techniques can detect any difference between the two fibril types. This is surprising given the large difference in morphology and Young's modulus of the fibrils. Moreover, it contrasts with our earlier vibrational sum-frequency generation (VSFG) spectroscopy measurements, which revealed a close to 100% β-sheet content for the straight fibrils whereas for short, worm-like fibrils approximately 50% helical or unordered structure was assigned (Chapter 2).[19] All the spectroscopic techniques described above are ensemble techniques, which average over many fibrils. Because the samples we measured are polymorphic, we need a different technique to directly link the peptide molecular structure to fibril morphology. Tip-enhanced Raman spectroscopy (TERS) provides spectroscopic information with nanoscale spatial resolution by scanning with an AFM equipped with a tip coated with a 10-20 nm Ag or Au particle and coupled to a Raman spectrometer. Because of the high local field enhancement of the Raman signal, it is possible to obtain Raman spectra from the material in the immediate proximity of the metalized tip, resulting in a spatial resolution in the nm scale. Recently, the Raman response from the surface of insulin amyloid fibrils[26,27] and hIAPP amyloid fibrils (Chapter 4 of this thesis) were determined.

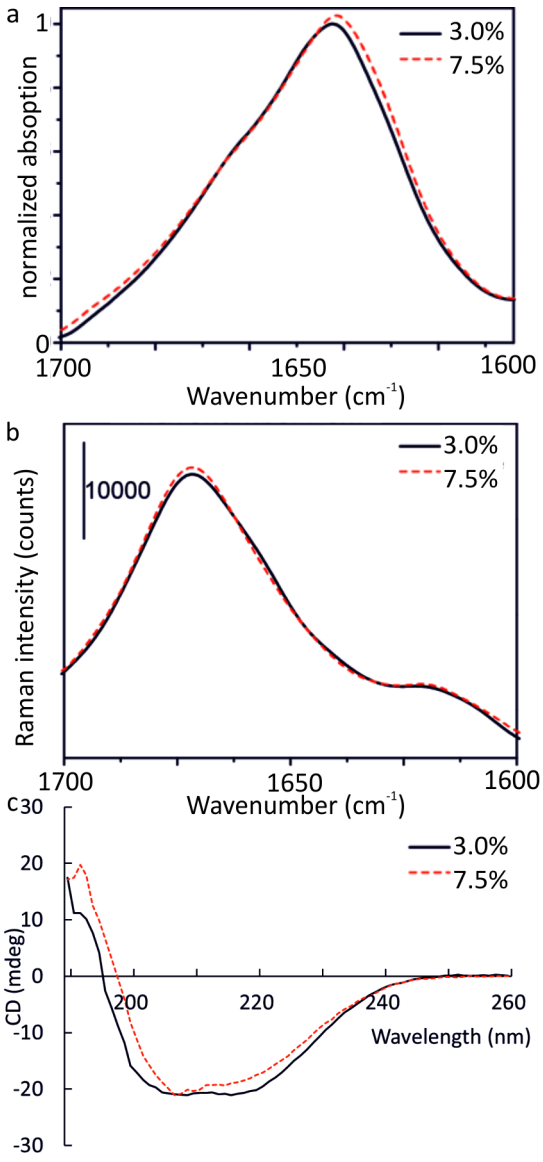

Figure 3.3: a) ATR/FT-IR spectra of amyloid fibrils formed at 3.0% (black) or 7.5% (red) β-lg. b) Raman spectra of amyloid fibrils formed at 3.0% (black) or 7.5% (red) β-lg. c) CD spectra of amyloid fibrils formed at 3.0% (black) or 7.5% (red) β-lg. For second derivatives and tables with fit parameters see SI Table 3.2 and SI Figure 3.3 and SI Figure 3.4.

For TERS spectroscopy on β-lg amyloid fibrils, suspensions formed at β-lg concentrations of 3.0% of 7.5% were dried on glass slides. The amide I region (1630-1680 cm^{-1}) was analyzed to determine the local molecular structure. Peaks between 1630 and 1655 cm^{-1} were assigned to unordered or α-helical structure and peaks between 1660 and 1680 cm^{-1} to β-sheets.[26-29] In some spectra a broad peak covering both regions, or two separated peaks were observed; these spectra were assigned to a third category called 'mixed' structures. In some spectra the peaks in the amide I region were suppressed, a phenomenon that is frequently observed in TERS and SERS experiments.[30,31]

Figure 3.4a shows an AFM image of part of a rigid, straight fibril formed at 3.0% β-lg. The black line indicates the position where 20 TERS spectra were obtained in spatial steps of 1 nm (Figure 3.4c). The amide I region of the spectra was analyzed for unordered or α-helical, β-sheet or mixed structures. We related the local molecular structure to the spatial information of the AFM image. The fibril has a remarkably heterogeneous surface structure with regions dominated by unordered or α-helical structure and some spectra showing β-sheet or mixed structures. For comparison, an AFM image and a grid of 10 x 5 TERS measurements on a worm-like fibril formed at 7.5% β-lg are shown (Figure 3.4b), again in steps of 1 nm. For clarity only the first 20 spectra are depicted in Figure 3.4d. The surface of this worm-like fibril is dominated by unordered/α-helical structure, but also contains small regions of mixed structures.

In order to compare the TERS data with ensemble measurements of the molecular structure, all TERS spectra with active amide I bands were analyzed. This analysis represents an average of 10 datasets for amyloids formed at 3.0% β-lg on 4 different straight fibrils, and 8 datasets on 6 worm-like fibrils formed at 7.5% β-lg. In total more than 350 spectra per condition were collected. For straight fibrils, 112 out of 350 spectra (32%) showed suppressed amide I bands. For worm-like fibrils, the number of suppressed amide I bands was 123 out of 399 spectra (31%). This phenomenon has been observed previously on TERS studies of insulin amyloid fibrils[26,27] and hIAPP amyloid fibrils (Chapter 4).

The datasets with active amide I bands (238 and 276 spectra for respectively straight and worm-like fibrils) were analyzed for unordered or α-helical, β-sheet and mixed structures. For 66% of the spectra of the straight fibrils and 77% of worm-like fibrils, only unordered or α-helical structures were observed (Figure 3.5a and SI Table 3.3). For straight fibrils, 10% of the spectra were classified as β-sheet and 24% as mixed structures. For worm-like fibrils these percentages were much lower: only 5% β-sheet and 17% mixed structures.

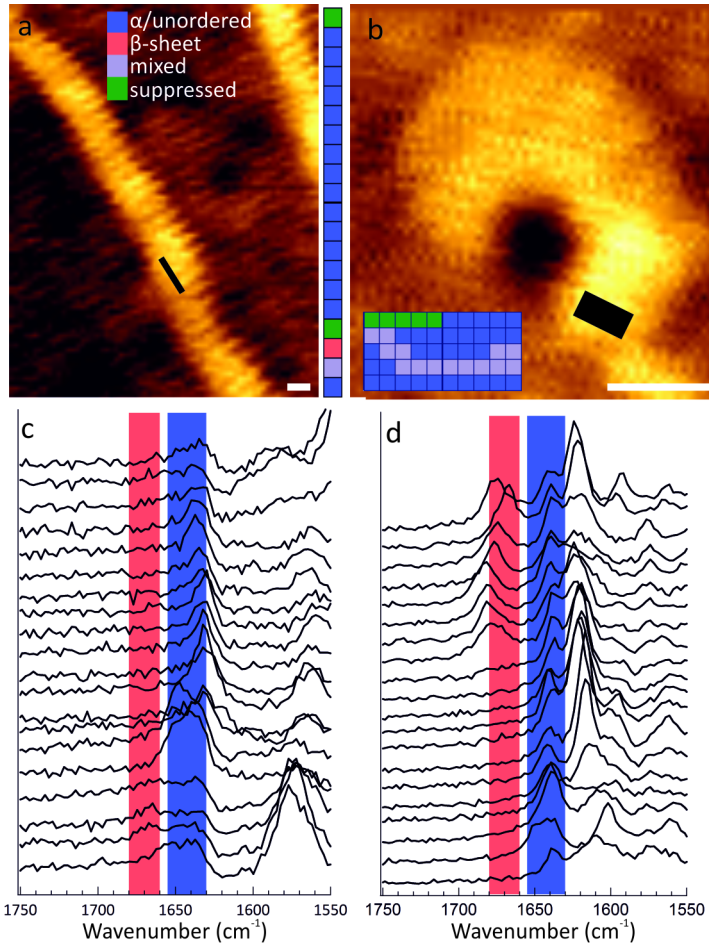

Figure 3.4: AFM images and corresponding TERS spectra obtained by sampling grids with 1-nm sized pixels of amyloid fibrils formed at a) 3.0% β-lg and b) 7.5% β-lg. Scale bar is 50 nm. c and d) Amide I region of the spectra corresponding to the regions indicated by black lines in a and b. Red band: β-sheet. Blue band: unordered/α-helical structure. In (d) only the first 20 spectra are shown, corresponding to the two bottom rows in the map in (b).

These data confirm the differences in molecular structure between straight and worm-like fibrils that we observed previously with VSFG (Chapter 2)[19], but the distinction is clearly more subtle in TERS. Apparently, TERS probes primarily the surface of the fibrils and to a lesser extent the β-sheet cores that are probed with bulk spectroscopy. The surface is more disordered for the worm-like fibrils, while in case of the straight fibrils the regular β-sheet core may be partly probed or the surface may be more ordered. The worm-like fibrils are expected to exhibit relatively short stretches of hydrogen-bonded

β-sheets along the axis, which results in less β-sheet structure observed with TERS. Our data show that only with surface-sensitive techniques like TERS and VSFG, it is possible to observe the differences between straight and worm-like fibrils. The large contrast in secondary structure between the worm-like and straight fibrils observed with VSFG can presumably be traced to the fact that VSFG is a coherent process, requiring the constructive addition of many oscillating dipoles in the far field; the worm-like fibrils exhibit spatial correlation lengths that are short compared to the coherence length required for efficient VSFG light emission, suppressing the signal from the β-sheets cores.

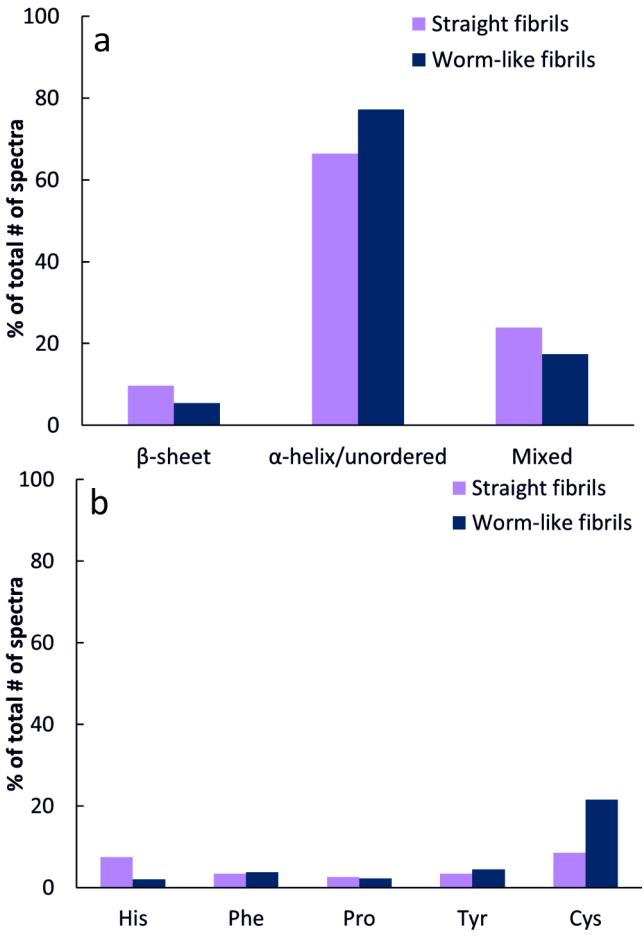

Figure 3.5: a) Ensemble analysis of the molecular structure observed with TERS for amyloid fibrils formed at 3.0% β-lg (purple) or 7.5% β-lg (blue). b) Ensemble analysis of the amino acid residues observed with TERS for amyloid fibrils formed at 3.0% β-lg (purple) or 7.5% β-lg (blue).

Besides the secondary structure, it is possible to identify specific amino acid residues with TERS through their unique vibrational bands, and determine their position at the fibril surface. We analyzed all spectra for peaks related to histidine (His), phenylalanine (Phe), proline (Pro), tyrosine (Tyr) and cysteine (Cys) (SI Table 3.4). Phe and Tyr were observed in 3 to 5% of all spectra for both fibril types (Figure 3.5b and SI Table 3.3). Pro was observed in only 2 to 3% of the spectra, although 8 of the 162 (5%) amino acid residues in β-lg monomer is Pro. This discrepancy may indicate that Pro is preferably in the core and not on the surface of the fibrils. For straight fibrils, His was observed much more frequently (7%) than for worm-like fibrils (2%). In both cases, this frequency is higher than expected from the amino acid sequence of β-lg, which features 2 His residues out of a total of 162 amino acids (1.2%). Cys was observed in 9% of the spectra for straight fibrils, and in 22% of the spectra for worm-like fibrils. These percentages are much higher than the expected value based on the number of Cys residues in β-lg monomer: 5 out of 162 (3.1%). Apparently Cys has a preference for the unordered or α-helical structure at the surface of the fibrils and not for the β-sheet core. This is in agreement with our TERS measurements on hIAPP amyloid fibrils reported in Chapter 4, for which we observed Cys in 15 to 25% of all spectra, while, from simple statistics, the expected percentage was 5%.

Concentration-dependent kinetics of amyloid formation. The kinetics of β-lg amyloid formation at acidic pH and elevated temperatures is known to be a multi-step process: first the monomers are hydrolyzed into a mixture of small peptides, of which a subset is thought to then fold and assemble into oligomers.[22] After this rate-determining step of oligomer formation, a relatively rapid growth of amyloid fibrils takes place.[32] It has been shown that amyloid fibrils formed at low β-lg concentration are built from peptides and contain no intact monomers.[22] For both fibril types, we measured the kinetics of hydrolysis by mass spectroscopy and SDS-PAGE and the kinetics of fibril formation by AFM.

We incubated β-lg monomer for 2, 4 or 24 hrs at pH=2 and 80°C and followed the hydrolysis in time by MALDI-TOF mass spectrometry. The mass spectra in Figure 3.6a-c clearly show a time-dependent decrease of the peak originating from the intact monomer (18.4 kDa) for samples incubated at 3.0% β-lg. (For comparison, a mass spectrum of β-lg monomers before incubation is shown in SI Figure 3.5.) After 4 hrs incubation (Figure 3.6b), there is still a large contribution of the intact monomer compared to the peptides. The decrease of the peak originating from the intact protein mainly takes place between 4 and 24 hrs. This is in contrast to the samples incubated at 7.5% β-lg, where after 4 hours the fraction of monomers is highly reduced (Figure 3.6d-e), although after 24 hrs incubation still a small fraction of monomers remains (Figure 3.6f).

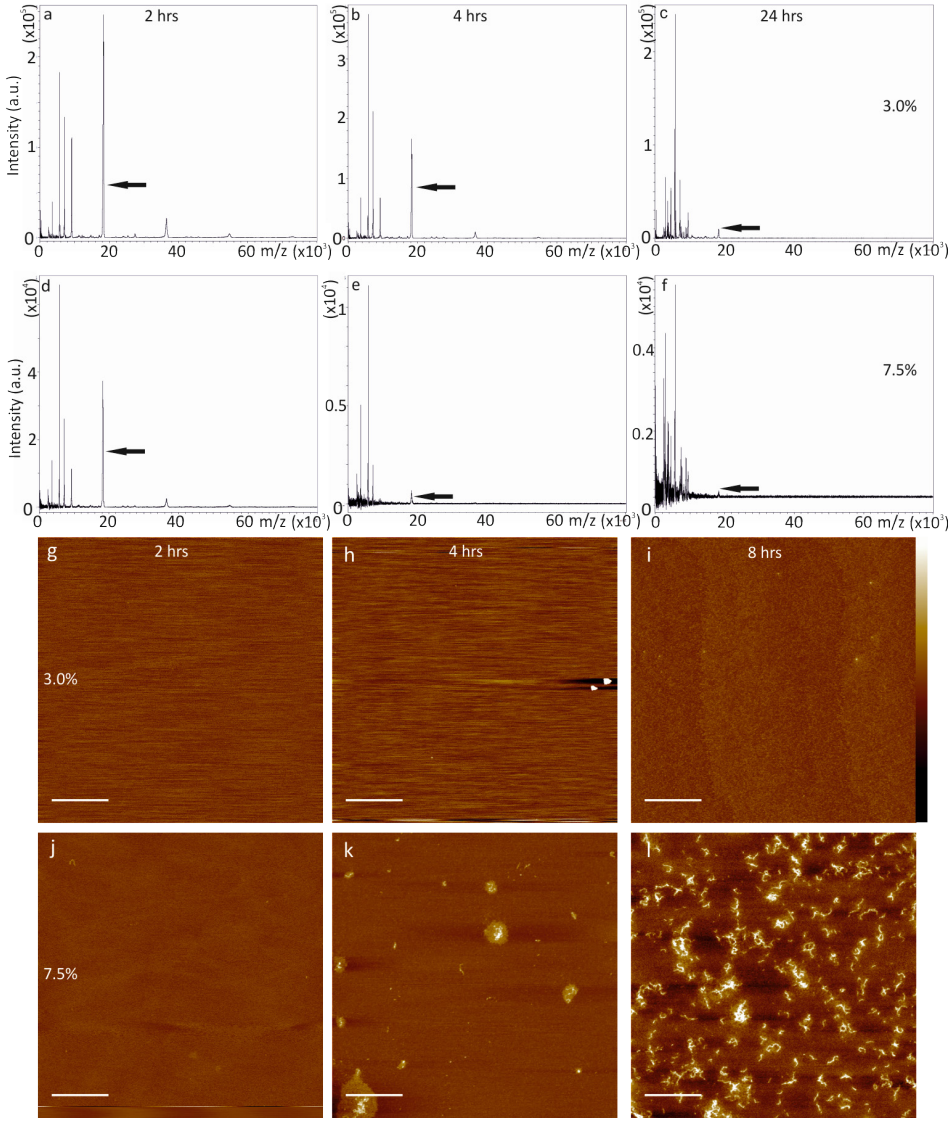

Figure 3.6: Mass spectra of β-lg incubated at 3.0% for a) 2 hrs; b) 4 hrs; c) 24 hrs; or at 7.5% for d) 2 hrs; e) 4 hrs; f) 24 hrs. The peak at ~18.4 x10^3 m/z corresponds to intact β-lg monomer. AFM images of β-lg incubated at 3.0% for a) 2 hrs; b) 4 hrs; c) 8 hrs; or at 7.5% for d) 2 hrs; e) 4 hrs; f) 8 hrs. Scale bars are 1 µm, height bar on the right hand side of panel (i) is 10 nm.

The formation of peptides and the decrease in the amount of intact monomers were qualitatively confirmed with SDS-PAGE (SI Figure 3.6). There are several possible explanations for the observation of the faster decrease of the ratio between intact monomers and peptides for samples incubated at 7.5% compared to those incubated at 3.0% β-lg. We suspect that (more) intact monomers are incorporated into the fibrils formed at 7.5% than at 3.0% β-lg, because oligomerization/fibril formation starts earlier. This would result in less non-aggregated, intact monomer in the sample. Another explanation could be that hydrolysis occurs faster in samples incubating at 7.5% β-lg than at 3.0% β-lg, but it is unclear why the hydrolysis rate would depend on protein concentration. To distinguish between these possibilities, mass spectrometry of filtered, dissociated fibrils in the same m/z range as probed in Figure 3.6 need to be performed.

Since the ratio between intact monomer and peptides decreases faster at higher protein concentration, we expect that refolding and oligomerization of the resulting peptides will also start earlier. To test this, we analyzed the morphology of the aggregates formed upon 2, 4 or 8 hrs with AFM (Figure 3.6g-l). At a concentration of 3.0% β-lg, first small aggregates were detected with AFM after 8 hrs incubation, observed as spheres with a height of 1-2 nm. At the same time, a few long fibrils were already observed (Figure 3.6i). At 7.5% β-lg, small spherical aggregates were observed already after 2 hrs and worm-like fibrils upon 4 hrs incubation. After longer incubation times the number of fibrils increased, but their morphology did not significantly change anymore. Although AFM images provide morphological information of the aggregates, only a small region of the sample is probed and it is not possible to quantify the results. It has been reported previously that oligomers stick less to the mica surface than fibrils[33], probably affecting the results.

We complemented the surface-based AFM assays with a thioflavin T (ThT) fluorescence assay, which can monitor the formation of amyloids in solution. ThT is a dye that binds to the β-sheets present in the amyloid fibril core. We indeed observe an increase of ThT fluorescence already upon incubation for 2 hrs for samples at concentrations of 7.5% β-lg, while for samples at 3.0% β-lg it takes 4 hrs before increased ThT fluorescence is detected (SI Figure 3.7).

Our data show that there is a difference between the formation kinetics of straight and worm-like fibrils: at high concentrations, the decrease of the ratio between intact monomers and peptides and aggregate formation takes place faster than at low concentrations.

Conclusions

We investigated the structural differences between straight and worm-like amyloid fibrils by AFM and a combination of surface and bulk vibrational spectroscopy techniques. AFM imaging revealed that the morphology of β-lg amyloid fibrils depends on the protein concentration during formation. At low concentration, the fibrils are long and straight, whereas at high concentration the fibrils are short and worm-like with a 40-fold lower persistence length. We hypothesized that this morphological difference could be caused by a difference in peptide composition or in molecular structure. Mass spectrometry showed that both fibril types are formed from peptide fragments, but no differences were observed between the fragments that were incorporated into the two fibril types. The bulk molecular structure was probed with FT-IR, Raman and CD spectroscopy. All three techniques reported high β-sheet contents and no differences between straight and worm-like fibrils. However, a difference in the surface structure of the two fibril types was revealed using TERS. The surface of both fibril types is heterogeneous and mainly contains unordered or α-helical structures. However, the straight fibrils have a higher β-sheet content on the surface than the worm-like fibrils, which is in line with the surface structure revealed with VSFG (Chapter 2).[19] To get a better understanding of the origin of the differences in morphology, rigidity and surface structure, we investigated the kinetics of fibril formation with AFM and mass spectrometry. We showed that the decrease of the ratio between intact monomer and peptides and the refolding of the peptides into fibrils is faster at high β-lg concentrations. In conclusion, straight and worm-like fibrils have a different surface structure, but it is only possible to probe this difference using surface-specific spectroscopic techniques. Furthermore, we show the importance of the assembly kinetics for the final structure and morphology of amyloid fibrils.

Materials and methods

Amyloid formation. β-lactoglobulin (β-lg) amyloid fibrils were prepared as described previously[19]. In short, bovine β-lg (genetic variants A and B, Sigma Aldrich, L0130) was dissolved in HCl dilution (pH=2.0). The solution was dialyzed extensively (Slide-a-lyzer, molecular weight cut-off (MWCO) 10kDa, Thermo) against an HCl solution (pH=2.0) and filtered (0.1 µm filter, Millipore) to remove aggregates. The final protein concentration was determined by UV-VIS spectrophotometry (Nanodrop, Thermo Scientific) at a wavelength of 280 nm based on an extinction coefficient of 16.8 mM^{-1} cm^{-1}.[34] Samples were heated in eppendorf tubes at 3.0 or 7.5% (w/w) in an oven at 80°C for 16 hrs without stirring. After quenching in ice water, the fibrils were separated from non-aggregated material by centrifugal filtering (Centrifugal filters, MWCO 100kDa, Millipore) at 1000 *g*. The retentate was washed with an HCl solution (pH=2) two

additional times. The filtered fibril suspension was centrifuged for 5 min at 2000 *g* to remove large fibril aggregates. To determine the final protein concentration, fibril suspensions were mixed with an equal volume of formic acid to solubilize the aggregated protein. The protein contents of these solutions were measured by spectrophotometry at a wavelength of 280 nm and compared to samples with known concentrations of β-lg.[35]

Atomic force microscopy (AFM). A drop of a diluted fibril suspension at a concentration of ~0.01 wt% was deposited onto freshly cleaved mica (Muscovite mica V-4, Electron Microscopy Sciences). After 5 min incubation, the sample was washed with HCl solution (pH=2.0) and dried in air. AFM images were acquired in tapping mode with a Dimension 3100 Scanning Probe Microscope (Bruker) using silicon cantilevers (TESPA, force constant 42 N/m, Bruker). Images were flattened using Nanoscope 6.14 software.

Fourier-Transform Infrared spectroscopy. The aqueous HCl solution was exchanged by a deuterium oxide based solution at pD=2.4 by 10-fold dilution and centrifuging for 3 times using centrifugal filters (MWCO 100 kDa, Millipore). Hereafter, the sample was incubated for 1 hr to allow for a full H/D exchange. A drop of 5 µL fibril suspension was air-dried on an ATR cell (single reflection, Thermo Spectra Tech, Thermo Fisher Scientific Inc.) at room temperature. ATR/FT-IR measurements were performed on a Nicolet 730 FT-IR spectrometer (Thermo Fisher Scientific Inc.) equipped with a liquid nitrogen cooled mercury cadmium telluride (MCT) detector. The spectral resolution was set to 4 cm^{-1} and for each measurement 256 spectra were averaged. The Happ-Genzel apodization function was used for the Fourier transformation. Quantitative secondary structure analysis of the amyloid samples based on the FT-IR absorption spectra was performed on the basis of the vibrational amide I band between 1600 and 1700 cm^{-1}. The general fitting procedure with Gaussian-shaped line widths of the spectral components was performed as described elsewhere [25] using OriginPro 8.5.1G software.

Raman spectroscopy. Samples for Raman spectroscopy were prepared by drying a drop of 5 µL fibril suspension on a silicon wafer. To yield a thick sample film, the procedure was repeated five times. Raman spectra were measured on a Bruker RFS 100/S spectrometer (Bruker Optics, Rheinstetten, Germany) using a 532 nm laser emission. The laser was focused onto the sample to a spot size of about 0.5 mm using a microscope (Bruker Raman Scope Senterra). For each sample spot, 5 spectra with 60 s recording time were averaged. The measured Raman spectra were corrected for the fluorescence signal using the LabSpec 5 software.

Circular dichroism (CD) spectroscopy. CD data were recorded using a J-815 spectrometer (Jasco) at 20°C. Filtered amyloid fibril samples were diluted in HCl dilution (pH=2.0) to protein concentrations of 0.03 wt% (~17µM) and measured in cuvettes with a path

length of 0.1 cm. CD spectra were collected over a range of 190-260 nm with a step size of 1 nm. Three measurements were averaged and the α-helical and β-sheet contents were determined using Dichroweb (database 7, CDSSTR, based on 48 proteins)[36,37].

Tip-enhanced Raman spectroscopy (TERS). Fibril suspensions were diluted in HCl dilution (pH=2.0) to concentrations of ~0.01%. A 20 µL aliquot was deposited onto cleaned glass slides, incubated for 5 min, washed with HCl dilution (pH=2.0) and dried in air. TERS measurements were performed on a setup comprised of an AFM (Nanowizard II, JPK, Germany) mounted on an inverted microscope (SP2750A, Acton Advanced, Princeton Instruments Roper Scientific, USA) with a CCD camera (Pixis 400, Princeton Instruments Roper Scientific, USA). The incident laser with λ= 532 nm (P = 0.42 mW on sample) was focused through a 40x (N.A. 1.35) oil immersion objective on the sample. The acquisition time was 10 s for all spectra. TERS tips were prepared by 25 nm silver evaporation on commercial AFM non-contact tips (NSG10, NT-MDT, Russia).

Mass spectrometry. Mass spectrometry experiments were performed according to the protocol of Akkermans et al.[22] Fibrils were dissolved by mixing in 0.15 M Tris-HCl buffer (pH=8.0) containing 8 M guanidine hydrochloride and 0.1 M dithiothreitol (DTT) and incubation for 1 hr. The solution was diluted in 50% (v/v) acetonitrile and 0.1% (v/v) TFA. 2 µL of the diluted sample was mixed with 18 µL of the matrix solution dimethoxy-4-hydroxycinnamic acid (CHCA) and 1 µL was dry spotted onto a 96 wells target plate. MALDI-TOF spectra were obtained using a SYNAPT G1 HDMS (Waters Corporation, Milford, USA), equipped with a 200 Hz Nd:YAG laser (355 nm) and was operating in positive V-reflectron mode with a 100-4000 Da mass range. For kinetics experiments, dialyzed and filtered β-lactoglobulin monomer solutions in HCl dilution at pH=2.0 were incubated in Eppendorf tubes in an oven at 80°C for 2, 4 or 24 hrs. After quenching in ice water, the suspensions were mixed in a 1:1 ratio with matrix solution (CHCA, as described above). 1 µl of the solutions was dry spotted on a 384 wells target plate and analyzed using a Ultraflex III MALDI TOF-MS (Bruker Daltonik GmbH, Bremen, Germany). The system is equipped with a 200 Hz Nd:YAG laser (355 nm, Smartbeam) and was operating in positive linear mode with a 0-80,000 Da mass range.

Amino acid analysis. Amino acid analysis upon hydrolysis was performed by Ansynth service B.V (The Netherlands) using high performance liquid chromatography (HPLC). Amyloid fibrils were prepared by incubation for 16 hrs, filtered and washed as described before.

SDS-PAGE. For SDS-PAGE, Precise Protein Gels 4-20% (Thermo Scientific) were used. β-lg monomer solution in HCl dilution (pH=2.0) was incubated at concentrations of 3.0% or 7.5% at 80°C for 2, 4, 8, 16 or 24 hrs. Samples were quenched on ice-water and mixed with sample buffer containing 10 mM Tris-HCl and 1 mM EDTA at pH=8.0. The gel was

run at 120V for 45 min using a running buffer containing 100 mM Tris, 100 mM HEPES and 0.1% SDS.

Thioflavin T fluorescence assay. Thioflavin T (ThT) was diluted in MilliQ water and filtered using a 0.1 µm filter (Millipore). β-lg monomer solution in HCl dilution (pH=2.0) was incubated at concentrations of 3.0% or 7.5% at 80°C for 2, 4, 8, 16 or 24 hrs. Samples were quenched on ice-water and mixed immediately with ThT solution to a final protein concentration of 100 µM and a ThT concentration of 100 µM in HCl solution (pH=2.0). Samples were measured in standard 96-well flat-bottom black microtiter plates (Nunc 237105) with a plate reader (PerkinElmer Victor X3) in combination with a 430 nm excitation filter and a 480 nm emission filter. All data are averages of 3 measurements and average fluorescence of a blank was subtracted.

Acknowledgment

We thank D. Schneider (Johannes Gutenberg Universitat, Mainz, Germany) for the kind possibility to make use of his CD spectrometer and S. Tans (FOM Institute AMOLF, The Netherlands) for the possibility to make use of the plate reader. We thank A. Kiss and S. Ellis (FOM Institute AMOLF, The Netherlands) for help with mass spectroscopy experiments. This work is part of the Industrial Partnership Programme (IPP) Bio(-Related) Materials (BRM) of the Stichting voor Fundamenteel Onderzoek der Materie (FOM), which is financially supported by the Nederlandse Organisatie voor Wetenschappelijk Onderzoek (NWO). The IPP BRM is co-financed by the Top Institute Food and Nutrition and the Dutch Polymer Institute.

References

(1) Stefani, M.; Dobson, C. M. *Journal of Molecular Medicine* **2003**, 81, 678.
(2) Gebbink, M.; Claessen, D.; Bouma, B.; Dijkhuizen, L.; Wosten, H. A. B. *Nature Reviews Microbiology* **2005**, 3, 333.
(3) Otzen, D.; Nielsen, P. H. *Cellular and Molecular Life Sciences* **2008**, 65, 910.
(4) Cherny, I.; Gazit, E. *Angewandte Chemie International Edition* **2008**, 47, 4062.
(5) Krebs, M. R. H.; Domike, K. R.; Cannon, D.; Donald, A. M. *Faraday Discussions* **2008**, 139, 265.
(6) Tycko, R. *Current Opinion in Structural Biology* **2004**, 14, 96.
(7) Knowles, T. P.; Fitzpatrick, A. W.; Meehan, S.; Mott, H. R.; Vendruscolo, M.; Dobson, C. M.; Welland, M. E. *Science* **2007**, 318, 1900.
(8) Nelson, R.; Sawaya, M. R.; Balbirnie, M.; Madsen, A. O.; Riekel, C.; Grothe, R.; Eisenberg, D. *Nature* **2005**, 435, 773.
(9) van Gestel, J.; de Leeuw, S. W. *Biophysical journal* **2007**, 92, 1157.
(10) MacPhee, C. E.; Dobson, C. M. *Journal of the American Chemical Society* **2000**, 122, 12707.
(11) Bromley, E. H. C.; Krebs, M. R. H.; Donald, A. M. *Faraday Discussions* **2005**, 128, 13.
(12) Gosal, W. S.; Clark, A. H.; Pudney, P. D. A.; Ross-Murphy, S. B. *Langmuir* **2002**, 18, 7174.

(13) Donald, A. M. *Soft Matter* **2008**, 4, 1147.
(14) van der Linden, E.; Venema, P. *Current Opinion in Colloid & Interface Science* **2007**, 12, 158.
(15) Foegeding, E. A. *Food Biophysics* **2006**, 1, 41.
(16) Hamada, D.; Tanaka, T.; Tartaglia, G. G.; Pawar, A.; Vendruscolo, M.; Kawamura, M.; Tamura, A.; Tanaka, N.; Dobson, C. M. *Journal of Molecular Biology* **2009**, 386, 878.
(17) Hamley, I. W. *Angewandte Chemie-International Edition* **2007**, 46, 8128.
(18) Adamcik, J.; Jung, J. M.; Flakowski, J.; De Los Rios, P.; Dietler, G.; Mezzenga, R. *Nature Nanotechnology* **2010**, 5, 423.
(19) vandenAkker, C. C.; Engel, M. F. M.; Velikov, K. P.; Bonn, M.; Koenderink, G. H. *Journal of the American Chemical Society* **2011**, 133, 18030.
(20) Bennink, M. L. *Personal communication*.
(21) Litvinov, R. I.; Faizullin, D. A.; Zuev, Y. F.; Weisel, J. W. *Biophysical journal* **2012**, 103, 1020.
(22) Akkermans, C.; Venema, P.; van der Goot, A. J.; Gruppen, H.; Bakx, E. J.; Boom, R. M.; van der Linden, E. *Biomacromolecules* **2008**, 9, 1474.
(23) Frare, E.; Polverino de Laureto, P.; Zurdo, J.; Dobson, C. M.; Fontana, A. *Journal of Molecular Biology* **2004**, 340, 1153.
(24) Mishra, R.; Sorgjerd, K.; Nystrom, S.; Nordigarden, A.; Yu, Y. C.; Hammarstrom, P. *Journal of Molecular Biology* **2007**, 366, 1029.
(25) Arrondo, J. L. R.; Muga, A.; Castresana, J.; Goni, F. M. *Progress in Biophysics & Molecular Biology* **1993**, 59, 23.
(26) Kurouski, D.; Deckert-Gaudig, T.; Deckert, V.; Lednev, I. K. *Journal of the American Chemical Society* **2012**, 134, 13323.
(27) Kurouski, D.; Deckert-Gaudig, T.; Deckert, V.; Lednev, I. K. *Biophysical journal* **2014**, 106, 263.
(28) Socrates, G. Infrared and Raman characteristic group frequencies; 3rd edition ed.; John Wiley & Sons: New York, 2004.
(29) Stewart, S. F., P.M. Spectrochim. *Acta A Mol. Biomol. Spectrosc.* **1999**, 55, 1641.
(30) Blum, C.; Schmid, T.; Opilik, L.; Metanis, N.; Weidmann, S.; Zenobi, R. *The Journal of Physical Chemistry C* **2012**, 116, 23061.
(31) Kurouski, D.; Postiglione, T.; Deckert-Gaudig, T.; Deckert, V.; Lednev, I. K. *The Analyst* **2013**, 138, 1665.
(32) Kroes-Nijboer, A.; Venema, P.; Bouman, J.; van der Linden, E. *Langmuir* **2011**, 27, 5753.
(33) Green, J. D.; Kreplak, L.; Goldsbury, C.; Blatter, X. L.; Stolz, M.; Cooper, G. S.; Seelig, A.; Kist-Ler, J.; Aebi, U. *Journal of Molecular Biology* **2004**, 342, 877.
(34) Veerman, C.; Baptist, H.; Sagis, L. M. C.; Van der Linden, E. *Journal of Agricultural and Food Chemistry* **2003**, 51, 3880.
(35) Klunk, W. E.; Jacob, R. F.; Mason, R. P. *Analytical Biochemistry* **1999**, 266, 66.
(36) Whitmore, L.; Wallace, B. A. *Biopolymers* **2008**, 89, 392.
(37) Whitmore, L.; Wallace, B. A. *Nucleic acids research* **2004**, 32, W668.

Supplementary Figures and Tables

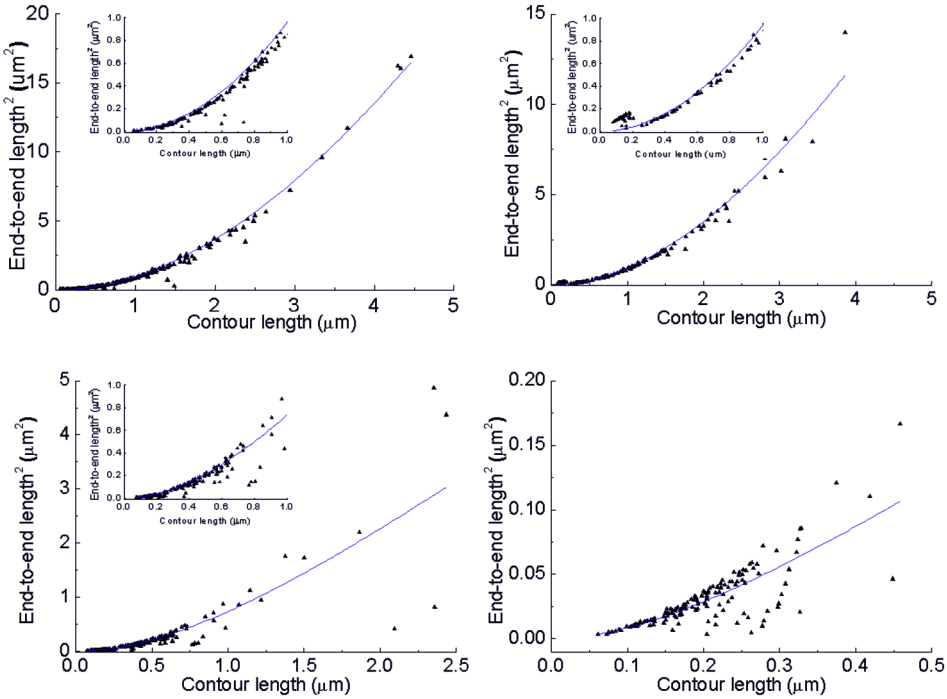

SI Figure 3.1: Squared end-to-end length vs contour length of amyloid fibrils on a mica surface formed at β-lg concentrations of a) 3.0%; b) 4.5%; c) 6.0%; d) 7.5%. Insets show a zoom of the small contour length region. At samples formed at 4.5% β-lg, a second population of short fibrils is observed.

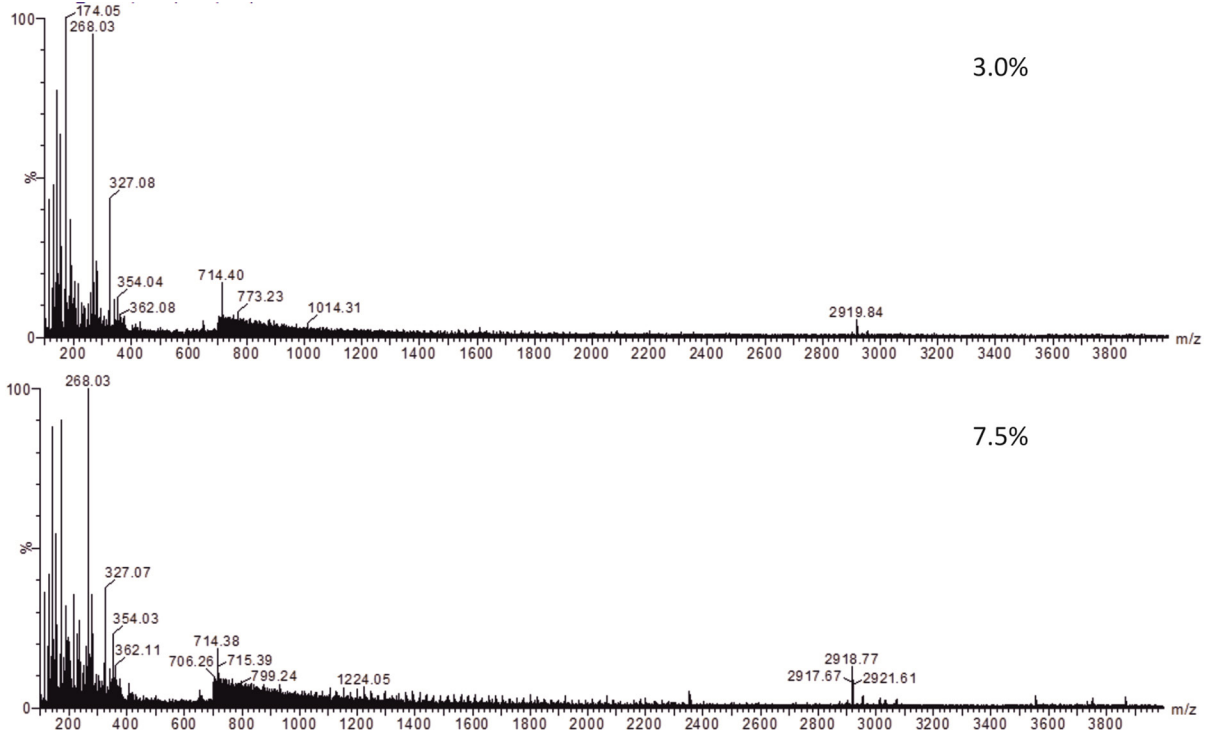

SI Figure 3.2: MALDI-TOF mass spectra of amyloid fibrils formed at 3.0% or 7.5% blg in 16 hrs. After incubation, fibrils were filtered to remove non-aggregated material and dissociated in guanidine chloride buffer and peptide fragments up to 4000 kDa were analyzed.

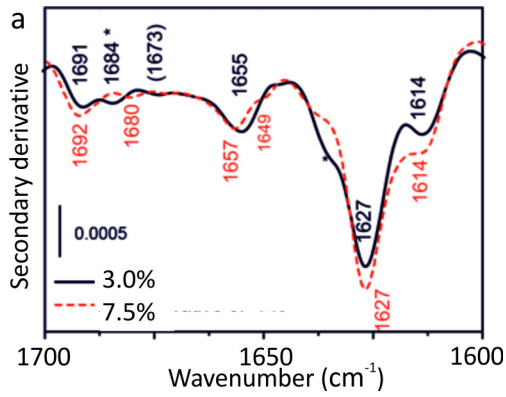

b	3.0% β-lg		7.5% β-lg	
Structure element	Position (cm^{-1})	Relative area (%)	Position (cm^{-1})	Relative area (%)
Not assigned	1612	4	1612	5
β-sheet	1629	72	1628	68
α-helical/unordered	1657	15	1657	21
β-turn	1675	9	1678	5
β-sheet	1689	0	1690	1

SI Figure 3.3: a) Second derivatives of ATR/FT-IR spectra of amyloid fibrils formed at 3.0% and 7.5% after incubation for 16 hrs. Spectra were measured on a diamond ATR setup. b) Quantitative analysis of secondary structure contributions based on Gausian fitting.

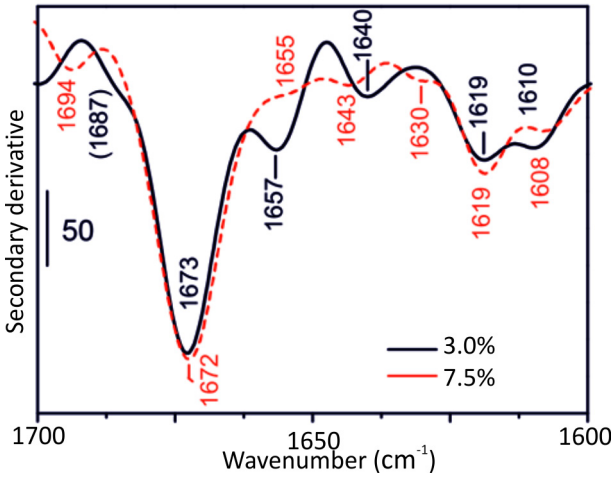

SI Figure 3.4: Second derivative of the Raman spectra of amyloid fibrils formed at 3.0% and 7.5% after incubation for 16 hrs.

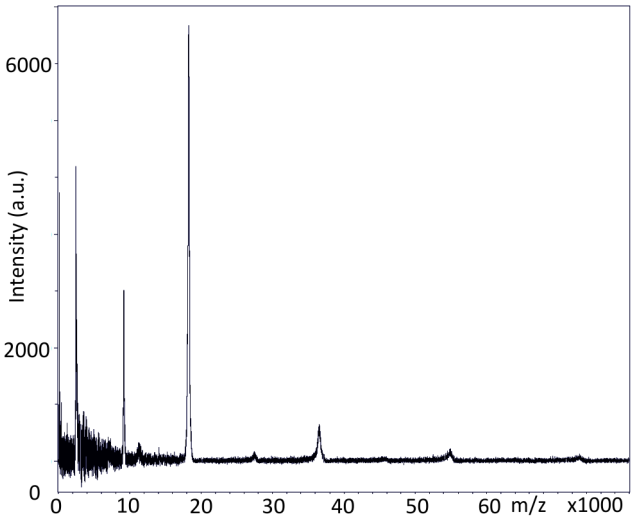

SI Figure 3.5: MALDI-TOF mass spectra of β-lg monomer. Main peak at 18400 m/z is monomer. Also peaks for di-, tri- and tetramers are observed.

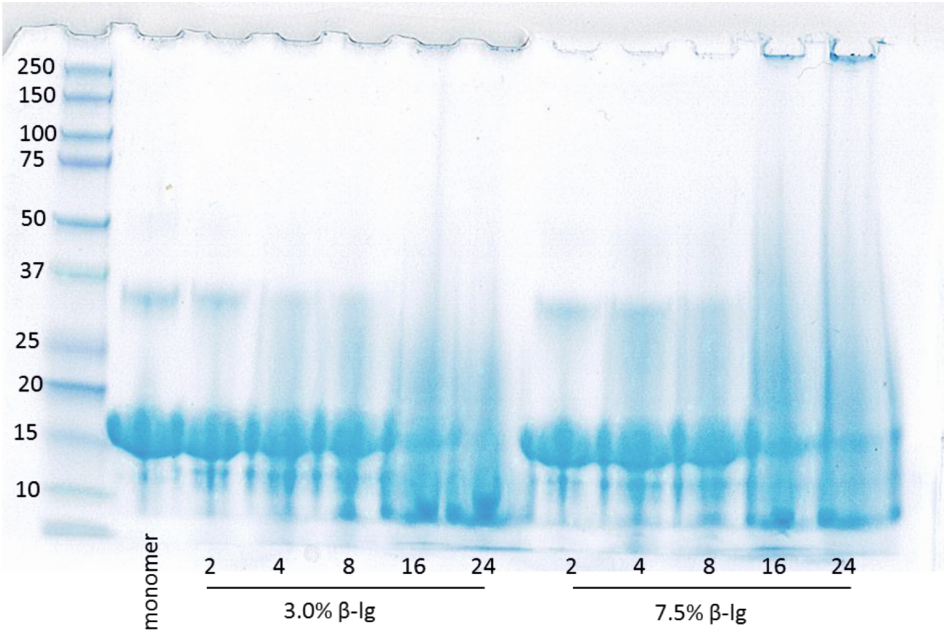

SI Figure 3.6: SDS PAGE analysis of the kinetics of β-lg monomer hydrolysis upon incubation at pH=2.0 and T=80^{o}C for 2, 4, 8, 16 or 24 hrs. The intensity of the band at approximately 18 kDa corresponding to intact monomer decreases at longer incubation times, but is still present upon 24 hrs incubation.

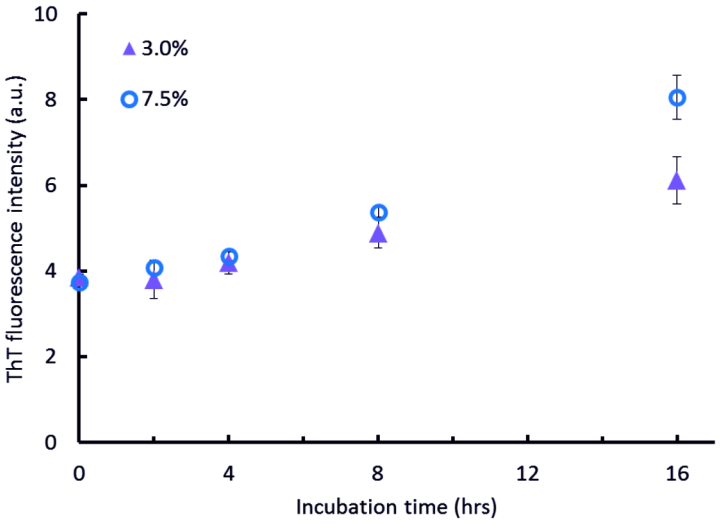

SI Figure 3.7: ThT fluorescence measurements of amyloid fibril formation kinetics in solution. β-lg monomer was incubated at pH=2.0 and 80°C at β-lg concentrations of 3.0% (purple triangles) or 7.5% (blue circles). In both cases, the samples were diluted in MilliQ/HCl at pH=2.0 to a protein concentration of 100 µg/mL, mixed with ThT, and immediately measured.

SI Table 3.1: Overview of peptides present in the amyloid fibrils formed at concentrations of 3.0% or 7.5% β-lg observed with MALDI-TOF mass spectrometry. Unless mentioned otherwise between brackets in the first column, these peptides can be derived by hydrolysis of both the A and B variant of β-lg.

Fragment	Theoretical mass (Da)	Straight fibrils formed at 3.0% β-lg	Straight fibrils formed at 7.5% β-lg
1-27	2896.5	X	X
1-28	3011.6	X	X
1-32	3437.7	X	
1-33	3552.9	X	X
1-52	5622.0	X	
1-53	5737.0	X	X
12-32	2238.2	X	X
12-33	2353.2	X	X
138-162	2916.6	X	X
97-128	3733.8	X	X
34-52	2084.1	X	X
34-53	2199.1	X	X
131-162	3748.9		X
54-85 (A)	3754.1	X	X
97-129 (A)	3851.4		X
130-162	3864.0	X	X
12-53	4536.0	X	X
99-137 (B)	4583.0		X
99-137 (A)	4583		X
53-96 (B)	5023.0		X
86-129 (B)	5033.0	X	X
86-129 (A)	5061.0	X	X

SI Table 3.2: Quantitative analysis of secondary structure contributions measured using CD spectroscopy.

Structure element	3.0% β-lg	7.5% β-lg
β-strand 1	15%	18%
β-strand 2	10%	10%
β-turns	20%	19%
α-helix 1	2%	3%
α-helix 2	5%	5%
Unordered	47%	45%

SI Table 3.3: Overview of measured percentages of structure and amino acid residues measured with TERS. Numbers are averages of datasets of 350 spectra for fibrils formed at 3.0% β-lg and 399 spectra for fibrils formed at 7.5% β-lg.

	Straight fibrils formed at 3.0% β-lg	Worm-like fibrils formed at 7.5% β-lg
Unordered/α	66%	77%
β-sheet	10%	5%
Mixed	24%	17%
His	7%	2%
Phe	3%	4%
Pro	3%	2%
Tyr	3%	5%
Cys	9%	22%

SI Table 3.4: Vibrational modes of amide I structure bands, amino acid side chains and functional groups as applied for analysis of TERS spectra. [26,28,29,31]

Unordered/α-helical	1630-1655 cm^{-1}
β-turn/ sheet	1660-1680 cm^{-1}
Histidine (His)	1494 cm^{-1}, 1331 cm^{-1}, 1183 cm^{-1}
Phenylalanine (Phe)	1038 cm^{-1}, 1010 cm^{-1}
Proline (Pro)	899-902 cm^{-1}
Tyrosine (Tyr)	856 cm^{-1}, 826 cm^{-1}
Cysteine (Cys)	803 cm^{-1}, 767 cm^{-1}, 745 cm^{-1}, 692 cm^{-1}, 674 cm^{-1}, 668 cm^{-1}

Chapter 4

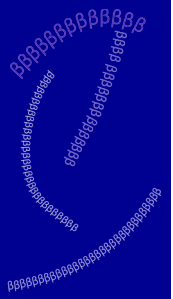

Nanoscale heterogeneity of the molecular structure of individual hIAPP amyloid fibrils revealed with tip-enhanced Raman spectroscopy

Based on: Corianne C. van den Akker, Tanja Deckert-Gaudig, Michael Schleeger, Krassimir P. Velikov, Volker Deckert, Mischa Bonn, Gijsje H. Koenderink (submitted for publication).

Abstract

Type 2 diabetes mellitus is characterized by protein misfolding and the subsequent pathological deposition of fibrillized protein, also called amyloid. It is thought that oligomers and/or amyloid fibrils formed from the human islet amyloid polypeptide (hIAPP or amylin) cause the death of β-cells in the pancreas by membrane damage. The molecular structure of hIAPP amyloid fibrils is dominated by β-sheet structure, as probed with vibrational spectroscopic techniques. However, with these techniques it is not possible to distinguish between different polymorphic forms or between the core and the surface of amyloid fibrils. Since the surface likely plays an important role in amyloid toxicity and membrane damage, it is essential to know its structure. We probed the surface molecular structure and amino acid residue composition of hIAPP amyloid fibrils with nanoscale resolution using tip-enhanced Raman spectroscopy (TERS). We show that the fibril surface mainly contains unordered or α-helical structures, in contrast to the core, which is composed of β-sheets. Both the surface structure and the amino acid residue composition are dependent on the pH during fibril formation. Furthermore, we show that TERS can probe hIAPP amyloid fibrils formed at a lipid interface, which is more representative of amyloids in vivo. Our results show that TERS is a valuable technique to investigate the molecular structure of amyloid fibrils with nanoscale spatial resolution and that it is possible to specifically probe the surface of fibrils, which is important to understand amyloid toxicity.

Introduction

Amyloid fibrils are self-assembled, β-sheet-rich aggregates formed by a large class of peptides and proteins. Many protein-misfolding diseases, such as type 2 diabetes mellitus and Alzheimer's disease, are characterized by the pathological deposition of amyloid fibrils.[1] These fibrils are generally a few nanometers in diameter and up to several micrometers in length. Structurally, amyloid fibrils are defined by a universal cross-β core structure that is stabilized by hydrogen bonds, causing a remarkably high mechanical rigidity.[2,3] However, amyloid fibrils are highly polymorphic. Depending on assembly conditions such as pH and ionic strength, different fibril morphologies such as twisted fibrils or ribbons can be formed.[4,5] Furthermore, under any given conditions, multiple polymorphic forms are typically observed.[6-8]

Human islet amyloid polypeptide (hIAPP), also called amylin, forms amyloid fibrils in the pancreas of patients suffering from type 2 diabetes mellitus and causes death of β-cells.[9,10] The hIAPP monomer is co-secreted with insulin by the β-cells in the islets of Langerhans and is thought to play a role in the regulation of glucose homeostasis.[11] Interactions of hIAPP with lipid membranes are thought to play an important role in the pathogenesis of diabetes.[12,13] Both oligomers[14,15] and fibrils[16,17] may be cytotoxic, via membrane binding and disruption of membrane integrity. On supported lipid bilayers, hIAPP has been shown to cause extensive membrane remodeling during amyloid formation.[12,18] Furthermore, membranes are thought to catalyze hIAPP oligomer formation.[13] It has been shown that negatively charged lipids can dramatically accelerate amyloid fibril formation of hIAPP as well as various other peptides.[19,20] Upon membrane binding, hIAPP monomers adopt an intermediate conformation with part of the residues incorporated into an α-helix.[20,21] Subsequently, amyloid fibrils with β-sheet structures are formed.[21,22]

While the kinetics of hIAPP self-assembly into amyloid fibrils, both in bulk solution and at lipid interfaces, have been studied extensively[8,19,23,24], structural characterization of hIAPP amyloid fibrils is still challenging. The use of X-ray crystallography and solution nuclear magnetic resonance (NMR) is limited due to the insolubility and non-crystallinity of amyloid fibrils. Recently, several models of hIAPP protofibrils have been suggested based on solid-state NMR and X-ray techniques.[25-27] However, the polymorphic nature of hIAPP amyloids results in significant differences between models. Vibrational spectroscopy measurements have suggested that the molecular structure of hIAPP amyloids is dominated by β-sheets[21,22,28], while nonaggregated hIAPP is mainly unstructured[29]. However, conventional vibrational spectroscopy provides an ensemble measurement and therefore averages out the distinct structures of different polymorphic fibril types.[30-32] Moreover, it is not possible to distinguish between the

structure of the core and the surface of the fibrils. It is important to know the surface structure, since this determines interactions of fibrils with each other and with cell membranes. Moreover, the fibril surface can potentially exert a cytotoxic effect.[33]

It was recently demonstrated that information on the structural heterogeneity as well as the surface structure of amyloid fibrils can be obtained using tip-enhanced Raman spectroscopy (TERS). In TERS, an atomic force microscope (AFM) with a metallized tip is coupled to a Raman spectrometer. Plasmonic effects at the tip apex upon laser irradiation result in a strong local Raman scattering enhancement by a factor of 10^6.[34-37] The lateral spatial resolution is dependent on the dimension and shape of the tip and can reach values below 3 nm for biomolecules measured under ambient conditions.[38-40] TERS can therefore be used to map the structure of individual amyloid fibrils with nanometer resolution, as demonstrated in studies of insulin fibril surfaces[40-42] and nanotapes formed from β-amyloid(1-40) peptide fragments[43].

Here we use TERS to investigate the surface structure of hIAPP amyloid fibrils with various morphologies. We compare fibrils formed in bulk solution at two different pH levels, and fibrils formed at a lipid interface composed of 1,2-dihexadecanoyl-sn-glycero-3-phospho-(1'-rac-glycerol) (DPPG). We show that TERS can map the secondary structure and the distribution of amino acid residues with nanometer lateral resolution. By comparing the surface molecular structure with the overall structure of hIAPP amyloid fibrils measured using bulk spectroscopy, we demonstrate that TERS probes primarily the fibril surface. While the fibril core is predominantly composed of β-sheets, the surface is heterogeneous and contains mainly unordered or α-helical structures. For fibrils formed at acidic conditions, the β-sheet content was higher than for fibrils formed at neutral conditions. Fibrils formed on a lipid interface had a similar structure as fibrils formed in bulk.

Results and discussion

hIAPP amyloid fibrils were prepared in bulk solution at pH=2.0 and pH=7.8 (both below the isoelectric point of hIAPP at 8.8[44]), and imaged using atomic force microscopy (AFM) and scanning transmission electron microscopy (STEM) (Figure 4.1a, SI Figure 4.1 and SI Figure 4.2). Fibrils at both pH values had lengths of up to hundreds of nm and diameters between 5 and 15 nm. A subpopulation of fibrils with lengths up to several micrometers in length was also observed with STEM, however, all TERS measurements were performed on shorter fibrils.

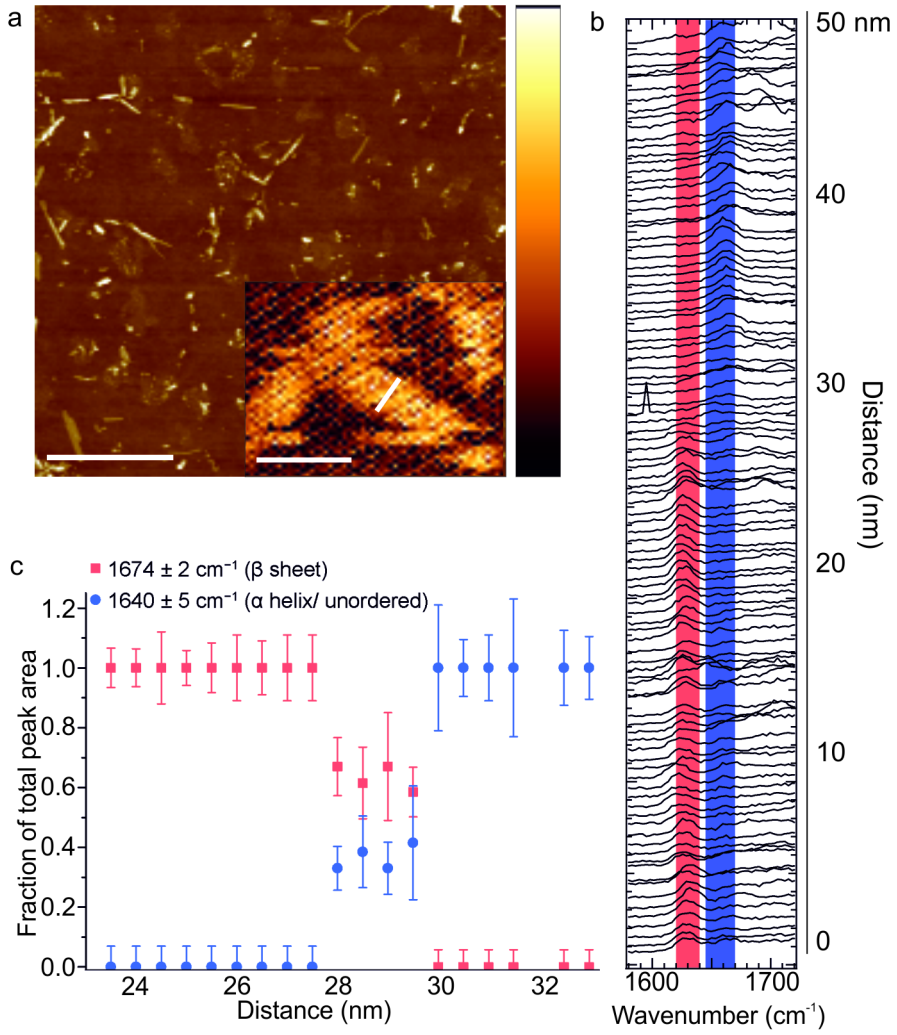

Figure 4.1: a) AFM image of hIAPP fibrils formed at pH=2.0. Scale bar is 1 µm, height bar is 20 nm. Inset: AFM image obtained by scanning with a TERS AFM tip. White line represents positions of the 100 TERS measurements that were recorded with 0.5 nm intervals along a line perpendicular to the fibril axis. Scale bar is 100 nm, height bar is 13.6 nm. b) Amide I region of the spectra. Red indicates band position for β-sheets, blue for unordered or α-helical structure. c) Relative secondary structure content in terms of β-sheets (red squares) and unordered or α-helical structure (blue circles) for spectra in the transition region (spectra numbers 45 to 65). The distance on the x-axis corresponds to the distance from the first measurement point in Figure 4.1b.

hIAPP amyloid fibrils were deposited on glass slides, dried in air, and probed by TERS using an instrument described previously.[40,45] The inset of Figure 4.1a shows an example of a single hIAPP amyloid fibril formed at pH=2.0, which was imaged using a standard AFM tip modified for TERS measurements. As a result of the silver particle attached to the AFM tip, the AFM image has a limited spatial resolution. However, the dimensions of the fibril are still clearly visible. Perpendicular to the fibril axis, 100 Raman spectra were measured in 0.5-nm steps along a single line, at the position indicated in white. To exclude possible effects caused by contamination of the AFM tip, a reference spectrum was recorded on the glass substrate after each grid or line measurement. To determine the local peptide molecular structure, the amide I region (1630-1680 cm^{-1}) of all 100 spectra was analyzed (Figure 4.1b). Protein secondary structures were assigned as β-sheet if the maximum of the band in the amide I region was at a wavenumber between 1660 and 1680 cm^{-1} and as unordered or α-helical for wavenumbers between 1630 and 1655 cm^{-1} (SI Table 4.1)[40,41,45-47]. Some spectra exhibited a broad band that was spread over both regions, or they showed two distinct peaks. These spectra were allocated in a third group and considered as mixtures of β-sheet and unordered or α-helical structures[40]. The TERS spectra measured along a line perpendicular to the fibril axis clearly show a very distinct and abrupt transition from β-sheet to unordered or α-helical structure. One side of the fibril shows predominantly β-sheet structure. Approximately at the center of the fibril, a transition region of four spectra shows both β-sheet and unordered or α-helical structure. The other side of the fibril is dominated by unordered or α-helical structure. For a more detailed analysis, 20 spectra in the transition region were baseline-corrected and fitted with two Gaussian peaks. The relative peak intensities associated with the secondary structure content was inferred and plotted as a function of the distance across the fibril (Figure 4.1c). This shows clearly the transition from only β-sheet to only unordered or α-helical spectral intensity within a very small transition region (0.5 nm between points). Furthermore, it shows that the structure of this amyloid fibril is not homogeneous, but that different molecular structures are present on the fibril surface. The transition could indicate a twist of the amyloid fibril, as was speculated previously in case of insulin amyloid fibrils.[40] Another possibility is that the surface of the amyloid fibril contains clusters of a certain structure.

Not all amyloid fibrils showed such clear domains of homogeneous structure with sharp transitions in between. SI Figure 4.3b-c show a topography image and a grid of 2 x 60 measurement points obtained in steps of 0.5 nm measured on another hIAPP amyloid fibril formed at pH=2.0. Also, 4 spectra with different amide I bands are shown to give an example of our analysis (SI Figure 4.3a). This fibril has a heterogeneous molecular structure at the surface, dominated by unordered or α-helical structure, though also β-

sheet and mixed structures are observed. Suppressed amide I bands are observed for 16% of the spectra, consistent with earlier TERS measurements on amyloid fibrils prepared from insulin[45]. For comparison, SI Figure 4.3d-e show an image and a grid of a hIAPP amyloid fibril formed at pH=7.8. Spectra were measured in steps of 2 nm to analyze a large area of the fibril. Similar to the pH=2.0 fibril, this fibril also predominantly contains unordered or α-helical structures. Only a few spectra show β-sheet or mixed structures.

It has been suggested that TERS probes mainly the surface of amyloid fibrils.[40] However, in case of nanotapes formed from the Alzheimer's disease related Aβ(16-22) peptide, bulk spectroscopy showed similar spectra as TERS.[48] A depth range of the evanescent field between 10 to 15 nm has been concluded in AFM-TERS[36,49], and it has been estimated that the evanescent field decays very rapidly, by two orders of magnitude within the first 10 nm[50]. To get a better understanding of the axial (z-) resolution obtained by TERS on hIAPP amyloid fibrils, we compared TERS measurements with attenuated total reflection Fourier transform infrared (ATR/FT-IR) spectroscopy measurements. For ATR/FT-IR measurements, a drop of amyloid fibril suspension was dried on a diamond window and IR absorption spectra were measured (SI Figure 4.4). The amide I region was fitted and showed only β-sheet structure for both the amyloid fibrils formed at pH=2.0 and pH=7.8 (SI Table 4.2 and SI Table 4.3). This is in agreement with previous bulk spectroscopy measurements of hIAPP amyloid fibrils.[21,28] For comparison, we analyzed all TERS spectra with active amide I bands. This analysis represents an average of 6 datasets for hIAPP amyloid fibrils formed at pH=2.0 on 2 different fibrils and 7 datasets on 3 fibrils for hIAPP amyloid fibrils formed at pH=7.8. The same tip was used for all measurements on fibrils formed at one pH value. In total more than 250 spectra per condition were collected. For pH=2.0 fibrils, amide I bands were absent in 44 out of 323 spectra (15%) and in pH=7.8 fibrils in 61 out of 265 spectra (23%). This phenomenon is frequently observed in TERS and SERS experiments and is currently under investigation.[45,51]

Each spectrum was analyzed for β-sheet, unordered or α-helical, or mixed structure contributions. For amyloid fibrils formed at pH=2.0, more than 49% of the spectra showed only unordered or α-helical structure (Figure 4.2a and SI Table 4.4-4.6). For 36% of the spectra, only β-sheet was observed. The remaining spectra (15%) showed bands for both structures. For amyloid fibrils formed at pH=7.8, the percentage of β-sheet is much lower: 7% of the spectra showed only β-sheet structure, while more than 77% showed only unordered or α-helical structure and 16% showed mixed structures.

This result is clearly different from the result of bulk vibrational spectroscopy, which showed purely β-sheet structure for both amyloid fibrils formed under acidic and

neutral conditions. These data indicate that TERS probes indeed mainly the molecular structure of the hIAPP amyloid surface. The surface is heterogeneous and contains mostly unordered or α-helical structure, while the core of the amyloid fibrils is composed of β-sheets. The fact that we observe higher β-sheet contents for fibrils formed at pH=2.0 (36%, versus 7% for amyloid fibrils formed at pH=7.8) with TERS, could be related to differences in morphology of the fibrils formed under acidic conditions. Apparently more of the β-sheet rich core of the fibrils is probed with TERS, while for amyloid fibrils formed at pH=7.8 the β-sheet core is out of reach for the signal-enhancing field at the tip apex.

Using TERS, it is not only possible to determine the local molecular structure of amyloid fibrils, but also specific amino acid residues. hIAPP is a 37-amino acid long peptide (Figure 4.2b), containing four different amino acid residues that can be unambiguously distinguished by their characteristic Raman bands: histidine (His), phenylalanine (Phe), tyrosine (Tyr) and cysteine (Cys)[40] (SI Table 4.1). We calculated from the large datasets of all spectra, the percentage of spectra showing peaks related to specific amino acid residues (Figure 4.2c). Black lines indicate the expected percentage based on the sequence (1 out of 37 for His and Tyr, 2 out of 37 for Phe and Cys). His was observed in 2% of all spectra for amyloid fibrils formed at pH=2.0, close to the expected percentage of 2.7%. In fibrils formed at pH=7.8, the percentage of spectra showing His was approximately 4 times higher: 8%. Also Phe was observed much more frequently than expected statistically. This indicates that Phe is preferentially present on the surface of the amyloid fibrils, rather than in the core. Phe was detected more often on fibrils formed at pH=2.0 and at pH=7.8: respectively in 18% and 11% of all spectra. The same holds for Cys, which was observed in respectively 23% and 17% of all spectra for fibrils formed at pH=2.0 and pH=7.8. Tyr was observed in 6% of the spectra for amyloid fibrils formed at pH=2.0, close to the expected percentage. For fibrils formed at pH=7.8, Tyr was observed in 11% of the spectra, which is interesting since the only Tyr residue in a hIAPP peptide is found at its C-terminus. Therefore, this result indicates that fibrils formed under neutral conditions are folded in such a way that Tyr is preferentially present at the fibril surface. In contrast, in the fibrils formed under acidic conditions, Tyr appears to be masked by other amino acids. This is consistent with the higher β-sheet content for fibrils formed at pH=2.0 compared to fibrils formed at pH=7.8 measured with TERS. Previous TERS experiments with insulin amyloids indicated that the probability of finding Phe in a β-sheet area is more than 12 times higher than that in an unstructured or α-helical protein area.[40] This result was based on a dataset of 61 spectra. In our datasets for hIAPP fibrils, with more than 250 spectra with active amide I bands per condition, we did not observe clear indications of such preferences for any amino acids when we compared fibrils formed at different pH values (SI Figure 4.5).

Besides the vibrational markers for peptide molecular structure and specific amino acids, also bands for carbonyl (C=O), imino (NH_2^+) and amino (NH_3^+) groups can be readily identified in TERS spectra. The presence of a peak between 1680-1705 cm^{-1} or 1400 cm^{-1} was assigned to carbonyl groups and at 1080 cm^{-1} or 1144 cm^{-1} to imino and amino groups.[40,41,46] The origin of the carbonyl groups could be both the C-terminus and aspartic acid and glutamic acid residues. There could be a small overlap between carbonyl bands and the β-sheet band in the amide I region, but we expect this will be a minor effect.[40,45] We observed nearly the same occurrence of carbonyl groups and imino/amino groups on amyloid fibrils formed at pH=2.0, in respectively 5% and 7% of the spectra. For fibrils formed at pH=7.8, the percentages are approximately a factor of two higher: 12% for carbonyl and 11% for imino/amino groups. We do not know the origin of this difference.

To get a better understanding of the folding of hIAPP peptides into amyloid fibrils, we compared our TERS results to existing structural models. Luca and coworkers proposed different structural models with small variations for hIAPP protofilaments formed at pH=7.4 with a striated ribbon morphology (Figure 4.2d-e), based on solid-state nuclear magnetic resonance (NMR) measurements and transmission electron microscopy (TEM) imaging.[25] These models are based on four layers of parallel β-sheets, formed by two hIAPP molecules. The dimensions of the protofilaments were approximately 6 by 4 nm, comparable to the dimensions of the fibrils we observe. In the two models shown, Phe and Cys residues are mainly present at the surface of the fibril, consistent with our TERS results (Figure 4.2f-g). In the model in Figure 4.2f, the Tyr residues in both hIAPP molecules are exposed at the surface. In contrast, in the model in Figure 4.2g one of the Tyr residues is shielded by other amino acids. This could explain the difference in Tyr residue abundance observed with TERS in amyloid fibrils formed at pH=2.0 and pH=7.8. Another fibril structure model was derived from electron paramagnetic resonance (EPR), electron microscopy and computer modeling by Bedrood et al.[27] They observed hIAPP fibrils with a left-handed twisted morphology. Also their model is based on layers of parallel β-sheets, formed by the regions of residues 12-19 and 31-36. These regions are smaller than in the model of Luca et al., where residues 8-17 and 28-37 form the two β-sheets. In both models, the residues at the N-terminus are unstructured. The fact that we observed unordered or α-helical structures on the fibril surface is consistent with the predictions of the models of unstructured loops at the fibril surface.

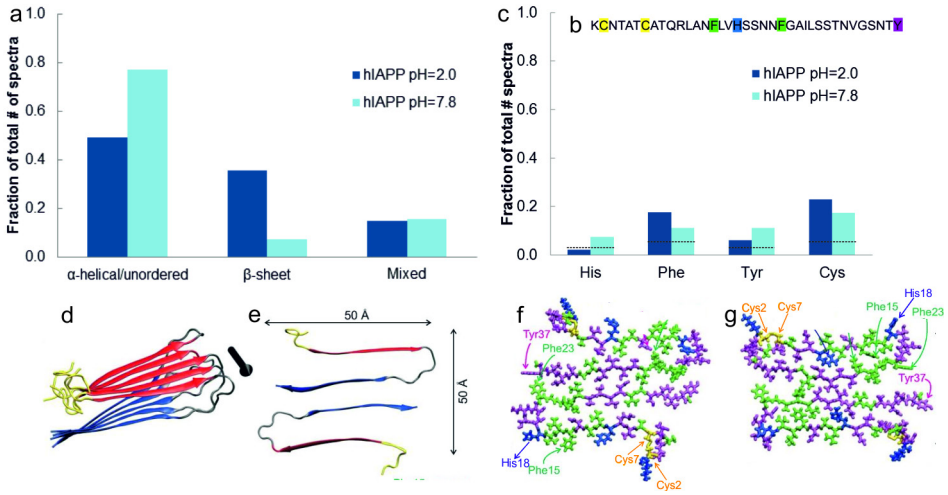

Figure 4.2: a) Molecular structure observed with TERS for hIAPP amyloid fibrils formed at pH=2.0 (dark blue) or pH=7.8 (light blue) averaged over datasets of more than 250 spectra with active amide I bands per condition. b) Sequence of hIAPP monomer. c) Percentage of the total number of spectra showing amino acid residues measured with TERS on hIAPP fibrils formed at pH=2.0 or pH=7.8. Dashed lines indicate the percentage expected based on the peptide sequence of hIAPP. d) Ribbon representation of one cross-β-molecular layer, with N- and C-terminal β-strand segments in red and blue, respectively. The black arrow indicates the fibril axis. e) Cross-sectional view of two hIAPP molecules in the protofilament. f and g) All-atom representations of two possible models, with hydrophobic residues in green, polar residues in magenta, positively charged residues in blue, and disulfide-linked cysteine residues in yellow. Figure 4.2d-g are adapted from Luca et al., Biochemistry 2007.[25]

It is generally assumed that hIAPP fibrils *in vivo* do not form in bulk solution, but at the plasma membrane.[19,23] Membrane-binding could affect the morphology and molecular structure of amyloid fibrils. To investigate the influence of lipid membranes on the molecular structure of hIAPP amyloid fibrils, we performed TERS measurements on amyloids formed at a simple model membrane. The hIAPP monomer solution was diluted to a concentration of 1 µM in water in a trough. As a model membrane, a monolayer of the anionic lipid 1,2-dihexadecanoyl-sn-glycero-3-phospho-(1'-rac-glycerol) (DPPG) was formed at the air-water interface. The surface pressure was approximately 30 mN/m. It has been shown before that hIAPP amyloids will form at the lipid monolayer under these conditions (Figure 4.3a).[21,22] When the peptide content at the lipid monolayer was transferred to a glass substrate, we indeed observed amyloid fibrils. The fibrils have diameters in the range of 3-10 nm and are up to 300 nm in length. We obtained 4 TERS datasets on 3 fibrils with the same tip. A total of 287 spectra were recorded, of which 149 displayed suppressed amide I bands (SI Table 4.7). The percentage of suppressed amide I bands (52%) is much higher than for fibrils

formed in bulk at pH=7.8 (23%) – this difference can be at least partly explained by shielding of the protein signal by the lipids. Lipid signals are apparent in at least 13% of the spectra. We compared the secondary structure on the surface of these fibrils to that of fibrils formed at pH=7.8 in bulk. Unordered or α-helical structure was observed in 68% of all spectra with an amide I band, slightly less than for amyloid fibrils formed in bulk at pH=7.8 (77%). In 11% of the spectra only β-sheet was observed, while 21% of the spectra showed both unordered or α-helical and β-sheet structure. We therefore conclude that the molecular surface structure of the fibrils formed at the lipid interface is not significantly different from fibrils formed in bulk. Nevertheless, our data do indicate subtle differences in the occurrence of amino acids at the surface of amyloid fibrils formed in bulk and at the lipid interface. His and Cys are observed more frequently in fibrils formed at the lipid interface, while Phe and Tyr are detected less frequently (see SI Table 4.4). Besides analysis of the local molecular structure and the amino acid residues, we also observed Raman bands characteristic of lipids on the fibrils. Bands at 1720-1750 cm^{-1} can be assigned to the ester-group of lipids[52,53]. Further marker bands for lipids are the bands at 1075-1090 cm^{-1} and 830-840 cm^{-1}, which can be assigned to PO_2-groups.[47,52-54] Because the band at 1075-1090 cm^{-1} does not overlap with protein bands, it is a reliable indicator of lipids. The band at 830-840 cm^{-1} is likely to interfere with the Tyr ring breathing mode, therefore we did not use it for lipid detection.

Figure 4.3b shows an AFM image of an amyloid fibril formed at a lipid interface. TERS measurements were performed along the black line in 1-nm steps. Figure 4.3c shows 7 of the 100 spectra that were measured at the position of the black rectangle, selected to show the diversity on the amyloid fibril surface. Spectra 1 and 2 show marker bands for lipids (PO_2), but no band in the amide I region. In spectrum 3 no amide I band, nor marker bands for lipids are measured. Spectra 4 and 5 contain unordered or α-helical structure bands, and the peaks between 1075 and 1090 cm^{-1} are assigned to lipids. Spectra 6 and 7 have peaks both for β-sheet and for unordered or α-helical structure. Furthermore, in spectrum 6 also a lipid marker band is observed. We conclude that the surface of the fibril is highly heterogeneous in molecular structure and is partly covered by lipid molecules. This is in agreement with other studies showing interactions between mature amyloid fibrils and lipid molecules, for hIAPP as well as for other peptides.[12,55] In future research, it will be interesting to investigate the effect of more complex and physiologically-relevant lipid membrane compositions.[56,57]

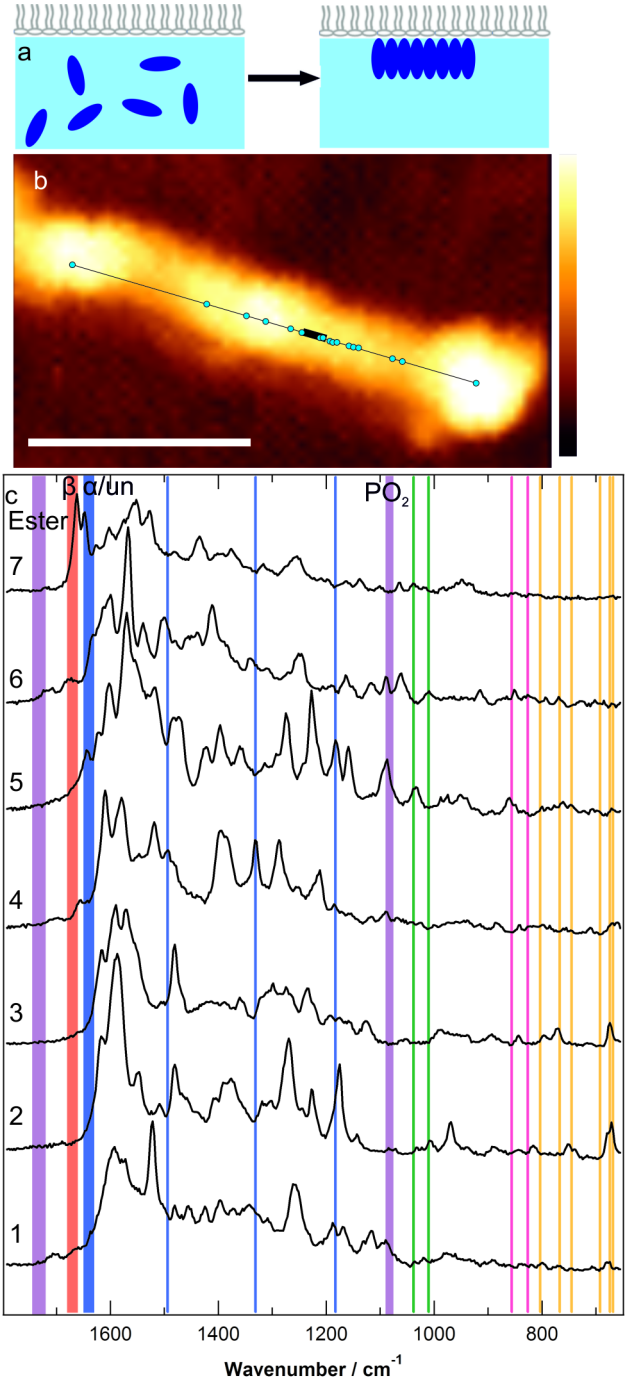
a
b
c
Ester
β α/un
PO2
7
6
5
4
3
2
1
1600
1400
1200
1000
800
Wavenumber / cm-1

Figure 4.3: a) Schematic of the formation of amyloid fibrils at the lipid interface. Left: hIAPP monomer in solution with a lipid monolayer at the air-water interface. Right: hIAPP amyloid fibrils formed at the lipid interface. b) AFM image of an amyloid fibril formed at a lipid interface. Black line indicates the entire line where TERS spectra were measured, the black box refers to the positions of the spectra shown in c. Blue circles indicate the positions of spectra showing lipids. Scale bar is 50 nm, height bar is 6.4 nm. c) Spectra measured at 1-nm steps on the amyloid fibril showing band for: 1 and 2) lipids. 3) no lipids and no amide I. 4 and 5) unordered or α-helical structure and lipids. 6) mixed structure and lipids 7) mixed structure. Bands: Red: β-sheet; Blue: unordered or α-helix; Green: lipids. Lines: Blue: His; Green: Phe; Pink: Tyr; Orange: Cys.

Conclusions

We have characterized the structure and amino acid residue composition of hIAPP amyloid fibrils using TERS. Our results show that TERS provides structural information with nanoscale resolution in the lateral direction. The surface of hIAPP amyloid fibrils is mainly composed of unordered or α-helical structure, while the core (which we probed with ATR/FT-IR) consists uniquely of β-sheets. Depending on the solution pH during formation, amyloid fibrils with various morphologies and structural compositions are formed. hIAPP amyloid fibrils formed in acidic environments showed higher β-sheet contents and less Tyr residues at their surface than amyloid fibrils formed under neutral conditions. Phe and Cys residues are more pronounced on the surface than expected based on the hIAPP protein sequence. This is in agreements with several models of hIAPP protofilaments based on NMR measurements, showing a β-sheet core with Phe and Cys residues on the surface of the fibrils.[25] Using our high-statistics protocol on a large number of spectra, we showed the proof of principle of structural characterization of hIAPP amyloid fibrils formed at a lipid interface, which is more representative of the situation *in vivo*. The amyloid fibrils were partly covered by lipid molecules and showed mainly unordered or α-helical structure at the surface. The surface structure of the fibrils was similar to that of fibrils formed under similar conditions in bulk solution, but the amino acid residues presented at the surface were partly different.

We showed that TERS gives valuable information about the molecular structure of the surfaces of hIAPP amyloid fibrils with high spatial resolution, which cannot be obtained with conventional spectroscopy techniques. The surface of amyloids is generally thought to play an important role in fibril toxicity and membrane damage. In future it will be interesting to apply the same technique to investigate amyloid fibrils formed from other disease-related peptides and their interactions with potential drugs.

Materials and methods

hIAPP amyloid formation. Synthetic hIAPP (Bachem H-7905) stock solutions were prepared by dissolving hIAPP powder in MilliQ water to a concentration of approximately 1 mg/mL. The solution was filtered using a 0.2 µm filter to remove aggregates. The peptide concentration was calculated using the absorption at 280 nm measured with a Nanodrop (Thermo Scientific) and an extinction coefficient of 1280 cm^{-1} M^{-1}.[22] The solution was aliquoted and stored at -80°C until use.

For amyloid formation in bulk, hIAPP solutions were diluted in 50 mM phosphate buffer at pH=2.0 or 5 mM phosphate buffer at pH=7.8 to concentrations of 73 µM. Samples were incubated in 96-wells plates on a shaking plate for 6 days at RT. For TERS measurements, a drop of the fibril suspension was incubated on clean glass slides for 10 min. The samples was washed with MilliQ and dried by air.

TERS samples for fibrils formed at the lipid monolayer were prepared using the inverse Langmuir-Schaefer technique.[58] For amyloid formation at the lipid monolayer, hIAPP was diluted to a concentration of 1 µM in water in a Langmuir-Blodgett trough with a surface area of 68 cm^2. A cleaned glass slide was placed in the solution parallel to the surface. Drops of a 1 mM solution of DPPG (Avanti Polar Lipids) in chloroform were evenly spread on the surface; in total 11 µl DPPG was added. The sample was incubated for 17 hrs at RT. No reduction of the liquid level was observed during this period. The solution was slowly removed until the glass slide went through the air-water interface. The sample was dried by air and stored under argon until the TERS measurement.

TERS measurements. TERS measurements for hIAPP fibrils formed in bulk were performed on a setup comprised of an AFM (Nanowizard I, JPK, Germany) mounted on an inverted microscope (Olymus IX, Japan). Spectra were collected with a confocal spectrometer (LabRam HR, Horiba Jobin Yvon, France) with a CCD camera (Innova 300c, USA). A 60x oil immersion objective (N.A. 1.45) was used to focus the laser (λ =530 nm, P = 0.42 mW on the sample). The acquisition time was 10 s.

For the TERS measurements for hIAPP fibrils formed at the lipid interface, a setup comprised of an AFM (Nanowizard II, JPK, Germany) mounted on an inverted Raman microscope with confocal spectrometer (SP2750A, Acton Advanced, Princeton Instruments Roper Scientific, USA) and CCD camera (Pixis 400, Princeton Instruments Roper Scientific, USA) was used. The incident laser (λ= 532 nm, P = 1 mW on sample) was focused through a 40x (N.A. 1.35) oil immersion objective on the sample. Spectra were collected with an acquisition time of 1-5 s.

TERS tips were prepared by 25 nm silver evaporation on commercial AFM non-contact tips (NSG10, NT-MDT, Russia).

Atomic Force Microscopy (AFM). For AFM samples, 40 µL of the hIAPP fibril suspension was incubated on freshly cleaved mica (15 x 15 mm) for 5 min. Samples were washed with MilliQ water and dried in air. AFM images were made in tapping mode on a Dimension 3100 scanning probe microscope (Bruker). Silicon cantilevers (TESPA, Bruker) with a spring constant of 42 N/m were used. Images were flattened using Nanoscope 6.14 software.

Scanning Transmission Electron Microscopy (STEM). Fibril suspensions were diluted to peptide concentrations of 15 µM. Samples for STEM were prepared by incubation of 1 µL of the fibril suspension on a carbon coated copper grid with 300 µm mesh size (TED PELLA INC) for 5 min. Excess liquid was removed, the samples were washed with MilliQ water and dried by air. Scanning transmission electron microscopy was performed on a Verios 460 microscope (FEI) operating at 25 kV. Images were obtained in bright field.

Fourier Transform Infrared (FT-IR) spectroscopy. Infrared spectroscopy was carried out on a Nicolet 730 FT-IR spectrometer (Thermo Fisher Scientific Inc., Pittsburgh, PA) equipped with a liquid nitrogen cooled mercury cadmium telluride (MCT) detector. The spectral resolution was 4 cm^{-1}, and for each measurement 256 spectra were averaged. The Happ-Genzel apodization function was used for the Fourier transformation. 5 µl of the respective amyloid suspension in buffer was hydrophobically attached onto the surface of a diamond attenuated total reflectance (ATR) cell (single reflection, Thermo Spectra Tech, Thermo Fisher Scientific Inc.) by drying of the suspension in air for a few minutes. Quantitative secondary structure analysis was based on the vibrational amide I band. Gaussian shaped line widths of spectral components were used for fitting as described elsewhere[59] using OriginPro 8.5.1G software.

Acknowledgment

We thank A. Lof and E. Garnett (FOM Institute AMOLF) for help with STEM imaging. This work is part of the Industrial Partnership Programme (IPP) Bio(-Related) Materials (BRM) of the Stichting voor Fundamenteel Onderzoek der Materie (FOM), which is financially supported by the Nederlandse Organisatie voor Wetenschappelijk Onderzoek (NWO). The IPP BRM is co-financed by the Top Institute Food and Nutrition and the Dutch Polymer Institute.

References

(1) Stefani, M.; Dobson, C. M. *Journal of Molecular Medicine* **2003**, *81*, 678.
(2) Knowles, T. P.; Fitzpatrick, A. W.; Meehan, S.; Mott, H. R.; Vendruscolo, M.; Dobson, C. M.; Welland, M. E. *Science* **2007**, *318*, 1900.
(3) Krebs, M. R. H.; Domike, K. R.; Cannon, D.; Donald, A. M. *Faraday Discussions* **2008**, *139*, 265.
(4) Jaikaran, E. T. A. S.; Clark, A. *Biochimica et Biophysica Acta (BBA) - Molecular Basis of Disease* **2001**, *1537*, 179.
(5) Volpatti, L. R.; Vendruscolo, M.; Dobson, C. M.; Knowles, T. P. J. *ACS Nano* **2013**, *7*, 10443.
(6) Zhang, S.; Andreasen, M.; Nielsen, J. T.; Liu, L.; Nielsen, E. H.; Song, J.; Ji, G.; Sun, F.; Skrydstrup, T.; Besenbacher, F.; Nielsen, N. C.; Otzen, D. E.; Dong, M. *Proceedings of the National Academy of Sciences* **2013**, *110*, 2798.
(7) Goldsbury, C.; Baxa, U.; Simon, M. N.; Steven, A. C.; Engel, A.; Wall, J. S.; Aebi, U.; Müller, S. A. *Journal of Structural Biology* **2011**, *173*, 1.
(8) Goldsbury, C.; Goldie, K.; Pellaud, J.; Seelig, J.; Frey, P.; Muller, S. A.; Kistler, J.; Cooper, G. J. S.; Aebi, U. *Journal of Structural Biology* **2000**, *130*, 352.
(9) Westermark, P.; Andersson, A.; Westermark, G. T. *Physiological Reviews* **2011**, *91*, 795.
(10) Cooper, G. J.; Willis, A. C.; Clark, A.; Turner, R. C.; Sim, R. B.; Reid, K. B. *Proceedings of the National Academy of Sciences U.S.A.* **1987**, *84*, 8628.
(11) Abedini, A.; Schmidt, A. M. *FEBS Letters* **2013**, *587*, 1119.
(12) Domanov, Y. A.; Kinnunen, P. K. J. *Journal of Molecular Biology* **2008**, *376*, 42.
(13) Jayasinghe, S. A.; Langen, R. *Biochimica et Biophysica Acta (BBA) - Biomembranes* **2007**, *1768*, 2002.
(14) Janson, J.; Ashley, R. H.; Harrison, D.; McIntyre, S.; Butler, P. C. *Diabetes* **1999**, *48*, 491.
(15) Anguiano, M.; Nowak, R. J.; Lansbury, P. T. *Biochemistry* **2002**, *41*, 11338.
(16) Engel, M. F. M. *Chemistry and Physics of Lipids* **2009**, *160*, 1.
(17) Engel, M. F. M.; Khemtemourian, L.; Kleijer, C. C.; Meeldijk, H. J. D.; Jacobs, J.; Verkleij, A. J.; de Kruijff, B.; Killian, J. A.; Hoeppener, J. W. M. *Proceedings of the National Academy of Sciences U.S.A.* **2008**, *105*, 6033.
(18) Green, J. D.; Kreplak, L.; Goldsbury, C.; Blatter, X. L.; Stolz, M.; Cooper, G. S.; Seelig, A.; Kist-Ler, J.; Aebi, U. *Journal of Molecular Biology* **2004**, *342*, 877.
(19) Knight, J. D.; Miranker, A. D. *Journal of Molecular Biology* **2004**, *341*, 1175.
(20) Knight, J. D.; Hebda, J. A.; Miranker, A. D. *Biochemistry* **2006**, *45*, 9496.
(21) Fu, L.; Ma, G.; Yan, E. C. Y. *Journal of the American Chemical Society* **2010**, *132*, 5405.
(22) Engel, M. F. M.; vandenAkker, C. C.; Schleeger, M.; Velikov, K. P.; Koenderink, G. H.; Bonn, M. *Journal of the American Chemical Society* **2012**.
(23) Jayasinghe, S. A.; Langen, R. *Biochemistry* **2005**, *44*, 12113.
(24) Padrick, S. B.; Miranker, A. D. *Biochemistry* **2002**, *41*, 4694.
(25) Luca, S.; Yau, W.-M.; Leapman, R.; Tycko, R. *Biochemistry* **2007**, *46*, 13505.
(26) Wiltzius, J. J. W.; Sievers, S. A.; Sawaya, M. R.; Cascio, D.; Popov, D.; Riekel, C.; Eisenberg, D. *Protein Science* **2008**, *17*, 1467.
(27) Bedrood, S.; Li, Y.; Isas, J. M.; Hegde, B. G.; Baxa, U.; Haworth, I. S.; Langen, R. *Journal of Biological Chemistry* **2012**, *287*, 5235.
(28) Kayed, R.; Bernhagen, J.; Greenfield, N.; Sweimeh, K.; Brunner, H.; Voelter, W.; Kapurniotu, A. *Journal of Molecular Biology* **1999**, *287*, 781.

(29) Kapurniotu, A. *Biopolymers* **2001**, *60*, 438.
(30) Petkova, A. T.; Leapman, R. D.; Guo, Z.; Yau, W.-M.; Mattson, M. P.; Tycko, R. *Science* **2005**, *307*, 262.
(31) vandenAkker, C. C.; Engel, M. F. M.; Velikov, K. P.; Bonn, M.; Koenderink, G. H. *Journal of the American Chemical Society* **2011**, *133*, 18030.
(32) Goldsbury, C.; Frey, P.; Olivieri, V.; Aebi, U.; Müller, S. A. *Journal of Molecular Biology* **2005**, *352*, 282.
(33) Stefani, M. *Current Protein & Peptide Science* **2010**, *11*, 343.
(34) Domke, K. F.; Pettinger, B. *Chemphyschem* **2010**, *11*, 1365.
(35) Bailo, E.; Deckert, V. *Chemical Society reviews* **2008**, *37*, 921.
(36) Schmid, T.; Opilik, L.; Blum, C.; Zenobi, R. *Angewandte Chemie-International Edition* **2013**, *52*, 5940.
(37) Pozzi, E. A.; Sonntag, M. D.; Jiang, N.; Klingsporn, J. M.; Hersam, M. C.; Van Duyne, R. P. *ACS Nano* **2013**, *7*, 885.
(38) Ichimura, T.; Fujii, S.; Verma, P.; Yano, T.; Inouye, Y.; Kawata, S. *Physical Review Letters* **2009**, *102*.
(39) Deckert-Gaudig, T.; Deckert, V. *Current Opinion in Chemical Biology* **2011**, *15*, 719.
(40) Kurouski, D.; Deckert-Gaudig, T.; Deckert, V.; Lednev, I. K. *Journal of the American Chemical Society* **2012**, *134*, 13323.
(41) Deckert-Gaudig, T.; Kämmer, E.; Deckert, V. *Journal of Biophotonics* **2012**.
(42) Kurouski, D.; Deckert-Gaudig, T.; Deckert, V.; Lednev, Igor K. *Biophysical Journal* **2014**, *106*, 263.
(43) Paulite, M.; Blum, C.; Schmid, T.; Opilik, L.; Eyer, K.; Walker, G. C.; Zenobi, R. *ACS Nano* **2013**.
(44) Bjellqvist, B.; Hughes, G. J.; Pasquali, C.; Paquet, N.; Ravier, F.; Sanchez, J.-C.; Frutiger, S.; Hochstrasser, D. *Electrophoresis* **1993**, *14*, 1023.
(45) Kurouski, D.; Postiglione, T.; Deckert-Gaudig, T.; Deckert, V.; Lednev, I. K. Amide I *Analyst* **2013**, *138*, 1665.
(46) Stewart, S.; Fredericks, P.M. *Spectrochim. Acta A Mol. Biomol. Spectrosc.* **1999**, *55*, 1641.
(47) Socrates, G. *Infrared and Raman Characteristic Group Frequencies*; 3rd edition ed.; John Wiley & Sons: New York, 2004.
(48) Paulite, M.; Blum, C.; Schmid, T.; Opilik, L.; Eyer, K.; Walker, G. C.; Zenobi, R. *ACS Nano* **2013**, *7*, 911.
(49) Bohme, R.; Mkandawire, M.; Krause-Buchholz, U.; Rosch, P.; Rodel, G.; Popp, J.; Deckert, V. *Chemical Communications* **2011**, *47*, 11453.
(50) Downes, A.; Salter, D.; Elfick, A. *Journal of Physical Chemistry B* **2006**, *110*, 6692.
(51) Blum, C.; Schmid, T.; Opilik, L.; Metanis, N.; Weidmann, S.; Zenobi, R. *The Journal of Physical Chemistry C* **2012**, *116*, 23061.
(52) Böhme, R.; Cialla, D.; Richter, M.; Rösch, P.; Popp, J.; Deckert, V. *Journal of Biophotonics* **2010**, *3*, 455.
(53) Bohme, R.; Richter, M.; Cialla, D.; Rosch, P.; Deckert, V.; Popp, J. *Journal of Raman Spectroscopy* **2009**, *40*, 1452.
(54) Lefevre, T.; Subirade, M. *Biopolymers* **2000**, *54*, 578.
(55) Zhao, H.; Tuominen, E. K.; Kinnunen, P. K. *Biochemistry* **2004**, *43*, 10302.
(56) Cao, P.; Raleigh, D. P. *Biochemistry* **2012**, *51*, 2670.
(57) Wang, H.; Cao, P.; Raleigh, D. P. *Journal of Molecular Biology* **2013**, *425*, 492.
(58) Lee, K. Y. C.; Lipp, M. M.; Takamoto, D. Y.; Ter-Ovanesyan, E.; Zasadzinski, J. A.; Waring, A. J. *Langmuir* **1998**, *14*, 2567.

(59) Arrondo, J. L. R.; Muga, A.; Castresana, J.; Goni, F. M. *Progress in Biophysics & Molecular Biology* **1993**, *59*, 23.

Supplementary Figures and Tables

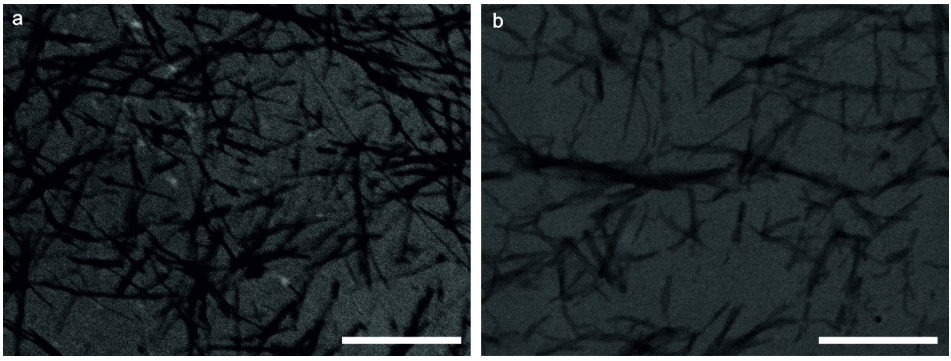

SI Figure 4.1: STEM images of hIAPP amyloid fibrils formed in bulk solution. Fibrils were formed in a) 50 mM phosphate buffer at pH=2.0; b) 5 mM phosphate buffer at pH=7.8. Scale bars are 500 nm.

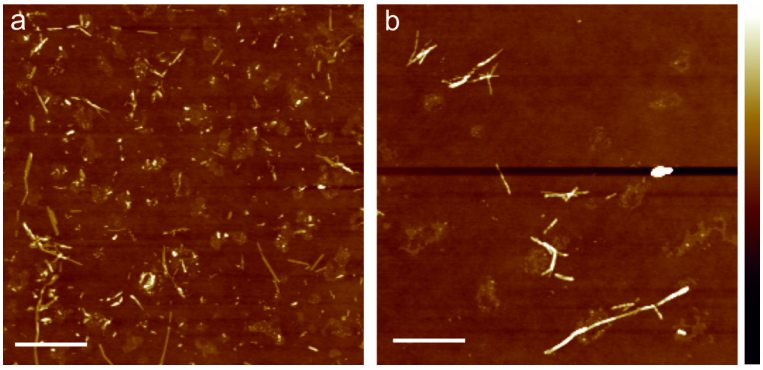

SI Figure 4.2: AFM topography images of hIAPP fibrils formed in bulk solution and deposited and dried on a mica surface. Fibrils were formed in a) 50 mM phosphate buffer at pH=2.0; b) 5 mM phosphate buffer at pH=7.8. Scale bars are 1 µm and AFM height calibration bar is 20 nm.

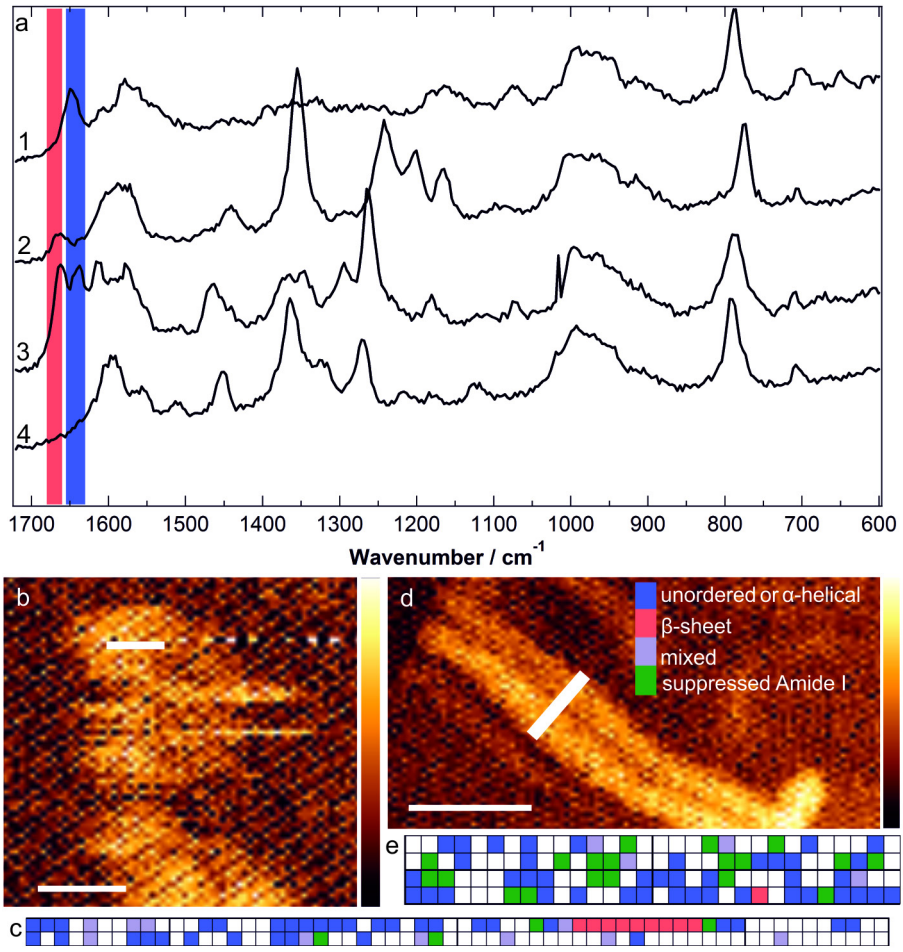

SI Figure 4.3: a) Spectra showing examples of amide I bands assigned to 1) unordered orα-helical structures; 2) β-sheet structures; 3) mixed structures or 4) suppressed amide I band. b-d) Images and structural maps of hIAPP amyloid fibrils formed at pH=2.0 (b and c) or pH=7.8 (d and e). White rectangles in the AFM topographies indicate the position of the measurements, recorded at positions spaced 0.5 nm (b) or 2 nm (d) apart. Colors in the map encode the local structure as judged from the amide I region. Blue: unordered or α-helical structure; Red: β-sheet; Purple: Mixed; Green: Suppressed amide I peak. White: no spectral information was obtained, due to a loss of feedback. Scale bars are 50 nm, height bars are b) 13.3 nm and d) 14.9 nm.

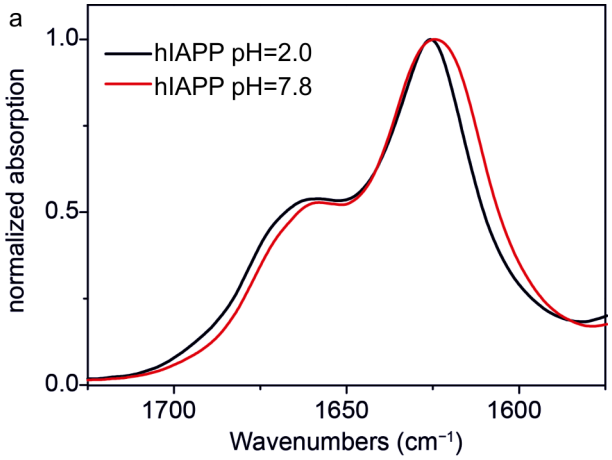

SI Figure 4.4: ATR/FT-IR spectra of hIAPP amyloid fibrils formed at pH=2.0 (red) or pH=7.8 (black).

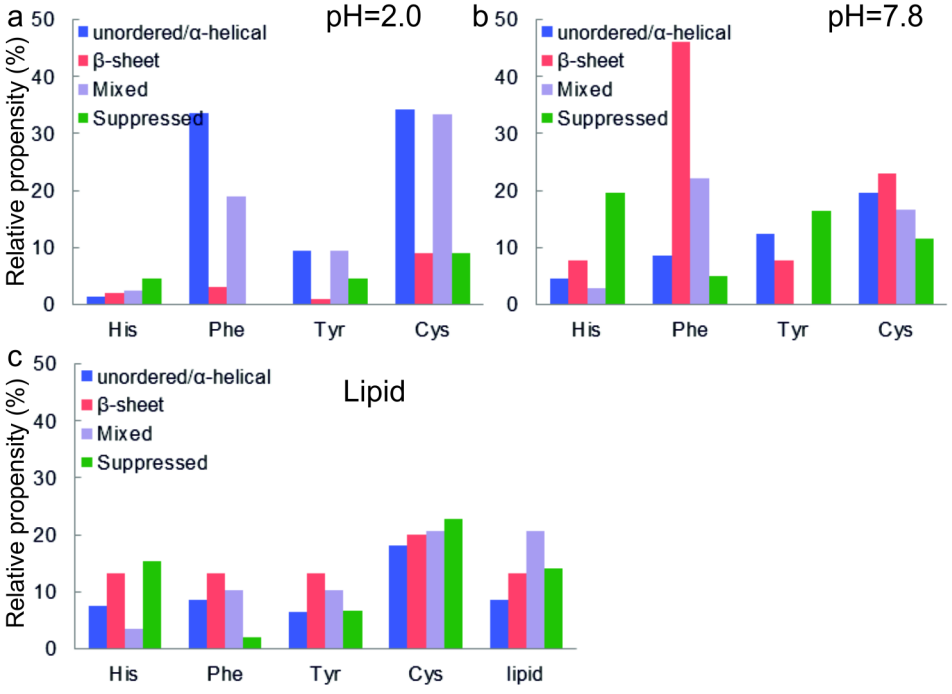

SI Figure 4.5: Relative propensity plots of amino acid residues for unordered/α-helical structure (blue), β-sheets (red), mixed structures (purple) and suppressed amide I bands (green) for hIAPP fibrils formed a) in bulk at pH=2.0; b) in bulk at pH=7.8; c) at a lipid interface.

SI Table 4.1: Vibrational modes of amide I structure bands, amino acid side chains and functional groups.[40,45-47]

	Wavenumber
Unordered/α-helical	1630-1655 cm^{-1}
β-sheet	1660-1680 cm^{-1}
Histidine (His)	1494 cm^{-1}, 1331 cm^{-1}, 1183 cm^{-1}
Phenylalanine (Phe)	1038 cm^{-1}, 1010 cm^{-1}
Tyrosine (Tyr)	856 cm^{-1}, 826 cm^{-1}
Cysteine (Cys)	803 cm^{-1}, 767 cm^{-1}, 745 cm^{-1}, 692 cm^{-1}, 674 cm^{-1}, 668 cm^{-1}
Amide (NH^{2+}/NH^{3+})	1144 cm^{-1}, 1080 cm^{-1}
Carbonyl (C=O)	1660-1705 cm^{-1}, 1400 cm^{-1}

SI Table 4.2: Peak fitting results of ATR/FT-IR spectra for hIAPP fibrils formed at pH=2.0.

Peak position	Relative area	Assignment
1621 cm^{-1}	30%	β-sheet
1626 cm^{-1}	36%	β-sheet
1661 cm^{-1}	28%	β-turn
1677 cm^{-1}	6%	β-sheet

SI Table 4.3: Peak fitting results of ATR/FT-IR spectra for hIAPP fibrils formed at pH=7.8.

Peak position	Relative area	Assignment
1626 cm^{-1}	59%	β-sheet
1660 cm^{-1}	32%	β-turn
1675 cm^{-1}	9%	β-sheet

SI Table 4.4: Overview of measured percentages of structure and amino acid residues.

	Bulk fibrils pH=2.0	Bulk fibrils pH=7.8	Fibrils at lipid monolayer
Unordered/α	49%	77%	68%
β-sheet	36%	7%	11%
Mixed	15%	16%	21%
His	2%	8%	11%
Phe	18%	11%	6%
Tyr	6%	11%	7%
Cys	23%	17%	21%
C=O	5%	12%	*
NH_2/NH_3	7%	11%	14%

* $COOH/COO^-$ was not analyzed in samples containing lipids, because of the overlap of bands.

SI Table 4.5: Overview of measured percentages of structure and amino acid residues per grid for bulk fibrils formed at pH=2.0.

	Grid 1	Grid 2	Grid 3	Grid 4	Grid 5	Grid 6
# active amide I	34	52	61	99	25	8
# suppressed	13	4	11	0	10	6
Unordered/α	85%	63%	10%	39%	96%	75%
β-sheet	0%	17%	62%	53%	0%	13%
Mixed	15%	19%	28%	8%	4%	13%
His	2%	4%	3%	0%	6%	0%
Phe	2%	11%	11%	28%	40%	0%
Tyr	4%	9%	0%	0%	14%	57%
Cys	28%	73%	17%	4%	3%	21%
C=O	15%	4%	7%	0%	3%	7%
NH_2/NH_3	19%	4%	11%	0%	9%	0%

SI Table 4.6: Overview of the number of active amide I and suppressed bands and measured percentages of structure and amino acid residues per grid for bulk fibrils formed at pH=7.

	Grid 1	Grid 2	Grid 3	Grid 4	Grid 5	Grid 6	Grid 7
# active amide I	16	36	46	46	4	35	21
# suppressed	10	16	19	10	4	0	2
Unordered/α	69%	89%	89%	33%	50%	100%	100%
β-sheet	6%	3%	2%	22%	50%	0%	0%
Mixed	25%	8%	9%	46%	0%	0%	0%
His	4%	15%	11%	4%	13%	0%	4%
Phe	12%	13%	11%	23%	0%	0%	0%
Tyr	8%	6%	5%	2%	88%	29%	17%
Cys	8%	6%	9%	16%	50%	23%	61%
C=O	0%	13%	25%	9%	50%	3%	0%
NH_2/NH_3	8%	15%	11%	16%	0%	3%	9%

SI Table 4.7: Overview of the number of active amide I and suppressed bands and measured percentages of structure and amino acid residues per grid for fibrils formed at the lipid interface.

	Grid 1	Grid 2	Grid 3	Grid 4
# active amide I	39	31	15	53
# suppressed	28	30	13	78
Unordered/α	64%	77%	67%	66%
β-sheet	13%	10%	7%	11%
Mixed	23%	13%	27%	23%
His	12%	8%	14%	12%
Phe	10%	8%	11%	1%
Tyr	9%	5%	11%	7%
Cys	12%	16%	11%	30%
NH_2/NH_3	15%	21%	7%	11%
Lipids	25%	8%	7%	11%

Chapter 5

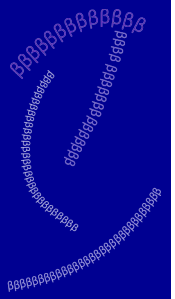

The polyphenol EGCG inhibits amyloid formation less efficiently at phospholipid interfaces than in bulk solution

Based on: Maarten F. M. Engel, Corianne C. van den Akker, Michael Schleeger, Krassimir P. Velikov, Gijsje H. Koenderink, Mischa Bonn: J. Am. Chem. Soc., 2012, 134 (36), pp 14781–14788

Abstract

Age-related diseases, like Alzheimer's disease and type 2 diabetes mellitus, are characterized by protein misfolding and the subsequent pathological deposition of fibrillized protein, also called amyloid. Several classes of amyloid-inhibitors have recently been tested, traditionally under bulk conditions. However, it has become apparent that amyloid fibrils and oligomers assemble and exert their cytotoxic effect at cellular membranes, rather than in bulk solution. Knowledge is therefore required of inhibitor activity specifically at the phospholipid membrane interface. Here we show, using surface-specific sum-frequency generation (SFG) spectroscopy and atomic force microscopy (AFM), that the commonly used (−)-epigallocatechin gallate (EGCG) is a much less efficient amyloid inhibitor at a phospholipid interface than in bulk solution. Moreover, EGCG is not able to disaggregate existing amyloid fibrils at a phospholipid interface, in contrast to its behavior in bulk. Our results show that interfaces significantly affect the efficiency of inhibition by EGCG inhibitors and should therefore be considered during the design and testing of amyloid inhibitors.

Introduction

Many protein misfolding diseases, such as Alzheimer's disease and type 2 diabetes mellitus, are characterized by the pathological deposition of amyloid fibrils.[1–3] Current hypotheses suggest that these fibrils, and/or their oligomeric precursors, cause cell death by disrupting cellular membranes.[4–6] Consequently, the inhibition of the formation of fibrils or oligomers has been a focus in the development of drugs for misfolding diseases.[7,8] In recent years several types of inhibitors have been tested for their ability to reduce amyloid cytotoxicity, using either cells[9–12] or in vitro model systems.[13–17] An important class of inhibitors is made up of polyphenols, which are thought to interact with amyloidogenic proteins via aromatic π–π interactions,[13,14,18–20] though the precise mechanism is an issue still under debate.[21,22] A particularly promising inhibitor is (−)-epigallocatechin gallate (EGCG), a natural component of green tea. This polyphenol inhibits fibrillation of several amyloidogenic peptides[9,20,23–25] and has even been shown to disaggregate existing fibrils.[22,23,26,27] Further, EGCG protects cells against amyloid-induced toxicity.[9,22,23] During *in vitro* studies, inhibitors are typically tested under bulk conditions, for which aggregating peptide and inhibitor are diffusing freely in solution, as has also been the case for studies on EGCG.[9,22–27] However, it is the cellular membrane, and not bulk solution, where amyloid fibrils and oligomers are thought to assemble and exert their cytotoxic effect.[4–6] In recent experiments on lipid- or glycosaminoglycan-mediated amyloid formation, modifications of inhibitor effectivity could be demonstrated.[28–31] It is therefore vital to know whether inhibitors are also effective at the phospholipid membrane interface.

Many techniques have become available for measuring fibril formation and its inhibition in bulk solution, such as the thioflavin T (ThT) assay and electron microscopy.[32] However, here we want to study these processes specifically and exclusively at the phospholipid interface. We exploit the unique sensitivity and spatial selectivity of vibrational sum-frequency generation (VSFG) to study amyloid fibrillation at the phospholipid interface. This approach was recently pioneered by the Yan group.[33,34] Here we use this technique to elucidate the effect of EGCG on fibril formation. In addition, atomic force microscopy (AFM) in combination with the Langmuir–Blodgett technique, to selectively probe only interfacial molecules, is used to investigate the morphology of species produced during aggregation at the phospholipid interface. VSFG provides information about the conformation and orientation of molecules at interfaces.[34–36] In VSFG, two pulsed laser beams, one at visible and one at infrared (IR) frequency, are focused to overlap at the interface. As a result of the interaction of the laser fields with molecules at the surface - and only those at the surface - light at the sum frequency of the visible and IR beams may be generated. When the IR frequency

matches that of a surface vibrational mode, this process may be resonantly enhanced. Protein conformations can be investigated through the C=O vibrations of the protein backbone (amide I region, 1600–1700 cm^{-1}), where the characteristic β-sheet structure of amyloid fibrils can be distinguished from structures such as random coil and α-helix.[37] VSFG spectroscopy is a sensitive, label-free method that so far has seen limited application in the study of interfacial amyloid secondary structure.[33,34,38]

Human islet amyloid polypeptide (hIAPP) forms fibrillar amyloid deposits in the pancreatic islets of Langerhans of patients with type 2 diabetes mellitus.[2] hIAPP fibrils and/or oligomers are thought to be involved in the death of the insulin-producing cells in these islets.[2–4,6] Like many amyloidogenic peptides, nonaggregated hIAPP is mainly unstructured, while fibrillar hIAPP is rich in β-sheet structure.[39] Current models of membrane-mediated IAPP fibrillation are based on transiently populated α-helical intermediates.[40,41] It is thought that binding of these species to the membrane surface, especially the attachment of cationic amino acid residues to anionic membranes, facilitates an increase in the local protein concentration. Thereby conformational switching from helical to β-sheet structures and subsequent fibril growth is mediated. Different mechanisms of how amyloids induce cytotoxicity have been proposed,[42,43] such as the disruption of membranes by pore formation or nonspecific interaction.[44] We have chosen hIAPP for two reasons: First, the details of the aggregation of hIAPP, both in bulk and at the interface, have been described extensively.[3,39,45–48] Second, a recent study has shown that EGCG efficiently inhibits hIAPP aggregation in bulk.[23] As a model membrane, we use monolayers of the negatively charged lipid 1,2-dihexadecanoyl-*sn*-glycero-3-phospho-(1'-*rac*-glycerol) (DPPG), since IAPP–lipid interactions have been investigated extensively with this system.[33,47,49] Also, DPPG accelerates IAPP aggregation, which allows for reasonable VSFG measuring times.[33] Here we combine VSFG with AFM to investigate IAPP aggregation and its inhibition by EGCG exclusively at a phospholipid interface. We demonstrate that EGCG has a strongly reduced efficiency to inhibit the formation of hIAPP amyloid fibrils at the phospholipid interface, in contrast to its behavior in bulk. Moreover, we show that while EGCG disaggregates hIAPP fibrils in bulk, EGCG has no effect on fibrils at the phospholipid interface, even when present in large molar excess.

Results and discussion

We used VSFG and AFM to gain insight into the inhibition of amyloid fibril formation by EGCG specifically at the physiologically relevant phospholipid interface. The phospholipid interface was obtained by depositing phospholipid molecules at the air–water interface of a buffered solution of hIAPP molecules in a trough. First, we examined assembly of hIAPP into amyloid fibrils at the phospholipid interface in the absence of EGCG. Addition of nonaggregated hIAPP to buffer, to a final peptide concentration of 1 μM, resulted in an increase of the surface pressure to ∼20 mN/m, showing that nonaggregated hIAPP is surface active, like many amphiphilic peptides. This observation is in agreement with earlier studies of hIAPP[46] and other amyloidogenic proteins and peptides.[54,55] Subsequently, the negatively charged phospholipid DPPG was deposited at the interface up to a surface pressure of ∼30 mN/m, which corresponds to the packing density of lipids in biological membranes.[51] At this surface pressure, a DPPG monolayer adopts, at room temperature, the liquid condensed phase.[56] In the absence of lipids, hIAPP does not convert to β- sheet-rich structures on the time scale of our VSFG experiments (see SI Figure 5.1 and SI Table 5.3). We exclude the presence of pre-existing aggregates by the fact that we observe a characteristic lag phase in ThT fluorescence assays. Presence of pre-existing aggregates would have resulted in an immediate increase in fluorescence intensity.[1] Additionally, no amyloid fibrils are observed by AFM 10 min after adding lipids to the freshly prepared hIAPP solution (Figure 5.1a). However, after 17 h of incubation, the interface showed the abundant presence of fibrils with diameters in the range of 3–7 nm, typical of amyloid fibrils (Figure 5.1b).

VSFG enabled us to follow the kinetics of fibrillation specifically at the phospholipid interface, as shown in Figure 5.1d. The peptide and the phospholipid both contribute to the spectra but in different wavenumber regions. The phospholipid displays a carbonyl stretch vibration around 1730 cm^{-1}, while the peptide shows peaks in the amide I region (1600–1700 cm^{-1}). Note that EGCG has no vibrational modes in this frequency region. We have fitted a three-component Lorentzian function to the SFG spectra using one component for the carbonyl stretch vibration of DPPG (1730 cm^{-1}) and two components to describe the amide I region (see SI methods and a list of fit parameters in SI Table 5.1 and SI Table 5.2; an example fit to the spectrum after 14 min is shown as a red line in Figure 5.1d).

The two amide I components are centered at 1652 and 1672 cm^{-1}, suggesting a contribution of α-helix or random structure and β-sheet or turns, respectively.[33,34,36,57,58] At early times, the amide I region is dominated by α-helix or random structure (1652 cm^{-1}), between which we cannot distinguish. These spectra are consistent with the AFM

images showing that the peptide is initially nonaggregated. However, as time progresses, the contribution of β-sheet/turns (1672 cm^{-1}) increases. After 8–10 h, the peptide is fully converted from α- helix or random structure to β-sheet or turns, consistent with prior SFG measurements.[33,34] As amyloid fibrils are characterized by the dominant presence of β-sheet content, we assign the increase in the 1672 cm^{-1} component mainly to increased β-sheet structure, rather than β-turns.[33,34,36,57,58] We assume, that the β-sheet content is directly related to formation of mature fibrils. In the absence of lipids, hIAPP does not convert to β-sheet-rich structures at the surface on the time scale of our SFG experiment (see SI Figure 5.1 and SI Table 5.3). This confirms the catalyzing role of lipids in hIAPP aggregation, observed previously for liposomes.[49]

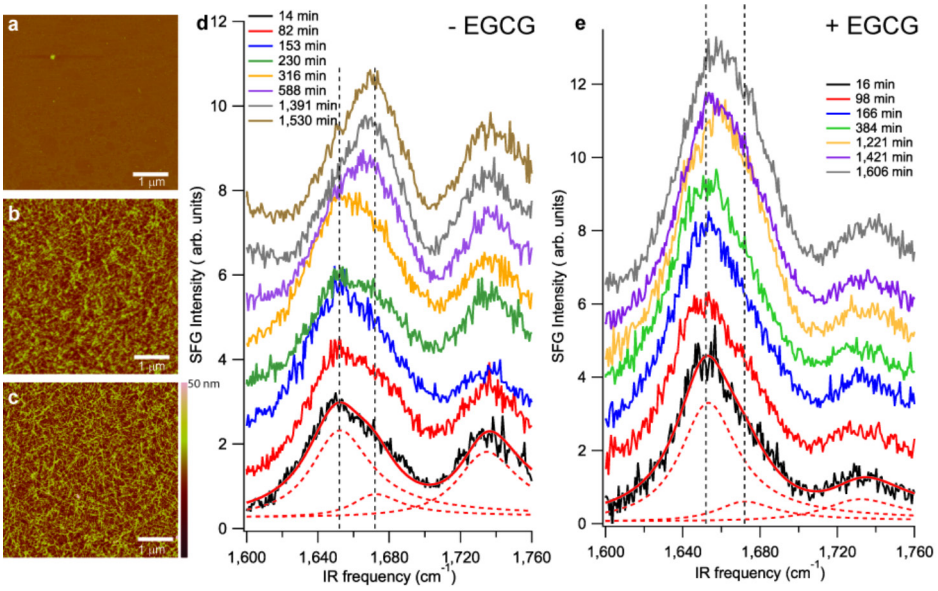

Figure 5.1: AFM images and SFG spectra measured during hIAPP aggregation at the phospholipid interface in the presence or absence of EGCG. AFM images after hIAPP aggregation for a) 10 and b) 1020 min in the absence of EGCG, and d) VSFG spectra taken at various time points. c) AFM image after hIAPP aggregation in the presence of EGCG at a 1:1 hIAPP:EGCG molar ratio for 1020 min, and e) corresponding VSFG spectra. The vertical dashed lines in panels d and e indicate IR frequencies of 1652 and 1672 cm^{-1}, respectively. Red lines through the bottom spectra are exemplary results of the global fit; the dashed red lines show the three individual components of each fit.

To assess the influence of EGCG on fibrillation both in bulk solution and at the phospholipid interface, we followed hIAPP fibrillation in both situations in the presence of an equimolar amount (1 μM) of EGCG. For the quantification of bulk fibril formation, we use a ThT assay, in which the thioflavin fluorescence serves as a reporter for the presence of fibrils (Figure 5.2a).[53] Note that the ThT assay cannot separate interfacial and bulk contributions to the fluorescence; its application is therefore restricted to bulk experiments. In agreement with previous reports in bulk,[23] 1 μM of EGCG suffices to completely inhibit hIAPP aggregation in bulk experiments; the thioflavin fluorescence is completely suppressed in the presence of EGCG. AFM images confirm that no fibrils are formed under bulk conditions when EGCG is present at an equimolar concentration (Figure 5.2c), whereas abundant fibrils are present in absence of EGCG (Figure 5.2b). In contrast, the EGCG inhibitory activity is much reduced at the phospholipid interface; AFM images of the interface transferred onto mica showed the abundant presence of fibrils (Figure 5.1c), despite the presence of EGCG. Consecutive VSFG spectra taken during 24 h incubation of hIAPP in the presence of EGCG confirmed that there was significant conversion of hIAPP secondary structure from α-helix or random structure (1652 cm^{-1}) to β-sheet (1672 cm^{-1}) (see Figure 5.1e). However, the shift in peak position of the entire amide I band, which is a convenient indicator of peptide aggregation,[33] is significantly less in the presence of EGCG (7 cm^{-1}) than in its absence (20 cm^{-1}). Note that the relative SFG intensities of the phospholipid and hIAPP contributions in spectra taken in the presence of EGCG (∼0.8 and 5 au, respectively) are different than in the spectra taken in its absence (∼1 and 3 au, respectively), due to slightly smaller amounts of lipids that were deposited on the subphases for the experiment with EGCG. Fewer lipids result in a lower signal at 1730 cm^{-1} and leave more room at the surface for fibrils, causing a larger intensity in the 1652 cm^{-1} region. These small differences in surface lipids do not affect the interfacial fibrillation kinetics. To obtain quantitative information about the inhibition of hIAPP fibrillation at the phospholipid interface by EGCG, we fitted the contributions of the α-helix/random structure (1652 cm^{-1}) component and the β-sheet (1672 cm^{-1}) component during hIAPP aggregation. Both contributions are expressed as the amplitude of the contribution to interfacial vibrational response divided by the full width at half-height (see methods, SI Table 5.1 and SI Table 5.2). The resulting values are normalized so that at every time the total amide I contribution equals one. As shown in Figure 5.2a, the relative amount of β-sheet intensity increases with time, both in the presence and absence of EGCG. However, in the presence of EGCG, the spectral amplitude reflecting the formation of β-sheet structure is reduced by a factor of 2. This suggests that, while it shows some activity also at the phospholipid interface, EGCG is markedly less effective at the interface than in bulk, where the inhibition is close to 100% in the same time (Figure 5.2a).

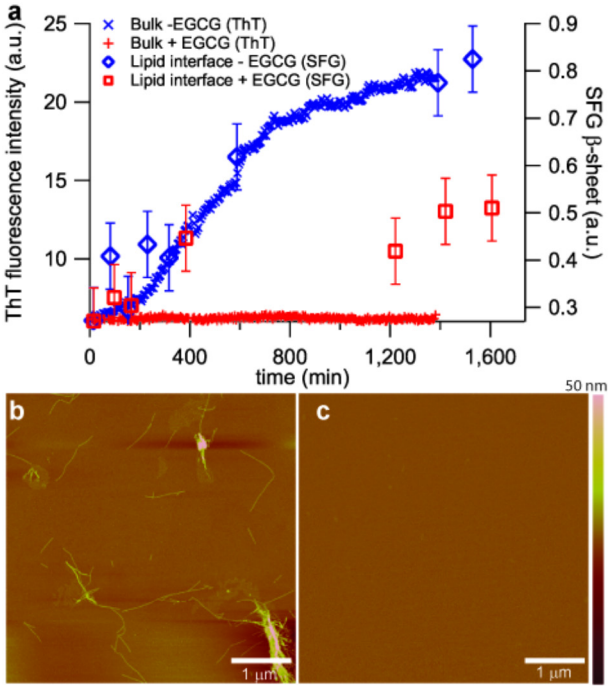

Figure 5.2: Comparison of the inhibitory effect of EGCG on hIAPP fibrillation in bulk and at the phospholipid interface. a) The formation of hIAPP amyloid fibrils in bulk was measured using a ThT fluorescence assay, showing the characteristic sigmoidal increase in fibril yield in the absence of EGCG (×) and virtually complete inhibition of fibril growth in the presence of EGCG at a 1:1 molar ratio (+). The formation of amyloid fibrils at the phospholipid interface was measured by determining the relative β-sheet intensity from the VSFG spectra, in absence (◇) and presence (□) of EGCG. AFM confirms that b) hIAPP fibrils have grown in bulk solution in the absence of EGCG and that c) an equimolar amount of EGCG completely inhibits fibril formation. From the SFG results, it is apparent that the inhibition efficiency of EGCG is much reduced at the lipid interface.

Another characteristic of EGCG that has been demonstrated under bulk conditions is its ability to disaggregate existing fibrils into unstructured smaller species.[9,23,26,27] We indeed observe this effect in our ThT assays when adding EGCG to preformed hIAPP fibrils in bulk conditions (Figure 5.3a), and we confirmed the breakdown of fibrils by AFM. Next, we asked whether EGCG is also able to reduce the β-sheet content of existing IAPP fibrils at the phospholipid interface. We formed hIAPP fibrils at the phospholipid interface by incubation for 17 h in absence of EGCG and then recorded VSFG spectra during the incubation of EGCG with the pre-existing fibrils. These measurements showed that the β-sheet content of hIAPP fibrils at the interface, at a bulk hIAPP concentration of 1 µM, is not reduced by 1 µM EGCG, even after incubation

for 2 days, in strong contrast with the situation in bulk (Figure 5.3a). Moreover, even at EGCG to hIAPP molar ratios of up to 1000, no disaggregation of interfacial hIAPP fibrils was observed, even after 24 h of incubation (Figure 5.3b). AFM measurements confirm that hIAPP fibrils indeed remain at the lipid interface (inset Figure 5.3b).

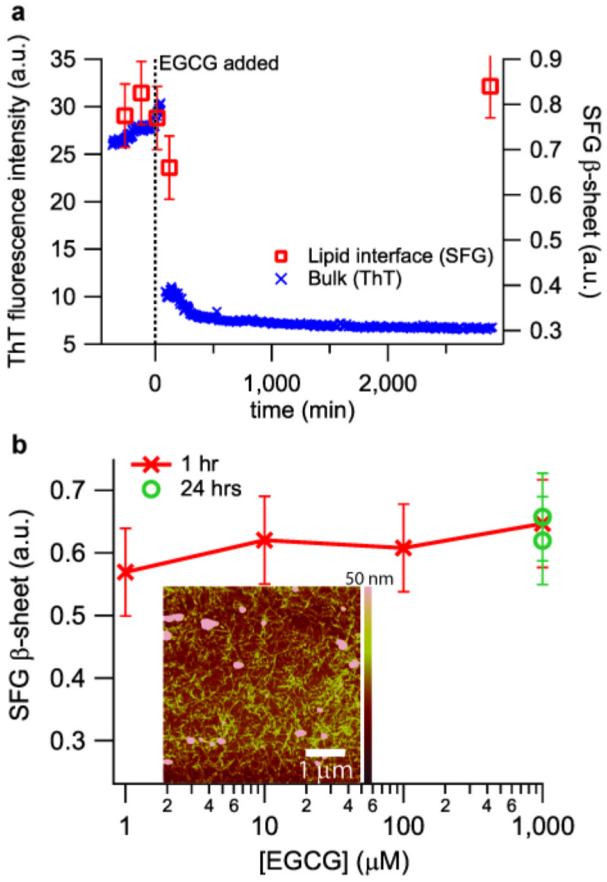

Figure 5.3: Effect of EGCG on preformed hIAPP fibrils in bulk and at the surface. a) Kinetics of disaggregation of preformed hIAPP fibrils with EGCG at a 1:1 molar ratio in bulk, followed by a ThT assay (×), compared to disaggregation at a lipid interface, followed by SFG (□). The dotted line at t = 0 indicates the time of addition of EGCG to the fibrils. b) The relative β-sheet/turn intensity from the VSFG spectra for incubation of preformed hIAPP fibrils for 1 h at the phospholipid interface (×) as function of EGCG concentration. Incubations for 24 h at 1 mM EGCG are also shown (○). The inset shows an AFM image of abundant hIAPP fibrils that remain at the DPPG interface after incubation with 100 µM EGCG for 24 h. The SFG spectra and fit parameters of the data in this figure are shown in Figure S2, SI Table 5.4 and SI Table 5.5.

To test whether a structurally different type of fibrils is formed at the interface which is more resistant to EGCG than fibrils formed in bulk solution, we investigated the effect of EGCG on interfacial fibrils in the absence of lipids. Fibrils were collected after overnight incubation at the lipid interface. AFM imaging showed that preformed interfacial fibrils are disaggregated upon incubation with EGCG in bulk (SI Figure 5.6), which strongly suggests that the apparent resistance of IAPP amyloids against EGCG at the lipid monolayer interface is not an intrinsic (e.g., structural) property of the interfacial amyloid fibril itself.

In the analysis of the VSFG data we assume a direct correlation between β-sheet content of hIAPP and the formation of mature fibrils. From VSFG data, we cannot exclude, however, the presence of oligomeric forms of hIAPP containing β-sheet structure elements. Such oligomers might form as intermediates during fibrillogenesis or upon disaggregation by EGCG. To confirm that the β-sheet content is indeed an unambiguous marker of the fibril state of hIAPP, FTIR experiments were performed. Changes in the secondary structure of hIAPP fibrils grown in bulk solution upon addition of ECGC were investigated by changes in the amide I absorption band. EGCG does not exhibit any FT-IR absorption band centered between 1680 and 1615 cm^{-1} (data not shown). Figure 5.4 shows the second derivative of the FT-IR absorption spectra (cf. SI Figure 5.7 for the raw absorption spectra). The airdried hIAPP film yields a pronounced amide I band. The minima in the respective second derivative spectrum identify the various distinct contributions to the amide I band related to different secondary structure types (Figure 5.4a). The predominant β-sheet character of the dry amyloid sample is evident by a pronounced minimum at 1625 and a weaker one at 1673 cm^{-1}. Their spectral positions appear at remarkable low wavenumbers, indicating the strong hydrogen-bond interactions typical for amyloids. The latter minimum coincides with the β-sheet marker band present in the VSFG spectra (Figure 5.1d,e). The position of two additional minima at 1646 and 1662 cm^{-1} may originate from smaller contributions of helical and/or unordered structures in hIAPP fibrils.[59] Structural transitions during the dissolution process of a 1:1 molar mixture of hIAPP fibrils and EGCG are followed by transmission FT-IR. The sample was suspended in deuterium oxide buffer to separate the amide I vibration from the water bending vibrational mode. Whereas the FT-IR absorption bands in the unaltered absorption spectra were low in intensity and the amide I band was affected by the broad background contribution of deuterium oxide centered at 1555 cm^{-1} (cf. SI Figure 5.7b), the second derivative spectra clearly identify the different contributions to the amide I spectra (Figure 5.4b). The first spectrum, taken 20 min after mixing EGCG and hIAPP fibrils, strongly resembles the second derivative spectrum of the dry hIAPP fibrils (Figure 5.4a), indicating the predominant amyloid state of the sample.

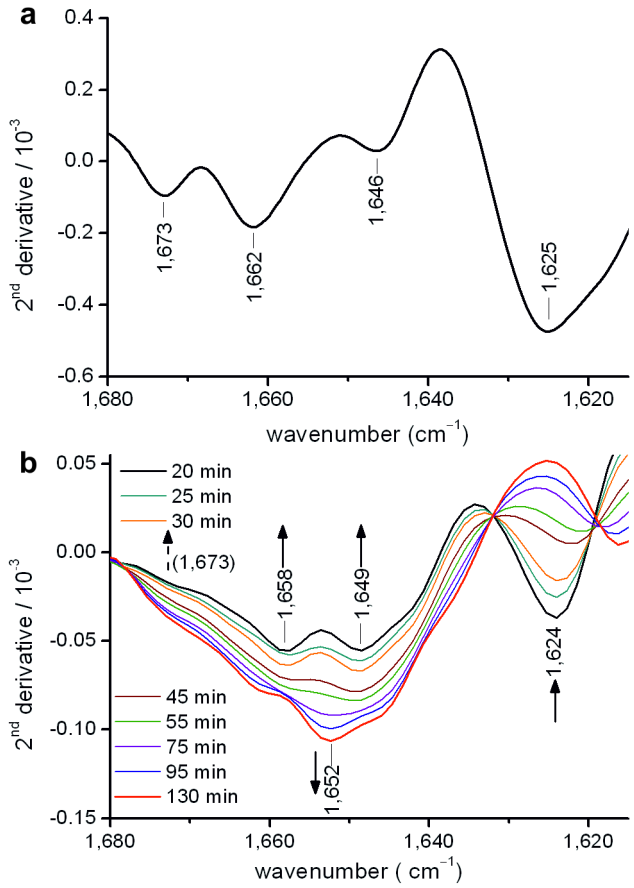

Figure 5.4: Second derivatives of the FT-IR absorption spectra in the spectral region of the amide I vibrational band of a) the ATR-spectrum of the dry IAPP fibril film and b) the transmission spectra of the IAPP disaggregation kinetics upon EGCG addition. The minima identify the center of the absorption bands, contributing to the respective FT-IR absorption spectrum. Bands at 1625 and 1673 cm^{-1} reveal the low- and high-frequency contribution of β-sheet secondary structure, present in the ATR spectrum and in the early kinetic spectra.

Slight shifts of the position of the minima can be attributed to the H/D exchange and the ongoing disaggregation process. The time dependence of disaggregation is demonstrated by the second derivative spectra measured at selected time points after mixing the hIAPP fibrils with EGCG as indicated in the legend of Figure 5.4b. All minima corresponding to the fibril state of hIAPP disappear successively within 130 min, most notably, including the minima corresponding to the β-sheet content of the sample. Simultaneously a new minimum is formed at 1652 cm^{-1}, which can be attributed to the formation of an α-helix.[59] The high α-helical content of the disaggregation products

suggests that monomeric hIAPP is formed.[60] These results clearly demonstrate that a break-up of fibrillar structures would be apparent from the SFG spectra. The fact that the SFG intensity associated with β-sheet content remains after addition of EGCG thus demonstrates the inability of ECGC to disrupt fibrils at the lipid interface.

Conclusions

By using VSFG supported by FT-IR in combination with AFM, we were able to show that EGCG has a considerably lower capacity toward the inhibition of hIAPP fibril formation at a phospholipid interface and is unable to disrupt the β-sheet structure of existing fibrils, in strong contrast with the efficient inhibition of fibril formation and disruption of pre-existing fibrils in bulk. The phospholipid monolayer apparently stabilizes the fibrils toward EGCG. This stabilization is the result of noncovalent interactions at the interface, enabled by the amphiphilicity of both fibrils and lipids. The interaction between lipids and fibrils at the surface is also apparent from the contribution to the surface tension of both entities.

The molecular origin of the low fibril-inhibition efficiency of EGCG at the interface likely originates from the simple inability of EGCG to access the binding site on the peptide due to the peptide's presence at the interface. EGCG has been suggested to interact with amyloidogenic peptides and proteins via aromatic residues.[14,15,20] These hydrophobic aromatic residues will be contained within the hydrophobic part of the phospholipid–air interface, rather than pointing toward bulk water. EGCG is simply not present in the interfacial hydrophobic region as is evident from: (i) the absence of an increase of the surface pressure when EGCG is added under an air–water or an air–DPPG interface (see SI Figure 5.3) and (ii) the absence of SFG signal in the CH stretch spectral region (2800–3200 cm^{-1}) from an EGCG solution interface (see SI Figure 5.4). A role may also be played by the competitive interaction of EGCG with lipids, which would serve to further reduce its effective interfacial concentration. Indeed, EGCG has been reported to interact with the neutral phospholipid dipalmitoylphosphatidylcholine (DPPC) and to a lesser extent with negatively charged lipids.[61,62] Hence the low interfacial fibril disaggregation efficiency of EGCG is concluded to result from a negligibly low interfacial concentration of EGCG. This effect cannot even be negated by increasing the bulk concentration by several orders of magnitude (Figure 5.3b).

Disaggregation experiments of interfacial fibrils in the absence of lipids demonstrate that their resistance against EGCG is not a property of the fibrils itself, as it would be the case if fibrils formed at the lipid interface are different from fibrils in bulk solution (SI Figure 5.6). This observation is consistent with the hypothesis that the ECGC is simply not interacting with the fibrils at the lipid interface.

The combined results presented here demonstrate that EGCG only partially inhibits the formation of β-sheet structure at the phospholipid interface, being ~50% less efficient at the interface compared to bulk. Moreover, EGCG is not able to disaggregate existing fibrils at an interface during the course of our experiments; the phospholipid interface negatively affects the efficiency of the inhibitor. Given that current hypotheses suggest that it is the cellular membrane where amyloid fibrils and oligomers assemble and exert their cytotoxic effect, phospholipid interfaces should be considered during the design and in vitro testing of amyloid inhibitors. We show here that SFG spectroscopy in conjunction with AFM provides a useful assay for testing the activity of amyloid inhibitors specifically at interfaces.

Materials and methods

Preparation of Solutions and Monolayers. Synthetic hIAPP (Bachem H-7905) stock solutions were prepared by dissolving freezedried peptide powder in Milli-Q water to a final concentration of ~1 mg/mL. This solution was filtered using a 0.2 μm filter. Immediately afterward, the concentration of hIAPP was measured using the absorbance at 280 nm and the known extinction coefficient of 1280 cm^{-1} M^{-1}.[50] The final concentration of the stock solution was typically between 120 and 160 μM. The solution was aliquoted and immediately stored at −80 °C until use. Once thawed, the contents of the tube were used within minutes, and left-over solution was discarded. EGCG (>95%, Sigma-Aldrich E4143) stock solutions were freshly prepared before each experiment as a 1 mM solution in Milli-Q water. All experiments were performed using a 10 mM sodium phosphate buffer at pH 7.4 which was filtered using a 0.2 μm filter before each experiment. The monolayer was prepared in a circular Teflon trough with a diameter of 80 mm. First, the trough was filled with 25 mL buffer either with or without 1 μM EGCG. Next, hIAPP stock solution was added to obtain a final hIAPP concentration of 1 μM. The solution was carefully mixed by pipetting up and down using a 1 mL pipet. After incubation for 10–15 min, 16 drops (0.5 μL) of a 1 mM solution of DPPG (Avanti Polar Lipids) in chloroform were evenly spread on the surface to obtain 107 $Å^2$ per phospholipid molecule (defined in absence of peptide).

These conditions were chosen in accordance with recent experiments of Fu et al.[33] The resulting surface pressure is around 30 mN/m, corresponding to the packing density of lipids in biological membranes.[51] The phospholipid–hIAPP interface was heterogeneous, i.e., SFG spectra were different at different locations at the interface likely due to clustering of fibrils [see SI Figure 5.5, Supporting Information (SI)]. To average the signal over a large surface area, the trough was rotated at ~10 rpm.

VSFG Spectroscopy. The VSFG spectroscopy setup has been described in detail elsewhere.[52] Briefly, a visible beam (vis) (800 nm, 20–30 μJ/pulse, spectral bandwidth of 25 cm^{-1}) is overlapped at the sample position with an infrared (IR) beam (2–3 μJ/pulse, 150 fs broadband), which is centered at 1675 cm^{-1} and has a spectral bandwidth of 150 cm^{-1}. Both beams are focused down to ∼100 μm beam waist. The incident angles of the vis and IR beams are 35° and 40°, respectively, both defined relative to the surface normal. The SFG light generated by the sample is detected with a monochromator connected to a charge-coupled device camera. All spectra were collected at 23.0 ± 0.2 °C under unpolarized SFG, s-polarized vis, and p-polarized IR conditions and integrated over 6 min. In contrast to recently published VSFG data on hIAPP aggregation,[33] we observe no amide I signal for hIAPP fibrillation using psp polarization conditions (corresponding to p-polarized SFG, s-polarized vis, and p-polarized IR settings).[38] To not unnecessarily lose signal photons, we decided to omit the output polarizer. Spectral analysis included background subtraction and division by the reference signal from a z-cut quartz plate that was taken immediately before or after the spectrum of the monolayer. Spectral fitting was performed using a three-component (two for the amide I signal and one for the phospholipid signal) Lorentzian model and included the maximum entropy method (MEM) analysis to verify the fit.[35] The equation used for the fit has been described previously and is commonly used to fit VSFG spectra.[33,35,37] The fitting procedure yields values for the amplitude and phase of the nonresonant susceptibility and for the amplitude, wavenumber, and line width (full width at half-maximum, fwhm) of each component, as shown in SI Table 5.1 and SI Table 5.2. Fitting was performed in Igor Pro 6.2 (WaveMetrics, Inc.) using a global fit procedure for all spectra from a single aggregation experiment, with the nonresonant contribution, the wavenumber, the full width at half height, and the peak maximum position linked for all spectra during the fit. The relative contribution of each component in the amide region was calculated by dividing the amplitude by the fwhm, followed by normalization to the maximum of the amide signal intensity. For the 1672 cm^{-1} component, this value is named “SFG β-sheet/turn”, as plotted in Figure 5.2a and Figure 5.3b. The value obtained is proportional to the amount of secondary structure when assuming that the IR and Raman dipole do not depend on the secondary structure and that orientation effects are canceled out by the random orientation of the fibrils in the plane of the surface. The error is estimated to be ±0.07 (au) for all SFG data points in Figure 5.2a and Figure 5.3b, based on the variation in fit results when different fit assumptions are made (for example, with or without requiring the widths of the resonances to be identical for all fits).

Atomic Force Microscopy (AFM). Samples for AFM were prepared using the Langmuir–Blodgett technique and a MicroTrough X (Kibron). The trough area was filled with 55 mL buffer, with or without 1 μM EGCG, and the surface area was set to 110 cm^2 using movable barriers to obtain the same area to volume ratio as in the trough used for SFG measurements. A freshly cleaved piece of mica (15 × 15 mm) was submerged, and hIAPP was added to obtain a final concentration of 1 μM. The solution was carefully mixed by pipetting up and down using a 1 mL pipet. After a stable surface pressure of ∼20 mN/m was reached, 32 drops (0.5 μL) of a 1 mM solution of DPPG in chloroform were evenly spread over the surface to obtain 107 $Å^2$ per lipid (defined in absence of peptide) after which the surface pressure increased to 30 mN/m. Next, the mica was pulled up through the surface at 5 mm/min while maintaining a constant surface pressure of 30 mN/m. The mica was air dried and used for AFM analysis using tapping mode AFM in air (Dimension 3100 scanning probe microscope, Veeco). Silicon cantilevers with a force constant of 5 N/m were used. Images were flattened using Nanoscope 6.14 software. For analysis of samples from the ThT test (see below), 40 μL samples were taken from the wells of the mitrotiter plates (see below) and incubated for 5 min on freshly cleaved mica, washed 2 to 3 times with 1 mL of Milli-Q water, and air dried. For the AFM analysis of the ThT experiment, a concentration of 10 μM hIAPP was used since 1 μM was too low for AFM analysis of bulk aggregation. The ThT curves for 10 μM also show complete inhibition of fibril formation in the presence of EGCG.

ThT Kinetics. The kinetics of hIAPP fibril formation was measured using the fluorescence intensity increase upon binding of the fluorescent dye ThT to hIAPP fibrils, a commonly used method to detect amyloid fibrils.[53] A plate reader (PerkinElmer Victor X3) was used to perform ThT experiments in standard 96-well flat-bottom black microtiter plates (Nunc 237105) in combination with a 430 nm excitation filter and a 480 nm emission filter. The assay was started by adding a few μL of a 140 μM hIAPP stock solution in Milli-Q to a solution of 10 μM ThT in 10 mM sodium phosphate at pH 7.4. The final hIAPP concentration was either 1 or 10 μM, and the total volume in each well was 150 μL. When required, EGCG (at a final concentration of 1 or 10 μM, always at a 1:1 molar ratio of hIAPP:EGCG) was added before the addition of hIAPP. The microtiter plate was covered using a transparent self-adhesive film to prevent evaporation from the wells. The microtiter plate was shaken before the measurement for 10 s by using the shaking function of the plate reader. Fluorescence was measured from the top every 5 min at 23 ± 1 °C.

Fourier Transform Infrared Spectroscopy (FT-IR). Infrared transmission measurements were carried out on a Vertex 70 FT-IR spectrometer (Bruker Optics, Ettlingen, Germany) using a deuterated triglycine sulfate detector (DTGS). The spectral resolution was 4 cm^{-1}, and for each measurement 256 spectra were averaged. The Blackmann–Harris 3-

term apodization function was used for the Fourier transformation. Bulk fibrils of hIAPP were grown in a 10 µM solution for 18 h while agitated. The sample was concentrated by ultrafiltration using centrifugal filters with molecular weight cutoff of 10 kDa (Amicon Ultra-4, Millipore, Cork, Ireland). The aqueous buffer was exchanged by a deuterium oxide-based sodium phosphate buffer at pD 7.4 by 10-fold dilution and concentration for 3 times. The sample of the approximate concentration of 200 µM was incubated for 5 h to allow for a full H/D exchange. The fibril suspension was mixed with an EGCG solution in deuterium oxide to yield a 1:1 molar ratio. The FT-IR transmission cuvette based on two CaF_2 windows was immediately assembled under a stream of nitrogen and sealed with vacuum grease (Baysilone-Paste, Bayer, Leverkusen, Germany). Spectral recording was started 20 min after mixing of the fibrils with ECGC, due to the assembling of the cuvette and the depletion time of atmospheric water vapor in the spectrometer. Spectra were recorded every 5 min for 12 h. No baseline correction was performed; the second derivative spectra were calculated using the OPUS software. Attenuated total reflection (ATR) spectra were measured on a single reflection ATR cell equipped with a diamond crystal (Spectra-Tech Foundation Performer, Thermo Scientific, Waltham, MA) on a Nicolet 730 FT-IR spectrometer (Thermo Scientific). Five µL of the aqueous hIAPP sample was deposited on the ATR crystal by drying at room temperature.

Acknowledgment

This work is part of the Industrial Partnership Programme (IPP) Bio(-Related) Materials (BRM) of the Stichting voor Fundamenteel Onderzoek der Materie (FOM), which is financially supported by the Nederlandse Organisatie voor Wetenschappelijk Onderzoek (NWO). The IPP BRM is cofinanced by the Top Institute Food and Nutrition and the Dutch Polymer Institute. This work is further supported by NanoNextNL, a micro- and nanotechnology consortium of the Government of The Netherlands and 130 partners.

References

(1) Chiti, F.; Dobson, C. M. *Annual Review of Biochemistry* **2006**, *75*, 333.
(2) Höppener, J. W. M.; Ahrén, B.; Lips, C. J. M. *New England Journal of Medicin* **2000**, *343*, 411.
(3) Engel, M. F. M. *Chemistry and Physics of Lipids* **2009**, *160*, 1.
(4) Kayed, R.; Head, E.; Thompson, J. L.; McIntire, T. M.; Milton, S. C.; Cotman, C. W.; Glabe, C. G. *Science* **2003**, *300*, 486.
(5) Lashuel, H. A.; Lansbury, P. T. *Quarterly Reviews of Biophysics* **2006**, *39*, 167.
(6) Engel, M. F. M.; Khemtémourian, L.; Kleijer, C. C.; Meeldijk, H. J. D.; Jacobs, J.; Verkleij, A. J.; de Kruijff, B.; Killian, J. A.; Höppener, J. W. M. *Proceedings of the National Acadamy of Sciences U.S.A.* **2008**, *105*, 6033.
(7) Cohen, F. E.; Kelly, J. W. *Nature* **2003**, *426*, 905.
(8) Herczenik, E.; Gebbink, M. F. B. G. *FASEB Journal* **2008**, *22*, 2115.

(9) Bieschke, J.; Russ, J.; Friedrich, R. P.; Ehrnhoefer, D. E.; Wobst, H.; Neugebauer, K.; Wanker, E. E. *Proceedings of the National Acadamy of Sciences U.S.A.* **2010**, *107*, 7710.
(10) Daval, M.; Bedrood, S.; Gurlo, T.; Huang, C. J.; Costes, S.; Butler, P. C.; Langen, R. *Amyloid Journal of Protein Folding Disorders* **2010**, *17*, 118.
(11) Alhamadsheh, M. M.; Connelly, S.; Cho, A.; Reixach, N.; Powers, E. T.; Pan, D. W.; Wilson, I. A.; Kelly, J. W.; Graef, I. A. *Science Translational Medicin* **2011**, *3*.
(12) Bulic, B.; Pickhardt, M.; Mandelkow, E. M.; Mandelkow, E. *Neuropharmacology* **2010**, *59*, 276.
(13) Gazit, E. *FASEB Journal* **2002**, *16*, 77.
(14) Shoval, H.; Lichtenberg, D.; Gazit, E. *Amyloid* **2007**, *14*, 73.
(15) Necula, M.; Kayed, R.; Milton, S.; Glabe, C. G. *Journal of Biolical Chemistry* **2007**, *282*, 10311.
(16) Sellin, D.; Yan, L.-M.; Kapurniotu, A.; Winter, R. *Biophysical Chemistry* **2010**, *150*, 73.
(17) Buell, A. K.; Esbjorner, E. K.; Riss, P. J.; White, D. A.; Aigbirhio, F. I.; Toth, G.; Welland, M. E.; Dobson, C. M.; Knowles, T. P. J. *Physical Chemistry Chemical Physics.* **2011**, *13*, 20044.
(18) Porat, Y.; Abramowitz, A.; Gazit, E. *Chemical Biology and Drug Design* **2006**, *67*, 27.
(19) Hudson, S. A.; Ecroyd, H.; Dehle, F. C.; Musgrave, I. F.; Carver, J. A. *Journal of Molecular Biology* **2009**, *392*, 689.
(20) Lopez Del Amo, J. M.; Fink, U.; Dasari, M.; Grelle, G.; Wanker, E. E.; Bieschke, J.; Reif, B. *Journal of Molecular Biology* **2012**.
(21) Armstrong, A. H.; Chen, J.; McKoy, A. F.; Hecht, M. H. *Biochemistry* **2011**, *50*, 4058.
(22) Ehrnhoefer, D. E.; Bieschke, J.; Boeddrich, A.; Herbst, M.; Masino, L.; Lurz, R.; Engemann, S.; Pastore, A.; Wanker, E. E. *Nature Structural and Molecular Biology* **2008**, *15*, 558.
(23) Meng, F.; Abedini, A.; Plesner, A.; Verchere, C. B.; Raleigh, D. P. *Biochemistry* **2010**, *49*, 8127.
(24) Norton, R. S.; Chandrashekaran, I. R.; Adda, C. G.; MacRaild, C. A.; Anders, R. F. *Biochemistry* **2010**, *49*, 5899.
(25) Almeida, M. R.; Ferreira, N.; Saraiva, M. J. *FEBS Letters* **2011**, *585*, 2424.
(26) Lee, S.; Bae, S. Y.; Kim, S.; Hwang, H.; Kim, H. K.; Yoon, H. C.; Kim, J. H.; Kim, T. D. *Biochemical and Biophysical Research Communications* **2010**, *400*, 531.
(27) Norton, R. S.; Chandrashekaran, I. R.; Adda, C. G.; MacRaild, C. A.; Anders, R. F. *Archives of Biochemistry and Biophysics* **2011**, *513*, 153.
(28) Saraogi, I.; Hebda, J. A.; Becerril, J.; Estroff, L. A.; Miranker, A. D.; Hamilton, A. D. *Angewandte Chemie International Edition* **2010**, *49*, 736.
(29) Meng, F. L.; Raleigh, D. P. *Journal of Molecular Biology* **2011**, *406*, 491.
(30) Knight, J. D.; Williamson, J. A.; Miranker, A. D. *Protein Science* **2008**, *17*, 1850.
(31) Bazar, E.; Sheynis, T.; Dorosz, J.; Jelinek, R. *Chembiochem* **2011**, *12*, 761.
(32) Nilsson, M. R. *Methods* **2004**, *34*, 151.
(33) Fu, L.; Ma, G.; Yan, E. C. Y. *Journal of the American Chemical Society* **2010**, *132*, 5405.
(34) Fu, L.; Liu, J.; Yan, E. C. *Journal of the American Chemical Society* **2011**, *133*, 8094.
(35) Sovago, M.; Vartiainen, E.; Bonn, M. *Journal of Physical Chemistry C* **2009**, *113*, 6100.
(36) Nguyen, K. T.; King, J. T.; Chen, Z. J*ournal of Physical Chemistry B* **2010**, *114*, 8291.
(37) Chen, X.; Wang, J.; Sniadecki, J. J.; Even, M. A.; Chen, Z. *Langmuir* **2005**, *21*, 2662.
(38) vandenAkker, C. C.; Engel, M. F. M.; Velikov, K. P.; Bonn, M.; Koenderink, G. H. *Journal of the American Chemical Society* **2011**, *133*, 18030.
(39) Kapurniotu, A. *Biopolymers Peptide Science* **2001**, *60*, 438.

(40) Knight, J. D.; Hebda, J. A.; Miranker, A. D. *Biochemistry* 2006, *45*, 9496.
(41) Lopes, D. H. J.; Meister, A.; Gohlke, A.; Hauser, A.; Blume, A.; Winter, R. *Biophysical journal* 2007, *93*, 3132.
(42) Mirzabekov, T. A.; Lin, M. C.; Kagan, B. L. *Journal of Biological Chemistry* 1996, *271*, 1988.
(43) Kayed, R.; Sokolov, Y.; Edmonds, B.; McIntire, T. M.; Milton, S. C.; Hall, J. E.; Glabe, C. G. *Journal of Biological Chemistry* 2004, *279*, 46363.
(44) Butterfield, S. M.; Lashuel, H. A. *Angewandte Chemie International Edition* 2010, *49*, 5628.
(45) Padrick, S. B.; Miranker, A. D. *Biochemistry* 2002, *41*, 4694.
(46) Engel, M. F. M.; Yigittop, H.; Elgersma, R. C.; Rijkers, D. T. S.; Liskamp, R. M. J.; de Kruijff, B.; Höppener, J. W. M.; Killian, J. A. *Journal of Molecular Biology* 2006, *356*, 783.
(47) Jayasinghe, S. A.; Langen, R. *Biochimica et Biophysica Acta* 2007, *1768*, 2002.
(48) Murphy, R. M. *Biochimica et Biophysica Acta* 2007, *1768*, 1923.
(49) Knight, J. D.; Miranker, A. D. *Journal of Molecular Biology* 2004, *341*, 1175.
(50) Koo, B. W.; Hebda, J. A.; Miranker, A. D. *Protein Science* 2008, *21*, 147.
(51) Demel, R. A.; Geurts van Kessel, W. S.; Zwaal, R. F.; Roelofsen, B.; van Deenen, L. L. *Biochimica et Biophysica Acta* 1975, *406*, 97.
(52) Smits, M.; Sovago, M.; Wurpel, G. W. H.; Kim, D.; Muller, M.; Bonn, M. *Journal of Physical Chemistry C* 2007, *111*, 8878.
(53) LeVine, H., 3rd *Methods of Enzymololgy.* 1999, *309*, 274.
(54) Ege, C.; Lee, K. Y. C. *Biophysical Journal* 2004, *87*, 1732.
(55) Canale, C.; Torrassa, S.; Rispoli, P.; Relini, A.; Rolandi, R.; Bucciantini, M.; Stefani, M.; Gliozzi, A. *Biophysical Journal* 2006, *91*, 4575.
(56) Gopal, A.; Lee, K. Y. *The journal of physical chemistry B* 2006, *110*, 22079.
(57) Wang, J.; Even, M. A.; Chen, X. Y.; Schmaier, A. H.; Waite, J. H.; Chen, Z. *Journal of the American Chemical Society* 2003, *125*, 9914.
(58) Castner, D. G.; Weidner, T.; Apte, J. S.; Gamble, L. J. *Langmuir* 2010, *26*, 3433.
(59) Arrondo, J. L. R.; Muga, A.; Castresana, J.; Goni, F. M. *Progress in Biophysics and Molecular Biology* 1993, *59*, 23.
(60) Nanga, R. P. R.; Brender, J. R.; Vivekanandan, S.; Ramamoorthy, A. *BBA Biomembranes* 2011, *1808*, 2337.
(61) Huh, N. W.; Porter, N. A.; McIntosh, T. J.; Simon, S. A. *Biophysical Journal* 1996, *71*, 3261.
(62) Nakayama, T.; Kajiya, K.; Kumazawa, S. *Bioscience, Biotechnology and Biochemistry* 2002, *66*, 2330.

Supplementary Figures and Tables

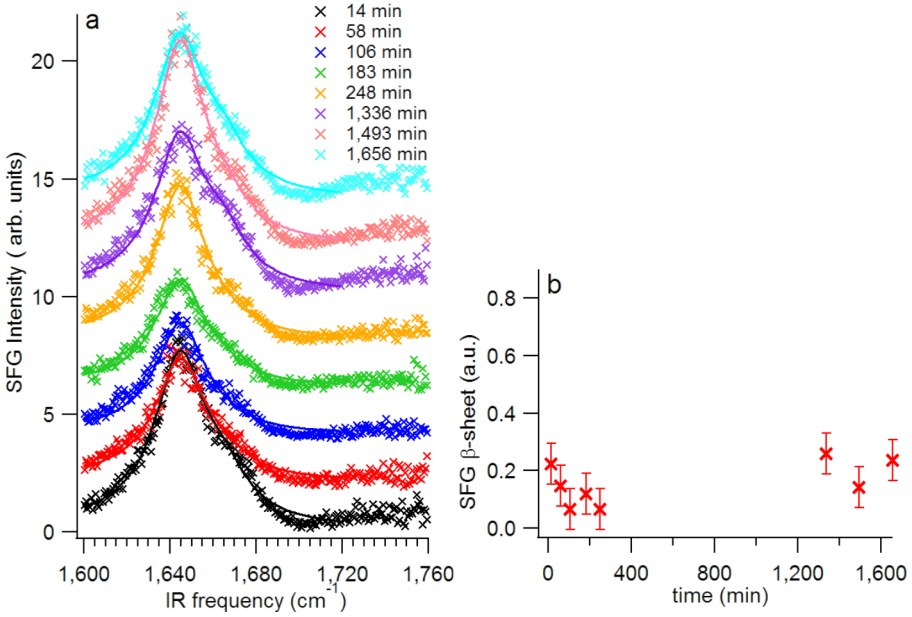

SI Figure 5.1: a) SFG spectra of 1 µM hIAPP at the air/water interface in absence of DPPG as a function of time. The solid lines represent the fits to the data. b) The relative β-sheet intensity from SFG as a function of time.

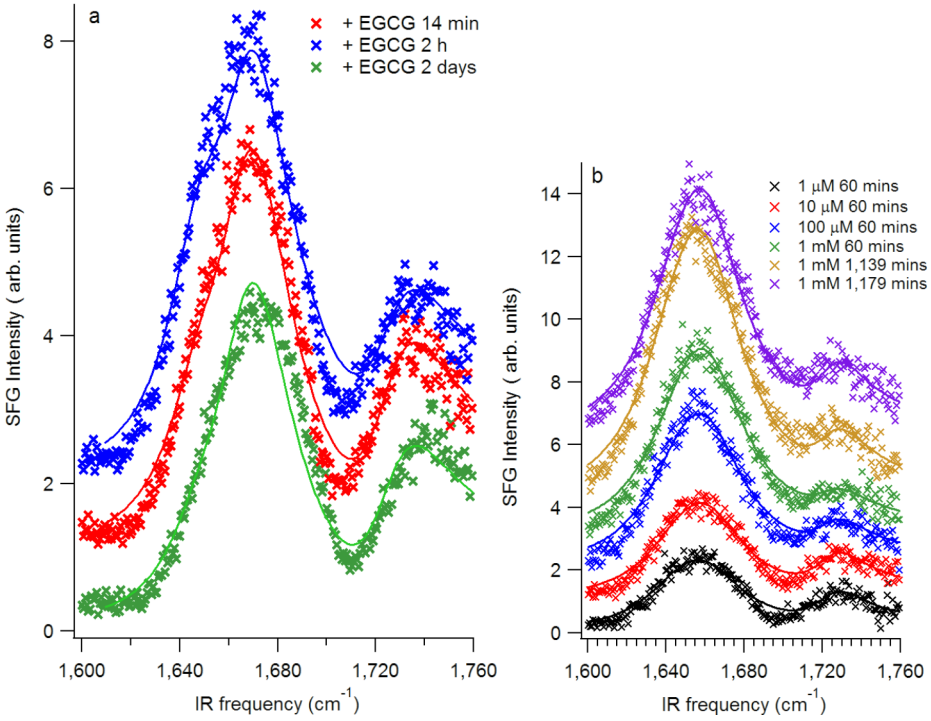

SI Figure 5.2: SFG spectra and fits of incubation of 1 µM hIAPP fibrils at the air/DPPG/water interface a) with 1 µM EGCG for three different times, and b) of incubation with different concentrations of EGCG at the air/DPPG/water interface. The solid lines represent the fits to the data.

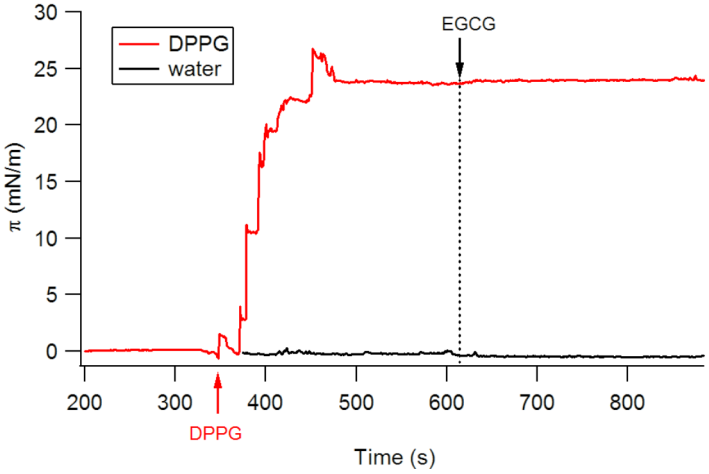

SI Figure 5.3: Change in surface pressure upon the addition of EGCG (1 µM final concentration) to a water interface (black) or DPPG interface (red). The dotted line indicates the time when EGCG is added. The black trace has been given an offset in the x-direction such that the time of EGCG injection matches that of the red trace.

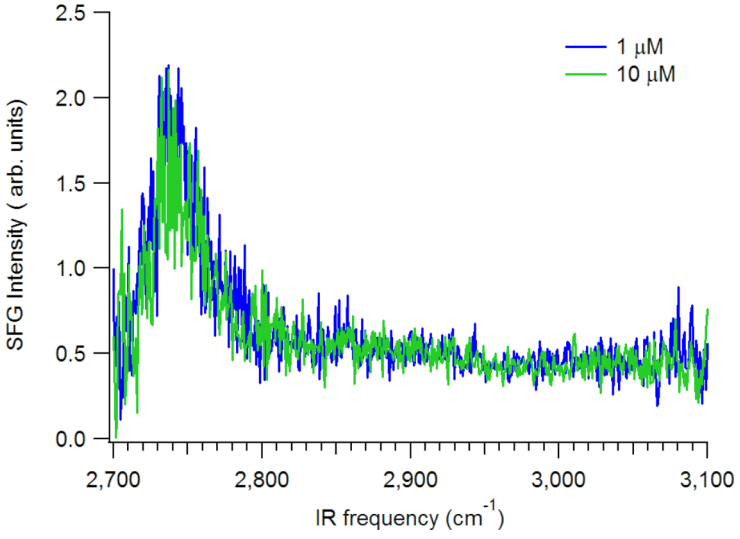

SI Figure 5.4: SFG spectra of EGCG at 1 and 10 µM in D_2O show the absence of any EGCG signal. The signal at 2,740 cm^{-1} stems from the free OD of surface water molecules.

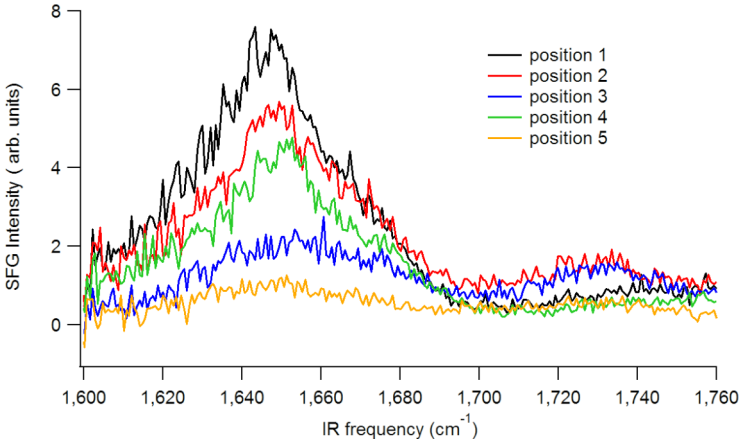

SI Figure 5.5: SFG spectra showing spatial heterogeneity of a hIAPP/DPPG interface. The spectra were measured at 5 different positions. The VSFG signals arise from an area with a size in the order of hundreds of µm. This is a much larger length scale than the scale seen in AFM images, in which a square of 5x5 µm is probed.

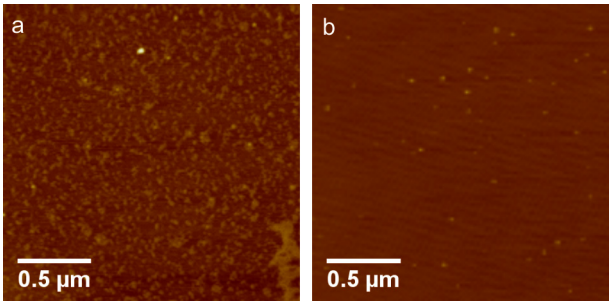

SI Figure 5.6: AFM images of hIAPP fibrils formed at the lipid-water interface before a) and after b) incubation with 100 #M EGCG for 1 hr.

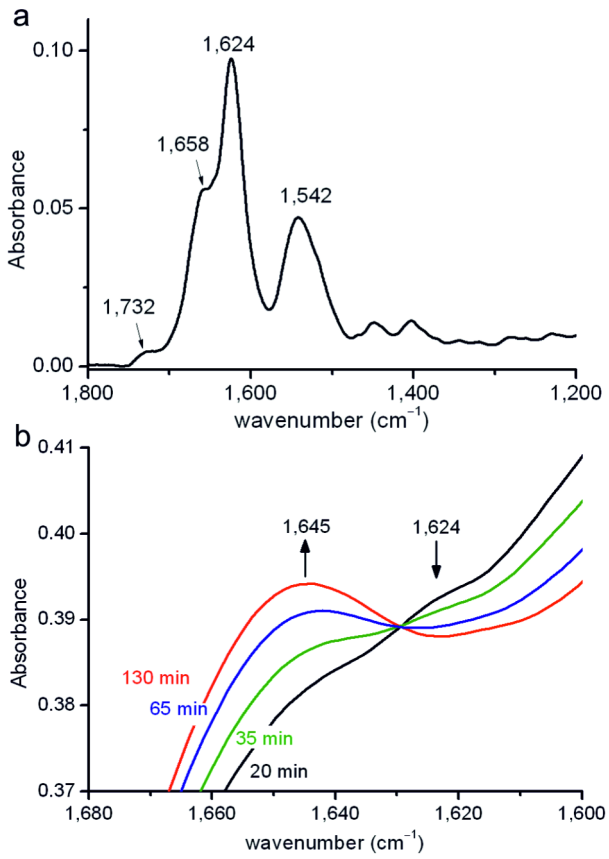

SI Figure 5.7: FT-IR absorption spectra of hIAPP. a) ATR spectrum of a dry amyloid film, showing vibrational bands at 1,732 cm^{-1} (C=O stretching vibrations of the C-terminal lysine), 1,658 and 1,624 cm^{-1} (amide I band corresponding to unordered/ helical structures and β-sheet structure, respectively) and 1,542 cm^{-1} (amide II band). b) Transmission FT-IR spectra of hIAPP and EGCG in a 1:1 molar ratio in D_2O, in the spectral region of the amide I band. Spectra were taken 20 min (red line), 35 min (green line), 65 min (blue line) and 130 min (black line) after mixing hIAPP and inhibitor. Over time, the band at 1624 cm^{-1} vanishes; a new band appears around 1,645 cm^{-1}; both changes are indicated by the two black arrows. The background absorption is due to a broad D_2O combination band centered at 1555 cm^{-1}.

SI Table 5.1: Fit parameters for fits of SFG spectra of IAPP-DPPG

time (min)	Ampl. 1 (a.u.)	Freq. 1 (cm^{-1})	FWHH 1 (cm^{-1})	Ampl. 2 (a.u.)	Freq. 2 (cm^{-1})	FWHH 2 (cm^{-1})	Ampl. 3 (a.u.)	Freq. 3 (cm^{-1})	FWHH 3 (cm^{-1})
14	20.4	1650.8	40.68	6.1	1670.5	32.8	16.9	1732.9	41.2
82	18.6	1650.8	40.68	10.3	1670.5	32.8	17.1	1732.9	41.2
153	23.8	1650.8	40.68	8.1	1670.5	32.8	11.1	1732.9	41.2
230	16.7	1650.8	40.68	10.3	1670.5	32.8	18.9	1732.9	41.2
316	21.1	1650.8	40.68	11.6	1670.5	32.8	16.2	1732.9	41.2
588	12.7	1650.8	40.68	16.6	1670.5	32.8	16.4	1732.9	41.2
1391	6.8	1650.8	40.68	18.9	1670.5	32.8	16.4	1732.9	41.2
1530	5.2	1650.8	40.68	19.7	1670.5	32.8	17.7	1732.9	41.2

For all fits, the non-resonant amplitude and phase were 0.53 and -1.24, respectively. The peak positions and the full width at half height (FWHH) are linked for the eight SFG spectra measured at different time points.

SI Table 5.2: Fit parameters for fits of SFG spectra of IAPP-DPPG with EGCG

time (min)	Ampl. 1 (a.u.)	Freq. 1 (cm^{-1})	FWHH 1 (cm^{-1})	Ampl. 2 (a.u.)	Freq. 2 (cm^{-1})	FWHH 2 (cm^{-1})	Ampl. 3 (a.u.)	Freq. 3 (cm^{-1})	FWHH 3 (cm^{-1})
16	30.2	1652.3	36.2	11.3	1670.2	36.4	16.6	1730	47.8
98	31.5	1652.3	36.2	15.0	1670.2	36.4	18.8	1730	47.8
166	33.1	1652.3	36.2	14.5	1670.2	36.4	17.0	1730	47.8
384	28.8	1652.3	36.2	23.3	1670.2	36.4	14.7	1730	47.8
1221	28.4	1652.3	36.2	20.6	1670.2	36.4	13.3	1730	47.8
1421	25.0	1652.3	36.2	25.4	1670.2	36.4	17.5	1730	47.8
1606	24.2	1652.3	36.2	25.4	1670.2	36.4	19.4	1730	47.8

For all fits, the non-resonant amplitude and phase were 0.28 and -1.14, respectively. The peak positions and the full width at half height (FWHH) are linked for the seven SFG spectra measured at different time points.

SI Table 5.3: Fit parameters for fits of SFG spectra of IAPP in absence of DPPG

time (min)	Ampl. 1 (a.u.)	Freq. 1 (cm^{-1})	FWHH 1 (cm^{-1})	Ampl. 2 (a.u.)	Freq. 2 (cm^{-1})	FWHH 2 (cm^{-1})
14	30.03	1645.4	28.3	8.2	1663.3	26.7
58	25.4	1645.4	28.3	4.1	1663.3	26.7
106	24.8	1645.4	28.3	1.7	1663.3	26.7
183	23.7	1645.4	28.3	3.0	1663.3	26.7
248	30.1	1645.4	28.3	2.0	1663.3	26.7
1336	27.8	1645.4	28.3	9.1	1663.3	26.7
1493	34.2	1645.4	28.3	5.3	1663.3	26.7
1656	28.7	1645.4	28.3	8.3	1663.3	26.7

For all fits, the non-resonant amplitude and phase were 0.41 and -1.8, respectively. The peak positions and the full width at half height (FWHH) are linked for the eight SFG spectra measured at different time points.

SI Table 5.4: Fit parameters for fits of SFG spectra of IAPP fibrils incubated with 1 4M EGCG for different times.

time (min)	Ampl. 1 (a.u.)	Freq. 1 (cm^{-1})	FWHH 1 (cm^{-1})	Ampl. 2 (a.u.)	Freq. 2 (cm^{-1})	FWHH 2 (cm^{-1})	Ampl. 3 (a.u.)	Freq. 3 (cm^{-1})	FWHH 3 (cm^{-1})
14	10.9	1648.7	30.2	45.2	1667.8	38.0	19.7	1725.5	37.7
120	17.3	1648.7	30.2	42.6	1667.8	38.0	16.0	1725.5	37.7
2880	6.6	1648.7	30.2	44.3	1667.8	38.0	17.9	1725.5	37.7

For all fits, the non-resonant amplitude and phase were 0.64 and -0.81, respectively. The peak positions and the full width at half height (FWHH) are linked for the three SFG spectra measured at different time points.

SI Table 5.5: Fit parameters for fits of SFG spectra of IAPP fibrils incubated with EGCG at different concentrations and for different times.

[EGCG] (mM)	time (min)	Ampl. 1 (a.u.)	Freq. 1 (cm^{-1})	FWHH 1 (cm^{-1})	Ampl. 2 (a.u.)	Freq. 2 (cm^{-1})	FWHH 2 (cm^{-1})	Ampl. 3 (a.u.)	Freq. 3 (cm^{-1})	FWHH 3 (cm^{-1})
0.001	60	10.5	1644.4	34.8	17.3	1661.4	43.4	9.3	1724.4	34.8
0.01	60	11.1	1644.4	34.8	22.5	1661.4	43.4	9.9	1724.4	34.8
0.1	60	15.2	1644.4	34.8	29.4	1661.4	43.4	8.1	1724.4	34.8
1	60	15.2	1644.4	34.8	34.7	1661.4	43.4	6.3	1724.4	34.8
1	1139	20.4	1644.4	34.8	41.4	1661.4	43.4	10.3	1724.4	34.8
1	1179	17.4	1644.4	34.8	41.5	1661.4	43.4	11.8	1724.4	34.8

For all fits, the non-resonant amplitude and phase were 0.37 and -0.90, respectively. The peak positions and the full width at half height (FWHH) are linked for the six SFG spectra.

Chapter 6

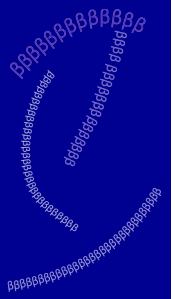

The polyphenol EGCG bundles and aggregates hen egg white lysozyme amyloid fibrils at neutral but not acidic pH

Based on: Corianne C. van den Akker, Tjado H.J. Morrema, Krassimir P. Velikov, Gijsje H. Koenderink (submission in preparation).

Abstract

Many diseases, including diabetes mellitus and Alzheimer's disease, are related to accumulation of aggregated (poly)peptides in tissues. These aggregates called amyloids are insoluble and up till now no adequate treatment of amyloid-related diseases is available. One of the most promising therapeutic agents is the polyphenol epi-gallocatechin-3-gallate (EGCG). It has been shown that EGCG inhibits amyloid formation for various peptides, often resulting in non-toxic oligomers. However, the mechanism behind the interactions between peptides and EGCG remains unclear. Also the knowledge on the effect of EGCG on mature amyloid fibrils is still limited. We investigated the effect of EGCG on amyloid fibrils formed from the model protein hen egg white lysozyme (HEWL) at neutral and acidic pH. We observe that at acidic pH EGCG does not affect the morphology or rigidity of HEWL amyloids fibrils. However, at neutral pH a subpopulation of thick fibrils was formed upon EGCG treatment. Electron microscopy imaging revealed that the thick fibrils formed large fibril aggregates. We show that the solution pH is an important factor in controlling the efficacy of EGCG as a therapeutic agent.

Introduction

Amyloids fibrils are protein aggregates that form from unfolded or (partially) unstructured peptides and proteins.[1] The formation of amyloids is thought to be a generic property of (poly)peptides, independent of their native fold or their amino acid sequence, although the sequence strongly influences the kinetics of amyloid formation.[2] More than 20 different human diseases are known to be related to amyloids, including type II diabetes mellitus and Alzheimer's disease.[3] These diseases have in common that a protein or peptide accumulates in an insoluble form in the affected tissue.[4] Although these macroscopic deposits of aggregates characterize protein misfolding diseases, it is thought that in many cases oligomers are substantially more cytotoxic than the fibrils.[5] Therapeutic strategies that have been proposed for treatment of amyloid-related diseases include hormones, antibodies, peptide fragments and natural antioxidants.[6] Ideally, the therapeutic agent should block the formation of oligomers and also dissociate mature fibrils into non-toxic species.[5] One of the most promising natural compounds is the polyphenol epi-gallocatechin-3-gallate (EGCG). EGCG is a catechin found in tea leaves (Figure 1a) that is thought to provide multiple health benefits since it is an antioxidant that scavenges free radicals.[6]

It has been shown that EGCG protects cells against amyloid-induced toxicity.[7-11] The reduced cytotoxicity is potentially related to the antioxidant activity of EGCG.[12] However, direct interactions of EGCG with misfolded proteins are also suggested to make a major contribution to its beneficial effects.[4] EGCG binds directly to intrinsically disordered Aβ and α-synuclein and promotes their assembly into large, non-toxic, spherical oligomers.[10] It has been shown that EGCG binds to the hydrophobic regions of several proteins, including Aβ, albumin and transthyretin.[4,13] Furthermore, it has been suggested that oxidized EGCG molecules react with free amines within the amyloid fibril, resulting in crosslinking of the fibrils.[13] EGCG inhibits fibril formation of several amyloidogenic peptides, including Aβ (Alzheimer's diseases), α-synuclein (Parkinson's disease), TTR (familial transthyretin amyloidosis) and hIAPP (type II diabetes mellitus).[9,11,14-17] Futhermore, EGCG is able to disaggregate or remodel existing amyloid fibrils (see also Chapter 4).[9,11,13,17] α-Synuclein amyloids were disaggregated into short fibrils upon incubation with EGCG for a few hours at pH=7.4.[11] Upon EGCG treatment for a few days, amorphous aggregates were formed.[11] Also α-synuclein fibrils formed amorphous aggregates that are less toxic to cells than the fibrils upon incubation with EGCG.[9] The fibril remodeling pathway is still unclear, but was shown to occur without an intermediate disassembly step.[9] No effect of EGCG on hydrophilic amyloid fibrils from the yeast prion Sup35NM was observed.[13] To investigate the effect of the hydrophilicity of the amyloid fibrils, the results were compared to amyloids fibrils with an increased

hydrophobicity obtained by mutation of two amino acids of the peptide. The hydrophobic amyloids formed a heterogeneous mix of intact fibrils and amorphous aggregates upon EGCG treatment for 24 hrs.[13]

The molecular mechanism by which EGCG interacts with amyloid fibrils and oligomers and remodels them is still unclear. Both charge-charge interactions[18] and π-π stacking interactions[14,19] of EGCG with proteins and amyloid fibrils have been reported. An important obstacle is that different studies have used different conditions for fibril assembly and incubation with EGCG. Well-controlled solution conditions are important, since the interactions between EGCG and HEWL involve noncovalent interactions that should depend on the solution pH and ionic strength.

Here we investigated the effect of EGCG on the morphology and rigidity of mature amyloid fibrils. As a model system we use amyloid fibrils formed from hen egg white lysozyme (HEWL). HEWL is a protein composed of 129 amino acid residues (Figure 1b). Its hydrophobic amino acid residues, which are likely to interact with EGCG based on prior studies of other proteins, are marked in Figure 1b. The most amyloidogenic part of HEWL is thought to be the stretch between amino acid residues 49 and 101.[20] Previously is was shown that EGCG reduces the alkali-salt mediated formation of HEWL amyloid fibrils upon incubation at pH=12.[21] Amorphous aggegates were observed upon incubation of HEWL monomer with EGCG under these using electron microscopy.[21] However, the effect of EGCG on mature HEWL fibrils is not known.

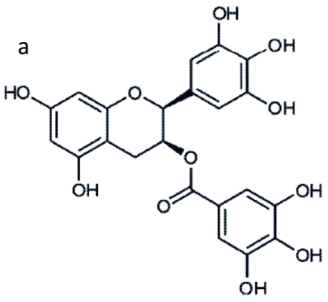

b
1 10 20 30 40
KVFGRCELAA AMKRHGLDNY RGYSLGNWVC AAKFESNFNT
41 50 60 70 80
QATNRNTDGS TDYGILQINS RWWCNDGRTP GSRNLCNIPC
81 90 100 110 120
SVNCAKKIVS SALLSSDITA DGNGMNAWVA WRNRCKGTDV
121 129
QAWIRGCRL

Figure 6.1: a) Molecular structure of EGCG. b) Amino acid sequence of HEWL. Hydrophobic amino acid residues are underlined. The most important amyloidogenic part is thought to be between amino acids residues 49 and 101.[21] V: Valine; F: Phenylalanine; C: Cysteine; L: Leucine; A: Alanine; M: Methionine; Y: Tyrosine; W: Tryptophan; P: Proline; I: Isoleucine.

Here we formed HEWL amyloids upon incubation at pH=2 and 65°C for 1 week. We compared the effect of EGCG on fibrils at the pH of formation, pH=2 and at pH=7, which is a more physiologically relevant pH level. We show that EGCG has no effect on the morphology and rigidity of fibrils at pH=2. However, at pH=7 a subpopulation of thick fibrils was formed upon incubation of preformed fibrils with EGCG in a 1:1 or 1:10 molar ratio of HEWL:EGCG. As a result, the ensemble-averaged persistence length of the fibrils increased in a dose-dependent manner at pH=7. Electron microscopy imaging revealed that the thick fibrils formed large fibril aggregates. We also show that the macroscopic viscosity of the suspensions decreases after incubation with EGCG, perhaps due to the sequestration of a fraction of the fibrils in thick fibrils and aggregates. We conclude that HEWL fibrils aggregate into thick bundles upon incubation with EGCG at pH=7, whereas at pH=2 EGCG is not able to induce any noticeable changes. Solution pH is therefore likely to be an important factor in controlling the efficacy of EGCG as a therapeutic agent.

Results and discussion

We investigated the effect of EGCG on the morphology of HEWL amyloid fibrils at pH=2 and pH=7 by imaging the fibrils after deposition and drying on a glass surface using tapping mode AFM in air. HEWL fibrils were formed by incubation at 65°C and pH=2 for 1 week. To remove non-aggregated material and small oligomers, the samples were filtered with 100kDa molecular weight cut-off filters. Long, thin fibrils with a length up to several micrometers were formed (Figure 6.2a-b). The fibrils were incubated with EGCG in a molar ratio of either 1:1 or 1:10 (HEWL:EGCG), for either 2 or 24 hrs, all at room temperature. At acidic pH (pH=2), we observed no visible effect of EGCG on the morphology of the fibrils based on AFM images (Figure 6.2c-f).

To test the effect of EGCG at neutral pH (pH=7), fibrils were transferred to water at pH=7 by filtration over 100 kDa molecular weight cut-off filters and washing with MilliQ water. The transfer process did not visibly change the morphology of the fibrils based on AFM images (Figure 6.3a-b). Note that in some AFM images of control samples, both at pH=2 and pH=7, short fragments were observed (Figure 6.3a). We do not know the origin of the variability between different images. Incubation with EGCG in a 1:1 HEWL:EGCG molar ratio at pH=7 for either 2 or 24 hrs did not result in a visible change fibril morphology (Figure 6.3c-d). However, upon incubation in a 1:10 HEWL:EGCG molar ratio, we observed a population of thick fibrils (Figure 6.3e-f).

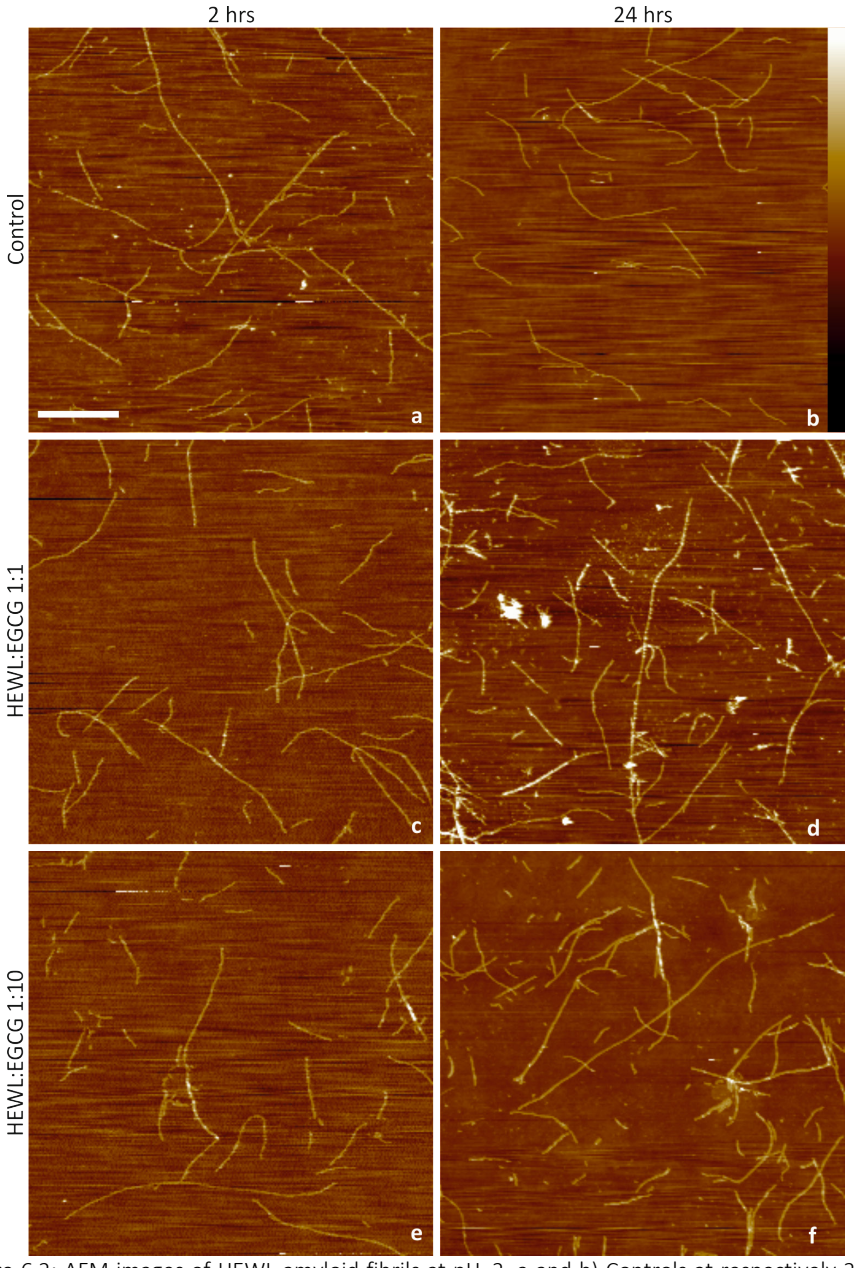

Figure 6.2: AFM images of HEWL amyloid fibrils at pH=2. a and b) Controls at respectively 2 and 24 hrs; c and d) Incubation with EGCG in 1:1 molar ratio HEWL:EGCG for 2 and 24 hrs ; e and f) Incubation with EGCG in 1:10 molar ratio HEWL:EGCG for 2 and 24 hours. Scale is the same for all images, scale bar is 2 µm, AFM height bar (right hand side of panel (b)) is 20 nm.

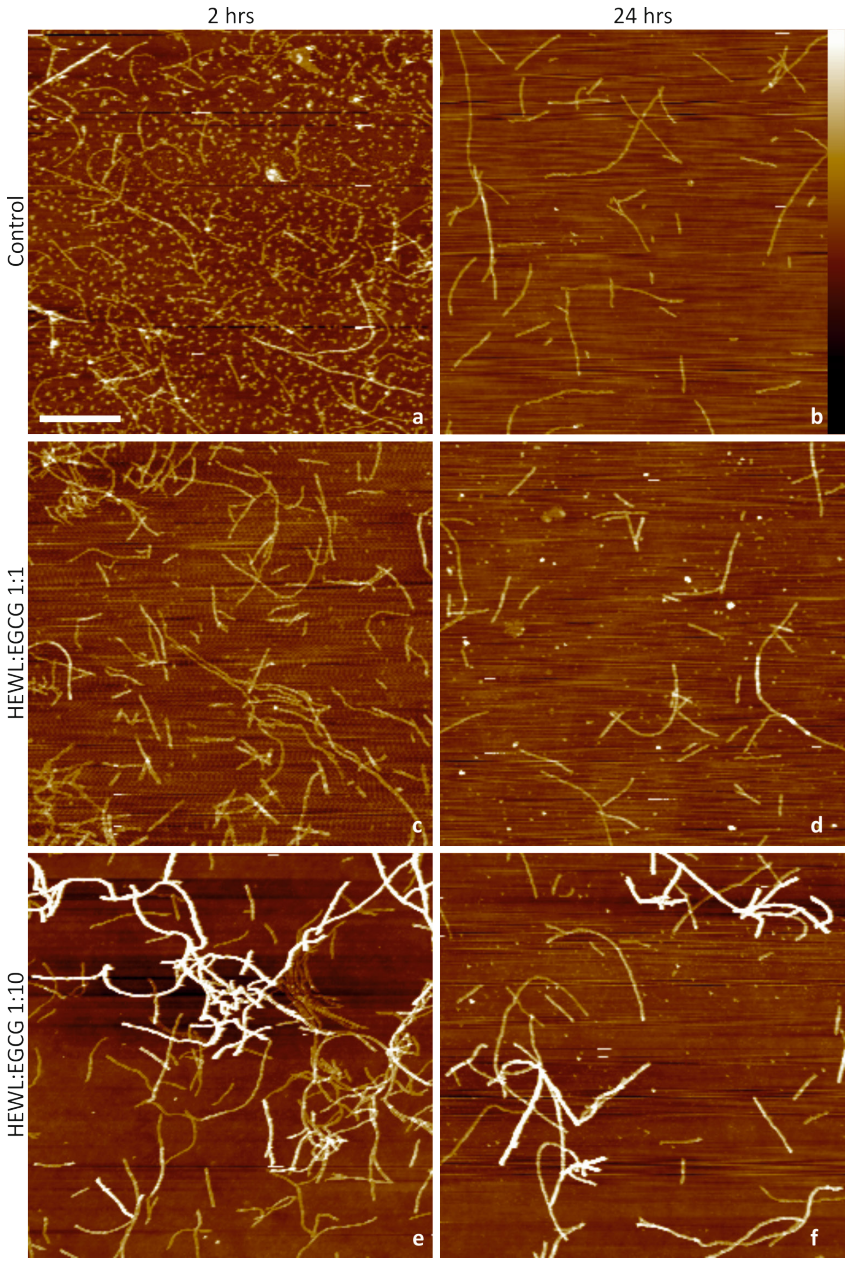

Figure 6.3: AFM images of HEWL amyloid fibrils at pH=7. a and b) Controls at respectively 2 and 24 hrs; c and d) Incubation with EGCG in 1:1 molar ratio HEWL:EGCG for 2 and 24 hrs ; e and f) Incubation with EGCG in 1:10 molar ratio HEWL:EGCG for 2 and 24 hours. Scale is the same for all images, scale bar is 2 µm, AFM height bar (right hand side of panel (b)) is 20 nm.

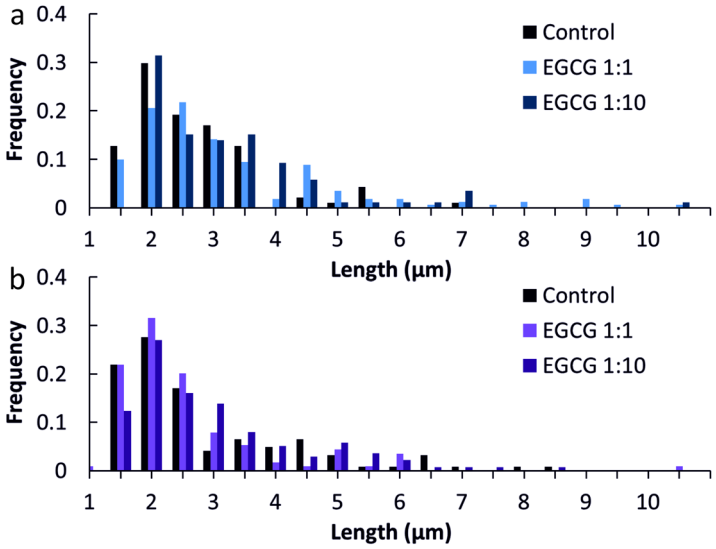

Figure 6.4: Length distributions of fibrils incubated for 24 hrs with EGCG in a 1:1 or 1:10 molar ratio HEWL:EGCG. a) Fibrils at pH=2. b) Fibrils at pH=7.

To investigate the effect of EGCG on the morphology of the fibrils in more quantitative detail, we measured the contour lengths and diameters of the fibrils by image analysis. Both at pH=2 and pH=7, the fibrils show a broad length distribution, with an average length of approximately 2 µm (Figure 6.4 and Table 6.1). The contour length did not change upon incubation with EGCG at either pH condition. For fibrils at pH=2, the average diameter was 3.7 ± 1.1 nm and remained unchanged upon incubation with EGCG (Figure 6.5a and Table 6.1). The fibrils at pH=7 had a similar diameter distribution with an average of 4.6 ± 1.4 nm (Figure 6.5b and Table 6.1). Upon incubation with EGCG, the diameter distribution of the fibrils at pH=7 shifts to higher values. The average diameter upon incubation with EGCG in a 1:1 molar ratio for 24 hrs increases to 5.6 ± 1.2 nm. Upon incubation with EGCG in a 1:10 molar ratio for 24 hrs, the average diameter increases even more, to 7.7 ± 1.4 nm. Although there were still thin fibrils present, a broad distribution of diameters was observed, with the thickest fibrils having diameters larger than 15 nm, indicating the formation of a new population of fibrils.

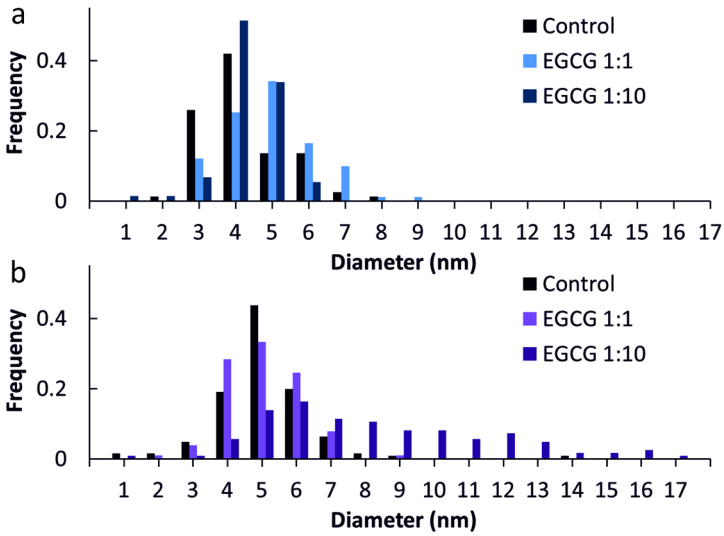

Figure 6.5: Diameter distributions of fibrils incubated for 24 hrs with EGCG in a 1:1 or 1:10 molar ratio HEWL:EGCG. a) Fibrils at pH=2. b) Fibrils at pH=7.

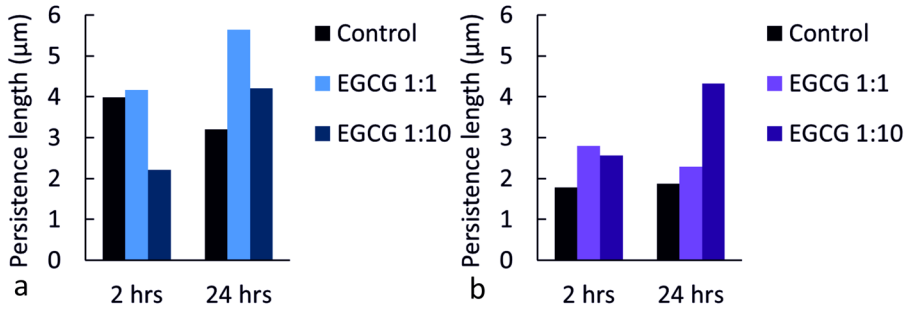

Figure 6.6: Persistence length of HEWL fibrils incubated for 2 or 24 hrs with no EGCG or with EGCG in a 1:1 or 1:10 HEWL:EGCG molar ratio at a) pH=2; b) pH=7.

Since the presence of the thick fibrils was the most striking change upon incubation with EGCG, we analyzed the surface topography of these thick fibrils more closely. The thick fibrils are composed of thin fibrils twisted together with a periodicity of approximately 120 nm (Figure 6.7b). We also observed a population of twisted fibrils in control samples, but these had a smaller diameter of around 6 nm and a smaller periodicity of approximately 90 nm. Previous AFM studies showed the presence of flat, ribbon-like fibrils of HEWL composed of up to 16 protofilaments upon incubation at pH=2 and 90°C.[22] However, these fibrils are clearly different in size and morphology than the twisted fibrils we observe in the presence of EGCG.

Table 6.1: Overview of the effect of incubation with EGCG in 1:1 or 1:10 molar ratio HEWL:EGCG on average contour length, diameter and persistence length of fibrils at pH=2 or pH=7. Average contour lengths and diameters are based on more than 86 fibrils per condition. For persistence length calculations only fibrils longer than 2 µm were used, the number of analyzed fibrils is indicated.

pH	EGCG	Incubation time (hrs)	Contour length (µm)	Diameter (nm)	Persistence length (µm)	# fibrils analyzed for persistence length
2	No EGCG	2			4.0	53
		24	1.9 ± 1.1	3.7 ± 1.1	3.2	50
2	1:1	2			4.2	38
		24	2.5 ± 1.7	4.4 ± 1.2	5.6	46
2	1:10	2			2.2	54
		24	2.5 ± 1.5	3.8 ± 0.9	4.2	34
7	No EGCG	2			1.8	65
		24	2.0 ± 1.4	4.6 ± 1.4	1.9	68
7	1:1	2			2.8	56
		24	1.9 ± 1.4	5.6 ± 1.2	2.3	66
7	1:10	2			2.6	53
		24	2.3 ± 1.4	7.7 ± 3.2	4.3	44

To investigate whether the change in diameter upon incubation with EGCG affects the bending rigidity of the fibrils, we determined the persistence length based on AFM images of a large ensemble of fibrils. Fibrils were imaged on glass, because in a parallel study we found evidence that the HEWL fibrils can equilibrate their conformations before adsorbing onto the surface (see also Chapter 7). This assumption is qualitatively validated by the absence of looped conformations. For all samples, only fibrils with a length over 2 µm were used in the analysis, to ensure that the transverse undulations of the fibrils are detectable by AFM. We analyzed the average mean-square angle $\langle \Theta^2 \rangle$ of dried fibrils as a function of the fibril contour length. The dependence was fitted by a theoretical model for semiflexible polymers, according to which $\langle \Theta^2(s) \rangle_{2D} = C/L_p$, where *s* is the segment length, *C* is the contour length and L_p is the persistence length[23]. For fibrils at pH=2, we obtained an average persistence length of 3.2 µm, similar to our observations in Chapter 7 and slightly higher than values reported in literature for HEWL amyloid fibrils formed under similar conditions[24]. Although we did not observe an effect of EGCG on the diameter at pH=2, the persistence length did appear to change slightly upon incubation in a 1:10 molar ratio for 2 hrs (2.2 µm) but not after incubation for 24 hrs (4.2 µm) (Figure 6.6a and Table 6.1).

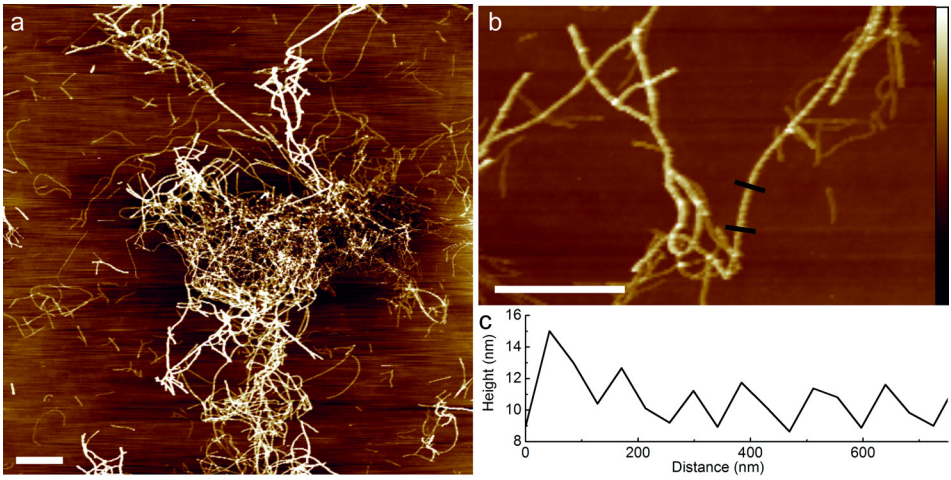

Figure 6.7: a) AFM image of fibrils incubated with EGCG at a 1:10 molar ratio EGCG:HEWL at pH=7 for 2 hrs. Scale bar is 2 µm, height bar (shown in (b)) is 20 nm. b) Zoom-in of thick fibrils formed upon incubation with EGCG at a 1:10 molar ratio for 2 hrs. Scale bar is 2 µm, height bar is 20 nm. c) Periodicity in height of the fibril section delimited by the black lines of the fibril in (b). The height fluctuations show a periodicity of approximately 120 nm. Thin fibrils in the same image do not show a periodicity.

The average persistence length of fibrils at pH=7 is 1.8 µm, approximately twice as low as at pH=2 (Figure 6.6b and Table 6.1). It is possible that the structure of the fibrils changes upon the change of pH, resulting in less rigid fibrils. Additional measurements of the persistence length in solution by time-lapse fluorescence imaging could help to settle this issue. Upon incubation with EGCG in a 1:1 molar ratio, the persistence length increases slightly compared to the control case, both for incubation times of 2 and 24 hrs. Incubation with EGCG in a 1:10 molar ratio results in a pronounced increase of the persistence length compared to the control case. After 2 hrs, the persistence length is increased from 1.8 µm to 2.6 µm, and after 24 hrs it is increased to 4.3 µm. These increases likely reflect the presence of the population of thick fibrils that was observed upon incubation with EGCG in a 1:10 molar ratio. It would be interesting to determine the persistence length of the population of thick fibrils separately, and compare this to the persistence length of the thin fibrils. However, it is complicated to compare these two populations using the method based on AFM images, because a large proportion of the thick fibrils forms aggregates. In future, the persistence length of this thick fibril population could be determined by the analysis of the undulations of freely fluctuating fibrils in water, as described in Chapter 7.

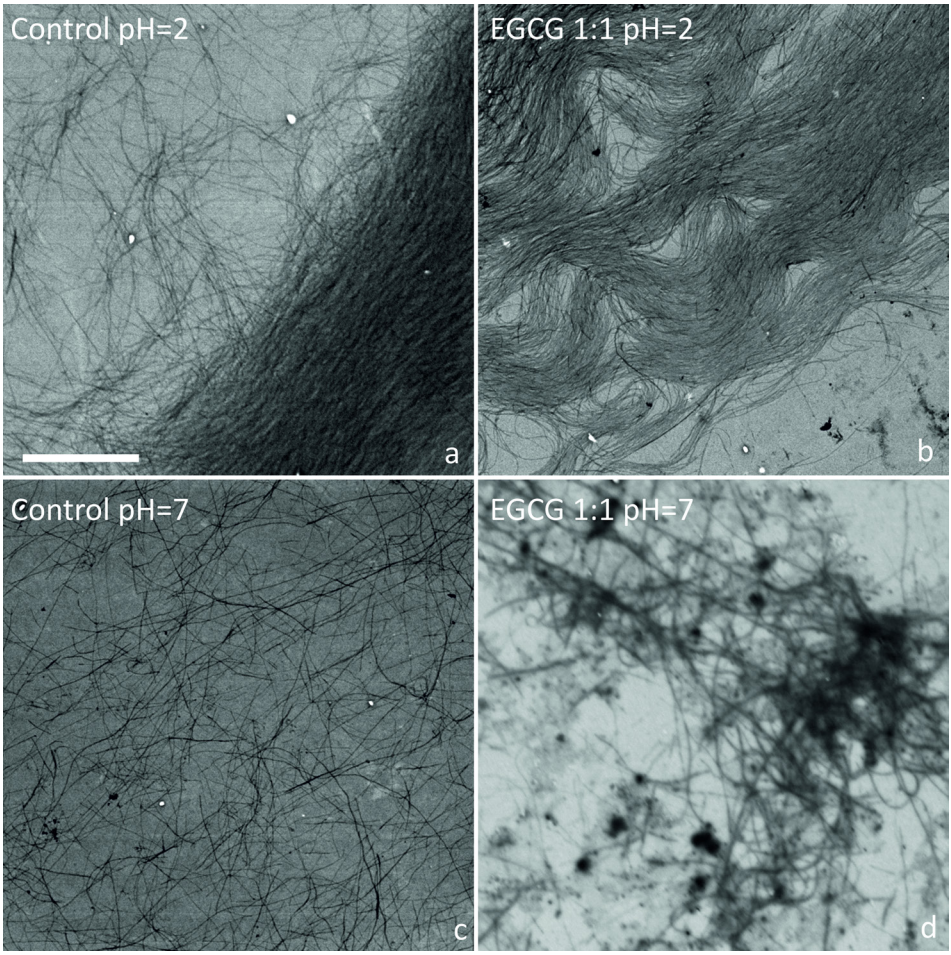

Figure 6.8: Scanning transmission electron microscopy (STEM) images of HEWL amyloid fibrils at a and b) pH=2 or c and d) pH=7. Fibrils in b and d were incubated with EGCG in a HEWL:EGCG 1:1 molar ratio for 24 hrs. At pH=2, no effect of EGCG is observed, while at pH=7 thick fibrils forming fibril aggregates (arrow 1 in (d)) and dense aggregates (arrow 2 in (d)) are observed.

AFM imaging at pH 7 revealed a few large aggregates that were mainly composed of thick fibrils (Figure 6.7a). These aggregates were not observed in any of the samples (with or without EGCG) at pH=2 or in the control samples at pH=7. The aggregation suggests that the surface of the thick fibrils may be changed upon incubation with EGCG, resulting in stronger interactions between the fibrils. Because with AFM only relatively small sample areas can be imaged, we investigated the formation of the large fibril aggregates more extensively using scanning transmission electron microscopy (STEM). Figure 6.8a shows a STEM image of control fibrils at pH=2. The fibrils are

variously distributed on the surface, being more randomly distributed in some places and bundled and aligned in other places. After incubation with EGCG in a 1:1 molar ratio for 24 hrs, the samples look similar in STEM, and no aggregates were observed (Figure 6.8b). At pH=7, the control fibrils formed a fine, isotropic network (Figure 6.8c). In the control sample, no aggregates were observed. However, upon incubation with EGCG in a 1:1 molar ratio for 24 hrs, the morphology of the network changed. Large fibril aggregates were observed (Figure 6.8d), mainly containing thick fibrils. The formation of fibril aggregates at pH=7 was observed previously for HEWL fibrils incubated with EGCG in a molar ratio of 5:1 (HEWL:EGCG) for 2 hrs.[25] However, in that study the fibril suspension was not filtered before incubation with EGCG, which makes it difficult to conclude whether the aggregates were formed from monomers, oligomers or mature fibrils. Besides the fibril aggregates, we observed also dense clusters in the STEM images of fibrils incubated with EGCG at pH=7. Similar clusters were also observed in STEM images of fibrils formed from β-lg without the presence of EGCG.

The observations that the morphology and persistence length of the fibrils changes and the fibrils form aggregates upon incubation with EGCG at pH=7 raises the question whether it is possible to observe a macroscopic change in network rheology. To test this, we measured the shear-rate dependent viscosity of the fibril suspensions (Figure 6.9a and b). The suspensions all exhibited strong shear-thinning behavior over the large range of shear rates that we measured (from 10^{3} to 10^{-3} s^{-1}), similar to suspensions of amyloid fibril suspensions formed from β-lactoglobulin (Chapter 8). Fibril suspensions at pH=2 incubated with EGCG in a 1:1 or 1:10 molar ratio did not show changes in viscosity. The fibril suspension at pH=7 showed a similar shear rate dependent viscosity as the control sample at pH=2. Upon incubation with EGCG in a 1:1 molar ratio, no changes in viscosity were observed. However, upon incubation in a 1:10 molar ratio, the low-shear viscosity decreased while the high-shear viscosity was unchanged. To compare the results of fibrils at pH=2 and pH=7, we plotted the viscosities measured at low (10^{-3} s^{-1}) and high (10^{3} s^{-1}) shear rate for all different conditions in Figure 6.9c and d. The low-shear viscosity decreases slightly for fibrils incubated with EGCG in a 1:10 molar ratio for 24 hrs, while the high-shear viscosity remains constant. This observation suggests that the direct interactions between fibrils, which contribute to the low-shear but not the high-shear viscosity, may be subtly changed. In principle, adhesive interactions would be expected to increase the low-shear viscosity. However, fibril aggregation and the resulting sample inhomogeneity may reduce the viscosity. Using rheology alone we cannot separate these effects.

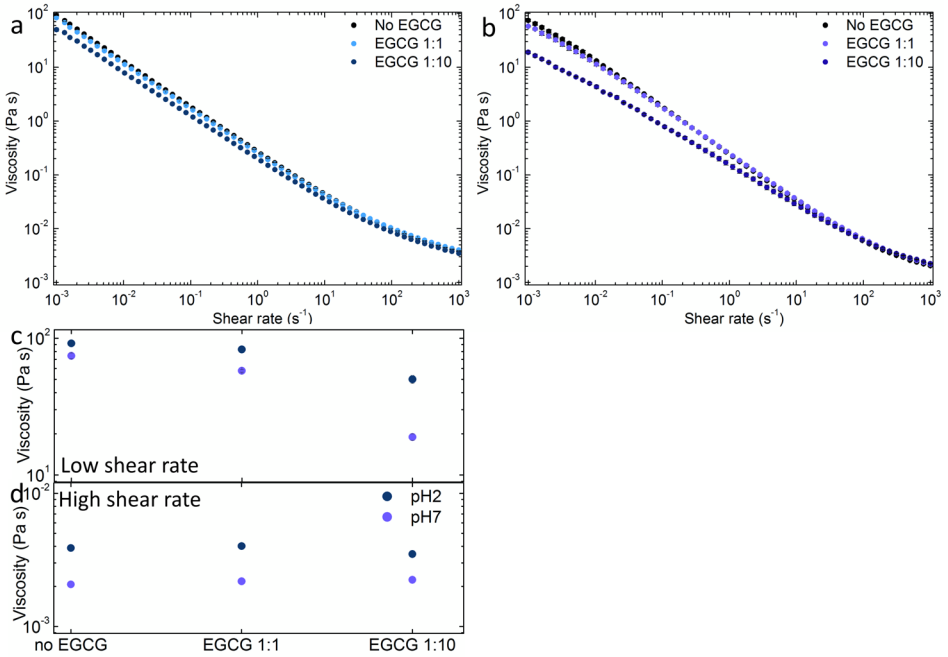

Figure 6.9: Shear rate dependent viscosity of suspensions of HEWL fibrils at a) pH=2 and b) pH=7, incubated without or with EGCG in a 1:1 or 1:10 HEWL:EGCG molar ratio for 24 hrs. c and d) Viscosities measured at low (10^{-3} s^{-1}) and high (10^{3} s^{-1}) shear rate, respectively, for fibril suspensions at pH=2 and pH=7. Error bars are smaller than the size of the symbols.

Several studies reported the formation of large amorphous aggregates upon incubation of mature amyloid fibrils with EGCG for a variety of proteins and peptides.[9,13,25] These results are reminiscent of our observation of the formation of large fibril aggregates upon incubation of HEWL fibrils with EGCG at pH=7. We show that the aggregates are mainly composed of thick fibrils. The thick fibrils are presumably bundles of amyloid fibrils. This is in agreement with a previous study of α-synuclein showing that EGCG treatment did not reverse the amyloid formation process, but directly bundled fibrils into thick fibrils and aggregates[9]. It was shown using fluorescence microscopy that upon incubation of red and green fluorescently labeled fibrils with EGCG, aggregates predominantly labeled by either the green or the red fluorophores were formed. It was proposed that the aggregates are less toxic to cells than the fibrils.[9] It has been shown that EGCG can interact with proteins and amyloid fibrils via charge-charge interactions[18] and π-π stacking interactions[14,19]. At pH=2, charge-charge interactions are unlikely, because both the amino acids and EGCG are protonated under acidic conditions. This may explain why we do not see any effect of EGCG on amyloid fibrils at pH=2, while there is a strong effect observed at pH=7.

Conclusions

We investigated the effect of EGCG on the morphology and bending rigidity of HEWL amyloid fibrils at pH=2 and pH=7. At pH=2, no effect of EGCG was observed, even after incubation for 24 hrs with a tenfold molar excess of EGCG. However, incubation with EGCG at pH=7 resulted in the formation of a subpopulation of thick fibrils. The thick fibrils with diameters up to 17 nm formed large fibril aggregates. At a molar ratio of 1:10 HEWL:EGCG, these thick fibrils were already observed after 2 hrs. No effect of EGCG on the contour length was observed, but the average diameter of HEWL fibrils increased from 4.6 ± 1.4 nm to 7.7 ± 3.2 nm in a dose-dependent manner. Also the average persistence length increased upon incubation with EGCG in a 1:10 molar ratio, from 1.9 µm to 4.3 µm upon incubation for 24 hrs. Large fibril aggregates and thick fibrils were also observed in STEM images of fibrils incubated with EGCG at pH=7, both upon incubation in a 1:1 molar ratio for 24 hrs and in a 1:10 molar ratio for 2 hrs. The low-shear viscosity decreased slightly upon incubation with EGCG in a 1:10 molar ratio for 24 hrs, likely due to the formation of thick fibril bundles and fibril aggregates. It is likely that charge-charge interactions between EGCG and the fibrils play an important role in the aggregation and bundling of fibrils since no effect of EGCG was observed at pH=2, when the amino acid residues are protonated, while EGCG was able to bundle amyloid fibrils at pH=7. More detailed follow-up studies of the effects of EGCG on the molecular packing structure of the fibrils and surface composition are needed to clarify how EGCG affects fibril morphology and organization. Such studies are a prerequisite to understand how EGCG may act as a potential therapeutic agent to combat amyloid-related diseases.

Materials and methods

Amyloid formation and incubation with EGCG. Hen egg white lysozyme powder (HEWL, Sigma Aldrich cat # 62970) was dissolved in an aqueous HCl solution (pH=2.0) and the pH was immediately adjusted to pH=2.0. HEWL was dissolved by stirring the solution for 1 hr at 4°C. To remove traces of electrolytes, the solution was dialyzed against a HCl solution (pH=2.0) at 4°C using a slide-a-lyzer (Thermo Scientific cat. #87732) with a molecular weight cut-off (MWCO) of 10 kDa. Aggregates were removed by filtration with a 0.1 µm filter (Sigma Aldrich #F7523). The protein concentration was calculated based on measurements of light absorption at 280 nm with a Nanodrop spectrophotometer (Thermo Scientific), using an extinction coefficient of 37,752 $M^{-1} cm^{-1}$.[26] Amyloid fibrils were formed by incubation of 30 mL of the monomer solution at a concentration of 1 mM in a polypropylene tube in an oven at 65°C for 7 days, while the solution was stirred using a magnetic stirrer. After 7 days, samples were quenched on ice water and fibrils were separated from small aggregates and monomers by filtration

using centrifugal filters (Amicon, Millipore cat.#UFC910024) with a MWCO of 100 kDa. Prewashed filters were centrifuged at 1000 g for 30 min and samples were subsequently washed 3 times with a HCl solution (pH=2.0) by repeating the centrifugation. For experiments at pH=7, the washing steps were performed with water instead of a HCl solution. No buffer was used, because it has been observed that fibrils aggregate in the presence of salts. EGCG powder (Sigma Aldrich cat # E4143) was dissolved in MilliQ or a HCl solution at pH=2. EGCG solutions were prepared freshly before each experiment to prevent degradation[27]. Amyloid fibrils were incubated with EGCG in a 1:1 or 1:10 molar ratio HEWL:EGCG for 2 or 24 hrs at room temperature in dark to prevent photodegradation[28].

Atomic Force Microscopy (AFM). Filtered fibril suspensions were diluted to protein concentrations of approximately 1 µM and 15 µL of the suspension was incubated on glass cover slips cleaned with isopropanol. After 3 minutes, the slides were washed with HCl solution at pH=2.0, and dried in air. Atomic force microscopy imaging was performed on a Dimension 3100 Scanning Probe Microscope (Bruker) using silicon cantilevers (TESPA, force constant 42 N/m, Bruker). All images were flattened using Nanoscope 6.14 software. The fibrils were manually tracked using the Simple Neurite Tracer plugin in Fiji.[29]

Scanning transmission Electron Microscopy (STEM). Fibril suspensions were diluted to peptide concentrations of 10 µM. Samples for STEM were prepared by incubation of 1 µL of the fibril suspension on a carbon coated copper grid with 300 µm mesh size (TED PELLA INC) for 5 min. Excess liquid was removed, the samples were washed with MilliQ water and dried in air. Scanning transmission electron microscopy was performed on a Verios 460 microscope (FEI) operating at 5 kV. Images were obtained in bright field. The image contrast was enhanced using ImageJ software.

Rheology. A stress-controlled rheometer (Physica MCR 501, Anton Paar) with steel cone (30 mm diameter, 1° angle) and plate thermostatted with a Peltier plate were used for rheometry. Evaporation was reduced by closing off the geometry with a cover during measurements. The nonlinear rheology was determined by measurement of the viscosity as a function of shear rate, with shear rates ramping down from 10^3 to 10^{-3} s^{-1}. All measurements were performed at T=21°C. All experiments were performed at least twice, error bars show the standard deviation.

Acknowledgment

The authors thank Norbert Mücke (DKFZ Heidelberg, Germany) for providing software for persistence length calculations and Andries Lof (FOM Institute AMOLF, The Netherlands) for assistance with STEM imaging. This work is part of the Industrial Partnership Programme (IPP) Bio(-Related) Materials (BRM) of the Stichting voor Fundamenteel Onderzoek der Materie (FOM), which is financially supported by the Nederlandse Organisatie voor Wetenschappelijk Onderzoek (NWO). The IPP BRM is co-financed by the Top Institute Food and Nutrition and the Dutch Polymer Institute.

References

(1) Dobson, C. M. *Nature* 2003, *426*, 884.
(2) Stefani, M.; Dobson, C. M. *Journal of Molecular Medicine* 2003, *81*, 678.
(3) Chiti, F.; Dobson, C. M. *Annual Review of Biochemistry* 2006, *75*, 333.
(4) Bieschke, J. *Neurotherapeutics* 2013, *10*, 429.
(5) Attar, A.; Rahimi, F.; Bitan, G. *Translational Neuroscience* 2013, *4*, 385.
(6) He, J.; Xing, Y. F.; Huang, B.; Zhang, Y. Z.; Zeng, C. M. *Journal of Agricultural and Food Chemistry* 2009, *57*, 11391.
(7) Jayasena, T.; Poljak, A.; Smythe, G.; Braidy, N.; Münch, G.; Sachdev, P. *Ageing Research Reviews* 2013, *12*, 867.
(8) Bieschke, J.; Russ, J.; Friedrich, R. P.; Ehrnhoefer, D. E.; Wobst, H.; Neugebauer, K.; Wanker, E. E. *Proceedings of the National Academy of Sciences of the United States of America* 2010, *107*, 7710.
(9) Lopez del Amo, J. M.; Fink, U.; Dasari, M.; Grelle, G.; Wanker, E. E.; Bieschke, J.; Reif, B. *Journal of Molecular Biology* 2012, *421*, 517.
(10) Meng, F.; Abedini, A.; Plesner, A.; Verchere, C. B.; Raleigh, D. P. *Biochemistry* 2010, *49*, 8127.
(11) Norton, R. S.; Chandrashekaran, I. R.; Adda, C. G.; MacRaild, C. A.; Anders, R. F. *Biochemistry* 2010, *49*, 5899.
(12) Ferreira, N.; Saraiva, M. J.; Almeida, M. R. *Febs Letters* 2011, *585*, 2424.
(13) Engel, M. F. M.; vandenAkker, C. C.; Schleeger, M.; Velikov, K. P.; Koenderink, G. H.; Bonn, M. *Journal of the American Chemical Society* 2012.
(14) Palhano, F. L.; Lee, J.; Grimster, N. P.; Kelly, J. W. *Journal of the American Chemical Society* 2013, *135*, 7503.
(15) Choi, Y. T.; Jung, C. H.; Lee, S. R.; Bae, J. H.; Baek, W. K.; Suh, M. H.; Park, J.; Park, C. W.; Suh, S. I. *Life Sciences* 2001, *70*, 603.
(16) Li, M. H.; Jang, J. H.; Sun, B. X.; Surh, Y. J. In *Signal Transduction Pathways, Chromatin Structure, and Gene Expression Mechanisms as Therapeutic Targets*; Diederich, M., Ed. 2004; Vol. 1030, p 317.
(17) Ehrnhoefer, D. E.; Bieschke, J.; Boeddrich, A.; Herbst, M.; Masino, L.; Lurz, R.; Engemann, S.; Pastore, A.; Wanker, E. E. *Nature Structural & Molecular Biology* 2008, *15*, 558.
(18) Kim, H.-S.; Quon, M. J.; Kim, J.-a. *Redox Biology* 2014, *2*, 187.
(19) Ozdal, T.; Capanoglu, E.; Altay, F. *Food Research International* 2013, *51*, 954.
(20) Porat, Y.; Abramowitz, A.; Gazit, E. *Chemical Biology & Drug Design* 2006, *67*, 27.

(21) Frare, E.; Polverino de Laureto, P.; Zurdo, J.; Dobson, C. M.; Fontana, A. *Journal of Molecular Biology* **2004**, *340*, 1153.
(22) Ghosh, S.; Pandey, N. K.; Dasgupta, S. *International Journal of Biological Macromolecules* **2013**, *54*, 90.
(23) Lara, C. c.; Adamcik, J.; Jordens, S.; Mezzenga, R. *Biomacromolecules* **2011**, *12*, 1868.
(24) Mücke, N.; Kreplak, L.; Kirmse, R.; Wedig, T.; Herrmann, H.; Aebi, U.; Langowski, J. *Journal of Molecular Biology* **2004**, *335*, 1241.
(25) Lara, C.; Usov, I.; Adamcik, J.; Mezzenga, R. *Physical Review Letters* **2011**, *107*, 238101.
(26) Mishra, R.; Sorgjerd, K.; Nystrom, S.; Nordigarden, A.; Yu, Y. C.; Hammarstrom, P. *Journal of Molecular Biology* **2007**, *366*, 1029.
(27) Sang, S. M.; Lee, M. J.; Hou, Z.; Ho, C. T.; Yang, C. S. *Journal of Agricultural and Food Chemistry* **2005**, *53*, 9478.
(28) Bianchi, A.; Marchetti, N.; Scalia, S. *Journal of Pharmaceutical and Biomedical Analysis* **2011**, *56*, 692.
(29) Longair, M. H.; Baker, D. A.; Armstrong, J. D. *Bioinformatics* **2011**.

Chapter 7

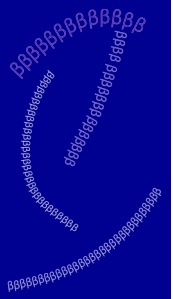

Measuring the bending rigidity of amyloid fibrils in solution

Based on: Corianne C. van den Akker, Floortje P. van de Poll, Paul J. Atzberger, Gijsje H. Koenderink (submission in preparation).

Abstract

Amyloid fibrils are fibrillar protein aggregates formed from (partly) unfolded proteins or peptides. They possess a high mechanical stiffness and strength, making them interesting candidates for applications in materials science or food texturing. A common measure of the mechanical properties of semiflexible fibers such as amyloids is the persistence length, L_p, which characterizes the bending rigidity. L_p has been determined for a variety of amyloid fibrils based on electron microscopy or atomic force microscopy imaging of an ensemble of fibrils immobilized on a flat support. However, deposition and drying of protein fibrils on a surface can potentially affect their conformation and structure. Furthermore, because measurements are averaged over a large number of fibrils, it is not possible to identify the polymorphism of amyloid fibrils. Here we determined the persistence length of amyloid fibrils formed from hen egg white lysozyme (HEWL) using two different approaches. The first approach was the standard atomic force microscopy approach, which involves imaging of a large ensemble of fibrils combined with image analysis to obtain the fiber conformations. We observed an average persistence length ranging between 2.5 and 4.4 μm, depending on the surface (mica or glass) on which the fibrils were immobilized and on fibril hydration. The second approach was to obtain time-lapse movies by fluorescence microscopy of the thermal bending undulations of freely fluctuating fibrils suspended in water. We observed a strikingly large variation in the persistence length of individual fibrils. For 8 fibrils, the persistence length varied between 0.7 to 6.7 μm, and for 2 fibrils the persistence length was even too large to measure by video microscopy. In summary, the two different techniques give similar average values of L_p in the range of several micrometers, but time-lapse imaging reveals a large variability for fibrils within the same sample. This variability is a signature of the structural polymorphism of amyloid fibrils.

Introduction

Amyloid fibrils are a broad class of biopolymers that can form by self-assembly from peptides or proteins that are in an unfolded or misfolded state.[1] It is thought that almost every (poly)peptide will form amyloids under appropriate conditions.[1] Some amyloids are associated with diseases like Alzheimer's disease and type II diabetes mellitus[2], where oligomers or fibrils are thought to damage the plasma membrane of cells, thus causing cell death.[3,4] The large mechanical stiffness of amyloid fibrils may contribute to their cytotoxicity.[4,5] Biophysical experiments have shown that amyloid fibrils behave as micron-sized semiflexible polymers with a persistence length that is comparable to their contour length.[6,7] Interestingly, Nature also makes functional use of this stiffness, using benign amyloid fibrils as a structural material for bacterial biofilms and protective shells of certain insect eggs.[8,9] Amyloid fibrils have excellent mechanical properties when compared to other biological and synthetic materials: their Young's modulus is comparable to that of silk and their ultimate tensile strength is comparable to that of steel.[6] Theoretical modeling suggests that these extraordinary mechanical properties mainly derive from the strongly hydrogen-bonded cross-β sheet structure that extends along the backbone of the fibrils.[7] The outstanding mechanical performance of amyloid fibrils coupled with the fact that amyloids can be formed from a wide range of peptide sequences implies that they can be useful for diverse applications. Fibrils formed from food-related proteins are for instance relevant for food texturing.[10] Furthermore, applications in nanostructured materials such as metalized nanowires and in tissue engineering have been suggested.[11-15]

Until now, the stiffness of amyloid fibrils has been investigated mainly by analysis of the conformation of an ensemble of fibrils deposited on a surface and imaged by atomic force microscopy (AFM) or (cryo-)electron microscopy (EM).[16-19] Assuming that the fibrils can be modeled as semiflexible polymers, the bending rigidity can be inferred from the persistence length L_p, which itself follows from the relation between the contour length C and the end-to-end distance E of the fibrils or from the tangent-tangent correlation function. This AFM/EM-based approach provides a global measure of the persistence length of a fibril, because the effect of thermal fluctuations on the chain conformation is evaluated on a large length scale. The AFM/EM-imaging based approach has two important drawbacks. First, the conformation of fibrils adsorbed on a surface is dependent on the strength of the interaction of the fibrils with the surface, as demonstrated by Brownian dynamics simulations and experiments on intermediate filaments and DNA chains adsorbed on different surfaces.[20,21] Second, the fibrils are often dried before imaging, which may affect the morphology and internal structure of the fibrils and thereby their stiffness. A further complicating factor is the well-known

polymorphism of amyloid fibrils, both in length, diameter and internal molecular packing structure.[22] This factor makes it difficult to interpret an average stiffness value based on AFM or EM measurements on an ensemble, and also complicates the interpretation of stiffness measurements obtained by bulk solution techniques such as light or X-ray scattering[23] and rheology[24].

One way to overcome this problem is to actively bend single amyloid fibrils that are deposited across nanoscale grooves using an AFM tip, an approach that has been demonstrated with insulin amyloid fibrils.[6,7] Based on the measured force-distance curves, the bending rigidity and maximal force before breakage could be calculated. An advantage of this technique is that the fibrils are measured in their natural, hydrated state. However, the experiments are technically challenging because of the small diameter of the fibrils.[25] A technically less demanding method to obtain the bending rigidity of fibrils in suspension is to take time-lapse movies of freely fluctuating fibrils in solution by fluorescence microscopy. Rather than extracting the persistence length from the static shapes of an ensemble of fibrils, the persistence length is determined for a single fibril by tracking its shape fluctuations over time. To our knowledge, there is one study where this method was used for amyloid fibrils.[26] The method revealed average persistence lengths of 3.6 and 7.0 μm for two different types of yeast prion amyloid fibrils with contour lengths between 3 and 10 μm and a diameter of 4.5 nm. Force-extension experiments with optical tweezers reported in the same study revealed average persistence lengths of 1.5 and 3.3 μm, respectively. It is possible that the discrepancy is related to structural polymorphism, which is common for amyloid fibrils and should lead to variability in persistence lengths. In addition to the bending rigidity, time-lapse imaging of thermally fluctuating filaments can also reveal the bending dynamics, as demonstrated for actin filaments and microtubules[27-31], as well as carbon nanotubes[32] and DNA nanotubes[33].

Here we investigate the bending rigidity of single amyloid fibrils formed from the model protein hen egg white lysozyme (HEWL), comparing the time-lapse imaging approach where shape fluctuations of single fibrils in solution are analyzed with the more well-established AFM approach of analyzing the shapes of an ensemble of fibrils immobilized on a flat substrate. We perform AFM imaging on dried as well as hydrated fibrils, and compare measurements obtained on two different surfaces, mica and glass. With all analysis methods, we find persistence lengths in the micrometer range. However, the time-lapse imaging approach reveals a remarkable variability of the persistence length among different fibrils, ranging from 0.7 and 6.7 μm for a collection of 8 representative fibrils. This large variability indicates structural polymorphism of fibrils formed under the same conditions.

Results and discussion

To investigate the morphology of the HEWL amyloid fibrils, we performed AFM imaging of fibrils deposited on mica and dried in air. Figure 7.1a shows an AFM image of fibrils formed from HEWL incubated at pH=2.0 and 65°C. The contour length distribution is broad with an average value of 2.6 ± 2.0 µm based on measurement of 275 fibrils (Figure 7.1b). The distribution of the fibril diameters, obtained from the fibril heights, is plotted in Figure 7.1c, showing two distinct populations: one centered around 3.5 nm and another centered around 6 nm. The average diameter was 3.6 ± 1.2 nm, based on diameter measurements on 189 fibrils. The fibrils with diameters around 6 nm are twisted and show a periodicity of approximately 90 nm. These results show that the amyloid sample is polymorphic both in length and diameter. To investigate whether drying affects the fibril morphology, we also imaged hydrated fibrils using liquid AFM. The average diameter was similar to that of the dried fibrils, 3.4 ± 1.1 nm, based on measurements on 128 fibrils, suggesting that drying does not significantly change the morphology. The average length was 1.9 ± 1.3 µm, slightly shorter than that observed for dried fibrils. This difference may be due to a different population of fibrils that binds to the surface for liquid AFM. For liquid AFM, the fibril suspension is 10 times more concentrated compared to the experiments in air, and the binding of fibrils to the surface takes place over hours instead of minutes. The samples for AFM in air are prepared by incubation of a fibril suspension on mica for 3 min and subsequent washing and drying of the sample. Some of the amyloid fibrils are probably washed off the surface. Furthermore, the differences in sample preparation likely affect the equilibration of the fibrils that are bound to the surface. We conclude that drying does not noticeable change the fibril morphology.

We calculated the persistence length as a measure of the bending rigidity of the fibrils based on AFM images of a large ensemble of fibrils. We assume that the fibril conformations are equilibrated before the fibrils adsorb to the surface. This assumption is qualitatively validated by the absence of looped conformations. The energy necessary for creating a bend with an angle Θ in a semi-flexible fibril with a contour length C, Young's modulus Y and area moment of inertia I is given by[21]:

$$E = Y\, I\, \Theta^2 / 2C\ . \qquad (1)$$

According to the equipartition theorem, the persistence length L_p of a thermally fluctuating semiflexible fibril is[21]:

$$Y\, I = k_B\, T\, L_p \qquad (2)$$

where k_B is the Boltzmann constant and T is the temperature.

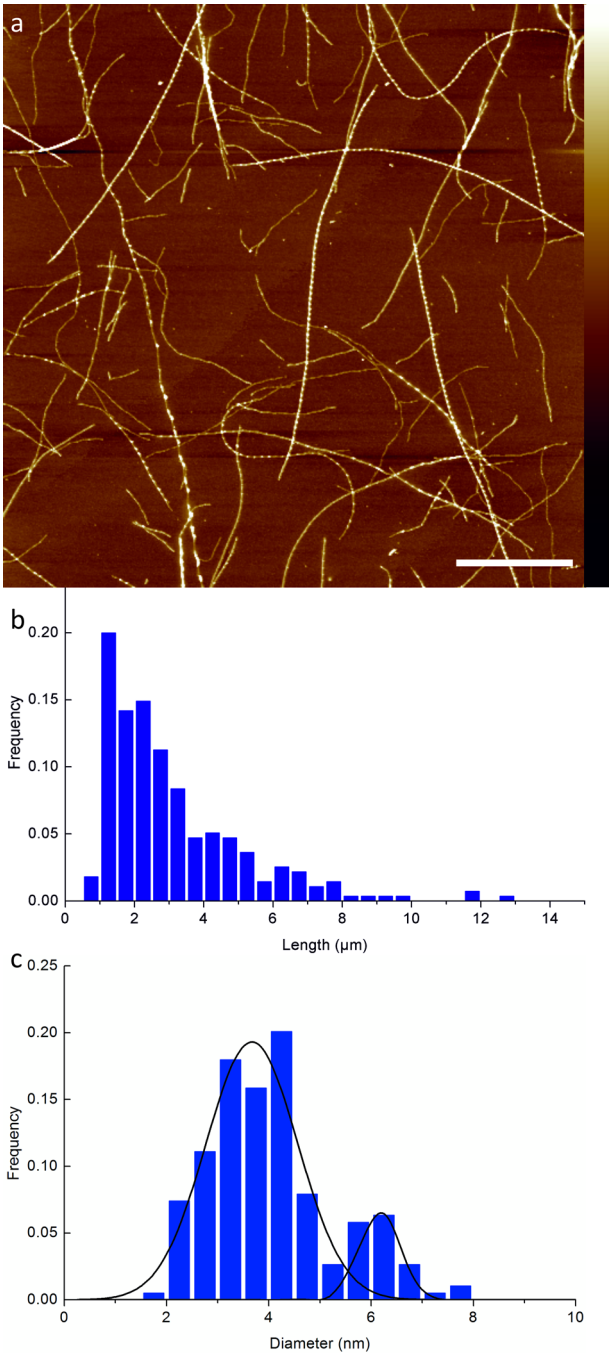

Figure 7.1: a) AFM image of dried HEWL amyloid fibrils at pH=2.0 on mica. Scale bar is 2 µm and height bar is 10 nm. b) Length distribution of 275 HEWL amyloid fibrils measured in AFM images.

c) Diameter distribution of 189 HEWL amyloid fibrils. The distribution is fitted with two Gaussian peaks (black lines).

The normalized probability distribution function in two dimensions for a semiflexible fibril bent by an angle Θ is Gaussian and can be written as[21]:

$$P(\Theta(C))_{2D} = \sqrt{\frac{L_p}{2\pi C}} e^{-L_p \Theta^2/2C} \quad (3)$$

Two different approaches are generally used to infer the average persistence length of the fibrils from an ensemble of conformations. The first approach is to calculate the ensemble-averaged mean-square angle $\langle \Theta^2 \rangle$, dependent on segment length s[21]:

$$\langle \Theta^2(s) \rangle_{2D} = \frac{C}{L_p} \quad (4)$$

The second approach is to compute L_p from the ensemble-averaged mean-square end-to-end distances $\langle E^2 \rangle$ of the fibrils[21]:

$$\langle E^2(s) \rangle_{2D} = 4L_p C \left(1 - \frac{2L_p}{C}\left(1 - e^{-C/2L_p}\right)\right) \quad (5)$$

If the fibrils are not equilibrated, the conformation depends on the surface adsorption mechanism and the model described above only yields an apparent persistence length.[21]

Table 7.1: Conformational statistics of HEWL amyloids adsorbed on either mica or glass and imaged by AFM under different conditions (dried or in liquid). The persistence lengths were computed taking into account only fibrils longer than 2 µm.

Sample	$\langle C \rangle$(µm)	$L_{p\langle \Theta^2 \rangle}$ (µm)	$L_{p\langle E^2 \rangle}$ (µm)	# of fibrils
Mica dried	4.1 ± 2.0	4.4	6.1	99
Mica liquid	3.2 ± 1.3	2.5	3.1	43
Glass dried	3.4 ± 1.3	3.8	4.6	70

We followed both approaches to analyze L_p based on AFM images of the HEWL amyloid fibrils imaged on mica. For all samples, only fibrils with a length over 2 µm were used in the analysis to ensure that the transverse undulations of the fibrils are resolvable in AFM images. The mean-square angle $\langle \Theta^2 \rangle$ of dried fibrils was plotted as a function of contour length C and fitted with equation (4) (Figure 7.2a). We found an average value of L_p of 4.8 µm for a dataset of 99 fibrils (Table 7.1). However, the linear fit is quite poor, indicating that the mica surface influences the equilibration of the fibrils[21]. A better linear fit was obtained when the offset was a free parameter (grey line in Figure 7.2a), as has been proposed before[21], although this fit is not in accordance to equation (4). This fit results in L_p = 4.4 µm, slightly lower than the value of 4.8 µm obtained with

the fit using equation (4). To investigate whether drying affects the apparent persistence length, we also analyzed the shapes of hydrated fibrils imaged on mica using liquid AFM. Based on measurements on 43 fibrils, the average persistence length was L_p = 2.5 µm for a linear fit with zero offset and L_p = 2.4 µm for a linear fit with non-zero offset. Thus, the hydrated fibrils appear two-fold more flexible than the dried fibrils. It is difficult to conclude whether this difference corresponds to a real change in fibril stiffness. As explained above, the different sample preparation protocols for liquid AFM and air-AFM may select for a different fibril population on the surface. In support of this explanation, the population of dried fibrils that was used for persistence length measurements was on average longer than that of the hydrated fibrils, with average contour lengths of respectively 4.1 ± 2.0 µm and 3.2 ± 1.3 µm. Moreover, the differences in sample preparation may also affect the binding and equilibration of fibrils on the surface. To resolve this issue, it will be interesting in future work to perform AFM-based nanoindentation to measure the Young's modulus independent of fibril conformation as has been shown before for α-synuclein amyloid fibrils[34].

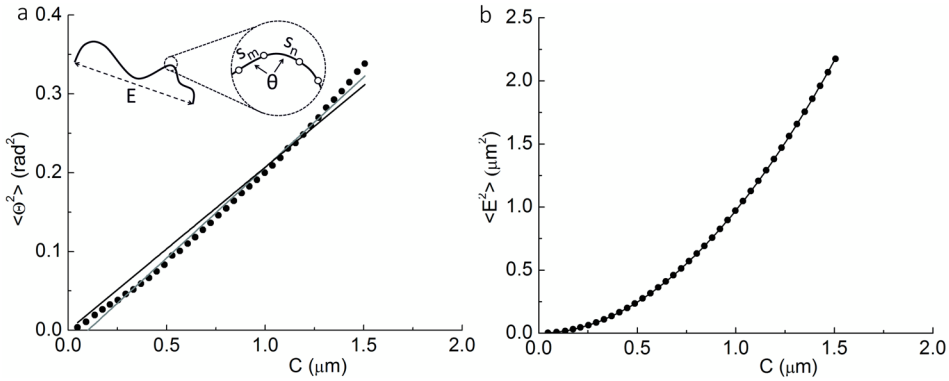

Figure 7.2: a) $\langle \Theta^2 \rangle$ as a function of contour length C of dried fibrils imaged on mica. The dataset was fitted with equation (4) (black line). Grey line is the linear fit where the offset is a free parameter. Inset shows a fibril with end-to-end length E and angle Θ between segments s_m and s_n. b) Mean-square end-to-end distance $\langle E^2 \rangle$ plotted as a function of contour length C. Black line is the fit with equation (5).

To investigate whether the surface affects the conformation of the fibrils, we compared the results obtained for fibrils adsorbed on mica with similar experiments on glass. Previous experiments with intermediate filaments showed that these filaments appeared more flexible on mica than on glass, because mica traps the fibrils on the surface before they are thermally equilibrated.[21] In total, 70 dried fibrils with an average length of C = 3.4 ± 1.3 µm were analyzed. The fit for the plot of $\langle \Theta^2 \rangle$ as a function of C using equation (4) gave an offset close to zero. For a forced-fit through zero, we found

L_p = 3.8 μm, while for a fit in which the intercept was a free parameter, L_p = 3.6 μm. This value of L_p lies in between the values measured for fibrils imaged in liquid and in air on mica. We conclude that the conformation of the amyloid fibrils imaged on mica may be affected by trapping on the surface. Therefore, to obtain a more precise measure of the persistence length from conformations measured on mica, fibril-surface interactions should be incorporated into the statistical model.

To test the sensitivity of the persistence length values on the analysis method, we also analyzed L_p for the same datasets using equation (5). The squared end-to-end length E^2 was plotted as a function of C and fitted with equation (5), as shown in Figure 7.2b for dried fibrils imaged on mica. We found L_p = 6.1 μm for dried fibrils imaged on mica and L_p = 3.1 μm for hydrated fibrils imaged in liquid on mica (Table 7.1). For dried fibrils imaged on glass, we determined L_p = 4.6 μm. For all samples the apparent L_p is larger when determined using equation (5) instead of equation (4). We anticipate that, because L_p is larger than the contour length of most of the fibrils, the analysis method based on equation (5) is less sensitive than the method based on equation (4) because it only takes into account the first bending mode. In contrast, equation (4) determines the bending of short segments of the fibril, resulting in a better estimation of L_p.

Because the confinement of the fibrils on a surface and drying can influence their apparent persistence length, we also determined the mechanical properties of fibrils freely fluctuating in liquid. The fibrils were fluorescently labeled and confined within a thin, quasi-two-dimensional layer between two non-sticky glass surfaces to ensure that the fibrils remained in focus. The sample chamber was well-sealed to prevent evaporation and fluid flows, so that only thermal forces acted upon the fibrils. Figure 7.3 shows 9 frames of a movie of a single fibril that exhibits thermal bending fluctuations. We imaged fluctuating single fibrils with lengths ranging between approximately 3 and 20 μm. Most fibrils showed only minor bending fluctuations, similar to the fibril shown in Figure 7.3.

We analyzed the images of the fibrils using statistical analysis of the time-dependent ensemble of shapes that a single fibril adopts when subjected to thermal forces[31]. The fluorescence images were analyzed based on a fibril contour representation expressed in a spectral basis of orthogonal polynomials, developed by Valdman et al.[27,28] For each image, the contour was fitted and the first 8 modes were analyzed. In Figure 7.4a, an example of the mode variances of the fluctuations of a fibril with a contour length of 3.9 μm is shown. The dashed line represents a fit to the worm-like chain model[31]. For this fibril, we analyzed 111 frames and determined L_p = 0.8 μm.

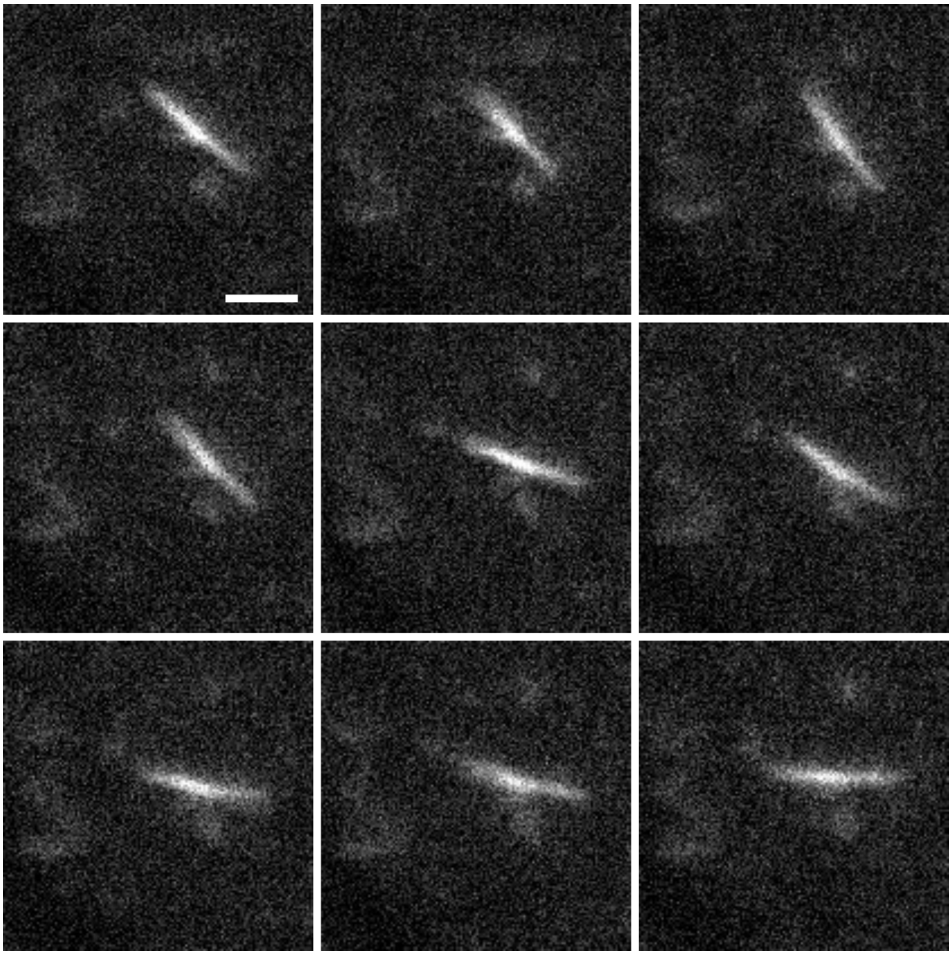

Figure 7.3: Fluorescence images of a single HEWL amyloid fibril labeled with Nile Red. Images were recorded at 4.9 fps with an exposure time of 100 ms. Time between subsequent images shown here is 0.2 s. The fibril is free to perform rotational and translational diffusion, indicating that the top and bottom glass surfaces are well passivated. Bending fluctuations are barely perceptible. Scale bar is 2 µm.

We applied this method to a total of 8 single amyloid fibrils with contour lengths between 3.4 µm and 4.7 µm. Per fibril, 46 to 280 images were analyzed to determine L_p. We obtained a range of persistence lengths between 0.7 µm and 6.7 µm (Figure 7.5 and Table 7.2). The average value of L_p for this small dataset of 8 fibrils was 2.4 µm, while the average contour length C was 3.9 ± 0.5 µm. For this analysis, two independent sources of error have to be considered. Noise in the microscopy images causes a localization error when localizing the filament contour.

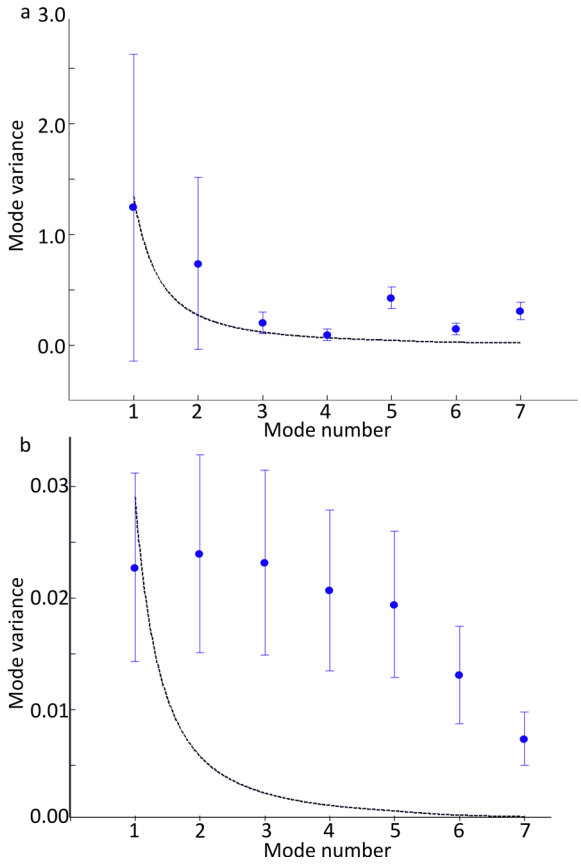

Figure 7.4: Mode variance (nondimensional) plotted as a function of mode number for the thermal fluctuations of a fibril. Dashed lines are the fits with a worm-like chain model. a) Results for a fibril with a contour length 3.9 µm and a persistence length of 0.8 µm. b) Results for a fibril with a contour length 9 µm whose bending fluctuations are too small to analyze by video tracking.

Table 7.2: Overview of the contour length, persistence length determined based on thermal fluctuations in free solution, and number of frames that was analyzed per fibril.

Fibril	C (µm)	L_p (µm)	# of images
1	3.4	0.7	97
2	3.5	1.6	325
3	3.6	1.7	46
4	3.7	2.1	238
5	3.9	0.8	111
6	4.0	1.4	104
7	4.6	6.7	129
8	4.7	4.5	280

The second source of error, the sampling error, is caused by the finite number of images which is analyzed per fibril. It was calculated that a good approximation of L_p is obtained when 100 or more images per fibril are analyzed.[27] We analyzed for 7 out of 8 fibrils more than 100 images (Table 7.2). For simulated images of a fibril with known L_p and a high noise level, a measurement uncertainty of approximately 10% for L_p has been predicted.[27] This indicates that the range of L_p that we observed for the amyloid fibrils is due to structural heterogeneity of the fibrils and not to errors in the analysis.

We also obtained time-lapse movies of two long fibrils showing no visible fluctuations. In these cases, it was impossible to determine the persistence length (Figure 7.4b). The fact that we did not observe fluctuations even though the fibrils had long lengths of 9 and 19 μm indicates that their persistence length was larger than this length scale.

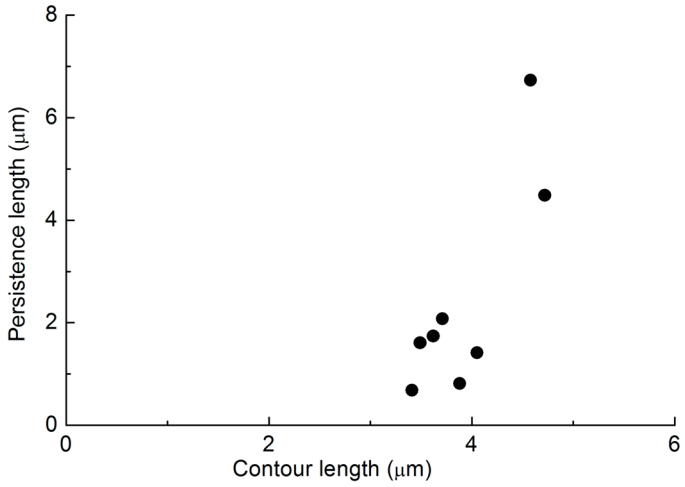

Figure 7.5: Persistence length plotted as a function of contour length for 8 individual fibrils, determined based on their spectrum of thermal fluctuations.

The average value of L_p that we obtained from time-lapse imaging of single fibrils in solution is similar to that of hydrated fibrils adsorbed on mica and slightly lower than the values measured for dried fibrils on glass. However, the dataset of the fluctuating fibrils is small (8 fibrils), so this comparison is only qualitative until we have more data. Nevertheless, we can already conclude that there is a pronounced variability in persistence length among fibrils, which probably drives the broad distribution that is also seen in AFM. This variability is not surprising given the polymorphism of the amyloid fibrils that we observe in our AFM images. For a homogeneously elastic cylindrical rod of radius r, L_p varies as r^4, indicating that polydispersity in diameter will result in a large spread of L_p. Unfortunately it is not possible to determine the diameter

of the analyzed fibrils from our fluorescent microscopy images, so we cannot conclude whether the large range of persistence lengths is related only to a variation in fibril diameter or whether the molecular packing structure of the fibrils varies too. Furthermore, we do not know the shape of the fibril cross-section. For amyloid fibrils composed of 2 or more protofilaments, ribbon-like as well as nanotube-like packings have been reported.[18,35,36] Another complicating factor is that the stiffness of fibrils comprised of multiple protofilaments may be influenced by sliding between protofilaments.[37]

It has been reported previously that L_p of amyloids fibrils formed upon incubation of HEWL for several days at pH=2.0 and T=60°C is approximately 2.5 μm.[38] This analysis was based on AFM images of dried fibrils on mica or graphite, though no differences between the surfaces were specified. Also for amyloid fibrils formed from other proteins, like β-lactoglobulin and ovalbumin, persistence lengths between 1 and 3 μm have been reported.[16,18,38,39]

Conclusions

We determined the persistence length L_p of amyloid fibrils formed from HEWL using two approaches: by analysis of the time-dependent thermal fluctuations of individual fibrils in an aqueous environment, and by the analysis of the shapes of an ensemble of fibrils adsorbed on a surface. With both methods, we obtained persistence lengths of a few micrometers. The analysis of surface-adsorbed fibrils imaged with AFM showed that interactions of the fibrils with the substrate influenced the measurements of L_p: dried fibrils on mica had a larger apparent L_p than dried fibrils on glass. Hydrated fibrils imaged on mica had a smaller apparent L_p than dried fibrils on mica, but this difference may be a consequence of differences in sample preparation, leading to the analysis of a different population of fibrils. The analysis of the time-dependent thermal fluctuations of individual fibrils revealed a broad variability in L_p-values over almost an order of magnitude, with L_p ranging from 0.7 up to at least 6.7 μm. This variability indicates a large heterogeneity between fibrils in terms of diameter and/or internal packing structure. In future, we will enlarge this dataset to obtain a more precise overview of the persistence length of HEWL amyloid fibrils.

Materials and methods

HEWL fibril formation. Hen egg white lysozyme powder (HEWL, Sigma Aldrich cat # 62970) was dissolved in a HCl solution (pH=2.0) and the pH was immediately adjusted to pH=2.0. HEWL was dissolved by stirring the solution for 1 hr at 4°C. To remove traces of electrolytes, the solution was dialyzed against a HCl solution (pH=2.0) at 4°C using a slide-a-lyzer (Thermo Scientific cat. #87732) with a molecular weight cut-off (MWCO) of

10 kDa. Aggregates were removed by filtration with a 0.1 µm filter (Sigma Aldrich #F7523). The protein concentration was calculated based on measurements of light absorption at 280 nm with a Nanodrop spectrophotometer (Thermo Scientific), using an extinction coefficient of 37,752 $M^{-1}cm^{-1}$.[40] Amyloid fibrils were formed by incubation of 30 mL of the monomer solution at a concentration of 1 mM in a polypropylene tube in an oven at 65°C for 7 days, while the solution was stirred using a magnetic stirrer. After 7 days, samples were quenched on ice water and fibrils were separated from small aggregates and monomers by filtration using centrifugal filters (Amicon, Millipore cat.#UFC910024) with a MWCO of 100 kDa. Prewashed filters were centrifuged at 1000 *g* for 30 min and samples were subsequently washed 3 times with a HCl solution (pH=2.0) by repeating the centrifugation.

Glass surface passivation. Microscope glass slides and cover slips (Menzel Glaser, Thermo Fisher Scientific) were cleaned by incubation in base piranha (H_2O: NH_4:H_2O_2 in a volume ratio of 7:1:1) for 12 min. Glass slides and cover slips were subsequently washed with MilliQ water, dried with nitrogen and incubated for 1 hr in 2.5% 3-mercapto propyl trimethoxy silane (3-MPTS) in toluene. Silanized glass was washed first with toluene and then with ethanol, dried with nitrogen and baked overnight in an oven at 100°C. PEG (20 kDa mPEG maleimide, Laysan Bio Inc.) was melted on the glass and incubated in an oven at 80°C. After 1.5 to 2.0 hrs, PEG was washed off using preheated ethanol at a temperature of approximately 60°C and the glass was dried with nitrogen. Slides were used for experiments the same day. We also tried to bind mPEG to silanized glass by incubation with mPEG dissolved in water or phosphate buffer at room temperature, but this did not result in sufficient surface coverage to prevent nonspecific adhesion of fibrils to the surface.

Labeling and fluorescence microscopy. Nile Red (Sigma Aldrich cat. #72485) was dissolved in ethanol at a concentration of 10 µM and filtered using a 0.1 µm syringe filter to remove aggregates. HEWL amyloid fibrils at a concentration of 10 µM were mixed in a 1:1 ratio with the Nile Red solution, and further diluted in HCl solution (pH=2.0) in a 1:50 ratio. A drop of 1 µL was sandwiched between the glass slide and the cover slip and gentle pressure was applied to spread the solution. The chamber was sealed with Valap (Vaseline, lanolin and paraffin in a 1:1:1 ratio). Samples were imaged using an epi-fluorescence wide field microscope (Ti-Eclipse Nikon) equipped with a 100x oil immersion objective (numerical aperture 1.4) and a digital CCD camera (Coolsnap HQ2 Photometrics, Tucson AZ). Images were taken at 4.9 frames per second with an exposure time of 100 ms. Typically up to 400 frames could be collected before the sample photobleached after approximately 80 s.

Data analysis. Wide field epifluorescence time-lapse images of individual fluctuating amyloid fibrils were analyzed using analysis software in Matlab developed by P. Atzberger et al.[27,28] The analysis is based on the global fitting of an entire trial contour at once to a fluorescent image. To determine the initial contour of the fibril, a box that encloses the brightest pixels in the image is drawn. The diagonal that connects the corners with the highest average intensity is the initial contour for fitting. The contour representation is expressed in terms of the tangent angles parameterized by the arc-length and expanded in a basis of orthogonal polynomials. The flexural rigidity of the fibril was inferred by statistical analysis of the ensemble of biopolymer configurations at thermal equilibrium. By analysis of simulated ensembles of fluorescent images of a simulated fiber with known L_p and varying levels of background noise and gap artifacts (irregularities in fluorophore labeling), an error of <10% on the estimated persistence length was observed for the highest background noise. For a majority of low-to-moderate noise cases, the error was < 1%.

Atomic Force Microscopy. Filtered fibril suspensions were diluted to protein concentrations of approximately 0.01% (w/w) and 15 µL of the suspension was incubated on freshly cleaved mica (Muscovite mica V-4, Electron Microscopy Sciences) or glass slides that were rinsed with iso-propanol and dried by nitrogen. After 3 minutes, the surface of the mica or glass slide was washed with HCl solution at pH=2.0, and dried in air. Atomic force microscopy imaging was performed on a Dimension 3100 Scanning Probe Microscope (Bruker) using silicon cantilevers (TESPA, force constant 42 N/m, Bruker). For liquid AFM, the filtered fibril suspensions were diluted to protein concentrations of approximately 0.1% (w/w). A drop of the fibril suspension was pipetted on freshly cleaved mica, and measurements were started immediately at room temperature using silicon nitride cantilevers (SNL-10, force constant 0.24-0.35 N/m, Bruker). All images were flattened using Nanoscope 6.14 software.

Acknowledgment

We thank Norbert Mücke for providing software for persistence length analysis. This work is part of the Industrial Partnership Programme (IPP) Bio(-Related) Materials (BRM) of the Stichting voor Fundamenteel Onderzoek der Materie (FOM), which is financially supported by the Nederlandse Organisatie voor Wetenschappelijk Onderzoek (NWO). The IPP BRM is co-financed by the Top Institute Food and Nutrition and the Dutch Polymer Institute.

References

(1) Dobson, C. M. *Nature* **2003**, *426*, 884.
(2) Knowles, T. P.; Vendruscolo, M.; Dobson, C. M. *Nature reviews. Molecular cell biology* **2014**, *15*, 384.
(3) Jayasinghe, S. A.; Langen, R. *Biochimica et Biophysica Acta (BBA) - Biomembranes* **2007**, *1768*, 2002.
(4) Engel, M. F. M. *Chemistry and Physics of Lipids* **2009**, *160*, 1.
(5) Milanesi, L.; Sheynis, T.; Xue, W.-F.; Orlova, E. V.; Hellewell, A. L.; Jelinek, R.; Hewitt, E. W.; Radford, S. E.; Saibil, H. R. *Proceedings of the National Academy of Sciences* **2012**, *109*, 20455.
(6) Smith, J. F.; Knowles, T. P. J.; Dobson, C. M.; MacPhee, C. E.; Welland, M. E. *Proceedings of the National Academy of Sciences U.S.A.* **2006**, *103*, 15806.
(7) Knowles, T. P.; Fitzpatrick, A. W.; Meehan, S.; Mott, H. R.; Vendruscolo, M.; Dobson, C. M.; Welland, M. E. *Science* **2007**, *318*, 1900.
(8) Otzen, D.; Nielsen, P. H. *Cellular and Molecular Life Sciences* **2008**, *65*, 910.
(9) Fowler, D. M.; Koulov, A. V.; Balch, W. E.; Kelly, J. W. *Trends in biochemical sciences* **2007**, *32*, 217.
(10) van der Linden, E.; Venema, P. *Current Opinion in Colloid & Interface Science* **2007**, *12*, 158.
(11) Reynolds, N. P.; Styan, K. E.; Easton, C. D.; Li, Y. L.; Waddington, L.; Lara, C.; Forsythe, J. S.; Mezzenga, R.; Hartley, P. G.; Muir, B. W. *Biomacromolecules* **2013**, *14*, 2305.
(12) Li, C. X.; Mezzenga, R. *Nanoscale* **2013**, *5*, 6207.
(13) Ryan, D. M.; Nilsson, B. L. *Polymer Chemistry* **2012**, *3*, 18.
(14) Knowles, T. P. J.; Buehler, M. J. *Nature Nanotechnology* **2011**, *6*, 469.
(15) Scheibel, T.; Parthasarathy, R.; Sawicki, G.; Lin, X. M.; Jaeger, H.; Lindquist, S. L. *Proceedings of the National Academy of Sciences of the U.S.A.* **2003**, *100*, 4527.
(16) vandenAkker, C. C.; Engel, M. F. M.; Velikov, K. P.; Bonn, M.; Koenderink, G. H. *Journal of the American Chemical Society* **2011**, *133*, 18030.
(17) Relini, A.; Torrassa, S.; Ferrando, R.; Rolandi, R.; Campioni, S.; Chiti, F.; Gliozzi, A. *Biophysical Journal* **2010**, *98*, 1277.
(18) Adamcik, J.; Jung, J. M.; Flakowski, J.; De Los Rios, P.; Dietler, G.; Mezzenga, R. *Nature Nanotechnology* **2010**, *5*, 423.
(19) Gosal, W. S.; Morten, I. J.; Hewitt, E. W.; Smith, D. A.; Thomson, N. H.; Radford, S. E. *Journal of Molecular Biology* **2005**, *351*, 850.
(20) Mucke, N.; Klenin, K.; Kirmse, R.; Bussiek, M.; Herrmann, H.; Hafner, M.; Langowski, J. *Plos One* **2009**, *4*.
(21) Mücke, N.; Kreplak, L.; Kirmse, R.; Wedig, T.; Herrmann, H.; Aebi, U.; Langowski, J. *Journal of Molecular Biology* **2004**, *335*, 1241.
(22) Volpatti, L. R.; Vendruscolo, M.; Dobson, C. M.; Knowles, T. P. J. *ACS Nano* **2013**, *7*, 10443.
(23) Aymard, P.; Nicolai, T.; Durand, D.; Clark, A. *Macromolecules* **1999**, *32*, 2542.
(24) Sagis, L. M. C.; Veerman, C.; van der Linden, E. *Langmuir* **2004**, *20*, 924.
(25) Knowles, T. P. J.; Buehler, M. J. *Nature Nano* **2011**, *6*, 469.
(26) Castro, Carlos E.; Dong, J.; Boyce, Mary C.; Lindquist, S.; Lang, Matthew J. *Biophysical Journal* **2011**, *101*, 439.
(27) Valdman, D.; Atzberger, Paul J.; Yu, D.; Kuei, S.; Valentine, Megan T. *Biophysical Journal* **2012**, *102*, 1144.
(28) Valdman, D.; Lopez, B. J.; Valentine, M. T.; Atzberger, P. J. *Soft Matter* **2013**, *9*, 772.

(29) Brangwynne, C. P.; Koenderink, G. H.; Barry, E.; Dogic, Z.; MacKintosh, F. C.; Weitz, D. A. *Biophysical Journal* **2007**, *93*, 346.
(30) Brangwynne, C. P.; Koenderink, G. H.; MacKintosh, F. C.; Weitz, D. A. *Physical Review Letters* **2008**, *100*, 118104.
(31) Gittes, F.; Mickey, B.; Nettleton, J.; Howard, J. *Journal of Cell Biology* **1993**, *120*, 923.
(32) Duggal, R.; Pasquali, M. *Physical Review Letters* **2006**, *96*.
(33) Schiffels, D.; Liedl, T.; Fygenson, D. K. *ACS Nano* **2013**, *7*, 6700.
(34) Sweers, K.; van der Werf, K.; Bennink, M.; Subramaniam, V. *Nanoscale Research Letters* **2011**, *6*.
(35) Lara, C. c.; Adamcik, J.; Jordens, S.; Mezzenga, R. *Biomacromolecules* **2011**, *12*, 1868.
(36) Adamcik, J.; Lara, C.; Usov, I.; Jeong, J. S.; Ruggeri, F. S.; Dietler, G.; Lashuel, H. A.; Hamley, I. W.; Mezzenga, R. *Nanoscale* **2012**, *4*, 4426.
(37) Bathe, M.; Heussinger, C.; Claessens, M.; Bausch, A. R.; Frey, E. *Biophysical journal* **2008**, *94*, 2955.
(38) Lara, C.; Usov, I.; Adamcik, J.; Mezzenga, R. *Physical Review Letters* **2011**, *107*, 238101.
(39) Jordens, S.; Adamcik, J.; Amar-Yuli, I.; Mezzenga, R. *Biomacromolecules* **2010**, *12*, 187.
(40) Mishra, R.; Sorgjerd, K.; Nystrom, S.; Nordigarden, A.; Yu, Y. C.; Hammarstrom, P. *Journal of Molecular Biology* **2007**, *366*, 1029.

Chapter 8

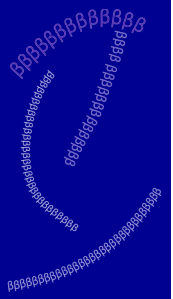

Viscoelastic properties of β-lactoglobulin amyloid fibrils

Based on: Corianne C. vandenAkker, Joachim Kohlbrecher, Jeanette Nguyen, M. Paul Lettinga, Gijsje H. Koenderink (submission in preparation).

Abstract

The milk protein β-lactoglobulin (β-lg) self-assembles into amyloid fibrils upon heating at low pH. These amyloid fibrils are a promising candidate for applications in food texturing and materials science, and have become a model system for the investigation of amyloid formation. The rheological behavior of suspensions of amyloid fibrils under shear flow is particularly relevant for their applications. In this study we compare the viscoelastic properties of suspensions of amyloid fibrils that differ in aspect ratio and persistence length (long and rigid versus short and worm-like). We find that both types of amyloid fibrils behave in suspension as soft solids with an apparent yield stress. Furthermore, the fibril suspensions exhibit a low percolation concentration and thixotropic behavior, indicative of weak attractive interactions between the fibrils. The fibrils exhibit strong shear-thinning behavior over a large range of shear rates. We show using a combination of rheology and small-angle neutron scattering (rheo-SANS) that the long, rigid fibrils align under shear, while for the short, worm-like fibrils no change in alignment is observed upon shear. This suggests that the strong shear-thinning behavior of short, worm-like fibrils is caused by weak attractive forces between the fibrils. We conclude that suspensions of β-lg amyloid fibrils behave rheologically as suspensions of weakly attractive, semi-flexible rods.

Introduction

β-Lactoglobulin (β-lg) is the main protein in whey and represents 0.2–0.4% (w/v) of skim milk.[1] In the native state, β-lg has a predominantly β-sheet structure.[2] Upon heating, it is capable of self-assembling into a variety of different supramolecular structures, dependent on the solution pH. At pH values below the isoelectric point (pH=5.1), β-lg is hydrolyzed and denatured and the resulting peptides self-assemble into thin fibers that have been identified as amyloid fibrils based on their cross-β sheet structure.[3-5] The self-assembly properties of β-lg make this protein (similar to other whey proteins) important for the dairy and food industry, especially for controlling the texture of a variety of foods.[6-8] At the same time, its tunable structuring capacity makes β-lg an interesting target for advanced applications in materials science such as scaffolds for tissue engineering.[9] Additionally, β-lg has become a major model protein for investigating the self-assembly mechanism and biophysical properties of amyloid fibrils.[2,3,10,11]

For applications of amyloid fibrils in food products, tissue engineering, and materials science, the rheological behavior of fibril suspensions and networks under shear flow are relevant. The rheology of a fibril network is in general determined by a combination of the intrinsic mechanical properties of the fibrils (in particular the bending rigidity) and the spatial organization of the fibrils and the nature of their interactions.[12] The spatial organization of amyloid fibril networks depends on the fibril concentration and on fibril rigidity: when the fibrils have a high aspect ratio (ratio of length over diameter, L/D), they can already form liquid crystalline phases or gels at rather low concentrations.[13] The structure of these gels will depend on the strength of the attractive interactions between the fibrils, ranging from homogeneous networks in case of no or weak attractions to heterogeneous fractal clusters in case of strong attractions.[12] The interactions between β-lg fibrils are not well-studied, but are thought to be dependent on the amino acid side chains that are exposed on the surface of the β-sheet core of the fibrils, which can for instance confer a pH-dependent electrostatic charge to the fibrils.[14] There are a number of prior rheological studies on β-lg amyloid fibrils, employing macroscopic shear rheometry. The linear viscoelastic moduli have been measured by small amplitude oscillatory shear measurements. These measurements until now have primarily focused on resolving the gelation time and critical percolation concentration of fibrils formed from β-lg and other food-related proteins including bovine serum albumin (BSA) and ovalbumin at pH=2.0.[13,15-20] However, a quantitative comparison of these rheology measurements with theoretical predictions for fibril suspensions is difficult, since fibril assembly under the conditions used in these experiments usually does not run to completion, yielding a complex mixture of fibrils, aggregates, and monomers. A number of studies showed that β-lg

fibril suspensions behave as weak viscoelastic gels, which was explained in terms of a percolation phenomenon.[16,21,22] Steady shear measurements were used to measure the shear-rate dependence of the viscosity of suspensions of whey protein fibrils with lengths of several micrometers. These data show strong shear-thinning behavior.[18,22] There are a few studies where the influence of ionic strength on the rheology was studied. For worm-like β-lg fibrils formed at pH=3.35 (persistence length of 35 nm, length of 130 nm and a diameter of 5 nm), the viscosity was shown to increase with protein concentration[21] and with increasing salt concentration.[18] However, since the effect of salt on rod flexibility and particle interactions is unknown, the mechanism behind this increase in viscosity has not been quantitatively explained.

We recently showed that the morphology and rigidity of β-lg amyloid fibrils are strongly dependent on the β-lg concentration when the fibrils are assembled in an aqueous solution of pH=2 and at 80^{o}C.[23] At high β-lg concentrations, around 7.5 wt%, short, worm-like fibrils are formed, while at lower β-lg concentrations, fibrils are long, straight, and rigid. Here we compare the linear and nonlinear rheological properties of suspensions of these two different types of β-lg amyloid fibrils. We show that both types of fibril suspensions are strongly shear-thinning. To understand the origin of this behavior, we combine rheology with small-angle neutron scattering (rheo-SANS) to probe shear-induced fibril alignment. We show that the long and rigid fibrils align under shear, while the orientations of the short, worm-like fibrils appears to be unaffected by shear. Furthermore, we show that weak attractive forces between fibrils play an important role in the mechanical properties of the amyloid fibril suspensions, leading to an apparent yield stress, thixotropic behavior, and probably contributing to the shear-thinning response.

Results and discussion

We compared the rheology of suspensions of β-lg amyloid fibrils differing in aspect ratio and persistence length. By forming β-lg fibrils in an aqueous solution of pH=2 and at 80^{o}C, we could form long and straight fibrils at a protein concentration of 3.0 wt% and short, worm-like fibrils at a protein concentration of 7.5 wt%. Typical images obtained by atomic force microscopy (AFM) are shown in Figure 8.1a-b. We showed previously that the persistence length of the long fibrils is approximately 3.8 μm, whereas the persistence length of the worm-like fibrils is only 90 nm (Chapter 2), even though the (average) diameters are similar (2.6 versus 2.9 nm).[23] The difference in bending rigidity thus reflects a different internal packing structure. For both fibril types, we find a broad length distribution. For the long fibrils, the lengths range from a few hundred nanometers up to 10 μm, with an average of 1 μm. For the worm-like fibrils, the average length is 200 nm, but in the fibril batch used in this chapter we also observed a

small fraction of long fibrils with lengths of up to a few micrometer (in contrast to the batches used in Chapters 2 and 3). The conversion of monomer into amyloid fibrils is approximately 50% upon incubation at 3.0 wt% β-lg and 80% at 7.5 wt% β-lg.[23] To exclude any effects of the large fraction of non-aggregated material on the rheological measurements, this material was removed by filtration over a 100 kDa molecular weight cut-off filter before experiments were performed, resulting in stock solutions of pure fibrils henceforth referred to as "long, straight fibrils" (originally formed at 3.0 wt%) and "short, worm-like fibrils" (originally formed at 7.5 wt% β-lg). To determine the concentration dependence of the rheology, we prepared dilutions of these stock solutions in HCl solutions at pH=2.

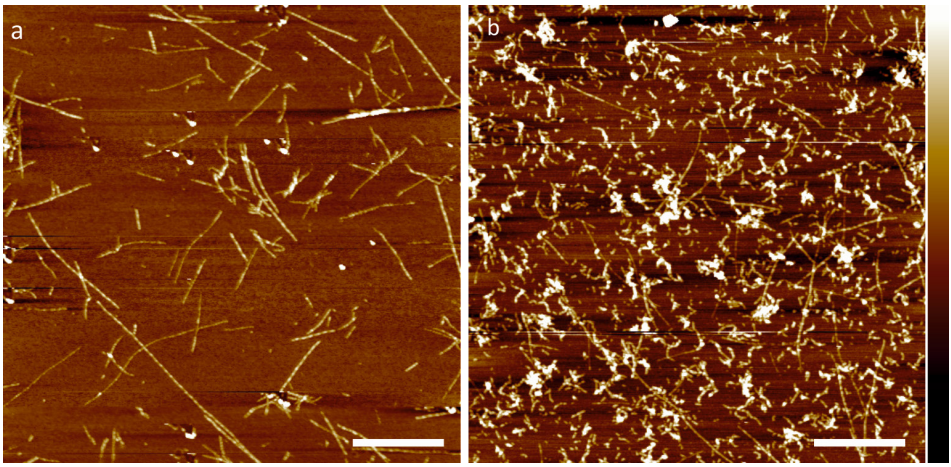

Figure 8.1: AFM images of a) long, straight fibrils and b) short, worm-like fibrils, formed by incubating a solution of β-lg in an aqueous solution of HCl (pH=2) at 80°C at two different protein concentrations (3.0 and 7.5 wt%, respectively). Scale bar in the images is 1 µm and the height scale (bar on the right hand side) is 10 nm.

To probe the viscoelastic properties of the two types of fibril suspensions, we performed oscillatory shear measurements at different fibril volume fractions as a function of oscillation frequency ω at a constant strain amplitude (γ=1%) that was small enough to ensure a linear response. Both fibril suspensions behave as soft solids, with an elastic modulus, $G'(\omega)$, that is larger than the viscous modulus, $G''(\omega)$, across the entire frequency range we probed (Figure 8.2a-b). Accordingly, the loss tangent, $\tan(\delta) = G''/G'$, was markedly smaller than 1, except at the lowest volume fractions (Figure 8.2c-d). G' was only weakly dependent on ω, also consistent with solid-like behavior. There is no indication of a characteristic frequency where G' and G'' cross-over, suggesting that, at least down to the lowest frequency probed, stresses do not relax. Both G' and G'' increase with increasing fibril volume fraction, φ. As shown in Figure

8.3a, the low-frequency elastic modulus (determined at ω=0.18 rad/s) for the straight and the worm-like fibrils is comparable in magnitude, reaching ca. 1 Pa for φ close to 1%. Note that the volume fraction ranges we probed are different for the two fibril types, with the highest volume fraction for the long, straight fibrils being ca. 8-fold lower than that for the worm-like fibrils.

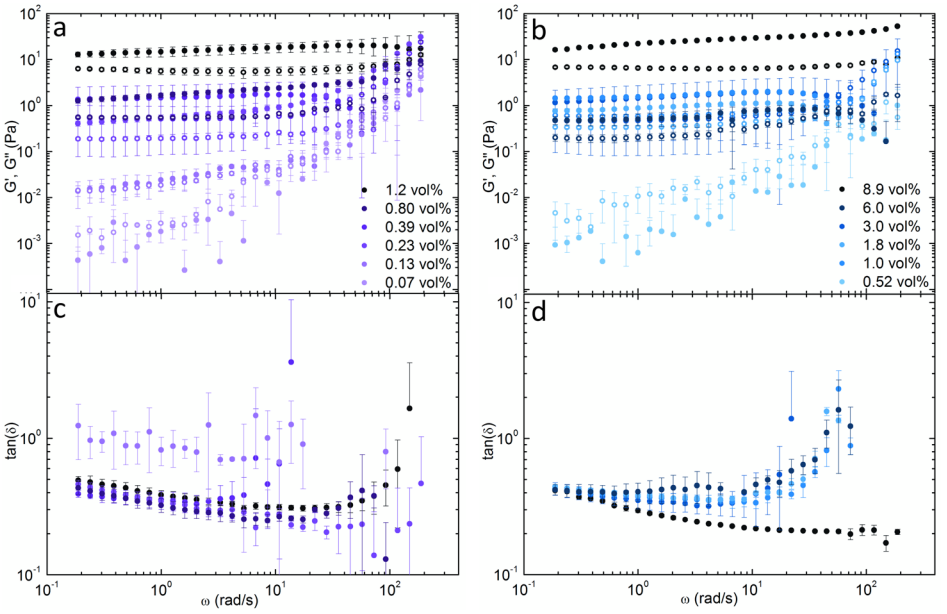

Figure 8.2: Oscillatory shear rheology of fibril suspensions over a range of volume fractions, φ (see legend) of a) long, straight fibrils; b) short, worm-like fibrils. The corresponding loss tangents are shown in c) and d), respectively. Data shown are averages of at least 3 replicates with standard deviations.

The strong increase of G' with φ suggests that the fibril suspensions may undergo a percolation transition. To estimate the critical percolation concentration c_p, we followed a procedure suggested previously in the context of whey protein fibrils[15,19,24]. Based on the expected scaling relation $G' \propto (\varphi - c_p)^t$ near a critical point[25], we replotted the data as $G'^{1/t}$ versus φ, where t is a scaling exponent (Figure 8.3b-c). Since we do not have enough data to make a reliable fit, we decided to assume a value of t=1.7, which was found for comparable amyloid samples[15,19]. When we plot the data in this way, we observe an apparent percolation threshold around c_p=0.1 vol% for long, straight fibril suspensions (Figure 8.3b) and c_p=0.2 vol% for short, worm-like fibrils (Figure 8.3c).

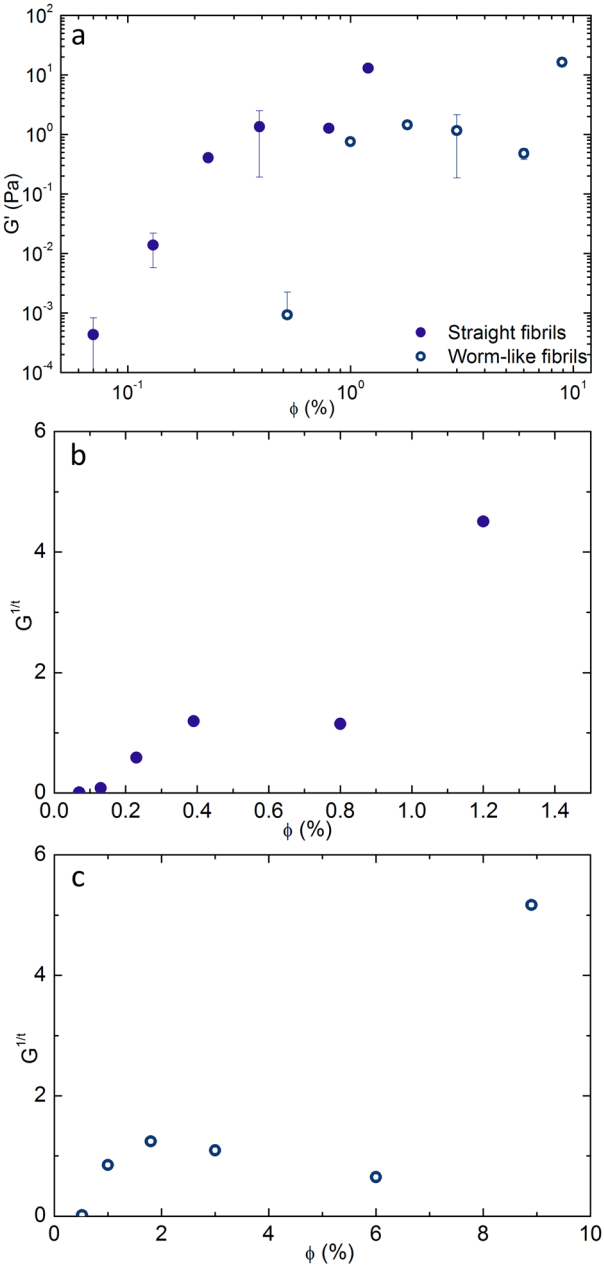

Figure 8.3: a) Storage modulus G' measured at a frequency ω = 0.18 rad/s as a function of φ for suspensions of long, straight fibrils (closed circles) and short, worm-like fibrils (open circles). These data are replotted as $G'^{1/t}$ (with t=1.7) versus φ for b) long, straight fibrils and c) short, worm-like fibrils.

These values for c_p are lower than reported previously for fibrils formed *in situ* between the rheometer plates. For β-lg at pH=2.0 that was heated for 10 hrs, c_p=2.3 vol% was reported at low ionic strength.[26] However, these samples were not filtered after fibril formation and contained approximately 40% non-aggregated β-lg, which is expected to increase the effective percolation concentration.[26] For single-wall carbon nanotube (SWNT) suspensions, which show comparable aspect ratios and persistence lengths as long, straight amyloid fibrils, c_p was reported at 0.18 vol%[27]. For an isotropic suspension of stiff rods that have a sufficiently large aspect ratio and interact only by excluded volume interactions, the percolation concentration is expected to scale inversely with aspect ratio according to $c_p = D/(2L)$, with D the diameter and L the length of the rod.[28,29] This model predicts c_p= 0.13 vol% for rods with an aspect ratio of 400, which corresponds to the average aspect ratio of the long, straight fibrils. This value is close to the experimentally observed estimation. For worm-like fibrils, which have an average aspect ratio of 70, the model predicts c_p of 0.7 vol%, which is higher than what we observe. The discrepancy is likely related to the fact that the worm-like fibrils are not well approximated as rigid rods, but may also indicate (weak) attractive interactions, which are known to lower the percolation transition.

To probe the non-linear rheology of the fibril suspensions, we performed constant shear tests at different shear rates $\dot{\gamma}$. Both fibril types exhibit a strong shear-thinning response over the full range of accessible shear rates (Figure 8.4a-b). There is no clear evidence of a low-shear plateau, suggesting that the suspensions possess a yield stress, consistent with their predominantly elastic response to an oscillatory shear. At high shear, the flow curves appear to tail off to reach a plateau value. The viscosity is concentration-dependent, showing an increase with increasing fibril volume fraction. To compare the shear-thinning response of the two fibril types, we determined the shear thinning index n by fitting a power-law to the data between $\dot{\gamma} = 10^{-2}$ - 10^{1} s^{-1}. As shown in Figure 8.4c, n is only weakly dependent on φ for both fibril types. For straight fibrils, n increases slightly with increasing φ, from 0.88 at the lowest volume fraction to 0.96 at the highest volume fraction. For worm-like fibrils, no clear trend is observed and n varies between 0.90 and 0.95. The viscosities measured at high (10^{3} s^{-1}) and low (10^{-3} s^{-1}) shear rate increase with increasing φ, both for straight and for worm-like fibrils (Figure 8.4d-e). Note that at these shear rates no clear-cut plateau for the viscosity was observed, but these shear rates are the limits at which we can reliably probe the viscosity. The shear-thinning behavior we observe is similar to that of suspensions of other rigid, long rods, like single-walled carbon nanotubes (SWNTs)[30], fd virus rods[31], chitin crystallites[32] and cellulose whiskers[33].

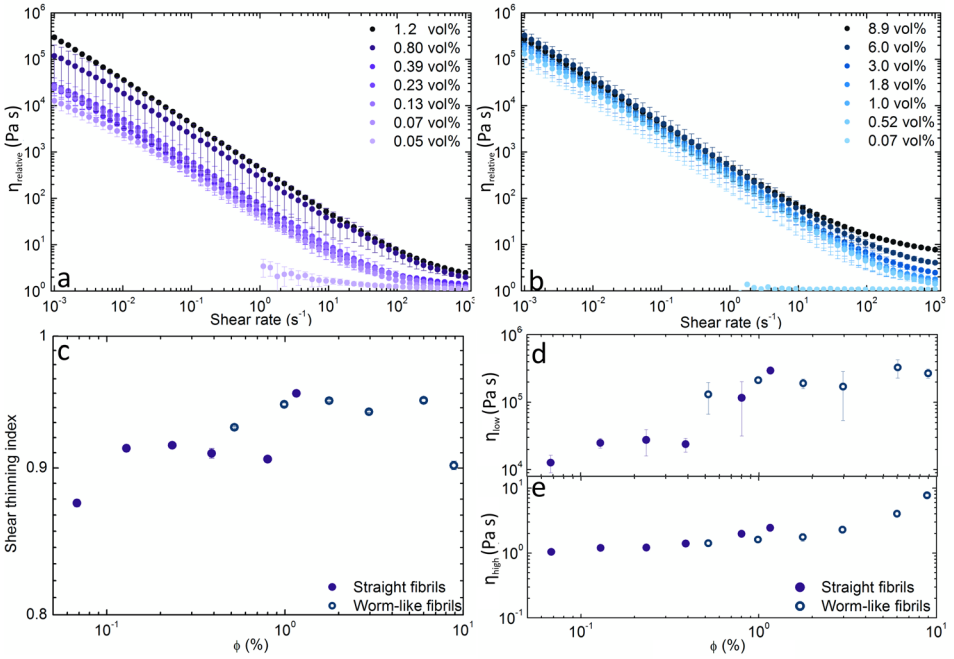

Figure 8.4: Flow curves of suspensions of a) long, straight and b) short, worm-like β-lg amyloid fibrils for different volume fractions, φ. Shear rate sweeps were measured with decreasing shear rate. c) Shear-thinning indices n as a function of φ, calculated using power-law fits to the flow curves over a range of shear rates between 10^{-2} and 10 s^{-1} for long, straight fibrils (closed circles) and short, worm-like fibrils (open circles). d-e) low-shear viscosity, η_0, measured at $\dot{\gamma} = 10^{-3}$ s^{-1}, (d) and high-shear viscosity, η_∞, measured at $\dot{\gamma} = 10^{3}$ s^{-1}, (e) for suspensions of long, straight fibrils (closed circles) and short, worm-like fibrils (open circles). Values are averages of at least 3 replicates. Error bars in (e) are smaller than the size of the symbols.

To obtain an estimate of the apparent yield stress, we plot the shear stress τ as a function of shear rate $\dot{\gamma}$ in Figure 8.5. Materials that remain solid until a critical shear stress is exceeded and become fluid-like above this critical shear stress are called yield stress materials.[34] The plateau at low $\dot{\gamma}$ indicates an apparent yield stress. For suspensions of long, straight fibrils, the apparent yield stress is strongly dependent on concentration, increasing from ca. 0.03 Pa at φ=0.13% to 0.3 Pa at φ=1.16%. In contrast, for worm-like fibrils, the apparent yield stress is only weakly dependent on concentration, ranging between 0.1 and 0.4 Pa for concentrations between 0.52 and 8.9 vol%.

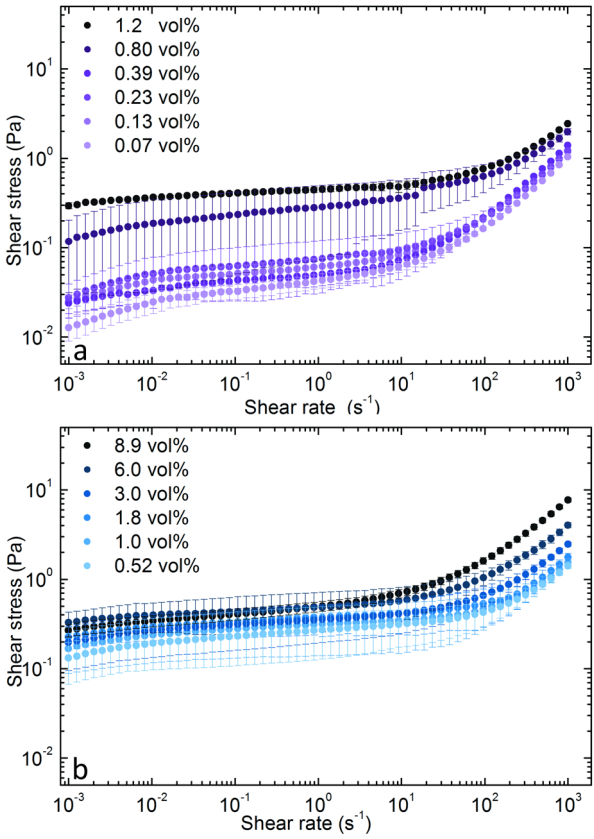

Figure 8.5: Shear stress as a function of shear rate for various volume fractions of suspension of amyloid fibrils. The plateaus at low $\dot{\gamma}$ provide a measure of the apparent yield stress of the suspensions. a) Straight, long fibrils; b) short, worm-like fibrils.

The solid-like nature of the suspensions and the presence of an apparent yield stress suggest that the fibrils may experience attractive interactions. Since amyloid fibrils are formed from unfolded proteins that refold into a cross-β sheet structure, it has been suggested that they may experience hydrophobic interactions.[35,36] As a further test whether attractive interactions are present, we tested whether the flow-induced structural changes observed during flow tests are reversible. For a sample with attractive rods, thixotropic behavior is expected. A thixotropic sample will show a continuous decrease of viscosity with time when flow is applied after it has been previously at rest. When the flow is discontinued, a subsequent recovery of viscosity in time is observed.[37] Thixotropy can be determined by experiments with a step-down in shear rate. Non-thixotropic viscoelastic fluids would react to such a step-down by a monotonic decrease of the stress to a new plateau value.

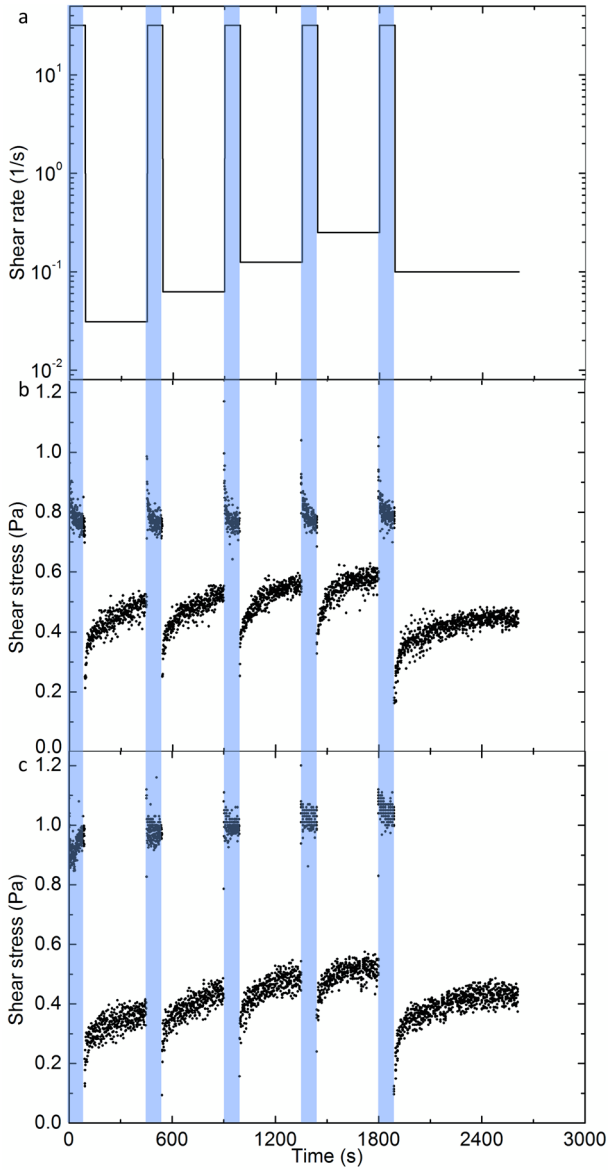

Figure 8.6: Experiments with a step-down in shear rate to test for thixotropic behavior. a) Applied protocol of steps in shear rate. Measured shear stress as a function of time for suspension of b) long, straight fibrils at 1.2 vol%, and c) short, worm-like fibrils at 8.9 vol%. High shear rate regimes are indicated in blue.

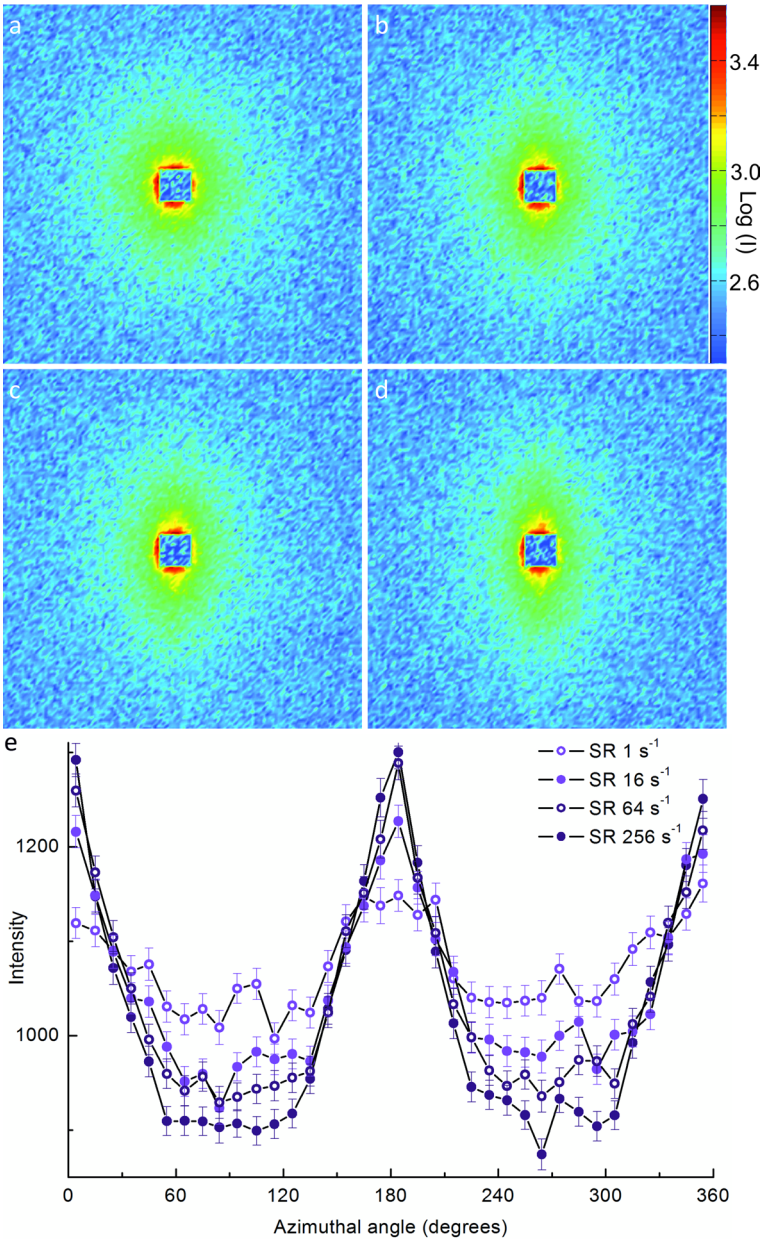

Figure 8.7: 2D-scattering patterns measured by small angle neutron scattering for suspensions of long, straight fibrils at 1.0 vol% in a Couette shear cell during steady shear experiments at shear rates of a) 1 s^{-1}; b) 16 s^{-1}; c) 64 s^{-1}; d) 256 s^{-1}. The square in the middle of all the images is the beam stop. The color bar on the top-right displays the intensity scale. e) Average intensity as a function of azimuthal angle. Intensity was averaged over segments of 10 degrees.

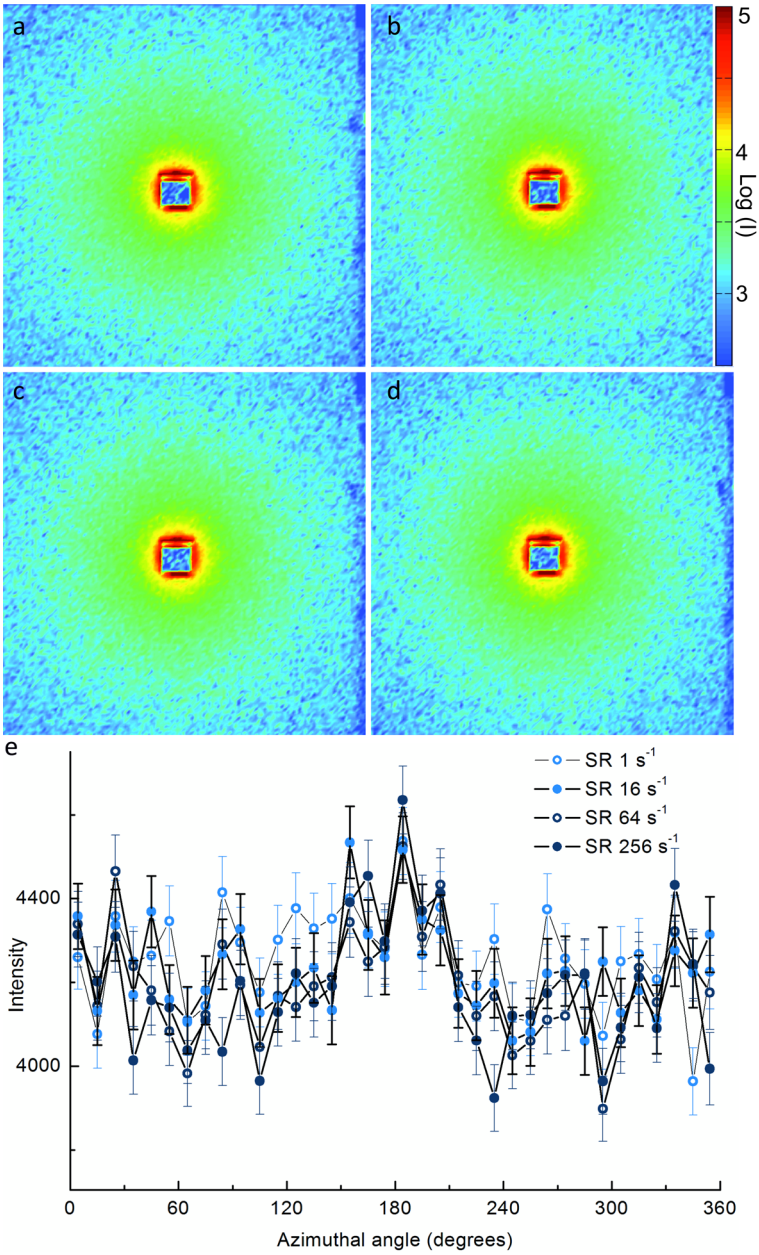

Figure 8.8: Neutron scattering for suspensions of short, worm-like fibrils at 4.5 vol% during steady shear experiments at shear rates of a) 16 s^{-1}; b) 64 s^{-1}; c) 256 s^{-1}; b) 512 s^{-1}. The square in the middle is the beam stop. e) Average intensity as a function of azimuthal angle. Intensity was averaged over segments of 10 degrees.

In contrast, the shear stress in an thixotropic material drops instantaneously to a lower value, and subsequently increases gradually to a new steady state.[37] We applied a protocol of several steps in shear rate: from $\dot{\gamma}$ = 32 s^{-1} to low values of $\dot{\gamma}$ ranging from 0.03 s^{-1} to 0.25 s^{-1} (Figure 8.6a), and measured the resultant shear stress σ over time. For both fibril types, we observed a drop of σ upon step-down of the shear rate, followed by a gradual increase to a steady state value (Figure 8.6b-c). This behavior proves that suspensions of both fibril types behave like thixotropic materials. Thixotropy has been reported for a large range of colloidal materials, including food products like mayonnaise and ice-cream[38] and whey protein aggregates[39]. The thixotropic behavior indicates weak attractive forces between the fibrils. When sheared, the structure is broken down in time, while when left at rest, the microstructure slowly rebuilds itself.[37,40]

These attractive interactions may contribute to the observed shear-thinning response of the fibril suspensions. However, it is also possible that shear-thinning originates from flow-induced alignment of the fibrils, which is a well-known phenomenon for rod-like particles with a high aspect ratio.[41] To test whether shear-induced alignment occurs, we probed the suspension structure under shear using small-angle neutron scattering (SANS). Figure 8.7 and Figure 8.8 show the 2D SANS intensities for amyloid fibril suspensions at various shear rates. For long, straight fibrils the scattering pattern is isotropic at rest and remains isotropic at a constant shear rate of 1 s^{-1} (Figure 8.7a), where significant shear-thinning has already taken place. At higher shear rates, in the range of $\dot{\gamma}$ = 16 to 256 s^{-1}, the scattering patterns reveal an increasing degree of anisotropy indicative of fibril alignment (Figure 8.7b-d). To quantify the anisotropy, we plotted the average intensity as a function of azimuthal angle for different shear rates in Figure 8.7e. It is indeed clear that at higher $\dot{\gamma}$ the anisotropy increases. In contrast, suspensions of the short, worm-like fibrils remained isotropic to a good approximation at all shear rates, even at the highest shear rate we measured, $\dot{\gamma}$ = 512 s^{-1} (Figure 8.8).

The SANS data do not only provide information on fibril orientations, but also on the structure of the fibrils and their spatial arrangement. To extract this information, we analyzed the radially averaged scattering intensity *I* as a function of the scattering wave vector *Q* for both samples at rest (Figure 8.9, filled circles). We observed two different contributions to the scattering intensity. The first contribution can be ascribed to (quasi-)spherical particles with a diameter of approximately 3 nm. These may correspond to the oligomers or short fibril fragments that are also observed in AFM images (Figure 8.1). When this contribution is subtracted from the data, a second contribution with a $Q^{-5/3}$-dependence of the scattering intensity is observed (open circles and in red the fit). This contribution corresponds to the expected scattering pattern of semi-flexible rods,

as has been reported for flexible polymer chains like DNA coils[42] and methylcellulose chains[43]. This dependence is expected for the worm-like fibrils, which have a persistence length slightly lower than their contour length. However, it is somewhat surprising that we observe a $Q^{-5/3}$-dependence for the straight fibrils, because based on their rigidity we would expect a Q^{-1}-dependence as observed for rigid rods. Rigid-rod behavior has been seen for β-lg amyloid fibrils before[44], as well as for multi-walled carbon nanotubes (MWNTs)[45,46] and single-walled carbon nanotubes (SWNTs)[45] with persistence lengths in the order of tens of micrometers[47]. Although the 5/3 scaling is similar for suspensions of straight and worm-like fibrils, the graphs in Figure 8.9 show subtle differences for the scattering of the two fibril types. However, quantification of the differences and determination of the Kuhn length is complicated because of the contribution of the (quasi-)spherical particles.

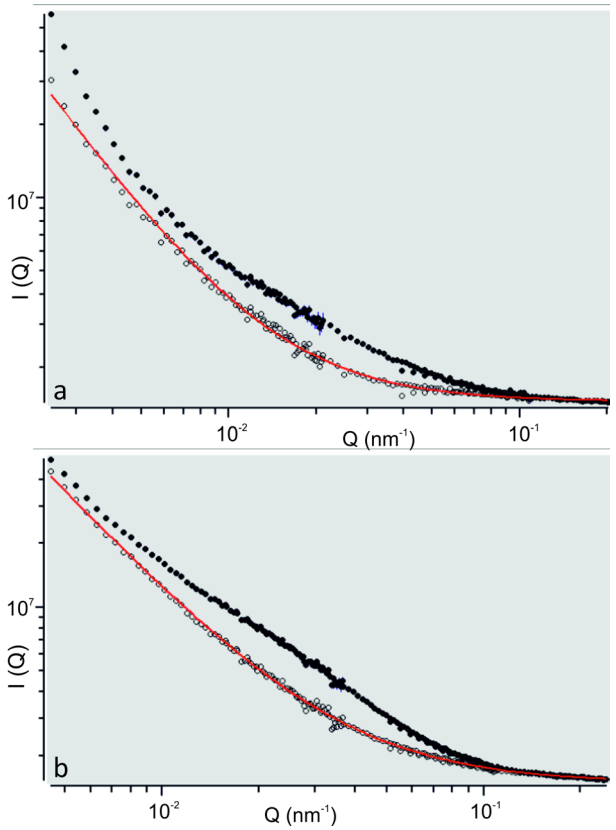

Figure 8.9: SANS scattering intensity *I* as a function of wave vector *Q* for suspensions of a) long, straight or b) short, worm-like fibrils measured at rest, combining data obtained at detector distances of 2, 6 and 18 m. Filled circles are the measured data points, which can be fitted by two distinct contributions to the scattering: open circles are the data points after subtraction of the

contribution of spherical particles and red line is the fit through the data points for the contribution of semi-flexible rods.

Conclusions

We probed the rheological properties of suspensions of long, straight and short, worm-like amyloid fibrils formed from β-lg. Both samples behave as weak viscoelastic solids with an apparent yield stress and strong shear-thinning behavior. Long, straight fibrils have a concentration-dependent yield stress of 0.3 to 3.0 Pa for concentrations between 0.07 and 1.16 vol%. Suspensions of short, worm-like fibrils have a yield stress between 0.1 and 0.4 Pa for concentrations between 0.52 and 8.9 vol%. The percolation concentration is estimated to be approximately 0.1 vol% for long, straight fibrils and 0.2 vol% for short, worm-like fibrils. The fibrils are weakly attractive, indicated by thixotropic behavior in shear rate step experiments. These weak attractive forces may contribute to the shear-thinning behavior. However, rheo-SANS measurements indicate that, at least for the long and straight fibrils, shear flow also causes flow-induced alignment. At rest, the SANS intensity plots reveal two scattering contributions: one from small (3 nm) (quasi-)spherical particles that may be oligomers or small fibril fragments and one from semiflexible fibers. The fiber contribution shows a $Q^{-5/3}$ dependence of the scattering intensity for both samples, indicating self-avoiding random walk behavior. Concluding, we described the rheological behavior of suspensions of different types of amyloid fibrils, which is essential for future applications of these fibrils.

Materials and methods

Amyloid formation. Beta-lactoglobulin (β-lg) amyloid fibrils were prepared as described before.[23] In short, bovine β-lg (genetic variants A and B, Sigma Aldrich, L0130) was dissolved in HCl dilution (pH=2.0), dialyzed extensively (Slide-a-lyzer, MWCO 10kDa, Thermo Scientific) against an HCl solution (pH=2.0) and filtered (0.1 µm filter, Millipore) to remove any aggregates. The final protein concentration was determined by spectrophotometry (Nanodrop, Thermo Scientific) at a wavelength of 280 nm based on an extinction coefficient of 16.8 mM^{-1} cm^{-1}.[48] Samples were heated in eppendorf tubes at 3.0 or 7.5% (w/w) in an oven at 80^{o}C for 16 hrs. After quenching in ice water, the fibrils were separated from non-aggregated material by centrifugal filtering (Centrifugal filters, MWCO 100kDa, Millipore) at 1000 *g*. Three washing and centrifugation steps were performed. The filtered fibril suspension was centrifuged for 5 min at 2000 *g* to remove large fibril aggregates. HCl solution in MilliQ water was replaced by D_2O (pD=2.4) by centrifugal filtering as described before. To determine the final protein concentration, fibril suspensions were mixed with an equal volume of formic acid to

solubilize the aggregated protein. The protein contents of these solutions were measured by spectrophotometry at a wavelength of 280 nm and compared to samples with known concentrations β-lg.[49]

Atomic force microscopy (AFM). A drop of a diluted fibril suspension at a concentration of ~0.01% was pipetted onto freshly cleaved mica. After 5 min incubation, the sample was washed with HCl solution (pH=2) and dried by air. AFM images were made in tapping mode with a Dimension 3100 Scanning Probe Microscope (Bruker) using silicon cantilevers (force constant 42 N/m). Images were flattened using Nanoscope 6.14 software.

Rheological measurements. A stress-controlled rheometer (Physica MCR 501, Anton Paar) with steel cone (30 or 40 mm diameter, 1° angle) and plate thermostatted with a Peltier plate were used for rheometry. To reduce evaporation, a cover was used. The complex shear modulus $G^*(\omega) = G'(\omega) + iG''(\omega)$, where the elastic modulus, $G'(\omega)$ represents the in-phase (storage) response, and the viscous modulus, $G''(\omega)$ represents the out-of-phase (loss) response. The frequency-dependent moduli of amyloid suspensions were measured by oscillatory tests using a small enough strain amplitude (γ=1.0%) to remain in the linear viscoelastic regime, and varying the radial frequency, ω=30-0.03 rad/s. The nonlinear rheology was determined by measurement of the viscosity as a function of shear rate $\dot{\gamma}$ with $\dot{\gamma}$=1000 - 0.001 s^{-1}. All measurements were performed at T=21°C unless mentioned otherwise.

Rheo-Small-angle neutron scattering (rheo-SANS). SANS-experiments were performed at the SANS I neutron beam at the SINQ spallation source at the Paul Schwerrer Institute (PSI, Villigen, Switzerland). The SANS and rheology data were acquired simultaneously by mounting an Anton Paar MCR 501 rheometer in the neutron beam. Rheology was measured in the strain-controlled mode with a quartz Couette geometry. The fibril suspensions were transferred to D_2O at pD=2.4 by 3 washing steps using centrifugal filtering (centrifugal filters, MWCO 100kDa, Millipore) 2 days prior to loading. All measurements were performed at room temperature. Data for steady shear experiments were acquired over an interval of approximately 7 minutes per experiment measured at a beam distance of 6 m for long, straight fibrils and 18 m for short, worm-like fibrils. Neutron scattering in rest for both samples was measured at beam distances of 2, 6 and 18 m. The data correction was performed using the GRASP V 3.99l software developed at the Institute Laue-Langevin (ILL) in Grenoble, France. The data were corrected for background and empty cell scatterings.

Small-angle X-ray scattering (SAXS). To probe the microstructure of the fibril suspensions in the quiescent (unsheared) state, small-angle X-ray scattering (SAXS) experiments were performed on fibril suspensions at varying volume fractions. Experiments were

performed at the DUBBLE beamline (BM 26A) of the European Synchrotron Radiation Facility (ESRF, Grenoble, France). Calibration of the q-scale was done by using the position of diffracted peaks from a standard silver behenate powder. Filtered fibril suspensions were contained in flat 2 mm thick glass capillaries with wall thickness of 0.01 mm. The exposure per sample was 1 min using a beam spot of 300x350 µm and the sample to detector distance was 2.8m. No beam damage of the samples was observed. All data was corrected for background scattering. For samples with volume fractions over the range of 0.18 to 1.8 vol%, both fibril types show isotropic scattering profiles, indicating that there is no fibril alignment (SI Figure 8.1).

Acknowledgment

We thank G. Portale and D. Hermida Merino (ESRF) for assistance with SAXS experiments and analysis. This work is part of the Industrial Partnership Programme (IPP) Bio(-Related) Materials (BRM) of the Stichting voor Fundamenteel Onderzoek der Materie (FOM), which is financially supported by the Nederlandse Organisatie voor Wetenschappelijk Onderzoek (NWO). The IPP BRM is co-financed by the Top Institute Food and Nutrition and the Dutch Polymer Institute.

References

(1) Loveday, S. M.; Wang, X. L.; Rao, M. A.; Anema, S. G.; Creamer, L. K.; Singh, H. *International Dairy Journal* **2010**, *20*, 571.
(2) Hamada, D.; Tanaka, T.; Tartaglia, G. G.; Pawar, A.; Vendruscolo, M.; Kawamura, M.; Tamura, A.; Tanaka, N.; Dobson, C. M. *Journal of Molecular Biology* **2009**, *386*, 878.
(3) Bromley, E. H. C.; Krebs, M. R. H.; Donald, A. M. *Faraday Discussions* **2005**, *128*, 13.
(4) Gosal, W. S.; Clark, A. H.; Pudney, P. D. A.; Ross-Murphy, S. B. *Langmuir* **2002**, *18*, 7174.
(5) Krebs, M. R. H.; Devlin, G. L.; Donald, A. M. *Biophysical journal* **2009**, *96*, 5013.
(6) Donald, A. M. *Soft Matter* **2008**, *4*, 1147.
(7) van der Linden, E.; Venema, P. *Current Opinion in Colloid & Interface Science* **2007**, *12*, 158.
(8) Foegeding, E. A. *Food Biophysics* **2006**, *1*, 41.
(9) Jones, O. G.; Mezzenga, R. *Soft Matter* **2012**, *8*, 876.
(10) Hamley, I. W. *Angewandte Chemie-International Edition* **2007**, *46*, 8128.
(11) Adamcik, J.; Jung, J. M.; Flakowski, J.; De Los Rios, P.; Dietler, G.; Mezzenga, R. *Nature Nanotechnology* **2010**, *5*, 423.
(12) Solomon, M. J.; Spicer, P. T. *Soft Matter* **2010**, *6*, 1391.
(13) Loveday, S. M.; Rao, M. A.; Creamer, L. K.; Singh, H. *Journal of Food Science* **2009**, *74*, R47.
(14) Knowles, T. P. J.; Buehler, M. J. *Nature Nano* **2011**, *6*, 469.
(15) Sagis, L. M. C.; Veerman, C.; van der Linden, E. *Langmuir* **2004**, *20*, 924.
(16) Krysmann, M. J.; Castelletto, V.; Kelarakis, A.; Hamley, I. W.; Hule, R. A.; Pochan, D. J. *Biochemistry* **2008**, *47*, 4597.

(17) Loveday, S. M.; Wang, X. L.; Rao, M. A.; Anema, S. G.; Singh, H. *Food Hydrocolloids* **2012**, *27*, 242.
(18) Loveday, S. M.; Su, J.; Rao, M. A.; Anema, S. G.; Singh, H. *International Dairy Journal* **2012**, *26*, 133.
(19) Veerman, C.; de Schiffart, G.; Sagis, L. M. C.; van der Linden, E. *International Journal of Biological Macromolecules* **2003**, *33*, 121.
(20) Bolisetty, S.; Harnau, L.; Jung, J.-m.; Mezzenga, R. *Biomacromolecules* **2012**.
(21) Mudgal, P.; Daubert, C. R.; Foegeding, E. A. *Food Hydrocolloids* **2009**, *23*, 1762.
(22) Akkermans, C.; van der Goot, A. J.; Venema, P.; van der Linden, E.; Boom, R. M. *Food Hydrocolloids* **2008**, *22*, 1315.
(23) vandenAkker, C. C.; Engel, M. F. M.; Velikov, K. P.; Bonn, M.; Koenderink, G. H. *Journal of the American Chemical Society* **2011**, *133*, 18030.
(24) van der Linden, E.; Sagis, L. M. C. *Langmuir* **2001**, *17*, 5821.
(25) Safran, S. A.; Webman, I. I.; Grest, G. S. *Physical review. A* **1985**, *32*, 506.
(26) Veerman, C.; Ruis, H.; Sagis, L. M. C.; van der Linden, E. *Biomacromolecules* **2002**, *3*, 869.
(27) Dalmas, F.; Cavaillé, J.-Y.; Gauthier, C.; Chazeau, L.; Dendievel, R. *Composites Science and Technology* **2007**, *67*, 829.
(28) Philipse, A. P.; Wierenga, A. M. *Langmuir* **1998**, *14*, 49.
(29) Kyrylyuk, A. V.; van der Schoot, P. *Proceedings of the National Academy of Sciences* **2008**, *105*, 8221.
(30) Davis, V. A.; Ericson, L. M.; Parra-Vasquez, A. N. G.; Fan, H.; Wang, Y. H.; Prieto, V.; Longoria, J. A.; Ramesh, S.; Saini, R. K.; Kittrell, C.; Billups, W. E.; Adams, W. W.; Hauge, R. H.; Smalley, R. E.; Pasquali, M. *Macromolecules* **2004**, *37*, 154.
(31) Schmidt, F. G.; Hinner, B.; Sackmann, E.; Tang, J. X. *Physical Review E* **2000**, *62*, 5509.
(32) Li, J.; Revol, J. F.; Marchessault, R. H. *Journal of Colloid and Interface Science* **1996**, *183*, 365.
(33) Bercea, M.; Navard, P. *Macromolecules* **2000**, *33*, 6011.
(34) Moller, P. C. F.; Fall, A.; Bonn, D. *Europhysics Letters* **2009**, *87*.
(35) Ghadami, S. A.; Khodarahmi, R.; Ghobadi, S.; Ghasemi, M.; Pirmoradi, S. *Biophysical Chemistry* **2011**, *159*, 311.
(36) Ikeda, S. *Food Hydrocolloids* **2003**, *17*, 399.
(37) Mewis, J.; Wagner, N. J. *Advances in Colloid and Interface Science* **2009**, *147-48*, 214.
(38) Stokes, J. R.; Telford, J. H. *Journal of Non-Newtonian Fluid Mechanics* **2004**, *124*, 137.
(39) Mleko, S.; Foegeding, E. A. *Journal of Food Science* **2000**, *65*, 139.
(40) Moller, P. C. F.; Mewis, J.; Bonn, D. *Soft Matter* **2006**, *2*, 274.
(41) Wang, H.; Christopherson, G. T.; Xu, Z. Y.; Porcar, L.; Ho, D. L.; Fry, D.; Hobbie, E. K. *Chemical Physics Letters* **2005**, *416*, 182.
(42) Hammouda, B.; Worcestery, D. *Biophysical journal* **2006**, *91*, 2237.
(43) Lott, J. R.; McAllister, J. W.; Arvidson, S. A.; Bates, F. S.; Lodge, T. P. *Biomacromolecules* **2013**, *14*, 2484.
(44) Arnaudov, L. N.; de Vries, R.; Stuart, M. A. C. *Journal of Chemical Physics* **2006**, *124*.
(45) Zhou, W.; Islam, M. F.; Wang, H.; Ho, D. L.; Yodh, A. G.; Winey, K. I.; Fischer, J. E. *Chemical Physics Letters* **2004**, *384*, 185.

(46) Yurekli, K.; Mitchell, C. A.; Krishnamoorti, R. *Journal of the American Chemical Society* 2004, *126*, 9902.
(47) Fakhri, N.; Tsyboulski, D. A.; Cognet, L.; Weisman, R. B.; Pasquali, M. *Proceedings of the National Academy of Sciences* 2009, *106*, 14219.
(48) Veerman, C.; Baptist, H.; Sagis, L. M. C.; Van der Linden, E. *Journal of Agricultural and Food Chemistry* 2003, *51*, 3880.
(49) Klunk, W. E.; Jacob, R. F.; Mason, R. P. *Analytical Biochemistry* 1999, *266*, 66.

Supplementary Figures and Tables

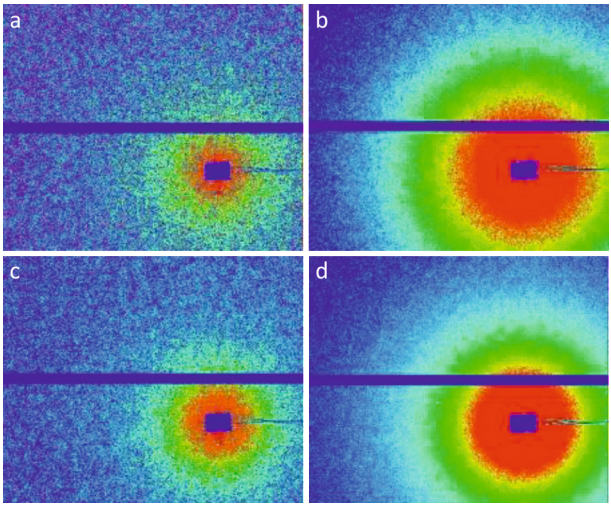

SI Figure 8.1: SAXS 2D images of unsheared fibril suspensions inside capillaries. a and b) long straight fibrils at respectively φ=0.18 vol% and φ=1.8 vol%; c and d) short, worm-like fibrils at φ=0.18 vol% and φ=1.8 vol%. All samples show isotropic scattering profiles. Rectangle with a thread on the right-hand side in the middle of all the images is the beam stop, blue lines are caused by the detector.

Appendix

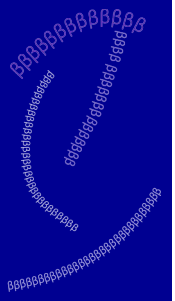

Summary

Approximately 15 to 20% of the human body consists of proteins and peptides, and a similar percentage is observed for bacteria. Proteins serve a wide range of functions in nature, for instance in transport, storage, movement, support and stability, or as antibodies, enzymes or hormones. Proteins are composed of strings of amino acids and can fold into complex three-dimensional structures. This molecular (or secondary) structure is essential for the execution of their function. A special case of a three-dimensional structure of proteins are amyloids. Amyloids are aggregates which are formed upon self-assembly of peptides and proteins of diverse sequence, native structure and function. It is thought that the amyloid state is an intrinsic characteristic of polypeptide molecules under denaturing conditions. Amyloid fibrils are generally several nanometers in diameter and up to micrometers in length. They are remarkably rigid and strong, properties which are thought to have their origin in the hydrogen-bonded β-sheet core. In nature, amyloids are wide spread, in organism ranging from bacteria and fungi to invertebrates and man. In many cases they serve a useful purpose, for example by providing protection or stability, in cell adhesion or aggregation. However, amyloids are also related to a broad range of human diseases, including Alzheimer's and Parkinson's disease and type II diabetes mellitus, in which oligomers and/or fibrils accumulate in tissue and cause cell death. From an engineering perspective, the excellent mechanical properties and the tunable properties of amyloids make that (non-toxic) amyloids are potential candidates for applications in foods, tissue engineering and materials science.

The central goal in this thesis is to investigate the biophysical properties of amyloid fibrils over a range of length scales: from molecular structure to single fibril rigidity and network mechanics. Insights into the relation between the molecular structure and the mechanical properties are essential to understand and control the assembly process of amyloid fibrils. This is important both for rational therapeutic treatment of amyloid-related diseases and for potential applications of amyloids. In this thesis, I described the study of the molecular structure of model amyloid fibrils using various vibrational spectroscopy techniques. The morphology and rigidity of amyloid fibrils were determined using atomic force microscopy, fluorescence microscopy and scanning transmission electron microscopy. Network mechanics were measured by macroscopic rheometry. I investigated on all these length scales distinct types of amyloid fibrils, with the aim to get a better understanding of the origin of structural polymorphism of amyloid fibrils. Furthermore, control of amyloid formation and disaggregation by the polyphenol epi-gallocatechin-3-gallate (EGCG), a natural compound which potentially can be used for treatment of amyloid-related diseases, was studied.

In the first part of this thesis I focused on the molecular structure of amyloid fibrils and their relation to the structural polymorphism observed for amyloids. In Chapter 2, the relation between the molecular structure, morphology and rigidity of amyloid fibrils was investigated. The model protein β-lactoglobulin (β-lg), a milk protein, forms distinct types of amyloid fibrils dependent on the protein concentration during incubation at acidic pH and high temperature. At low β-lg concentration, the fibrils that are formed are long and straight, as observed with atomic force microscopy (AFM). The persistence length, a measure for rigidity, was several micrometers, in the order of the contour length. At high β-lg concentrations, short, worm-like fibrils are formed with a 40 times lower persistence length. Using vibrational sum-frequency generation spectroscopy (VSFG), we showed that the β-sheet content of the straight fibrils was higher than that of the worm-like fibrils. In Chapter 3 I investigated the differences in molecular structure and composition of the two fibril types in more detail. Mass spectrometry experiments show that the composition of the two fibril types is similar. The molecular structure of the fibrils was investigated with various bulk spectroscopy techniques (circular dichroism, Fourier transform infrared and Raman spectroscopy). All three techniques showed a large contribution of the β-sheet core of the amyloid fibrils. Surprisingly, no differences in molecular structure were observed for the two distinct fibril types, in contrast to the VSFG measurements. A drawback of the bulk spectroscopic techniques is that it is not possible to distinguish between different polymorphic forms of amyloid fibrils, or between their core and the surface. Therefore the molecular structure of the surface of the fibrils was probed using tip-enhanced Raman spectroscopy (TERS). In TERS, AFM and Raman spectroscopy are combined, which provides the possibility to probe the molecular structure of the fibrils with nanometer resolution. I showed that the surface of both types of amyloids formed from β-lg mainly contains unordered or α-helical structures, in contrast to their β-sheet core. Although no differences between distinct fibril types could be observed using the bulk-spectroscopic techniques, TERS experiments showed that the β-sheet content on the surface of the long, straight fibrils was higher than that on the worm-like fibrils. To elucidate the origin of the difference in morphology and molecular structure, the kinetics of fibril formation were followed using mass spectrometry and AFM. With mass spectrometry the hydrolysis of β-lg monomers into peptide fragments was investigated. The ratio between intact monomers and peptide fragments decreased faster for samples at high than at low β-lg concentration. Probably this difference is caused by the incorporation of intact monomers into worm-like fibrils formed at high β-lg concentration, while straight fibrils are composed of peptides. Using AFM, fibrils were observed after shorter incubation times for samples incubating at high β-lg concentration than for samples at low

concentration. In summary, the origin of the difference in morphology and molecular structure of amyloid fibrils is likely related to their formation kinetics.

In Chapter 4 TERS was used to investigate amyloid fibrils formed from the diabetes-related peptide hIAPP in detail. To understand amyloid toxicity, it is important to know the surface structure of amyloids. The molecular structure and amino acid composition of the surface of the fibrils was probed with nanometer resolution. Similar to β-lg amyloids, the surface of the hIAPP fibrils is mainly composed of unordered or α-helical structures, in contrast to the core, which is composed of β-sheets. Dependent on the pH during fibril formation, fibrils with a different surface structure and amino acid residue composition are formed. Furthermore, the molecular structure of hIAPP fibrils formed at a lipid interface was probed, because it is thought that hIAPP forms amyloids at the plasma membrane *in vivo*.

In the second part of my thesis I focused on the effect of the green tea polyphenol EGCG on amyloid formation, morphology and rigidity. EGCG is one of the most promising therapeutic agents for treatment of amyloid-related diseases. In Chapter 5 the effect of EGCG on the formation of hIAPP amyloid fibrils at a lipid interface was studied. Although EGCG is able to inhibit amyloid formation efficiently in bulk solution, at lipid interfaces the inhibition is less efficient. The formation of amyloids was followed by probing the molecular structure of hIAPP using VSFG and by imaging the amyloids using AFM. EGCG is not able to disaggregate mature fibrils at a phospholipid interface, in contrast to fibrils in bulk solution, which were disaggregated upon incubation with EGCG. In Chapter 6 the effect of EGCG at neutral and acid pH on amyloid fibrils was studied. As a model protein, hen egg white lysozyme (HEWL) was used. I showed that at acidic pH EGCG does not affect the morphology or rigidity of the amyloid fibrils. However, at neutral pH a subpopulation of thick fibrils was formed upon incubation with EGCG. AFM and electron microscopy imaging revealed that the thick fibrils formed large fibril aggregates. In the second part of the thesis I showed that EGCG is able to disaggregate and bundle amyloid fibrils, but that the efficacy is highly dependent on the conditions, like solution pH and the presence of lipid interfaces. It is therefore important to consider the treatment conditions during the design and testing of amyloid inhibitors.

The third part of my thesis focused on the mechanics of amyloid fibrils and networks thereof. In Chapter 7 the rigidity of HEWL amyloid fibrils was investigated using different approaches. The first approach was the determination of the persistence length based on fibril conformations of a large ensemble of amyloid fibrils imaged using AFM. An average persistence length between 2.5 and 4.4 μm was measured, depending on fibril hydration and the use of glass or mica as imaging substrate. The disadvantage of this

approach is that the fibrils are immobilized and dried on a surface, which potentially can affect their conformation and structure. Therefore I also used a second approach: fibrils were labeled with a fluorescent dye and the thermal bending undulations of freely fluctuating fibrils suspended in water were imaged using fluorescence microscopy. The range of persistence lengths that was observed for 8 fibrils was remarkably large: between 0.7 and 6.7 μm. For 2 other fibrils, the persistence length was even too large to measure by video microscopy. In summary, the two different techniques give similar average values of the persistence length in the range of several micrometers, but time-lapse imaging reveals a large variability for fibrils within the same sample. This variability is a signature of the structural polymorphism of amyloid fibrils.

In the last chapter of this thesis, Chapter 8, I investigated suspensions of amyloid fibrils on the largest length scale. The rheological behavior of amyloid fibril suspension is particular relevant for their applications, for instance in materials science and food texturing. I compared the viscoelastic properties of suspensions of the two distinct types of β-lg amyloid fibrils described in Chapters 2 and 3: long, rigid versus short, worm-like fibrils. Both fibril types behave in suspension as soft solids with an apparent yield stress. Strong shear-thinning behavior over a large range of shear rates was observed. By using a combination of rheology and small-angle neutron scattering (rheo-SANS) it was shown that long, rigid fibrils align under shear, while for short, worm-like fibrils no change in alignment was observed, even at high shear rates. This suggest that the strong shear-thinning behavior of short, worm-like fibrils is caused by weak attractive forces between the fibrils. In conclusion, I showed that suspensions of β-lg amyloid fibrils behave rheologically as suspensions of weakly attractive, semi-flexible rods.

The research in this thesis is a tiny step forward towards a better understanding of the structure and mechanics of amyloid fibrils. However, many open questions remain yet unresolved. In all research on amyloid fibrils, their polymorphic nature should be kept in mind, because this can highly affect bulk measurements both of molecular structure and mechanical properties. To avoid this problem, techniques which can be used to study single amyloid fibrils are highly promising to resolve the properties of amyloid fibrils. For instance, to get a better understanding of the molecular structure of amyloid fibrils, it would be interesting to study amyloid fibrils formed from short peptides with known sequence, for example tri-peptides, with high spatial resolution using TERS. Probably this can lead to the development of a structural model of amyloid fibrils, which can be compared to models resolved from nuclear magnetic resonance (NMR) measurements. In this thesis I showed the proof of principle of measurements of the rigidity of single amyloid fibrils by analysis of their thermal undulations. This could be used to study distinct types of amyloids in more detail, to compare fibrils formed from

different peptides or proteins or to test the effect of molecules that interact with amyloids, for instance polyphenols. By combining fluorescence microscopy with AFM imaging, for example using microfluidic devices, it would be possible to relate high resolution morphologic information to fibril mechanics.

For the therapeutic treatment of amyloid-related diseases there is still a long way to go. Although recent results obtained with natural compounds such as polyphenols look promising, understanding of the interactions of EGCG on amyloid oligomers, fibrils and the effect on formation kinetics is still limited. Furthermore, as long as the origin and mechanism of amyloid-related diseases is not yet elucidated, a rational design of drugs to avoid or stop amyloid toxicity remains challenging.

Samenvatting

Amyloïden: van moleculaire structuur tot mechanische eigenschappen

Ongeveer 15 tot 20% van het menselijk lichaam bestaat uit eiwitten, ongeveer gelijk aan het eiwitpercentage van bacteriën. In de natuur spelen eiwitten een belangrijk rol in veel verschillende functies, bijvoorbeeld in transport, opslag, beweging, stevigheid en stabiliteit, of als antilichamen, enzymen of hormonen. Een eiwit is opgebouwd uit een lint van aminozuren en kan zich opvouwen in een specifieke, driedimensionale structuur. Deze structuur, de moleculaire of secundaire structuur genoemd, is essentieel voor de functie van het eiwit. Een speciale driedimensionale structuur van eiwitten zijn amyloïden. Amyloïden zijn aggregaten die kunnen worden gevormd als eiwitten in elkaar vouwen. Dit vouwingsproces is onafhankelijk van de sequentie, structuur en functie van het eiwit; er wordt gedacht dat de amyloïde vouwing een wezenlijke eigenschap is van eiwitten in hun gedenatureerde staat. Amyloïd fibrillen zijn meestal een paar nanometer in diameter en kunnen micrometers lang zijn. Ze zijn opvallend stijf en sterk, eigenschappen die waarschijnlijk worden veroorzaakt door de kern van β-sheets die gestabiliseerd worden door waterstofbruggen. Amyloïden komen veel voor in de natuur, zowel in bacteriën, schimmels, dieren en mensen. In veel gevallen vervullen ze een nuttige rol, onder andere bij het geven van stabiliteit of bescherming, en in celadhesie en cel aggregatie. Maar amyloïden spelen ook een rol in verschillende ziekten, bijvoorbeeld de ziekte van Alzheimer, de ziekte van Parkinson en type II diabetes mellitus. Oligomeren en/of amyloïd fibrillen kunnen ophopen in weefsels en organen en schade veroorzaken. Wanneer we vanuit een ander oogpunt naar amyloïden kijken, zijn (niet-schadelijke) amyloïden door hun speciale eigenschappen juist een aantrekkelijke kandidaat voor toepassingen in tissue engineering, materiaalkunde of de voedingsindustrie.

Het belangrijkste doel in dit proefschrift is de biofysische eigenschappen van amyloïden te onderzoeken over verschillende lengteschalen: van de moleculaire structuur tot de stijfheid van fibrillen en de mechanische eigenschappen van netwerken. Een beter inzicht in de relatie tussen de moleculaire structuur en de mechanische eigenschappen is essentieel om de vorming van amyloïden te kunnen begrijpen en controleren. Dit is aan de ene kant belangrijk om amyloïd-gerelateerde ziekten te kunnen bestrijden, en aan de andere kant voor potentiële toepassingen van amyloïden. In dit proefschrift beschrijf ik het onderzoek naar de moleculaire structuur van model amyloïd fibrillen gemeten met verschillende spectroscopische technieken. De morfologie en stijfheid van de amyloïd fibrillen werden bepaald door een combinatie van atomic force microscopy, fluorescentie microscopie en scanning transmission electron microscopy. De mechanische eigenschappen van netwerken van amyloïd fibrillen werd gemeten met

macroscopische reometrie. Op al deze lengteschalen werden verschillende typen amyloïd fibrillen onderzocht, met als doel beter te begrijpen wat de oorzaak is van polymorfisme. Ook heb ik het effect van het polyfenol epi-gallocatechin-3-gallate (EGCG), een potentieel medicijn voor de behandeling van amyloïd-gerelateerde ziekten, op de vorming en afbraak van amyloïden bestudeerd.

In het eerste deel van mijn proefschrift focus ik op het onderzoek naar de moleculaire structuur van amyloïden en de relatie tot polymorfisme. In Hoofdstuk 2 onderzocht ik de relatie tussen de moleculaire structuur, morfologie en stijfheid van amyloïd fibrillen. Het modeleiwit β-lactoglobuline (β-lg), een eiwit in melk, vormt twee verschillende typen fibrillen afhankelijk van de eiwitconcentratie tijdens incubatie bij een lage pH en hoge temperatuur. Bij lage β-lg concentraties worden lange, stijve fibrillen gevormd, terwijl bij een hoge β-lg concentratie de fibrillen kort en kronkelig zijn. De morfologie van de amyloïden werd onderzocht met atomic force microscopy (AFM). Voor beide typen fibrillen werd de persistentielengte, een maat voor de stijfheid, bepaald. Voor de lange fibrillen was de persistentielengte een paar micrometer, ongeveer gelijk aan hun lengte. Voor de korte fibrillen was de persistentielengte ongeveer 40 keer zo laag. Met vibrational sum-frequency generation (VSFG) spectroscopie lieten we zien dat lange, stijve fibrillen voor een groter deel bestaan uit β-sheets dan de korte, kronkelige fibrillen. In Hoofdstuk 3 ga ik dieper in op de verschillen in moleculaire structuur en compositie van de twee typen fibrillen. De moleculaire structuur werd met verschillende bulk spectroscopie technieken onderzocht (circular dichroism, Fourier transform infrared en Raman spectroscopie). Alle drie technieken laten een grote bijdrage van de β-sheet kern van de fibrillen zien. Opvallend genoeg werden er geen verschillen gevonden tussen de twee verschillende typen fibrillen, zoals met VSFG wel het geval was. Een nadeel van deze bulktechnieken is dat er geen onderscheid gemaakt kan worden tussen verschillende polymorfe vormen van fibrillen in een sample, of tussen de kern en het oppervlak van de fibrillen. Daarom onderzochten we de moleculaire structuur van het oppervlak van de fibrillen met tip-enhanced Raman spectroscopy (TERS). In TERS wordt de hoge resolutie van AFM gecombineerd met Raman spectroscopie, wat het mogelijk maakt de moleculaire structuur van amyloïden met nanometer-resolutie te bepalen. Ik heb laten zien dat het oppervlak van beide typen amyloïden gevormd van β-lg voornamelijk bestaat uit random of α-helix structuren, in groot contrast met hun kern van β-sheets. Ondanks dat er met de verschillende bulktechnieken geen onderscheid kon worden gemaakt tussen de typen fibrillen, lieten TERS metingen zien dat het gehalte β-sheet structuur op het oppervlak van de fibrillen hoger was voor de lange, stijve dan voor de korte kronkelige fibrillen. Om de oorsprong van de verschillen in morfologie, stijfheid en structuur te begrijpen werd de kinetiek van fibrilvorming onderzocht met massaspectrometrie en AFM. Met

massaspectroscopie werd de hydrolyse van de monomeren gevolgd. De verhouding tussen intacte monomeren en peptidefragmenten nam sneller af voor samples bij een hoge dan bij een lage β-lg concentratie. Mogelijk wordt dit verschil veroorzaakt doordat intacte monomeren in the korte, kronkelige fibrillen worden ingebouwd, terwijl dit niet of minder gebeurt bij de lange, stijve fibrillen. AFM liet zien dat bij een hoge eiwitconcentratie de eerste fibrillen na kortere incubatietijd werden gevormd dan bij samples met een lage eiwitconcentratie. Samenvattend is de oorsprong van het verschil in morfologie en moleculaire structuur van amyloïd fibrillen waarschijnlijk gerelateerd aan de kinetiek van fibrilvorming.

In **Hoofdstuk 4** werden amyloïd fibrillen gevormd van hIAPP, een peptide gerelateerd aan type 2 diabetes mellitus, onderzocht met TERS. Om de schadelijkheid van amyloïden beter te begrijpen is het belangrijk te weten wat de structuur van het oppervlak van amyloïden is. Met TERS werden de moleculaire structuur en de aminozuurcompositie van het oppervlak van hIAPP amyloïd fibrillen met nanometer-resolutie bepaald. Net zoals voor de β-lg amyloïden bestaat het oppervlak van hIAPP amyloïden voornamelijk uit random of α-helix structuren, terwijl de kern is opgebouwd uit β-sheets. Onder invloed van de pH-waarde tijdens vorming werden fibrillen met verschillende moleculaire structuur en aminozuurcompositie gevormd. Ook de moleculaire structuur van amyloïden gevormd in de aanwezigheid van een modelmembraan werd onderzocht, omdat *in vivo* hIAPP amyloïden waarschijnlijk vooral op het plasmamembraan van cellen worden gevormd.

In het tweede deel van mijn proefschrift focuste ik op het effect van het polyfenol EGCG, een bestandsdeel van groene thee, op amyloïd-vorming en op de morfologie en stijfheid van amyloïden. EGCG is een van de meest veelbelovende medicijnen om amyloïd-gerelateerde ziekten te behandelen. In **Hoofdstuk 5** werd het effect van EGCG op de vorming van hIAPP amyloïden in de aanwezigheid van een modelmembraan onderzocht. Ondanks dat EGCG de vorming van amyloïden in bulkoplossing efficiënt kan voorkomen, is het in aanwezigheid van een modelmembraan minder effectief. De vorming van amyloïden werd gevolgd door de moleculaire structuur te meten met VSFG en de morfologie te bepalen met AFM. EGCG breekt geen bestaande fibrillen af in de aanwezigheid van een modelmembraan, terwijl in bulkoplossing de amyloïd fibrillen wel afgebroken worden. In **Hoofdstuk 6** werd het effect van EGCG op amyloïd fibrillen bij verschillende pH-waarden bestudeerd. Amyloïden werden gevormd van het kippeneiwit lysozyme (hen egg white lysozyme, HEWL). In een zure omgeving kan EGCG de morfologie of stijfheid van fibrillen niet veranderen, maar bij een neutrale pH-waarde wordt een populatie van dikke fibrillen gevormd na incubatie met EGCG. AFM en elektronenmicroscopie lieten zien dat de dikke fibrillen grote aggregaten vormen. In het tweede deel van mijn proefschrift heb ik laten zien dat EGCG fibrillen kan afbreken

of bundelen, maar dat de efficiëntie erg afhankelijk is van de condities, zoals de pH-waarde en de aanwezigheid van een modelmembraan. Het is daarom essentieel om rekening te houden met de condities in het lichaam tijdens het onderzoek naar medicijnen voor amyloïd-gerelateerde ziekten.

Het derde deel van mijn thesis gaat over de mechanische eigenschappen van amyloïd fibrillen en netwerken. In Hoofdstuk 7 onderzocht ik met verschillende methoden de stijfheid van amyloïd fibrillen gevormd van HEWL. De eerste aanpak was het bepalen van de persistentielengte van de fibrillen op basis van de conformatie van een groot aantal fibrillen dat werd bekeken met AFM. De gemiddelde persistentielengte lag tussen 2.5 en 4.4 µm, afhankelijk van de hydratatie van de fibrillen en of er glas of mica als substraat voor AFM werd gebruikt. Het nadeel van deze aanpak is dat de fibrillen op een oppervlak plakken en worden gedroogd, wat hun eigenschappen kan beïnvloeden. Daarom gebruikte ik ook een andere methode: fluorescent gelabelde fibrillen werden bekeken met fluorescentiemicroscopie. De thermische buiging van 8 vrij-bewegende fibrillen in water werd geanalyseerd. De persistentielengte van deze 8 fibrillen viel in een range tussen 0.7 en 6.7 µm. Twee fibrillen waren zo stijf dat de persistentielengte niet kon worden bepaald met videomicroscopie. In conclusie geven de twee verschillende methoden vergelijkbare gemiddelde waarden van de persistentielengte in de orde grootte van enkele micrometers, maar met fluorescentiemicroscopie is het mogelijk de grote variabiliteit tussen fibrillen in een sample te detecteren. Deze variabiliteit laat de polymorfologie van de fibrillen zien.

In het laatste hoofdstuk, Hoofdstuk 8, heb ik suspensies van amyloïd fibrillen op de grootste lengteschaal onderzocht. De reologische eigenschappen van fibrilsuspensies zijn met name relevant voor toepassingen van amyloïden, bijvoorbeeld in de materiaalkunde of de voedingsindustrie. Ik heb de visco-elastische eigenschappen van suspensies van de verschillende typen amyloïden beschreven in hoofdstuk 2 en 3 vergeleken. Beide typen gedragen zich als soft solids met een yield stress. De viscositeit van de fibrilsuspensies neemt af bij een stijgende shear rate, ook wel shear-thinning gedrag genoemd. Door een combinatie van reologie en small-angle neutron scattering (rheo-SANS) te gebruiken kon ik laten zien dat lange, stijve fibrillen uitlijnen onder shear, maar korte, kronkelige fibrillen niet. Dit wekt de suggestie van het sterke shear-thinning gedrag van korte fibrillen wordt veroorzaakt door zwakke attractieve krachten tussen de fibrillen. Samenvattend heb ik laten zien dat suspensies van β-lg amyloïd fibrillen zich reologisch gedragen als suspensies van zwak-attractieve, semi-flexibele staven.

Het onderzoek in dit proefschrift is een klein stapje vooruit in een beter begrip van de structuur en mechanische eigenschappen van amyloïd fibrillen. Ondanks dat zijn er nog

veel open vragen. Het is belangrijk om in al het onderzoek naar amyloïd fibrillen hun polymorfe natuur in gedachte te houden, omdat dit de resultaten van onderzoek in bulk naar de structuur en mechanische eigenschappen erg kan beïnvloeden. Om dit probleem te omzeilen kan gebruik worden gemaakt van een aantal veelbelovende technieken waarbij enkele fibrillen in plaats van bulk samples kunnen worden onderzocht. Om de structuur van amyloïden te onderzoeken zou bijvoorbeeld gebruik kunnen worden gemaakt van TERS. Wanneer amyloïden gevormd van korte peptiden met een bekende sequentie met een hoge resolutie zouden worden onderzocht met TERS, is het misschien mogelijk een model van de structuur te ontwikkelen, dat kan worden vergeleken met modellen gebaseerd op nuclear magnetic resonance (NMR) experimenten. In dit proefschrift heb ik laten zien dat het mogelijk is de stijfheid van amyloïd fibrillen te bepalen door filmpjes gemaakt met fluorescentiemicroscopie te analyseren. Dit kan in de toekomst gebruikt worden om verschillende typen amyloïden in detail te onderzoeken, om amyloïden gevormd van verschillende eiwitten te vergelijken, of om het effect van moleculen die een interactie aangaan met amyloïden te testen. Door fluorescentiemicroscopie te combineren met AFM, bijvoorbeeld door het gebruik van microfluidics, zou het mogelijk worden de mechanische eigenschappen van fibrillen te relateren aan hun morfologie.

Er is nog een lange weg te gaan voor de behandeling van amyloïd-gerelateerde ziekten. Ondanks dat recente resultaten met natuurlijke moleculen zoals polyfenolen veelbelovend lijken, is er nog weinig duidelijkheid over de interacties tussen EGCG met oligomeren, fibrillen en het effect op de vorming van amyloïden. Tenslotte, zolang de oorsprong en het mechanisme van amyloïd-gerelateerde ziekten niet opgehelderd is, zal de zoektocht naar medicijnen die schade door amyloïden kunnen voorkomen een grote uitdaging blijven.

List of publications

Journal articles

C.C. vandenAkker, M. Schleeger, M. Bonn, G.H. Koenderink: *Structural basis for the polymorphism of β-lactoglobulin amyloid-like fibrils*. In: Uversky V, Lyubchenko Y: Bio-nanoimaging: Protein Misfolding & Aggregation. Waltham, MA: Elsevier (2014).

M. Schleeger, C.C. vandenAkker, T. Deckert-Gaudig, V. Deckert, K.P. Velikov, G.H. Koenderink, M. Bonn: *Amyloids : from molecular structure to mechanical properties*. Polymer 54, 2473–2488 (2013).

O.N. Karpus, H. Veninga, R.M. Hoek, D. Flierman, J.D. van Buul, C.C. vandenAkker, E. vanBavel, M.E. Medof, R.A. van Lier, K.A. Reedquist, J. Hamann: *Shear Stress–Dependent Downregulation of the Adhesion-G Protein–Coupled Receptor CD97 on Circulating Leukocytes upon Contact with Its Ligand CD55*. J Immunol 190, 3740-3748 (2013).

M.F.M. Engel, C.C. vandenAkker, M. Schleeger, K.P. Velikov, G.H. Koenderink, M. Bonn: *The Polyphenol EGCG Inhibits Amyloid Formation Less Efficiently at Phospholipid Interfaces than in Bulk Solution*. J. Am. Chem. Soc. 134, 14781-14788 (2012).

C.C. vandenAkker, M.F.M. Engel, K.P. Velikov, M. Bonn, G.H. Koenderink: *Morphology and persistence length of amyloid fibrils are correlated to peptide molecular structure*. J. Am. Chem. Soc. 133, 18030-18033 (2011).

C.C. vandenAkker, T. Deckert-Gaudig, M. Schleeger, K.P. Velikov, V. Deckert, M. Bonn, G.H. Koenderink: *Nanoscale heterogeneity of the molecular structure of individual hIAPP amyloid fibrils revealed with tip-enhanced Raman spectroscopy* (submitted for publication).

Conference contributions

Oral

C.C. vandenAkker, M.F.M. Engel, K. Velikov, M. Bonn, G.H. Koenderink: *Morphology and persistence length of amyloid fibrils are correlated to peptide molecular structure,* Dutch Soft Matter Meeting, Eindhoven, The Netherlands, November 2011.

C.C. vandenAkker, M.F.M. Engel, K. Velikov, M. Bonn, G.H. Koenderink: *Morphology and persistence length of amyloid fibrils are correlated to peptide molecular structure,* Physics@FOM, Veldhoven, The Netherlands, January 2012.

C.C. vandenAkker, M.F.M. Engel, K. Velikov, M. Bonn, G.H. Koenderink: *Characterization of β-lactoglobulin and hen egg white lysozyme fibrils over different length scales,*

International symposium on food rheology and structure, Zurich, Switzerland, April 2012.

C.C. vandenAkker, M. Schleeger, T. Deckert-Gaudig, V. Deckert, M. Bonn, G.H. Koenderink: *Unraveling the link between peptide molecular structure and morphology of amyloid fibrils,* KNAW biophysics meeting, Amsterdam, The Netherlands, November 2012.

C.C. vandenAkker, M. Schleeger, T. Deckert-Gaudig, V. Deckert, M. Bonn, G.H. Koenderink: *Unraveling the link between amyloid fibril mechanics and molecular conformation,* Biophysical Society Meeting, Philadelphia, USA, February 2013.

C.C. vandenAkker, M. Schleeger, T. Deckert-Gaudig, V. Deckert, M. Bonn, G.H. Koenderink: *Unraveling the molecular conformation of amyloid fibrils,* Molecular and Cellular Biophysics, Veldhoven, The Netherlands, October 2013.

C.C. vandenAkker, G.H. Koenderink: *Amyloids: connecting from single fibril mechanics to macroscopic rheology,* Physics@FOM, Veldhoven, The Netherlands, January 2014.

Poster

C.C. vandenAkker, G.H. Koenderink: *Morphology and micromechanics of amyloid nanofibrils,* NanoBioViews: Scanning Probe Microscopy and Optical Tweezers in Life Sciences, Berlin, Germany, October 2010.

C.C. vandenAkker, G.H. Koenderink: *Structure and micromechanics of amyloid nanofibrils,* Society of Rheology annual meeting, Santa Fe, USA, October 2010.

C.C. vandenAkker, M.F.M. Engel, M. Bonn, G.H. Koenderink: *Linking amyloid structure to amyloid fiber mechanics,* Research Meeting about Amyloid Fibrils, Prions and Precursors: Molecules for Targeted Intervention, Halle, Germany, August 2011.

C.C. vandenAkker, M.F.M. Engel, M. Schleeger, K.P. Velikov, M. Bonn, G.H. Koenderink: *Linking the peptide molecular structure of amyloid fibers to their mechanical properties.* XIII International Symposium on Amyloidosis, Groningen, The Netherlands, April 2012.

C.C. vandenAkker, J. Nguyen, M. Schleeger, M. Bonn, G.H. Koenderink: *Mechanical properties of amyloid fibrils over different length scales.* Physics@FOM, Veldhoven, The Netherlands, January 2013.

C.C. vandenAkker, Jeanette Nguyen, Michael Schleeger, Krassimir Velikov, Mischa Bonn, Gijsje Koenderink: *Amyloids: connecting from single fibril mechanics to macroscopic rheology.* Biophysical Society Meeting, San Francisco, USA, February 2014.

Dankwoord

Dit proefschrift zou niet geworden zijn wat het is zonder de hulp van een groot aantal mensen.

Gijsje, mede dankzij jou heb ik erg genoten van mijn onderzoek afgelopen jaren op AMOLF. Je hebt me veel vrijheid te geven om dat te onderzoeken waar mijn interesse naar uit gaat en om samen te werken met groepen in binnen- en buitenland. Je hebt me uitgedaagd en begeleid, en op die manier denk ik het beste in mij als wetenschapper naar boven gehaald.

Mischa, uiteindelijk staat er een stuk meer spectroscopie in mijn thesis dan ik van te voren had kunnen denken. Voor een groot deel is dat te danken aan jouw enthousiasme en ideeën. Dank dat je altijd snel tijd kon vrij maken om te overleggen, niet alleen over wetenschap maar ook over mijn toekomstplannen. Ik heb heel veel van je geleerd op verschillende gebieden.

Maarten, de eerste VSFG ervaring deed ik op samen met jou. Ik heb veel aan je gehad, zowel aan je enorme kennis over amyloïden, als ook je minitieus bijgehouden labjournals, die erg nuttig bleken nadat je bij AMOLF weg was. After Maarten left, I got you back, Michael. Always helpful, always kind, always willing to perform another experiment or to patiently explain another spectroscopy technique to me. Thank you so much for everything!

Mijn studenten Floortje, Daniella en Tjado hebben veel werk verricht, wat voor een belangrijk deel heeft bijgedragen aan hoofdstuk 6 en 7. Bedankt voor jullie enthousiasme, samenwerking en inbreng.

Also thanks to Krassi, who could give in one hour inspiration for experiments for a full year! I would also like to thank you for the opportunity to perform experiments at Unilever, with kind help of Ashok and Sandra. For the TERS experiments I had a great collaboration with Tanja and Volker Deckert. Thanks for your collaboration and hospitality in Jena. Pavlik, jij sleepte Jeanette en mij door de SANS-experimenten heen. Gelukkig is het in mijn boekje gekomen. Joachim, thanks for your help with SANS experiments and analysis. Anne, Ron, Andras and Shane, thanks for your collaboration on mass spec experiments, it was a great opportunity to perform these experiments at AMOLF and it resulted in a very important part of Chapter 3! Norbert, I met you at my very first conference, and in the last months of my PhD you were a great help with persistence length analysis, thank you for that. Paul, we discussed our work during the BPS meeting, and this resulted in a fruitful collaboration. Thanks for all your help with fluctuation analysis. De mannen van het Nanocenter, Hans, Gijs, Dimirty en Andries, brachten mij de eerste beginselen van AFM en STEM bij, de basis voor de resultaten die

in elk hoofdstuk van mijn thesis weer terug komen. Bedankt voor jullie hulp en interesse! A large number of people provided me with the possibility to perform experiments using their setups including prof. Schneider (CD), Sander Tans (plate reader), Yves Rezus and Huib Bakker (FT-IR), thank you all.

My dearest (ex-)Biosofties, thanks for all the time you spent on listening to amyloid stories. It was a great pleasure to work with you! Nicholas, I am very thankful for all your help (including moving), advices ("turn it off and on again") and the fact that I could share the happy and less happy moments of a fresh parenthood with you. I wish you, Ifon and Aubrey all the best! Jeanette, mede-amyloid-onderzoeker, eindelijk (bijna) klaar! Succes met jouw laatste loodjes! Thanks to everybody in the biolab, especially Vanda, Marjolein, Simone and Roland for all your input.

I had a great time at AMOLF, and an even better time in the PV. Many thanks to Martin, Ruben, James and Jeanette; it was a great pleasure to organize borrels and lunches together with you. Bob, ik heb goede herinneringen aan de maand in Boulder tijdens de summer school. Fijn dat jij er bij was! Also thanks to my (ex-)roomies in 1.35 (Daan, Marjon, Sergey, Roeland, Katja and Arif), and everybody else at AMOLF who made my PhD a great experience. Dear VU colleagues, thanks for the great times during the BPS meetings, I hope to meet you at the next BPS!

Afgelopen jaren heb ik behalve veel onderzoek gedaan, ook veel beleefd met vrienden en (schoon)familie; fijn dat jullie er zijn! Marjolein, Evelien en Pieter, ik kijk er naar uit ooit samen met jullie een artikel te publiceren! Jelte en Annelijn, Boukje en Bart, fijn dat we zo dicht bij elkaar wonen en dat we elkaar zo vaak zien. Ik ga dat missen komende jaren. Paps en mams, dankjulliewel dat jullie er altijd voor mij zijn. En mam, we waarderen het enorm dat je elke week op Jonna hebt gepast afgelopen jaar.

Jeroen, lievelings, zonder jou was ik waarschijnlijk nooit op AMOLF begonnen met mijn PhD, laat staan dat ik het had afgemaakt. Elk jaar beleven we samen een ander avontuurtje, en ik kijk enorm uit naar het volgende in California! Met jou erbij wordt het zeker leuk.